林盈廷

高雄醫學大學
生命科學院
生物科技學系 助理教授

第一教學大樓 N1038 室
校內分機：2792
ytlin@kmu.edu.tw

Reference Books

- Physical Chemistry for the Life Sciences
  (Engel, Drobny and Reid)
- Biophysical Chemistry
  (James P. Allen)

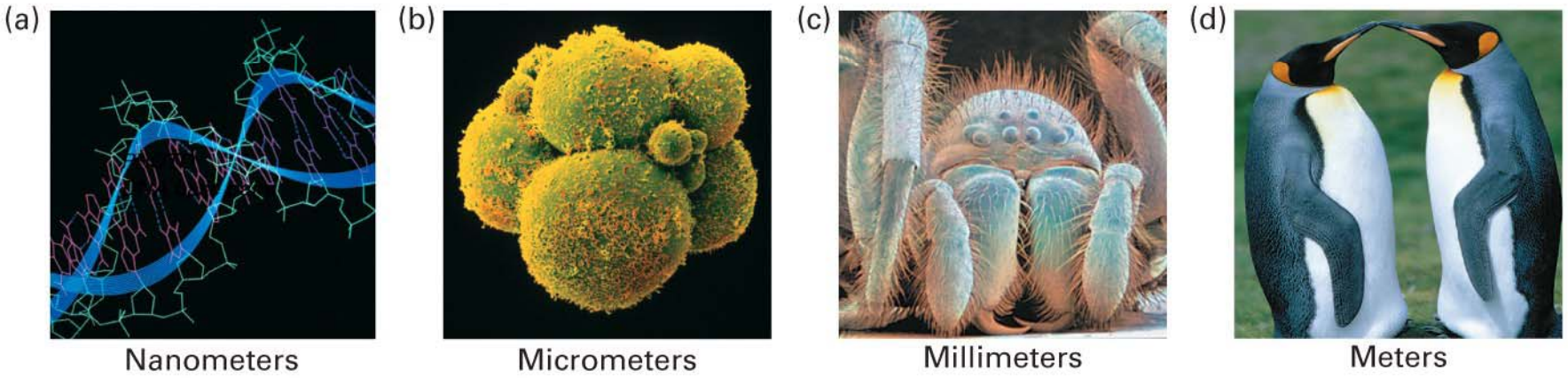

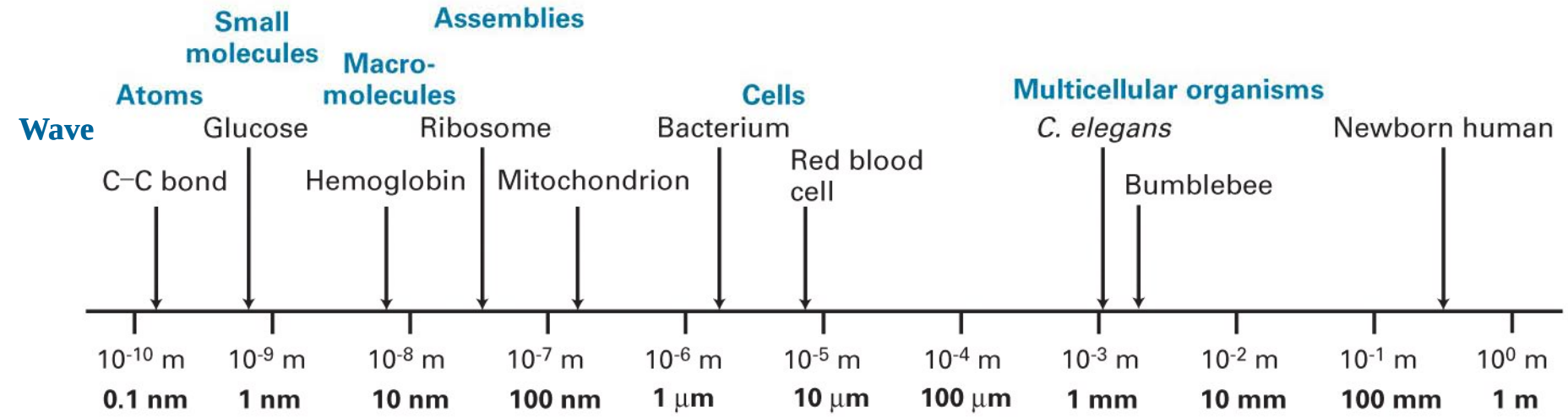

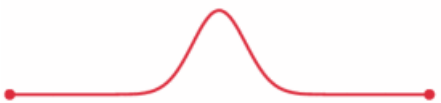

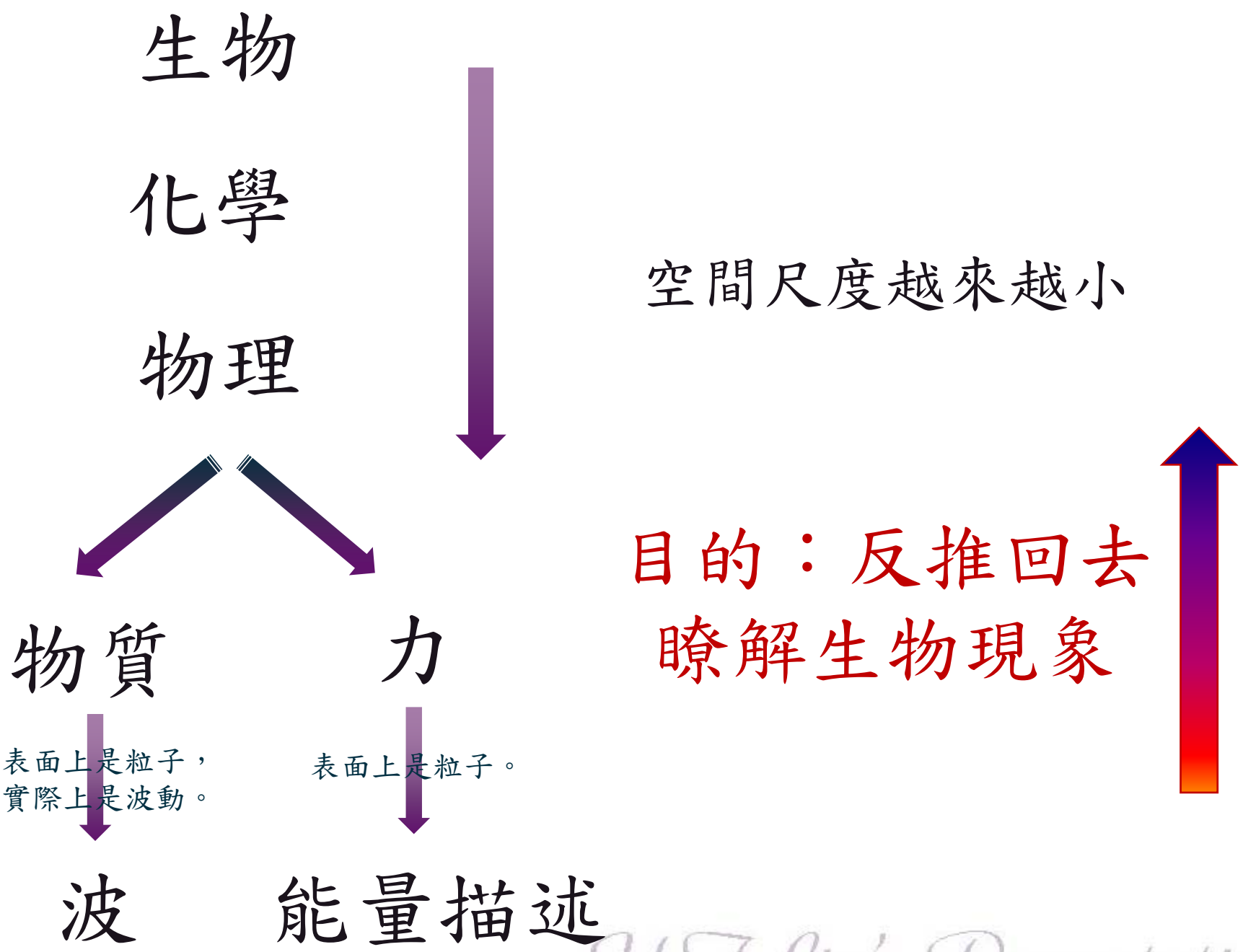

Lecture

Quantum Chemistry and Spectroscopy (II)

把物質切到最小，我們知道：
它表面上是粒子，實際上是波動。

Tiny Particle Wave equation

- Wind wave
- Airy wave theory
- Wave equation
- Acoustic wave equation
- Vibrations of a circular drum
- Standing wave
- Electromagnetic wave equation
- **Schrödinger equation**

Schröedinger equation

CORBIS-Bettmann

Figure 10.4 Erwin Schrödinger (1887–1961). Schrödinger proposed an expression of quantum mechanics that was different from but equivalent to Heisenberg's. His expression is useful because it expresses the behavior of electrons in terms of something we understand—waves. The Schrödinger equation is the central equation of quantum mechanics.

Schröedinger equation

$$-\frac{\hbar^2}{2m}\frac{d^2\psi}{dx^2}+V\psi=E\psi$$

Total energy

Potential energy

Kinetic energy

$$\hbar=\frac{h}{2\pi}=1.054\times10^{-34}\,Js$$

Chapter 13, Physical Chemistry for the Life Sciences (Engel, Drobny and Reid)

把物質切到最小，我們知道：
它表面上是粒子，實際上是波動。

Tiny Particle Wave equation

- Wind wave
- Airy wave theory
- Wave equation
- Acoustic wave equation
- Vibrations of a circular drum
- Standing wave
- Electromagnetic wave equation
- **Schrödinger equation**

Schröedinger equation

CORBIS-Bettmann

Figure 10.4 Erwin Schrödinger (1887–1961). Schrödinger proposed an expression of quantum mechanics that was different from but equivalent to Heisenberg's. His expression is useful because it expresses the behavior of electrons in terms of something we understand—waves. The Schrödinger equation is the central equation of quantum mechanics.

Schröedinger equation

$$-\frac{\hbar^2}{2m}\frac{d^2\psi}{dx^2}+V\psi=E\psi$$

Total energy

Potential energy

Kinetic energy

$$\hbar=\frac{h}{2\pi}=1.054\times10^{-34}\,Js$$

Chapter 13, Physical Chemistry for the Life Sciences (Engel, Drobny and Reid)

Quantum Chemistry 的七個法則

➔用來形成 Schröedinger equation

（也就是可用來描述電子的波動方程式）

Quantum Mechanics 的七個法則

Table 10.2 The postulates of quantum mechanics

Postulate I. The state of a system of particles is given by a wavefunction Ψ, which is a function of the coordinates of the particles and the time. Ψ contains all information that can be determined about the state of the system. Ψ must be single-valued, continuous, and bounded, and $|\Psi|^2$ must be integrable. (Discussed in section **10.2**)

Postulate II. For every physical observable or variable O, there exists a corresponding Hermitian operator $\hat{O}$. Operators are constructed by writing their classical expressions in terms of position and (linear) momentum, then replacing "x times" (that is, $x\,\cdot$) for each x variable and $-i\hbar(\partial/\partial x)$ for each p_x variable in the expression. Similar substitutions must be made for y and z coordinates and momenta. (Section **10.3**)

Postulate III. The only values of observables that can be obtained in a single measurement are the eigenvalues of the eigenvalue equation constructed from the corresponding operator and the wavefunction Ψ:

$$\hat{O}\Psi = K \cdot \Psi$$

where K is a constant. (Section **10.3**)

Postulate IV. Wavefunctions must satisfy the time-dependent Schrödinger equation:

$$\hat{H}\Psi = i\hbar\frac{\partial\Psi}{\partial t}$$

(Section **10.14**) (If it is assumed that Ψ is separable into functions of time and position, we find that this expression can be rewritten to get the time-independent Schrödinger equation, $\hat{H}\Psi = E\Psi$.) (section **10.7**)

Postulate V. The average value of an observable, $\langle O\rangle$, is given by the expression

$$\langle O\rangle = \int_{\substack{\text{all}\\\text{space}}} \Psi^{*}\hat{O}\Psi\, d\tau$$

for normalized wavefunctions. (Section **10.9**)

Postulate VI. The set of eigenfunctions for any quantum mechanical operator is a complete mathematical set of functions.

Postulate VII. If, for a given system, the wavefunction Ψ is a linear combination of nondegenerate wavefunctions Ψ_n which have eigenvalues a_n:

$$\Psi = \sum_n c_n\Psi_n \quad \text{and} \quad \hat{A}\Psi_n = a_n\Psi_n$$

then the probability that a_n will be the value of the corresponding measurement is $|c_n|^2$. The construction of Ψ as the combination of all possible Ψ_n's is called the *superposition principle.*

Quantum Mechanics 法則 1

Postulate I. The state of a system of particles is given by a wavefunction Ψ, which is a function of the coordinates of the particles and the time. Ψ contains all information that can be determined about the state of the system. Ψ must be single-valued, continuous, and bounded, and $|\Psi|^2$ must be integrable. (Discussed in section **10.2**)

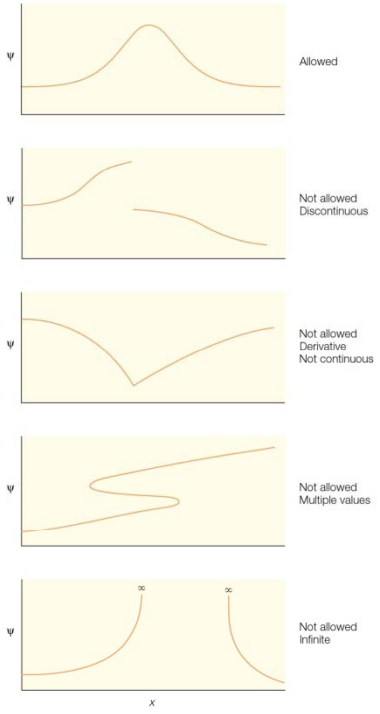

Quantum Mechanics 法則 2

Postulate II. For every physical observable or variable O, there exists a corresponding Hermitian operator $\hat{O}$. Operators are constructed by writing their classical expressions in terms of position and (linear) momentum, then replacing "x times" (that is, $x\cdot$) for each x variable and $-i\hbar(\partial/\partial x)$ for each p_x variable in the expression. Similar substitutions must be made for y and z coordinates and momenta. (Section **10.3**)

$$p_x \qquad \hat{O} = -i\hbar\left(\frac{\partial}{\partial x}\right)$$

Table 10.1 Operators for various observables and their classical counterparts[a]

Observable	Operator	Classical counterpart
Position	$\hat{x} = x \cdot$	x
	And so forth for coordinates other than x	
Momentum (linear)	$\widehat{p_x} = -i\hbar\dfrac{\partial}{\partial x}$	$p_x = mv_x$
	And so forth for coordinates other than x	
Momentum (angular)	$\widehat{L_x} = -i\hbar\left(\hat{y}\dfrac{\partial}{\partial z} - \hat{z}\dfrac{\partial}{\partial y}\right)$	$L_x = yp_z - zp_y$
Kinetic energy, 1-D[b]	$\hat{K} = -\dfrac{\hbar^2}{2m}\dfrac{d^2}{dx^2}$	$K = \dfrac{1}{2}mv_x^2 = \dfrac{p_x^2}{2m}$
Kinetic energy, 3-D[b]	$\hat{K} = -\dfrac{\hbar^2}{2m}\left(\dfrac{\partial^2}{\partial x^2} + \dfrac{\partial^2}{\partial y^2} + \dfrac{\partial^2}{\partial z^2}\right)$	$K = \dfrac{1}{2}m(v_x^2 + v_y^2 + v_z^2)$ $= \dfrac{p_x^2 + p_y^2 + p_z^2}{2m}$
Potential energy:		
Harmonic oscillator	$\hat{V} = \dfrac{1}{2}kx^2 \cdot$	$V = \dfrac{1}{2}kx^2$
Coulombic	$\hat{V} = \dfrac{q_1 \cdot q_2}{4\pi\epsilon_0 r}$.	$V = \dfrac{q_1 \cdot q_2}{4\pi\epsilon_0 r}$
Total energy	$\hat{H} = -\dfrac{\hbar^2}{2m}\left(\dfrac{\partial^2}{\partial x^2} + \dfrac{\partial^2}{\partial y^2} + \dfrac{\partial^2}{\partial z^2}\right) + \hat{V}$	$H = \dfrac{p^2}{2m} + V$

[a]Operators expressed in x, y, and/or z are Cartesian operators; operators expressed in r, θ, and/or ϕ are spherical polar operators.

[b]The kinetic energy operator is also symbolized by $\hat{T}$.

Quantum Mechanics 法則 3

Postulate III. The only values of observables that can be obtained in a single measurement are the eigenvalues of the eigenvalue equation constructed from the corresponding operator and the wavefunction Ψ:

$$\hat{O}\Psi = K \cdot \Psi$$

where K is a constant. (Section **10.3**)

observables

Quantum Mechanics 法則 4

Postulate IV. Wavefunctions must satisfy the time-dependent Schrödinger equation:

$$\hat{H}\Psi = i\hbar\frac{\partial\Psi}{\partial t}$$

time dependent

Quantum Mechanics 法則 5

Postulate V. The average value of an observable, $\langle O \rangle$, is given by the expression

$$\langle O \rangle = \int_{\substack{\text{all} \\ \text{space}}} \Psi^* \hat{O} \Psi \, d\tau$$

for normalized wavefunctions. (Section **10.9**)

average observables

Quantum Mechanics 法則 6

Postulate VI. The set of eigenfunctions for any quantum mechanical operator is a complete mathematical set of functions.

$$\int_{-\infty}^{\infty} \psi_i^*(x)\psi_j(x)dx = \begin{cases} 0, i \neq j \\ 1, i = j \end{cases} \qquad (13.21)$$

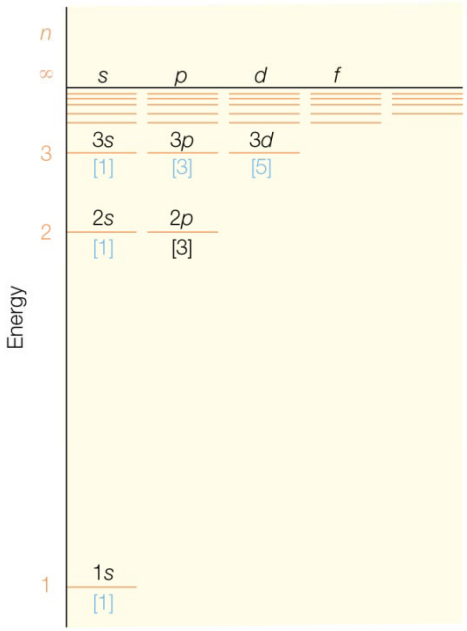

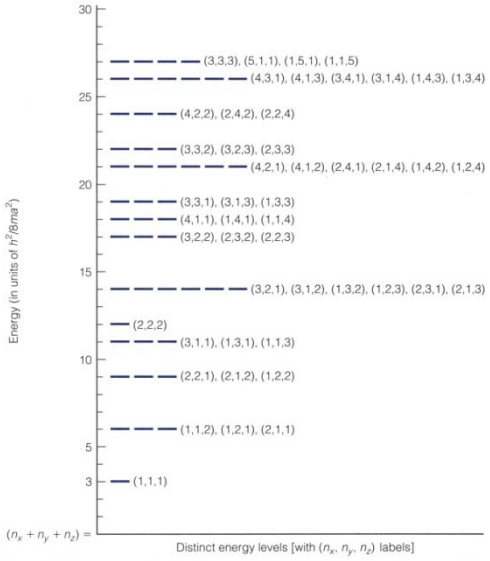

Figure 10.13 The energy levels of the 3-D particle-in-a-(cubical)-box. In this system, different wavefunctions can have the same energy. This is an example of degeneracy.

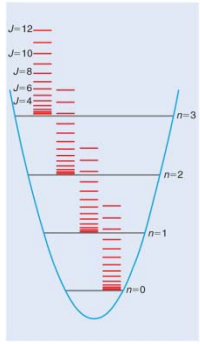

Figure: 18-08

Quantum Mechanics 法則 7

Postulate VII. If, for a given system, the wavefunction Ψ is a linear combination of nondegenerate wavefunctions Ψ_n which have eigenvalues a_n:

$$\Psi = \sum_n c_n \Psi_n \quad \text{and} \quad \hat{A}\Psi_n = a_n \Psi_n$$

then the probability that a_n will be the value of the corresponding measurement is $|c_n|^2$. The construction of Ψ as the combination of all possible Ψ_n's is called the *superposition principle*.

波

可以相加減

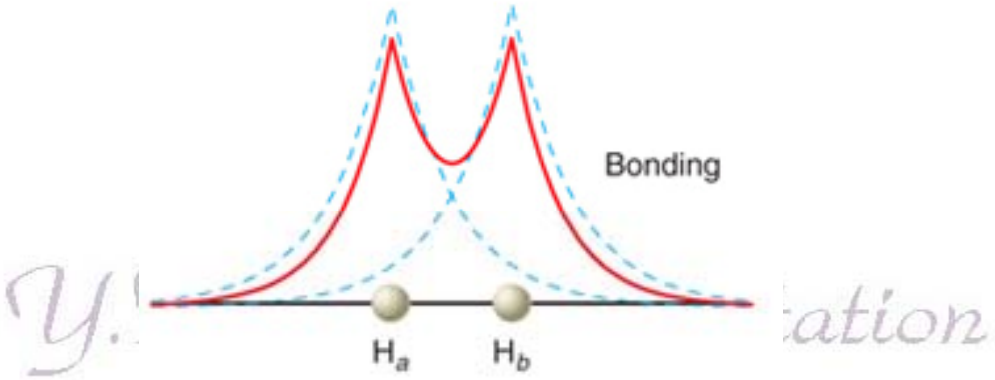

Different Systems

(Chapter 14 ~ Chapter 18)

- 不同的系統，
  有不同的 Schröedinger equation 的解

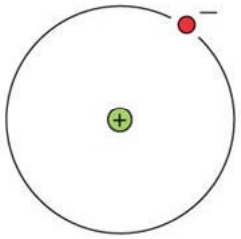

Schröedinger equation for hydrogen atom

$$-\frac{\hbar^2}{2m}\frac{d^2\psi}{dx^2}+V\psi=E\psi$$

E

ψ

TABLE 2.1 Selected Properties of the Three Basic Subatomic Particles

Name	Charge	Mass (amu)	Mass (grams)
Electron (e)	–1	5.4×10^{-4}	9.1095×10^{-28}
Proton (p)	+1	1.00	1.6725×10^{-24}
Neutron (n)	0	1.00	1.6750×10^{-24}

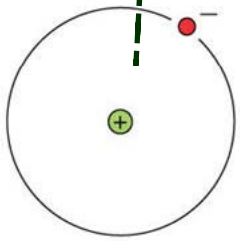

Different Systems

(Chapter 14 ~ Chapter 18)

- 不同的系統，
  有不同的 Schröedinger equation 的解

Schröedinger equation 的解，是 Orthogonal。

$$\int_{-\infty}^{\infty} \psi_i^*(x)\psi_j(x)dx = \begin{cases} 0, i \neq j \\ 1, i = j \end{cases} \qquad (13.21)$$

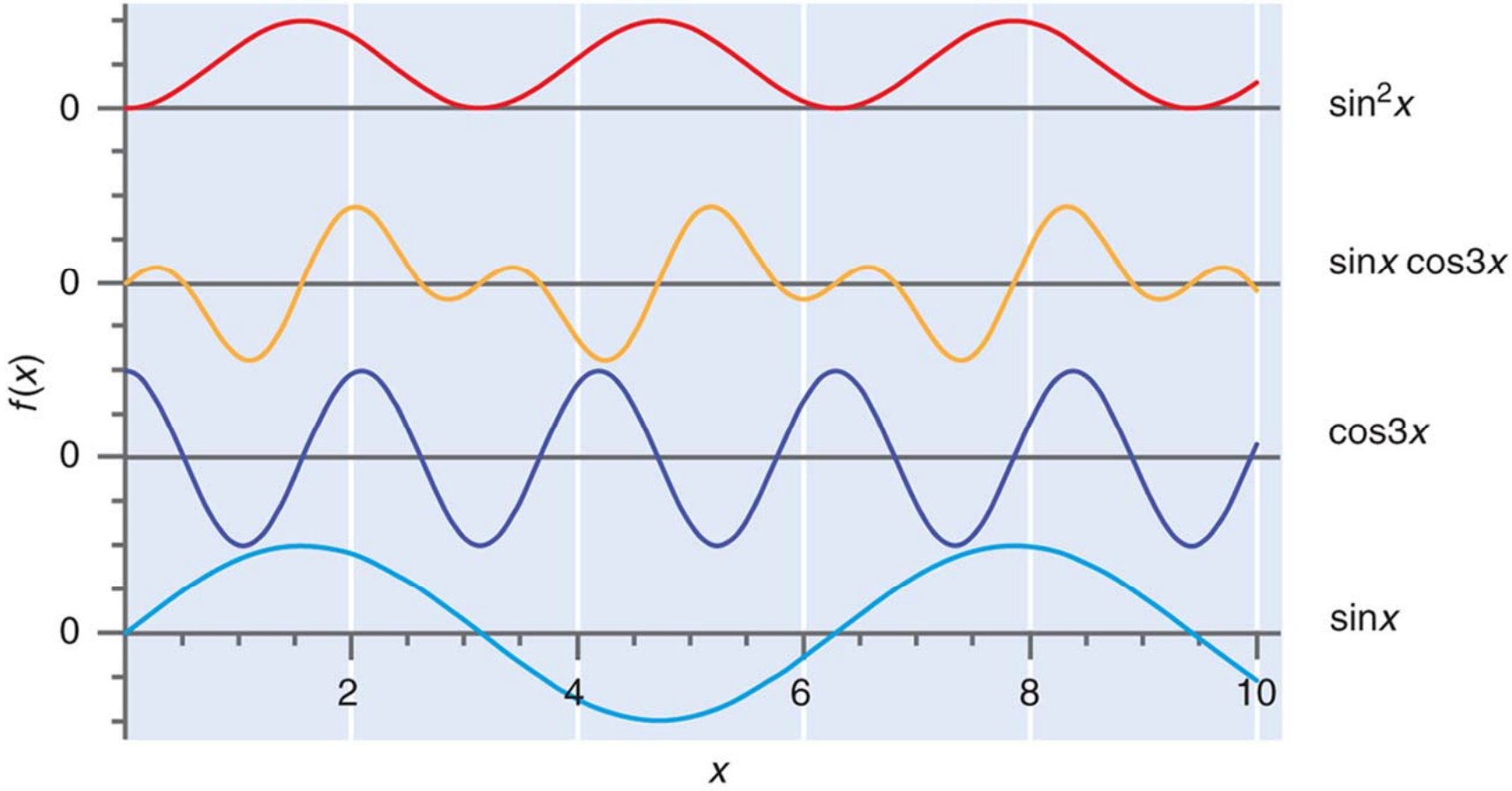

Figure: 13-02EP

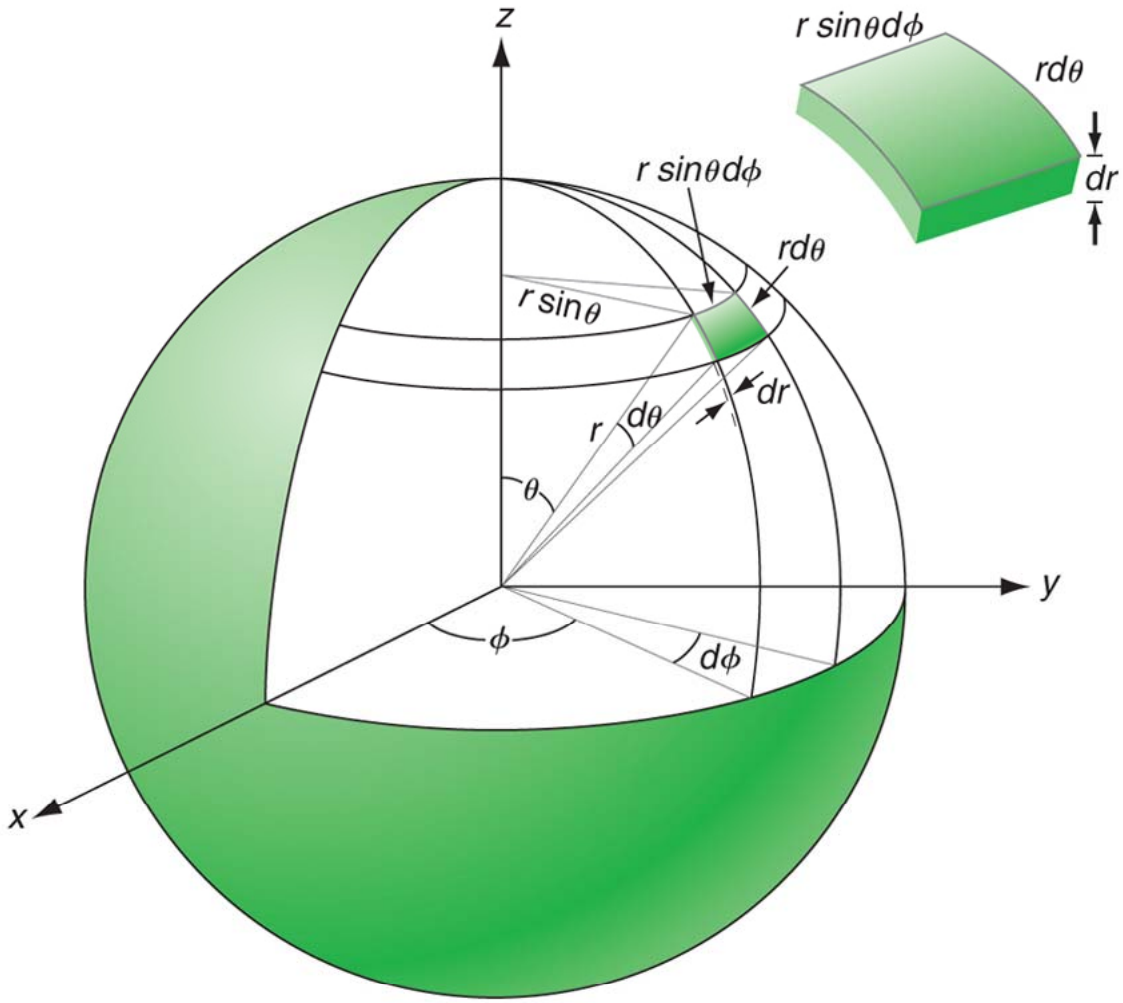

Figure: 13-07

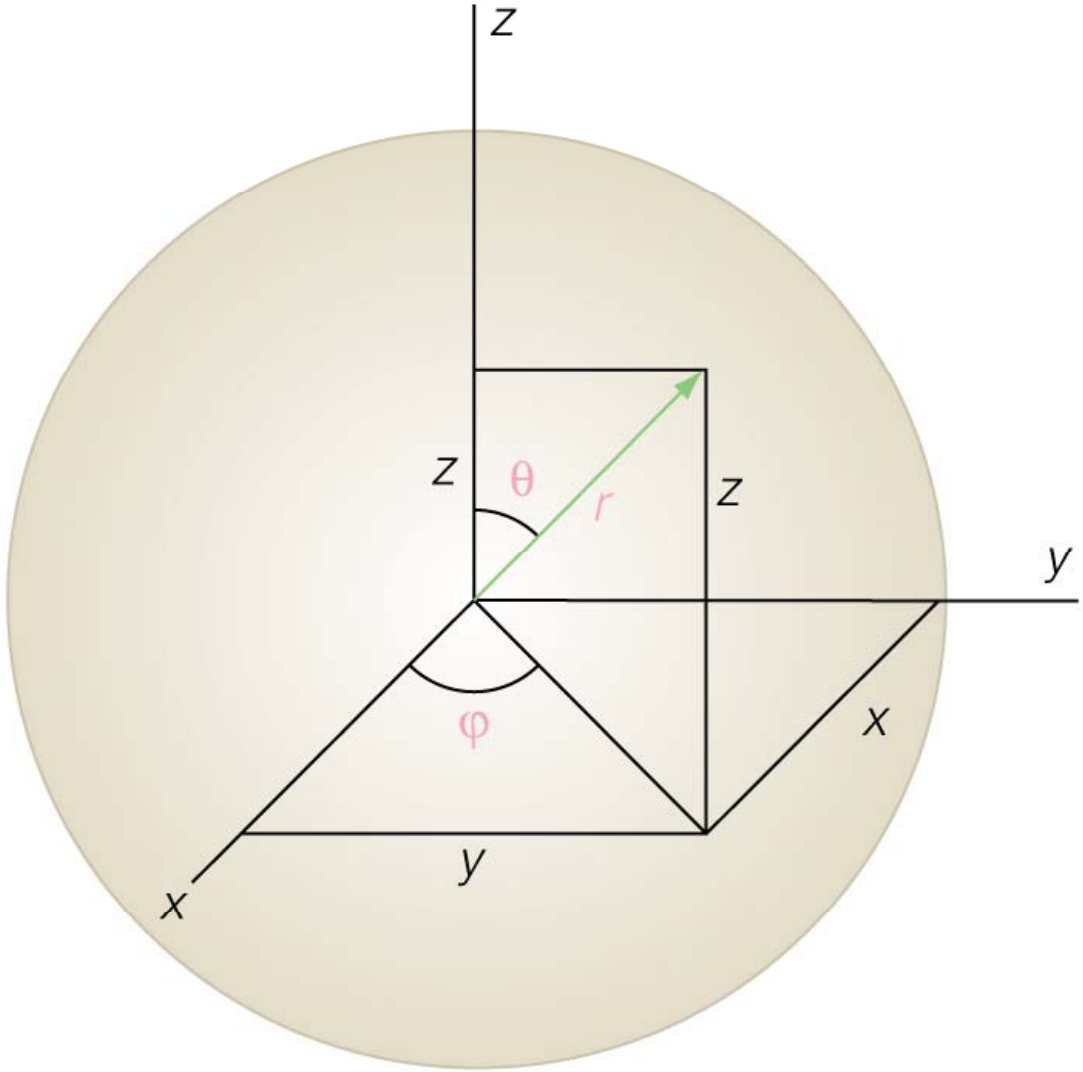

Physical Chemistry

For the Life Sciences

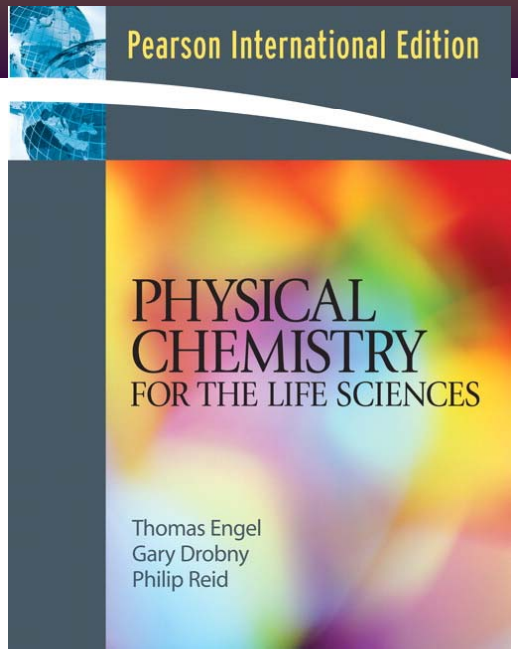

CHAPTER 19

Electronic Spectroscopy

- 19.1 The essentials of atomic spectroscopy
- 19.2 Analytical techniques based on atomic spectroscopy
- 19.3 The Doppler effect
- 19.4 The Helium-Neon laser
- 19.5 The energy of electronic transitions in molecules
- 19.6 The Franck-Condon principle
- 19.7 UV-Visible light absorption in polyatomic molecules

- 19.8 Transitions among the ground and excited states
- 19.9 Singlet-singlet transitions: absorption and fluorescence
- 19.10 Intersystem crossing and phosphorescence
- 19.11 Fluorescence spectroscopy and analytical chemistry
- 19.12 Singlet-molecule spectroscopy
- 19.13 Fluorescence resonance energy transfer (FRET)
- 19.14 Linear and circular dichroism

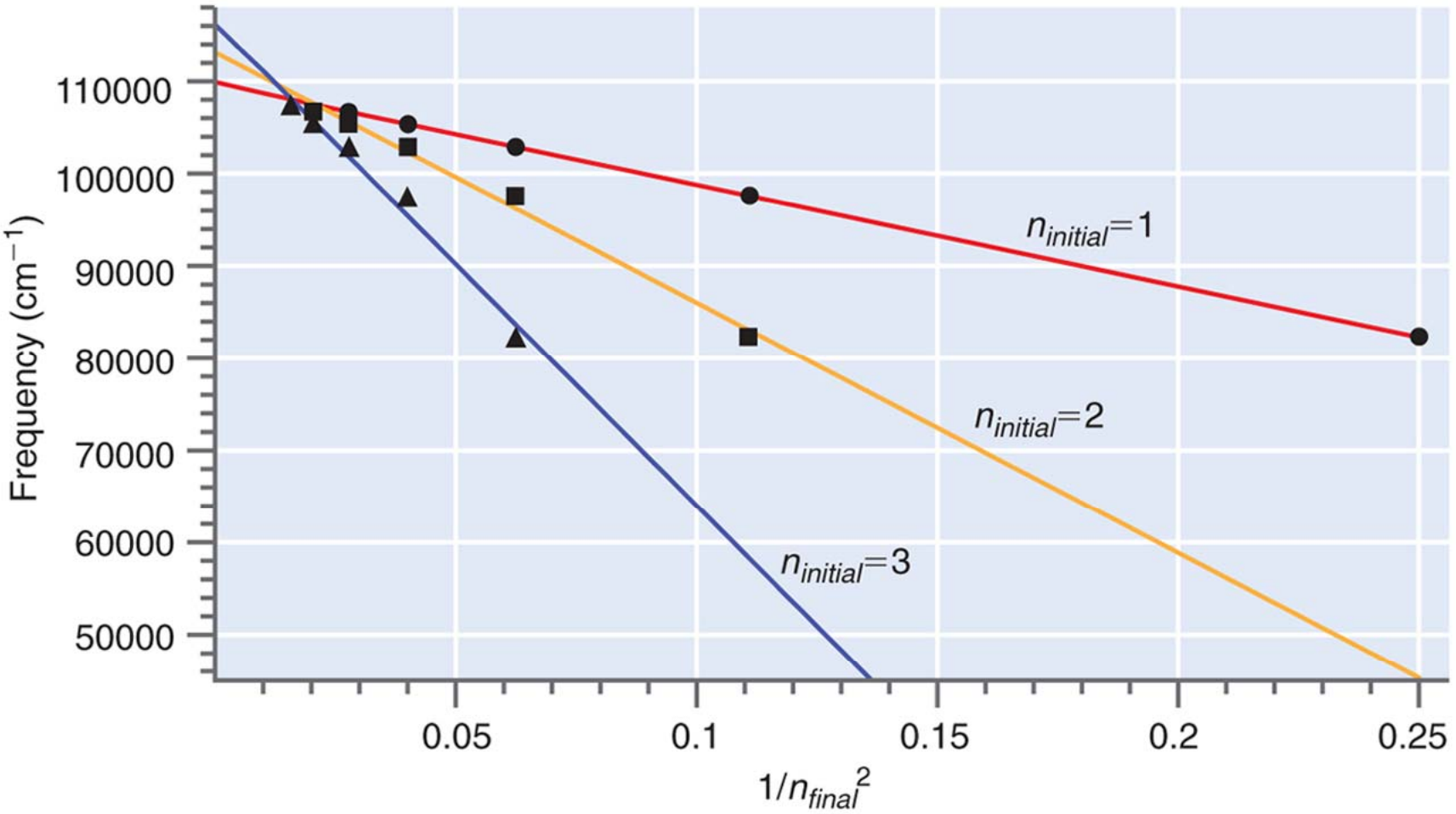

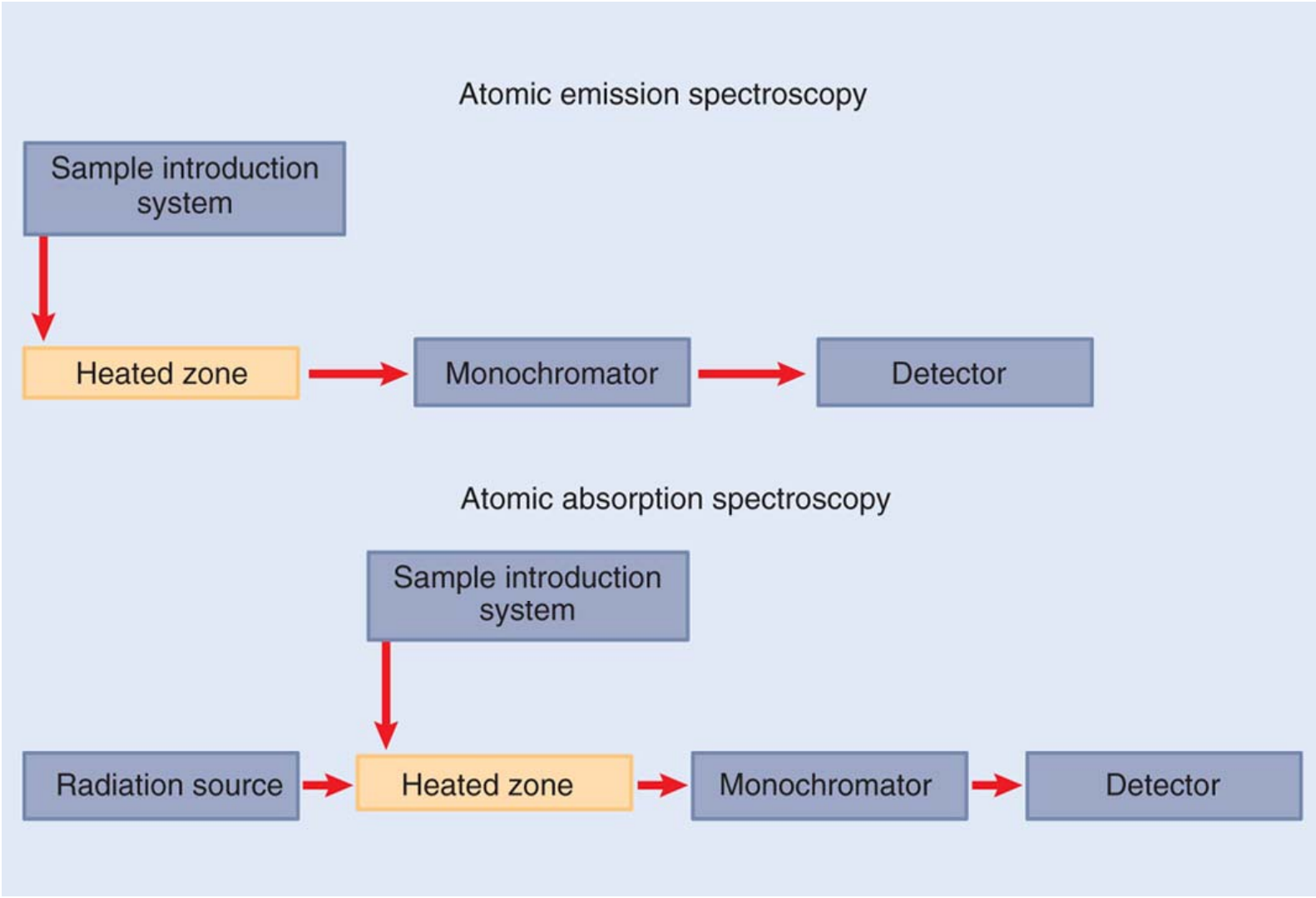

FIGURE 19.1

Schematic diagram of atomic emission and atomic absorption spectroscopies.

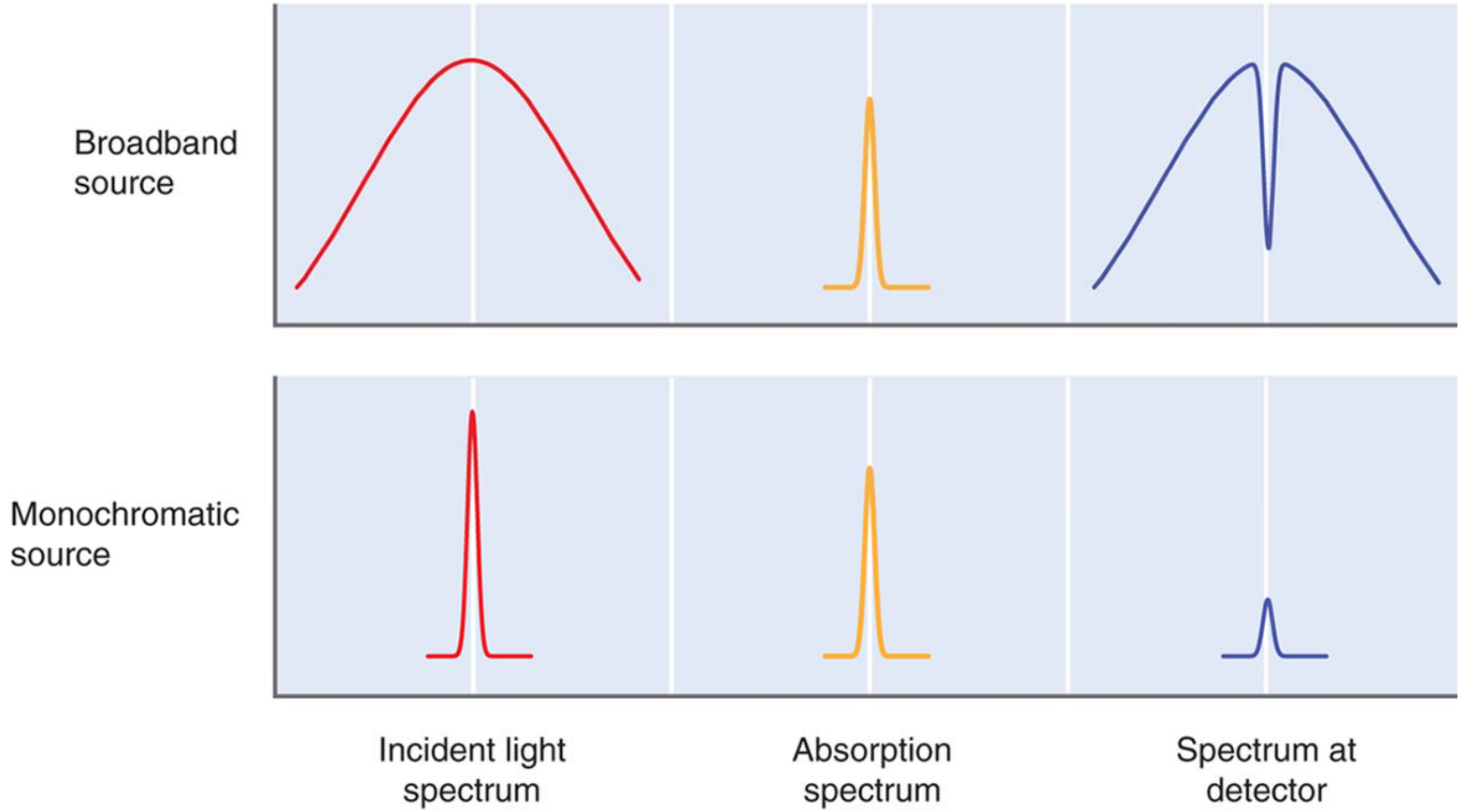

FIGURE 19.2

The intensity of light as a function of its frequency is shown at the entrance to the heated zone and at the detector for broadband and monochromatic sources. The absorption spectrum of the atomic to be detected is shown in the middle column.

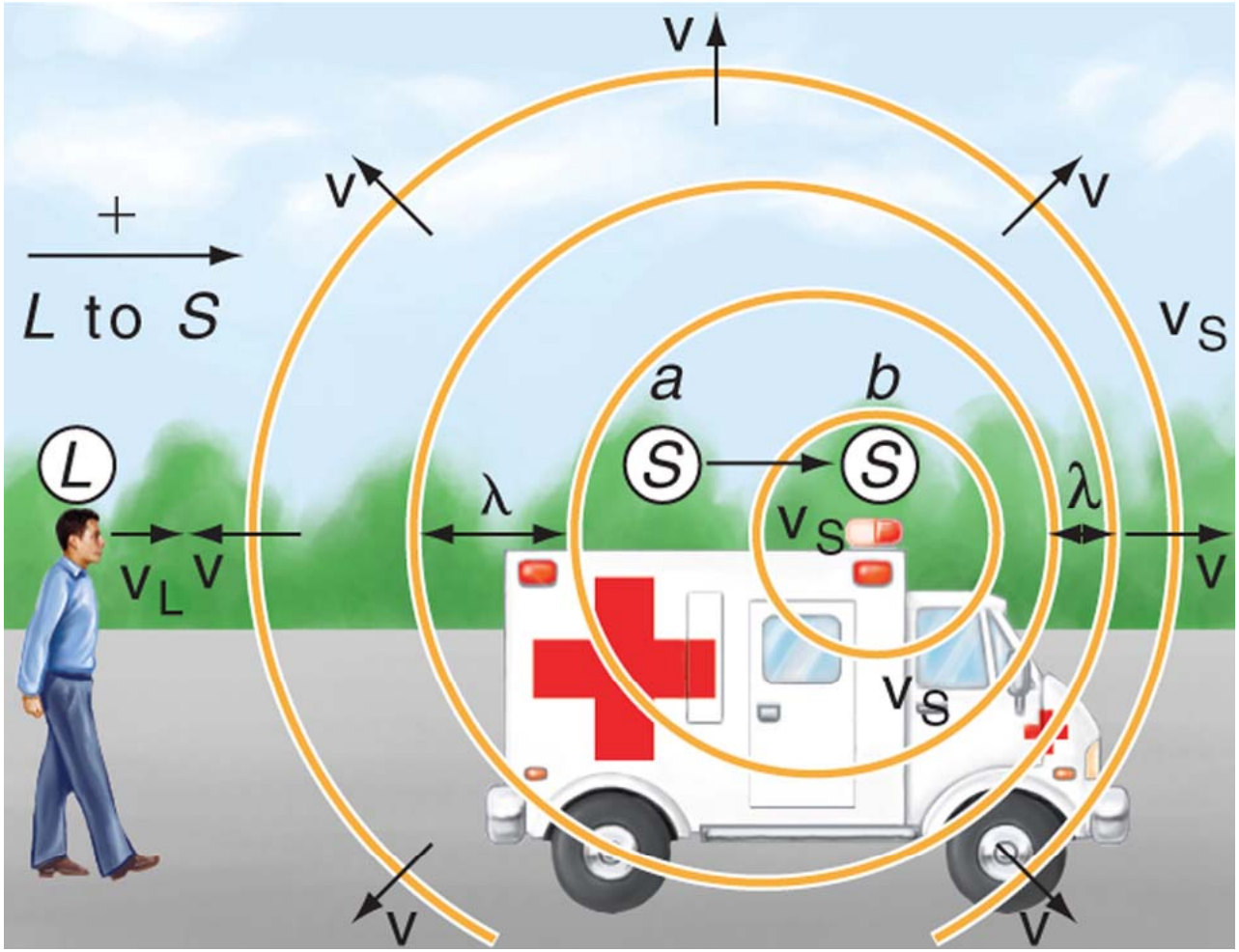

FIGURE 19.3

The frequency of light or sound at the position of the observer L depends on the relative velocity of the source S, V_S, and observer, V_L.

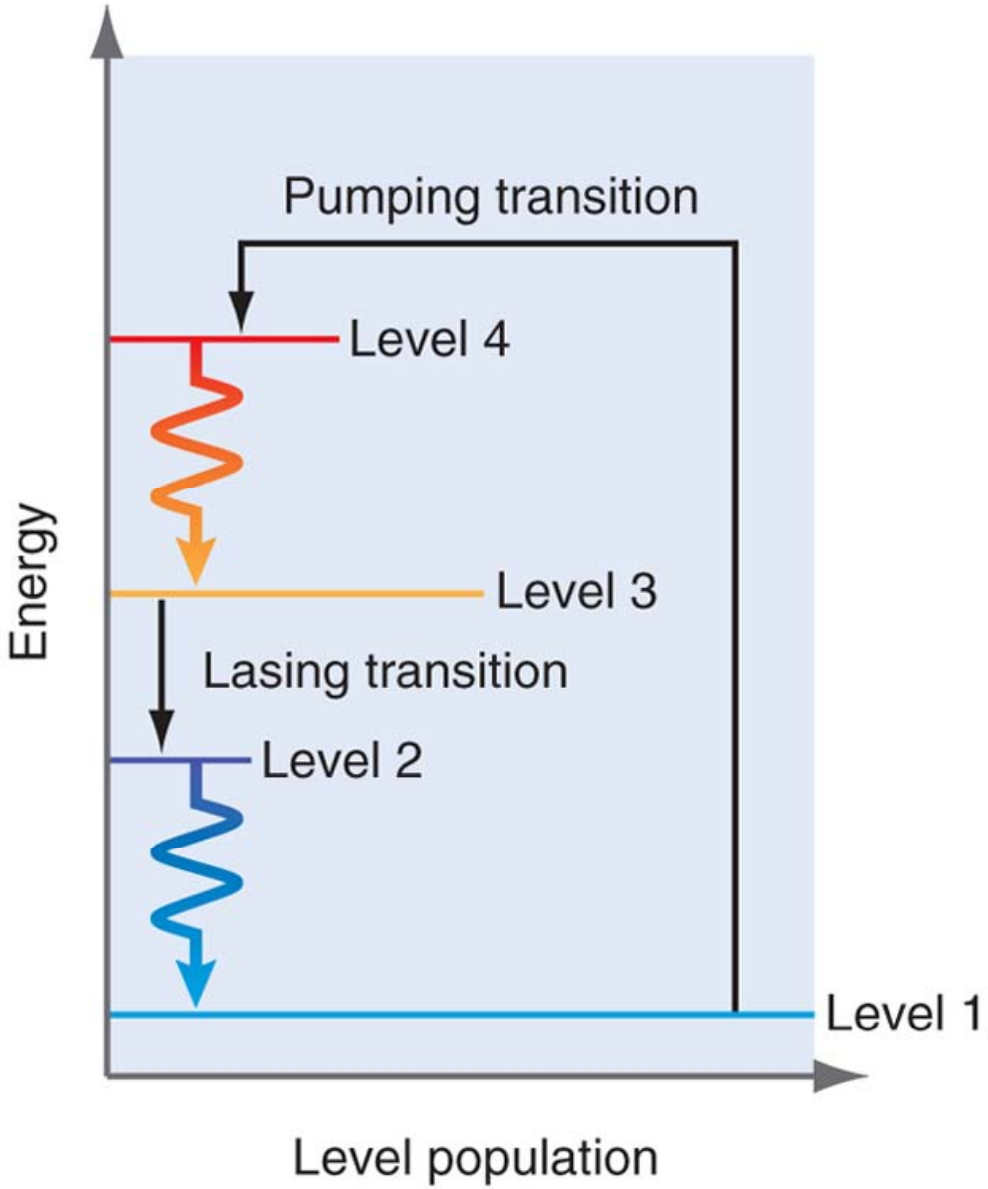

FIGURE 19.4

Schematic representation of a four-state laser. The energy is plotted vertically, and the level population is plotted horizontally.

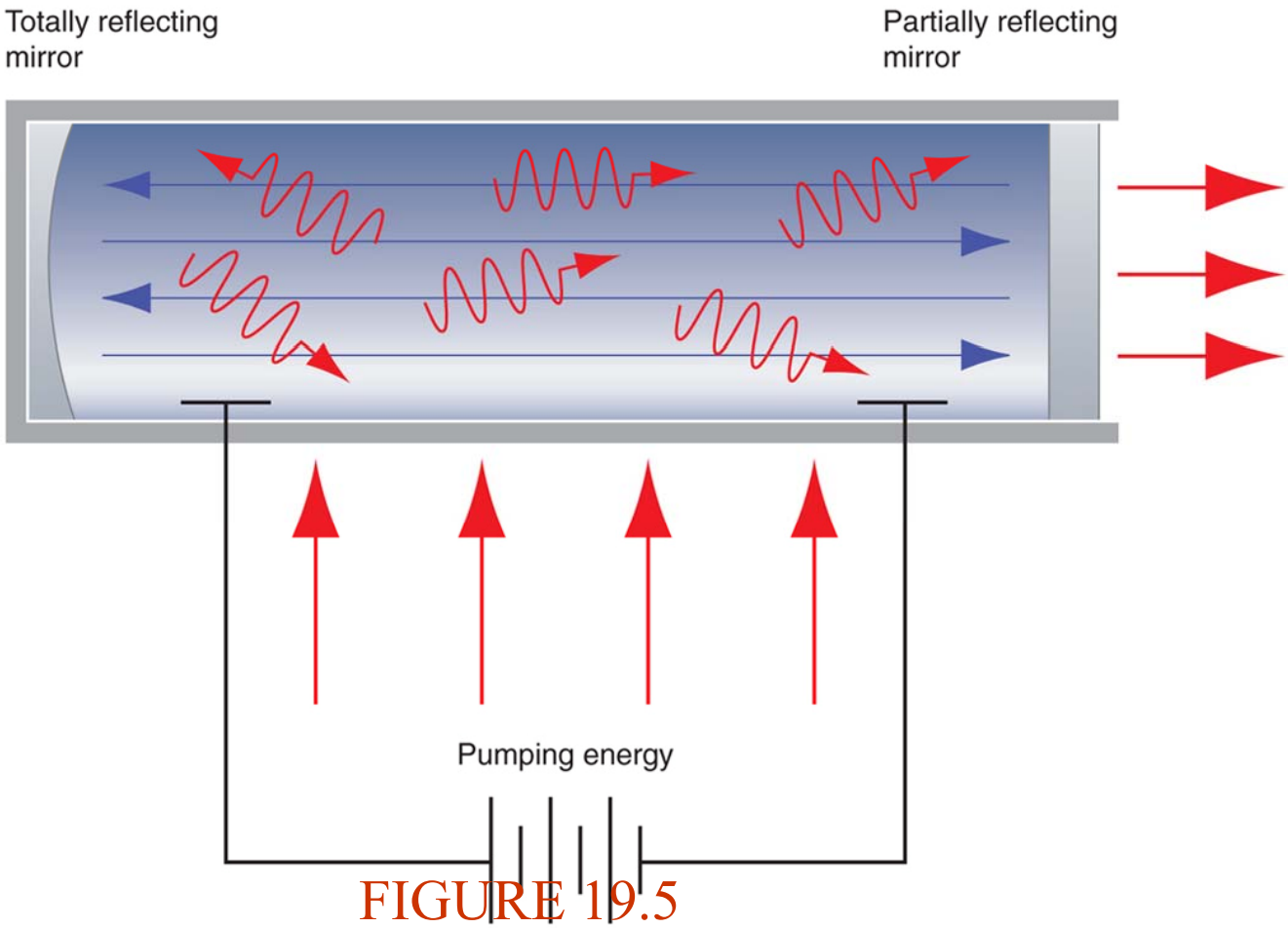

FIGURE 19.5

Schematic representation of a He-Ne laser operated as an optical resonator. The parallel lines in the resonator represent coherent stimulated emission that is amplified by the resonator, and the waves represent incoherent spontaneous emission events.

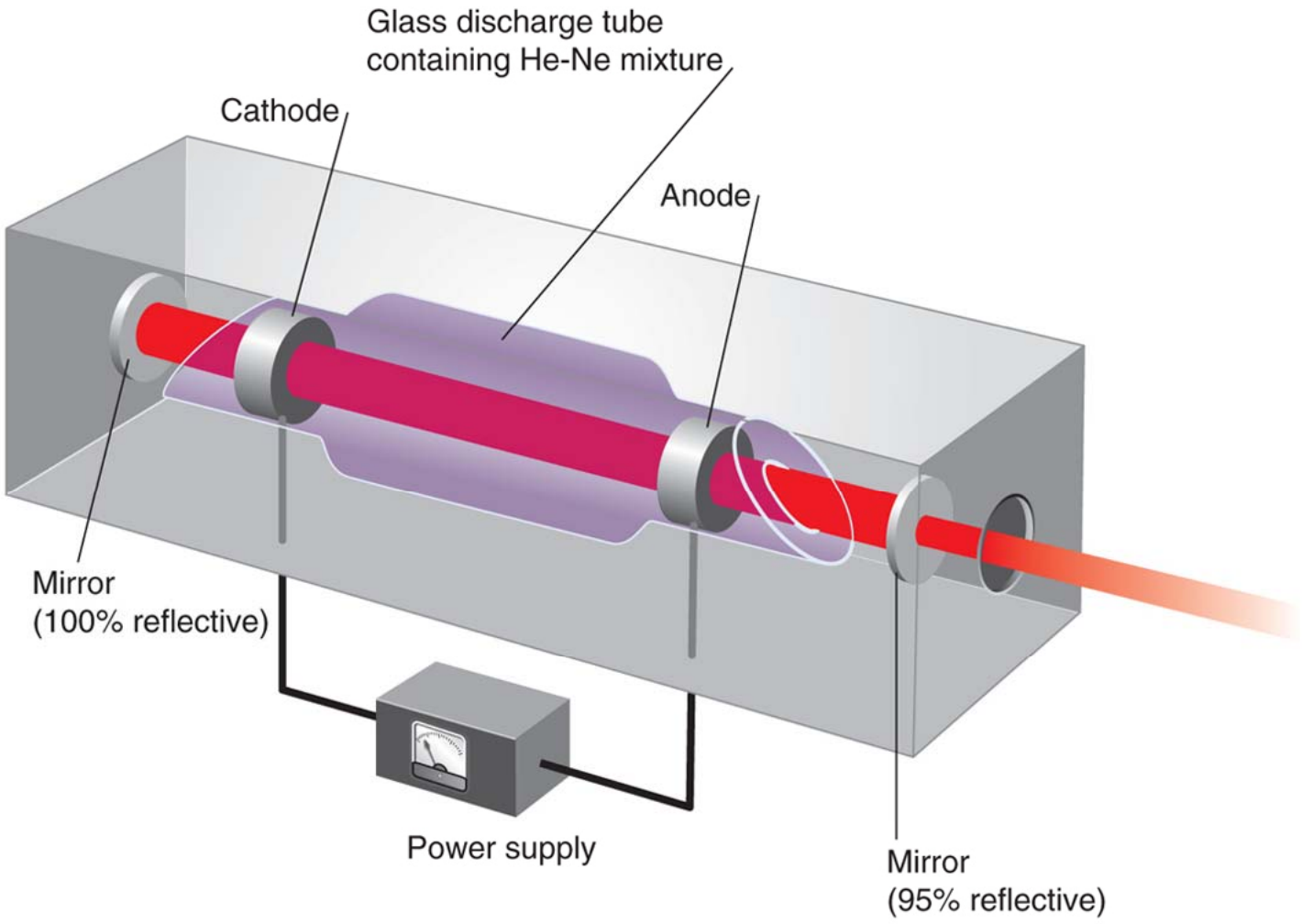

FIGURE 19.6

Schematic diagram of a He-Ne laser.

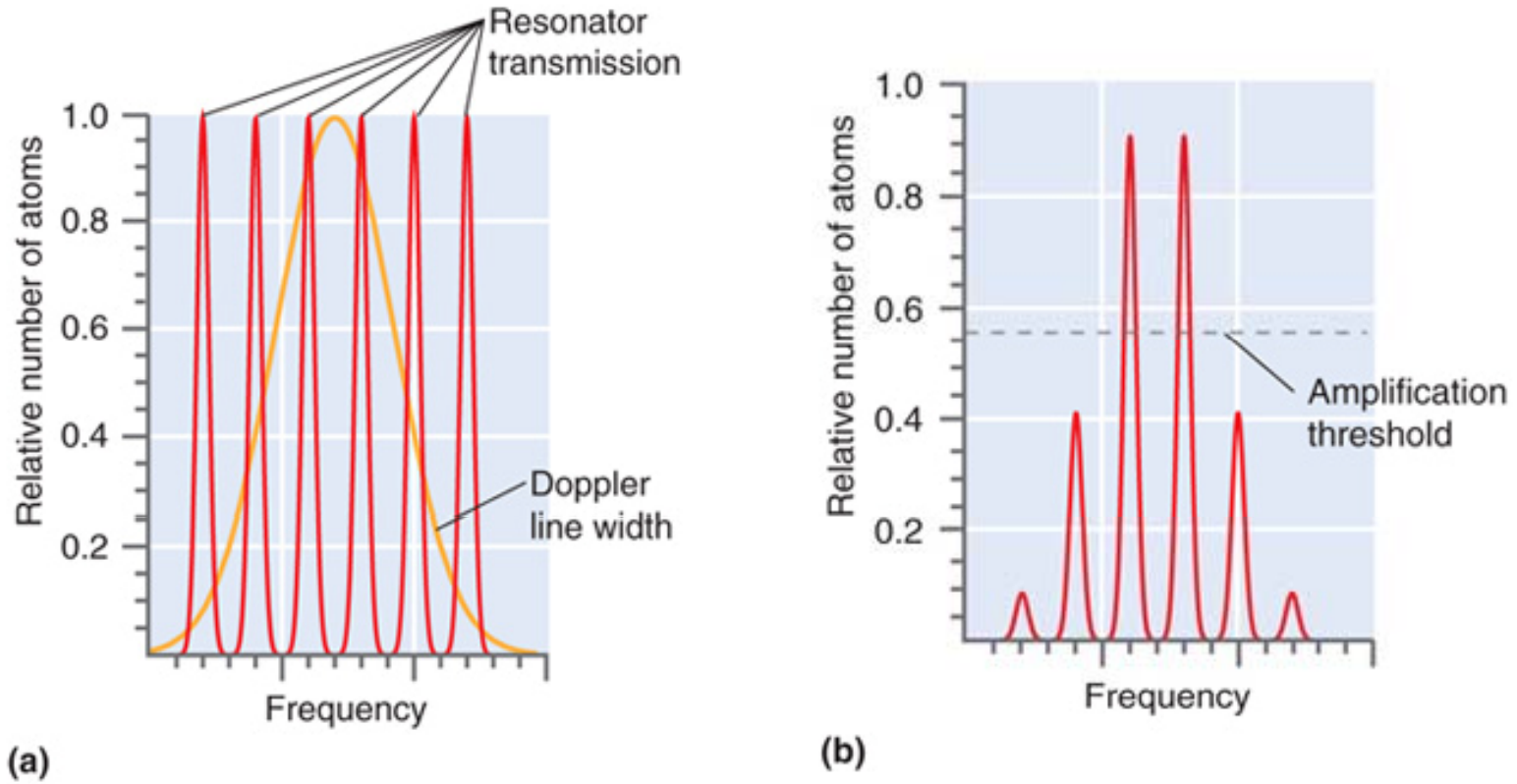

FIGURE 19.7

The line width of a transition in a He-Ne laser is Doppler broadened through the Maxwell-Boltzmann velocity distribution. (a) The resonator transmission decreases the line width of the lasing transition to less than the Doppler limit. (b) The amplification threshold further reduces the number of frequencies supported by the resonator.

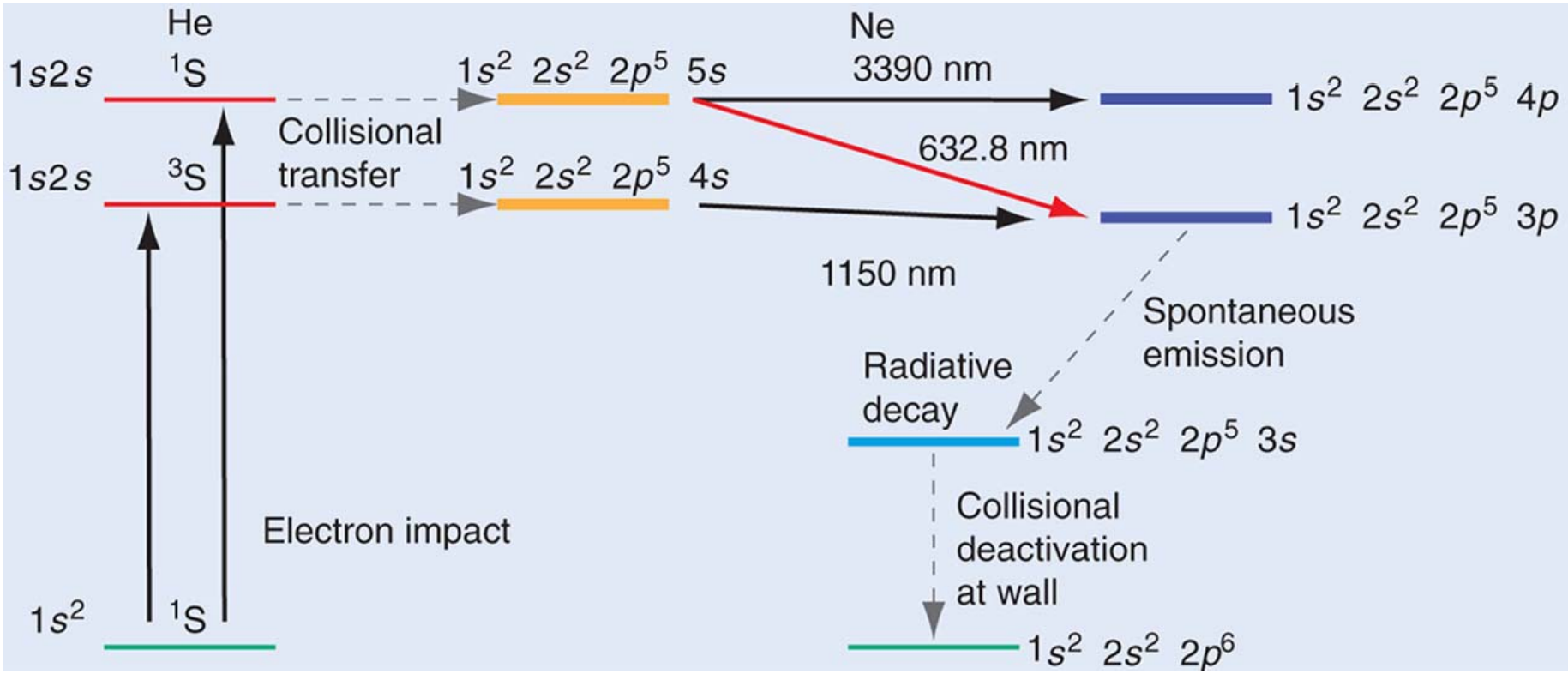

FIGURE 19.8

Transitions in the He-Ne laser. The slanted solid show three possible lasing transitions.

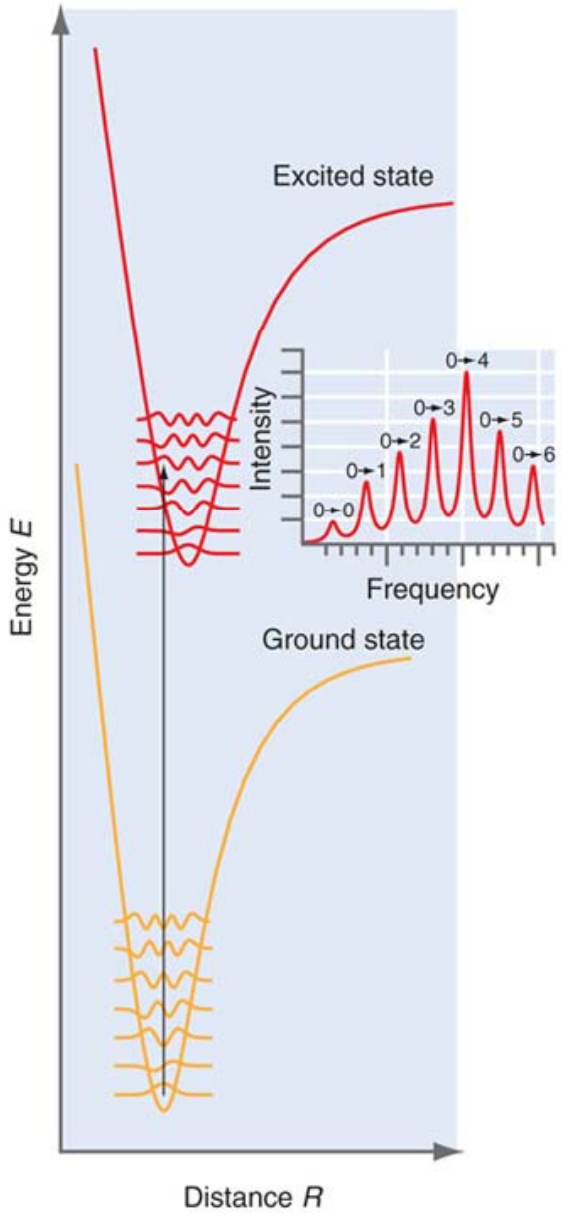

FIGURE 19.9

The relation between energy and bond length is shown for two electronic states. Only the lowest vibrational energy levels and the corresponding wave functions are shown. The vertical line shows the most probable transition predicted by the Frank-Condon principle. The inset shows the relative intensities of different vibrational lines in an absorption spectrum for the potential energy curve shown.

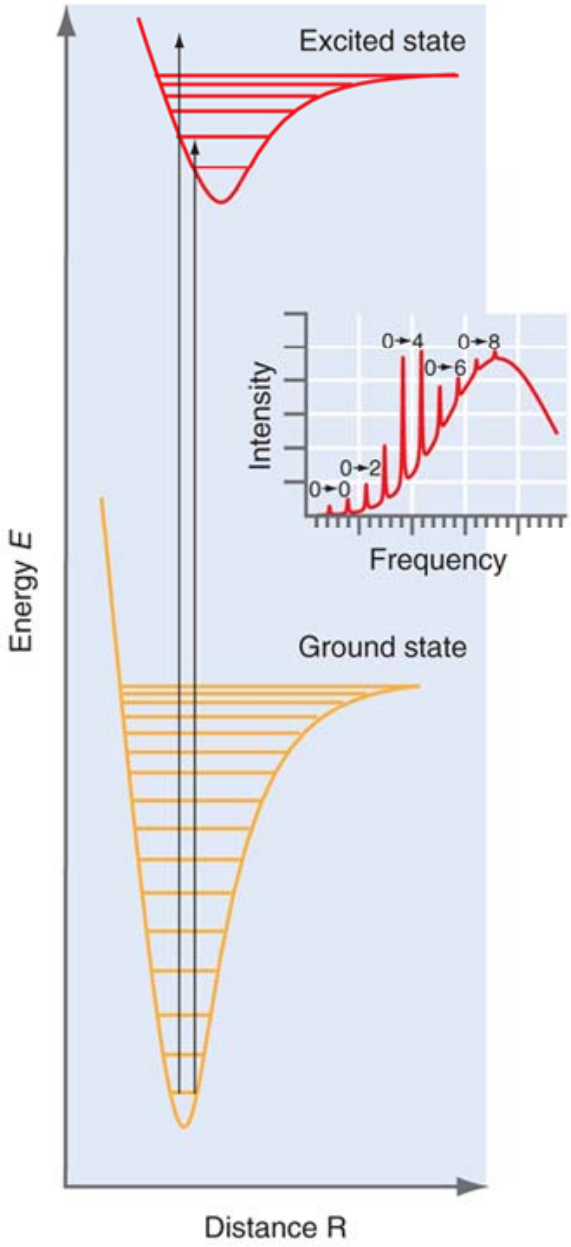

FIGURE 19.10

For absorption from the ground vibrational state of the ground electronic state to excited electronic state, a continuous energy spectrum will be observed for sufficiently high photon energy. A discrete energy spectrum is observed for an incident light frequency $v < E/h$. A continuous spectrum is observed for higher frequency.

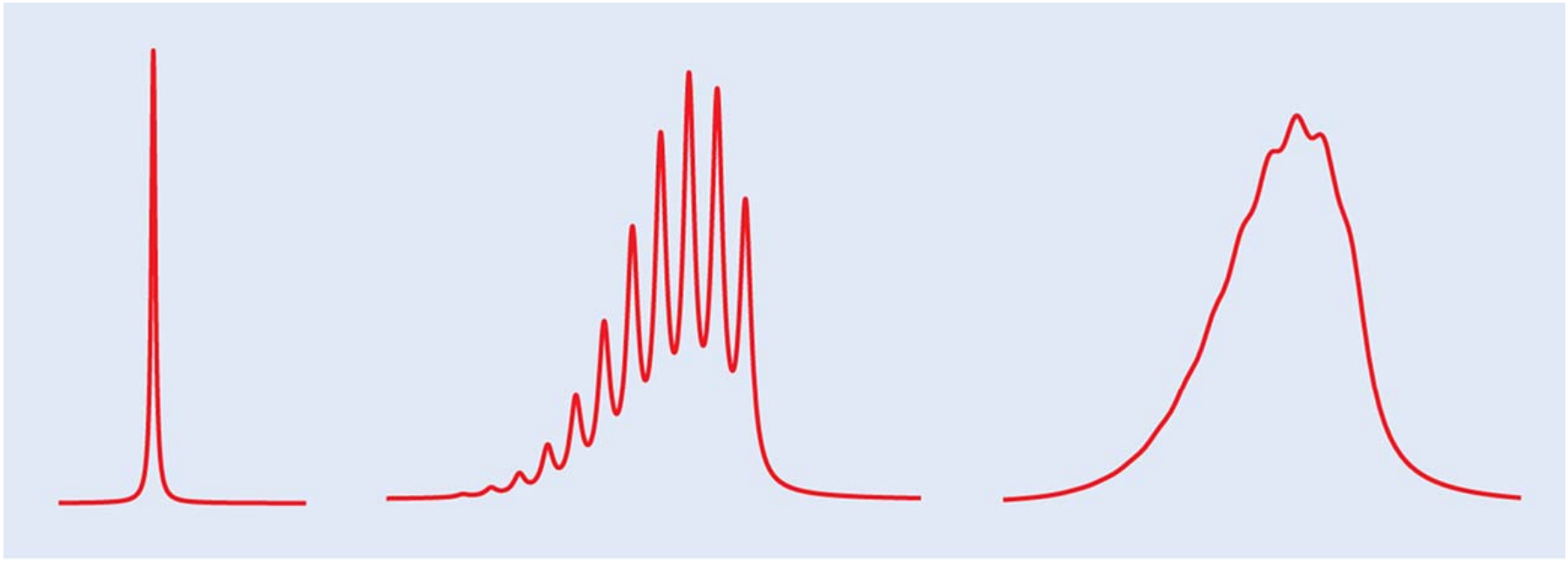

FIGURE 19.11

The intensity of absorption in a small part of the UV-visible range of the electromagnetic spectrum is shown schematically for (a) an atom, (b) a diatomic molecule, and (c) a polyatomic molecule.

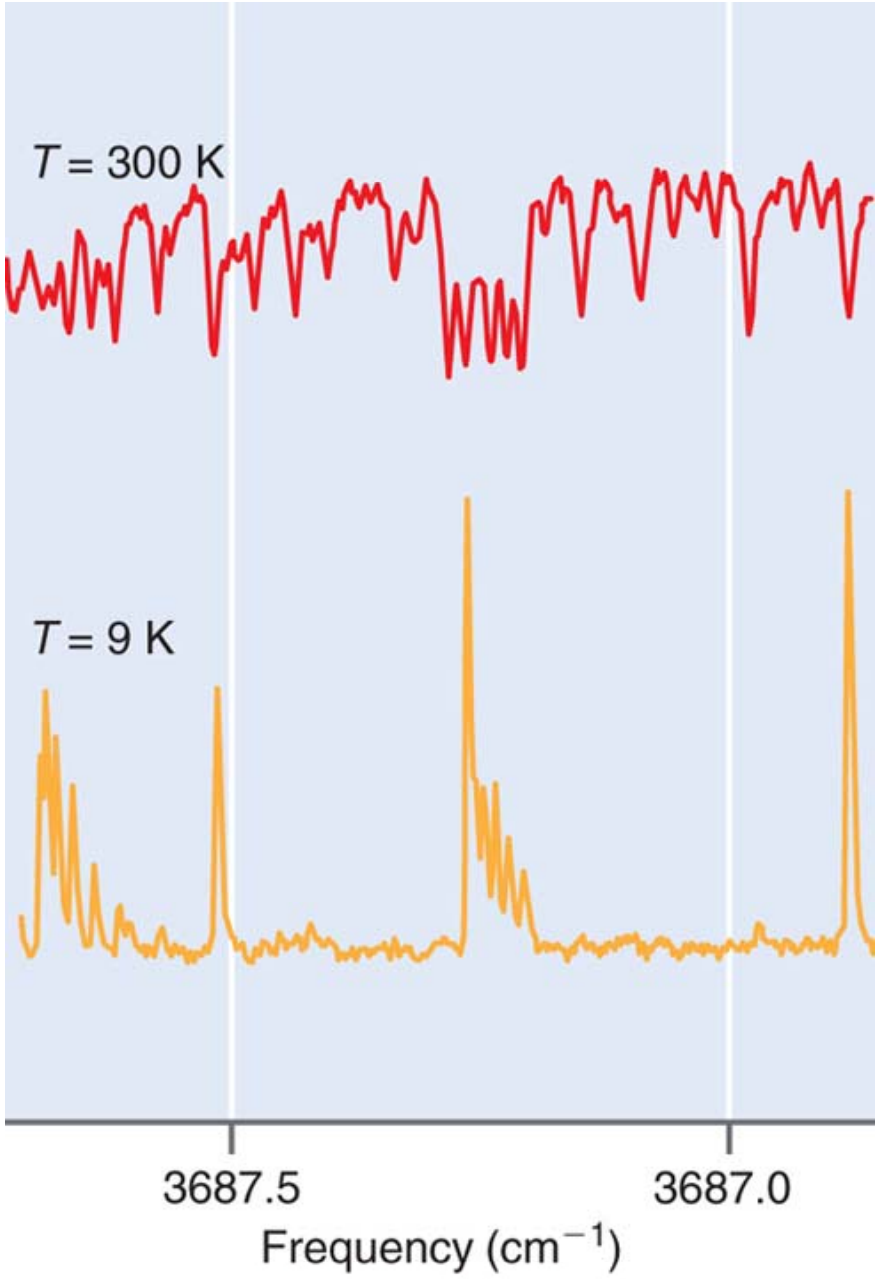

FIGURE 19.12

A small portion of the electronic absorption spectrum of methanol is shown at 300and 9 K using expansion of a dilute mixture of methanol in He through a nozzle into a vacuum. At 300K, the molecule absorbs almost every everywhere in the frequency range. At 9 K, very few rotational and vibrational state are populated, and individual spectral features corresponding to rotational fine structure are observed.

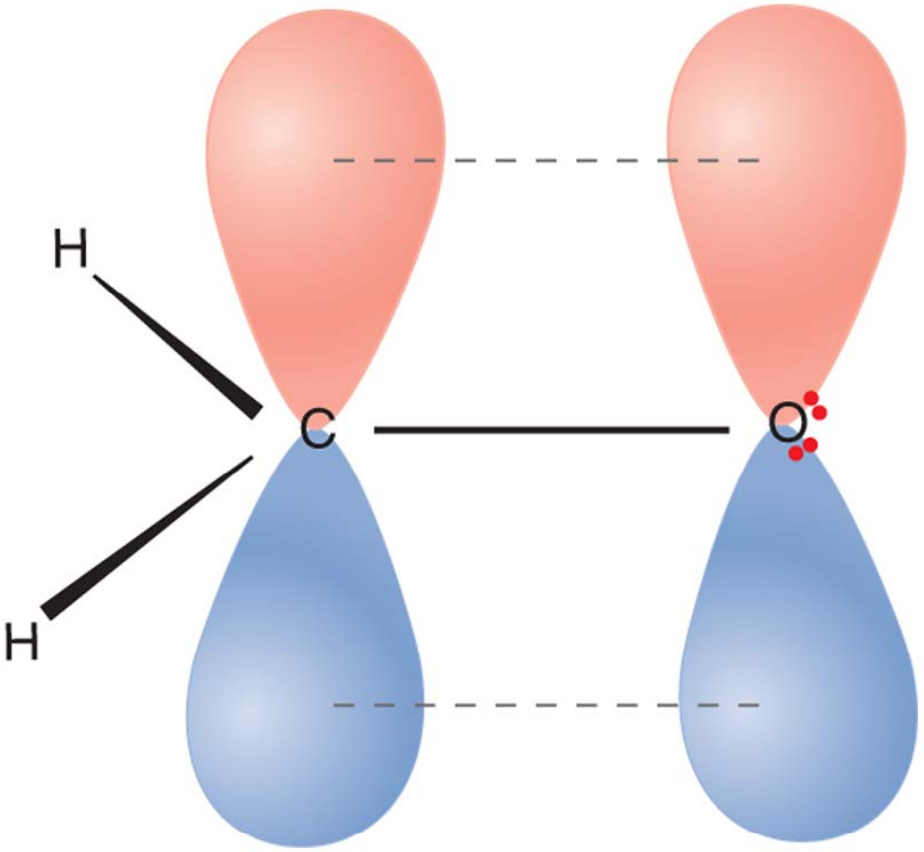

FIGURE 16.13

Valence bond picture of the formaldehyde molecule. The solid lines indicate σ bonds and the dashed lines indicate a π bond. The nonequivalent lone pairs on oxygen are also shown.

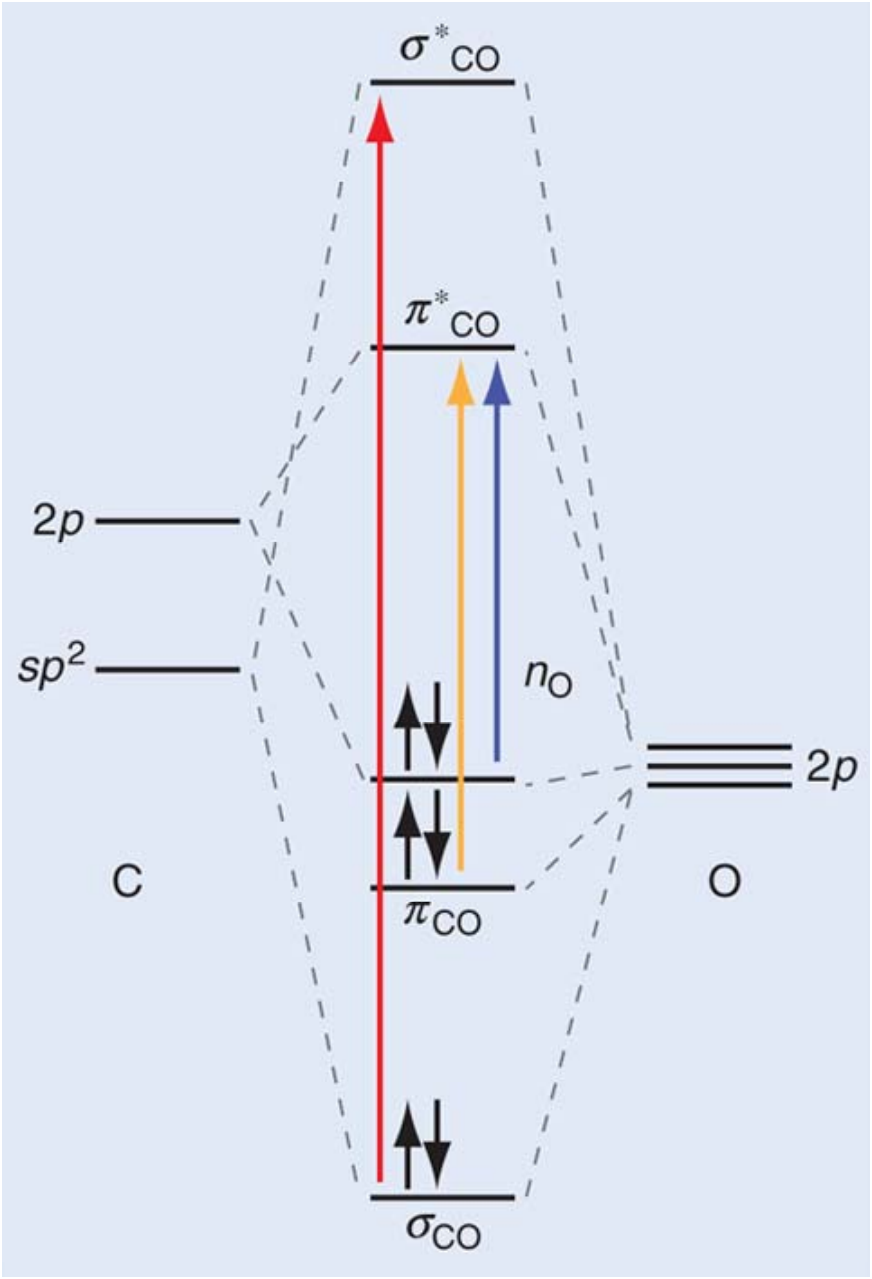

FIGURE 19.14

A simplified MO energy diagram is shown for the C—O bonding interaction in formaldehyde. The most important allowed transitions between these levels are shown. Only one of the sp^2 orbitals on carbon is shown because the other two hybrid orbitals form σ_{CH} bonds.

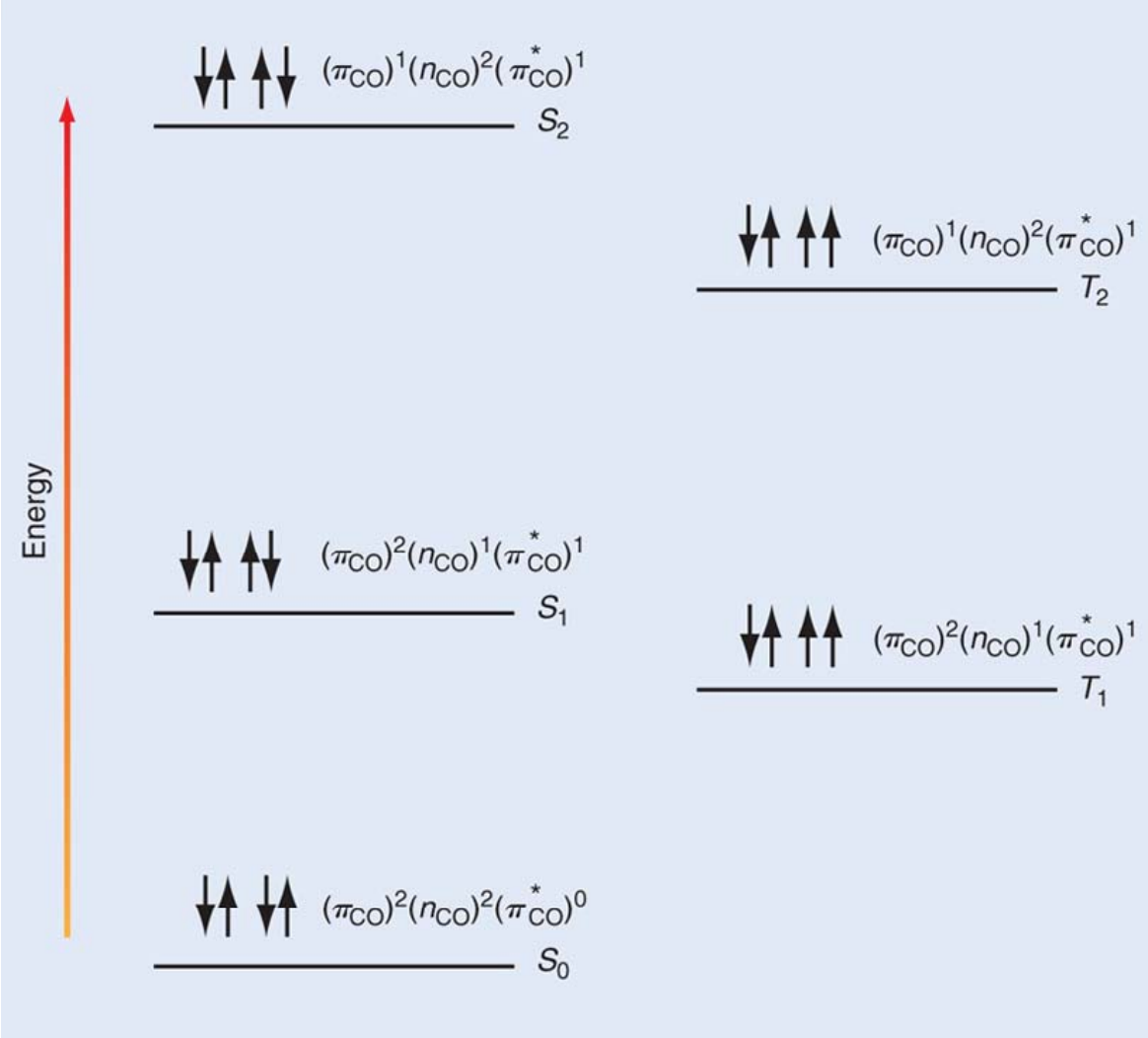

FIGURE 19.15

The ground state of formaldehyde is a singlet and is designated S_0. Successively high energy singlet and triplet states are designated S_1, S_2, T_1, and T_2. The electron configurations and the alignment of the unpaired spins for the states involved in the most important transitions are also shown. The energy separation between the singlet and triplet states has been exaggerated in this figure.

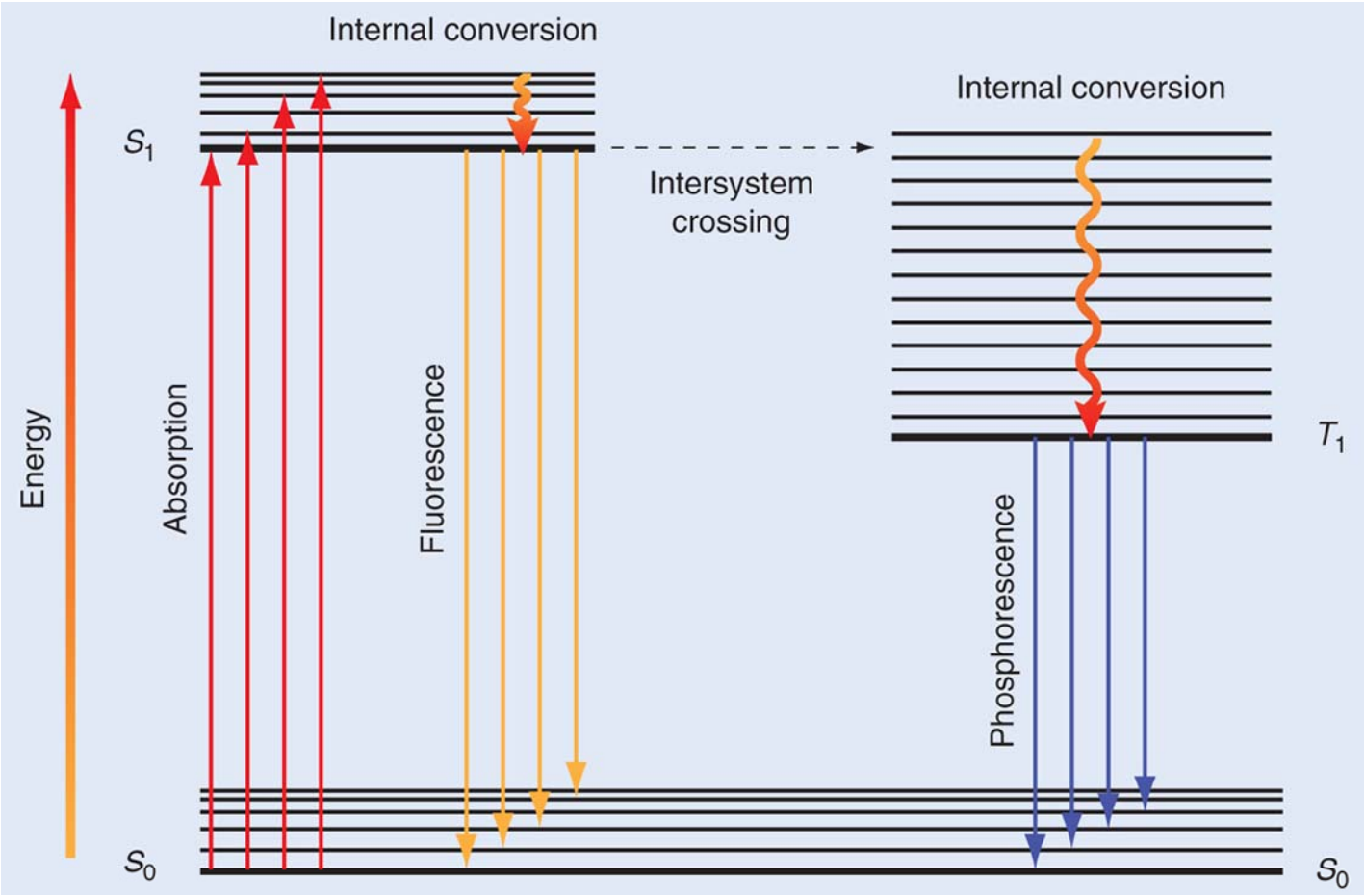

FIGURE 19.16

Possible transitions among the ground and excited electronic states are indicated. The spacing between vibrational levels is exaggerated in this diagram. Rotational levels have been omitted for reasons of clarity.

TABLE 19.1 Characteristic Parameters for Common Chromophores

Chromophore	Transition	λ_{max} (nm)	ε_{max} ($dm^3\ mol^{-1}\ cm^{-1}$)
N=O	$n \rightarrow \pi^*$	660	200
N=N	$n \rightarrow \pi^*$	350	100
C=O	$n \rightarrow \pi^*$	280	20
NO_2	$n \rightarrow \pi^*$	270	20
C_6H_6 (benzene)	$\pi \rightarrow \pi^*$	260	200
C=N	$\pi \rightarrow \pi^*$	240	150
C=C—C=O	$\pi \rightarrow \pi^*$	220	2×10^5
C=C—C=C	$\pi \rightarrow \pi^*$	220	2×10^5
S=O	$\pi \rightarrow \pi^*$	210	1.5×10^3
C=C	$\pi \rightarrow \pi^*$	180	1×10^3
C—C	$\sigma \rightarrow \sigma^*$	<170	1×10^3
C—H	$\sigma \rightarrow \sigma^*$	<170	1×10^3

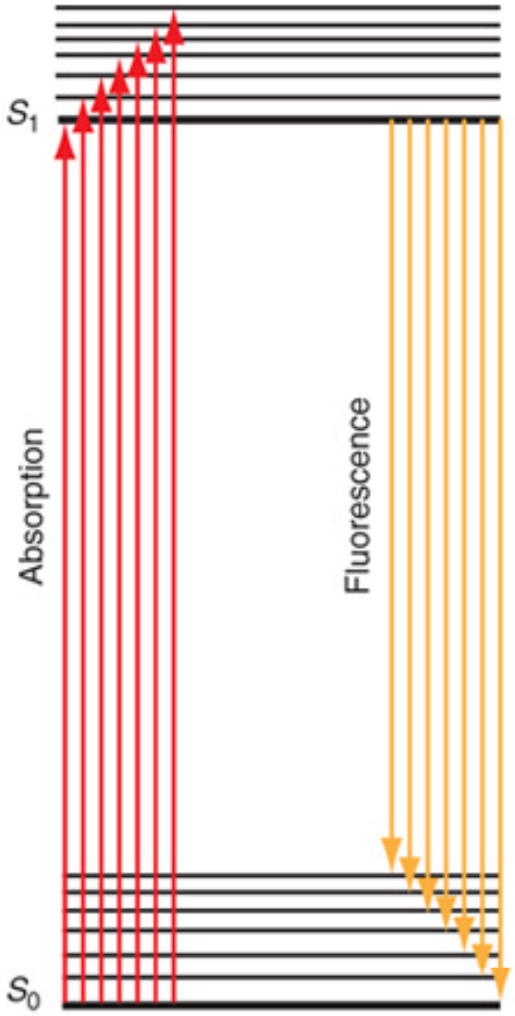

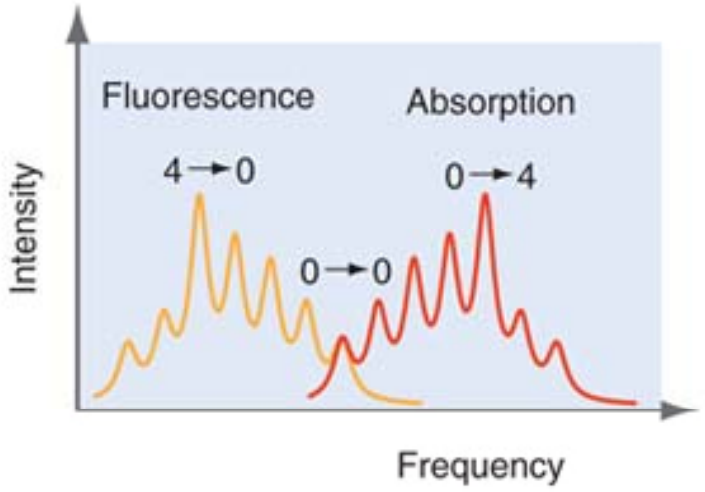

FIGURE 19.17

Illustration of the absorption and fluorescence bands expected if internal conversion is fast relative to fluorescence. The relative intensities of individual transitions within the absorption and fluorescence bands are determined by the Franck-Condon principle.

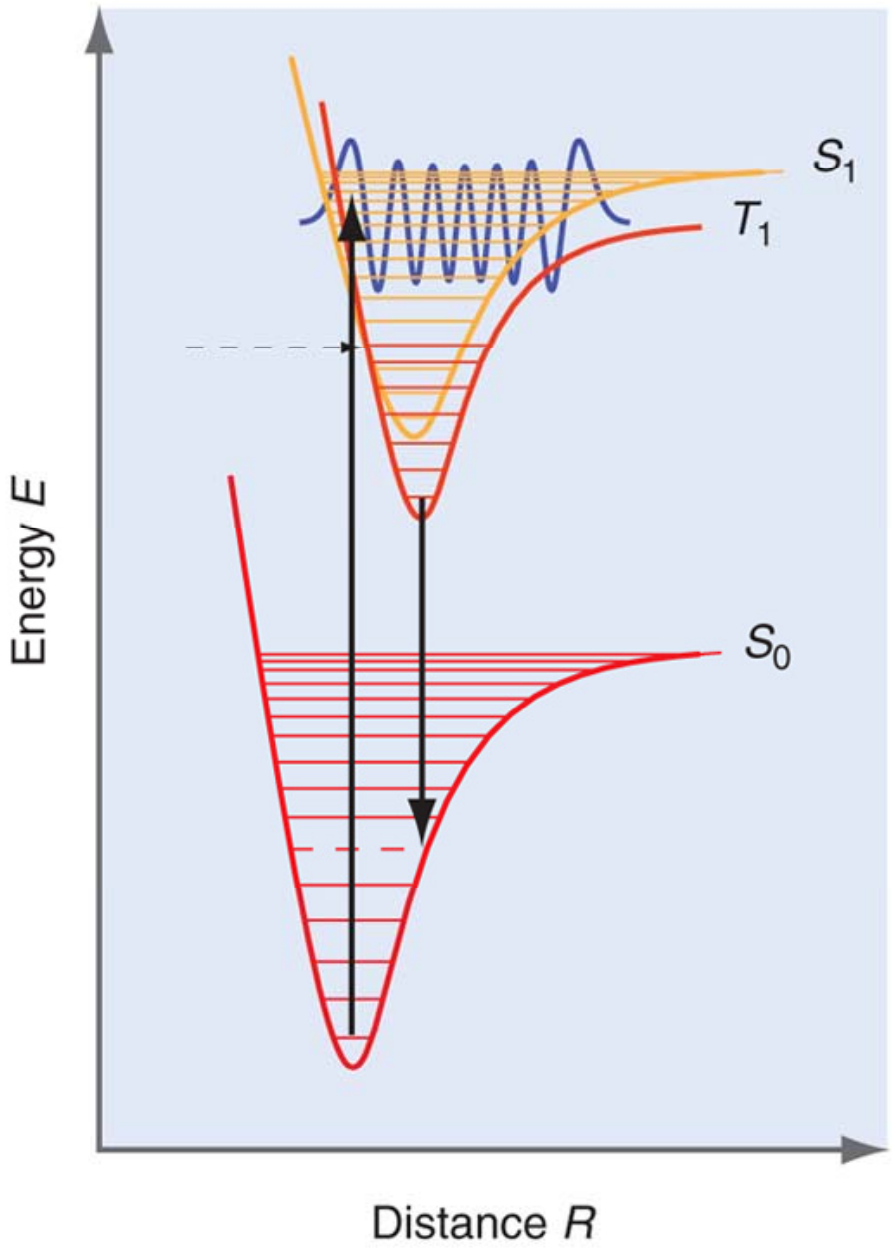

FIGURE 19.18

Process giving rise to phosphorescence illustrated for a diatomic molecule. Absorption from S_0 leads to population of excited vibrational states in S_1. The molecule has a finite probability of making a transition to an excited vibrational state of T_1 if it has the same geometry in both states and if there are vibrational levels of the same energy in both states. The dashed arrow indicates the coincidence of vibrational energy levels in T_1 and S_1. For reasons of clarity, only the lowest vibrational levels in T_1 are shown. The initial excitation to S_1 occurs to a vibrational state of maximum overlap with the ground state of S_0 as indicated by the blue vibrational wave function.

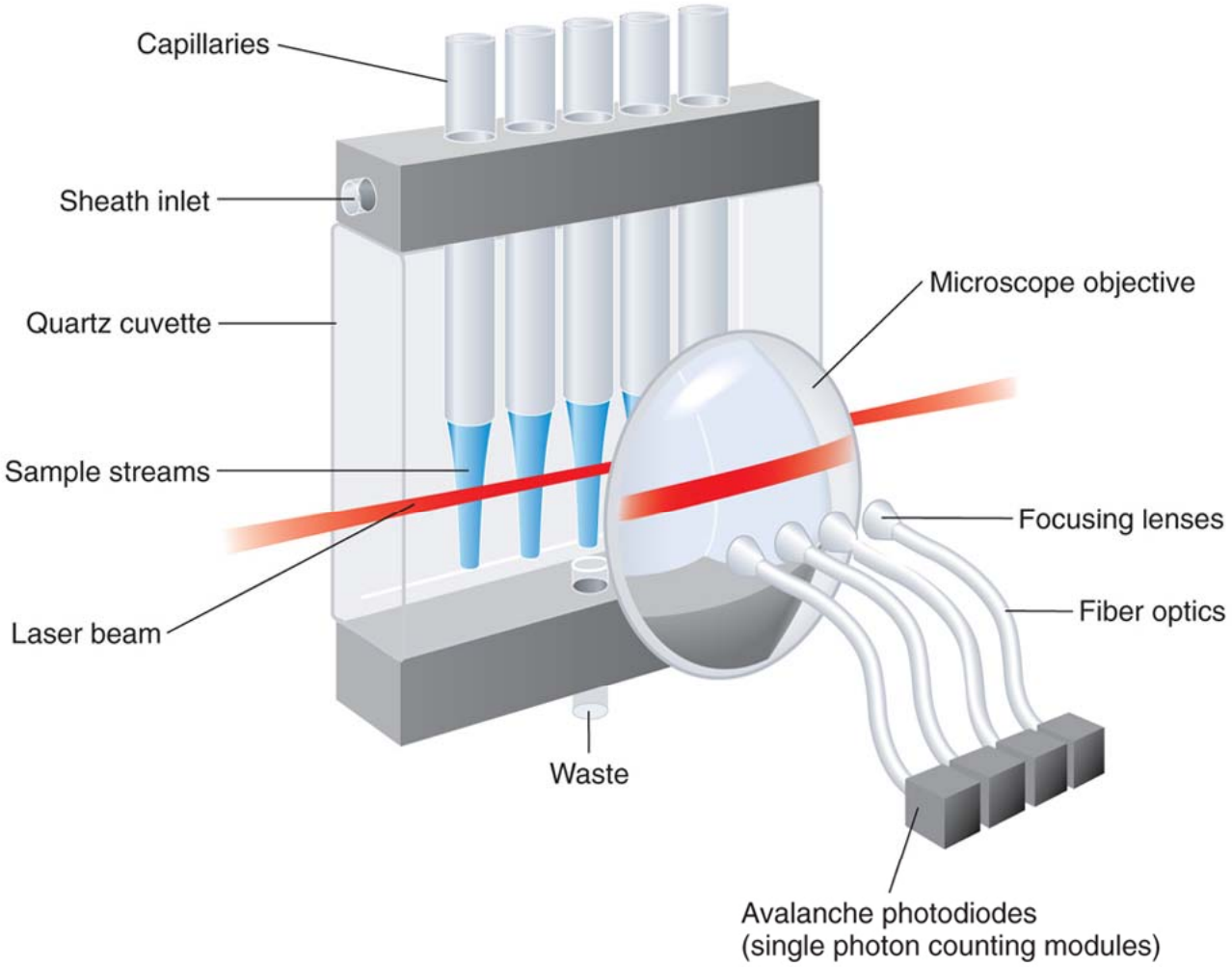

FIGURE 19.19

Schematic diagram of the application of fluorescence spectroscopy in the sequencing of the human genome.

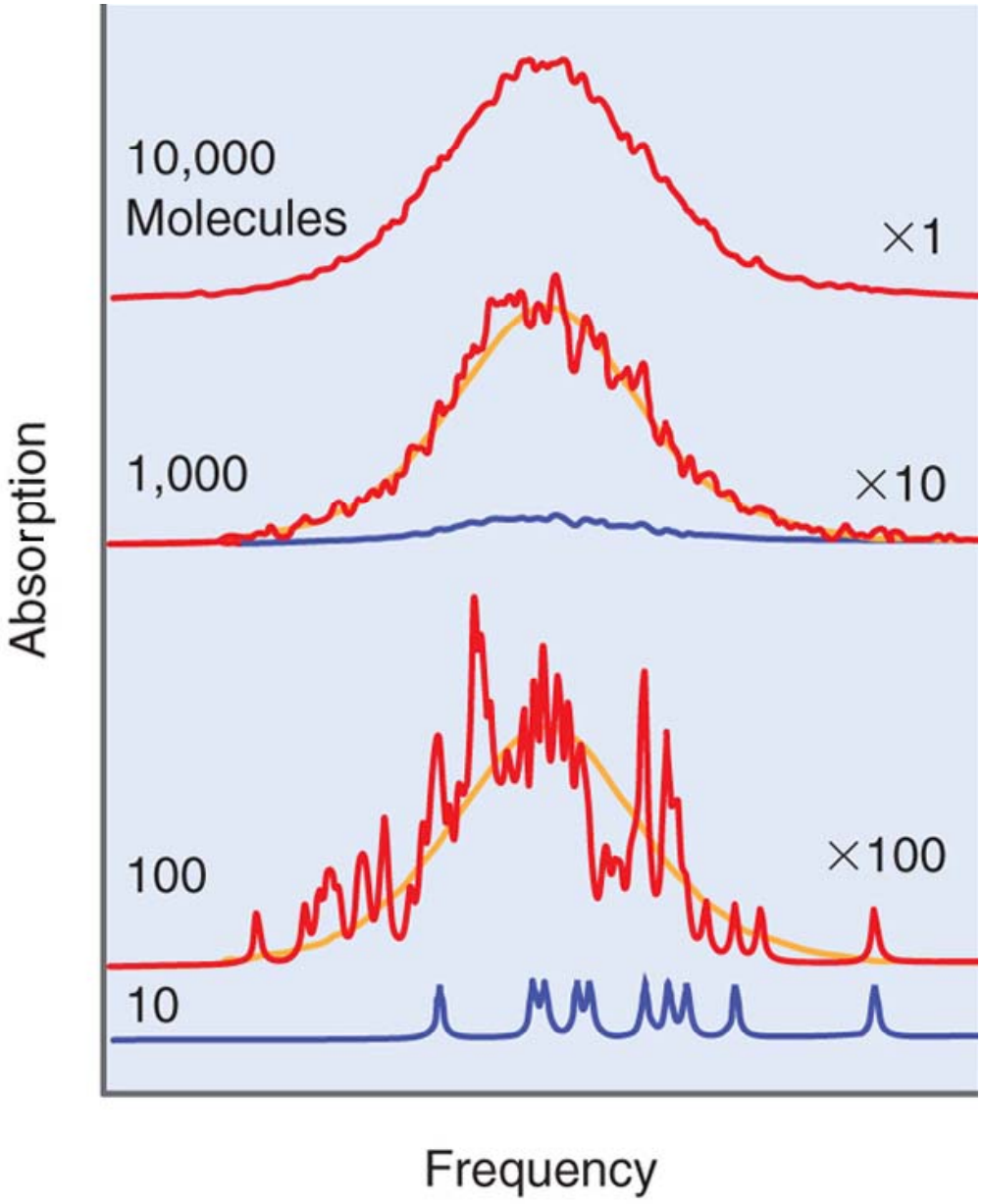

FIGURE 19.20

The absorption spectrum of an individual molecule is narrow, but the peak occurs over a range of frequencies for different molecules as shown in the lowest curve for 10 molecules in the sampling volume. As the number of molecules in the sampling volume is increased, the observed peak shows inhomogeneous broadening and is characteristic of the ensemble rather than of an individual molecule.

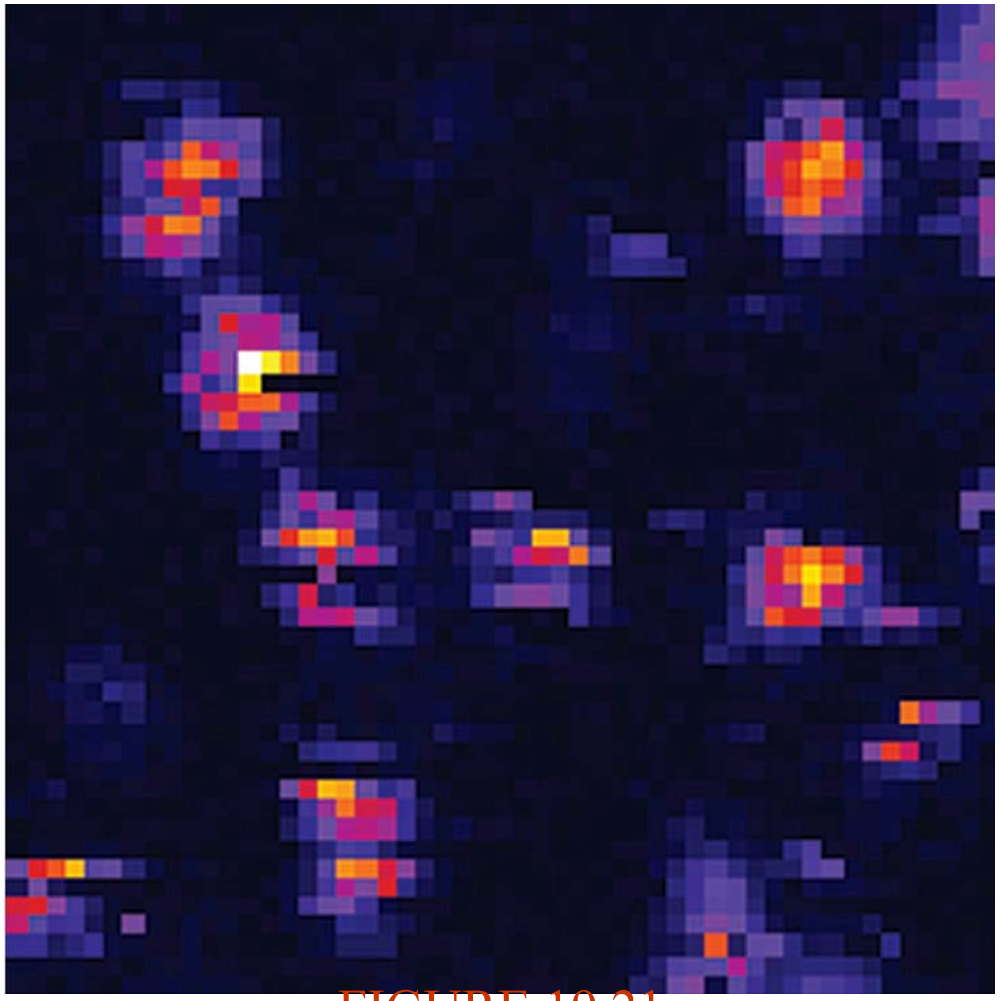

FIGURE 19.21

Microscope image of single Rhodamine B dye molecules on glass obtained using a confocal scanning microscope. The bright spots in the image correspond to fluorescence from single molecules. The image dimension is 5×5 μm.

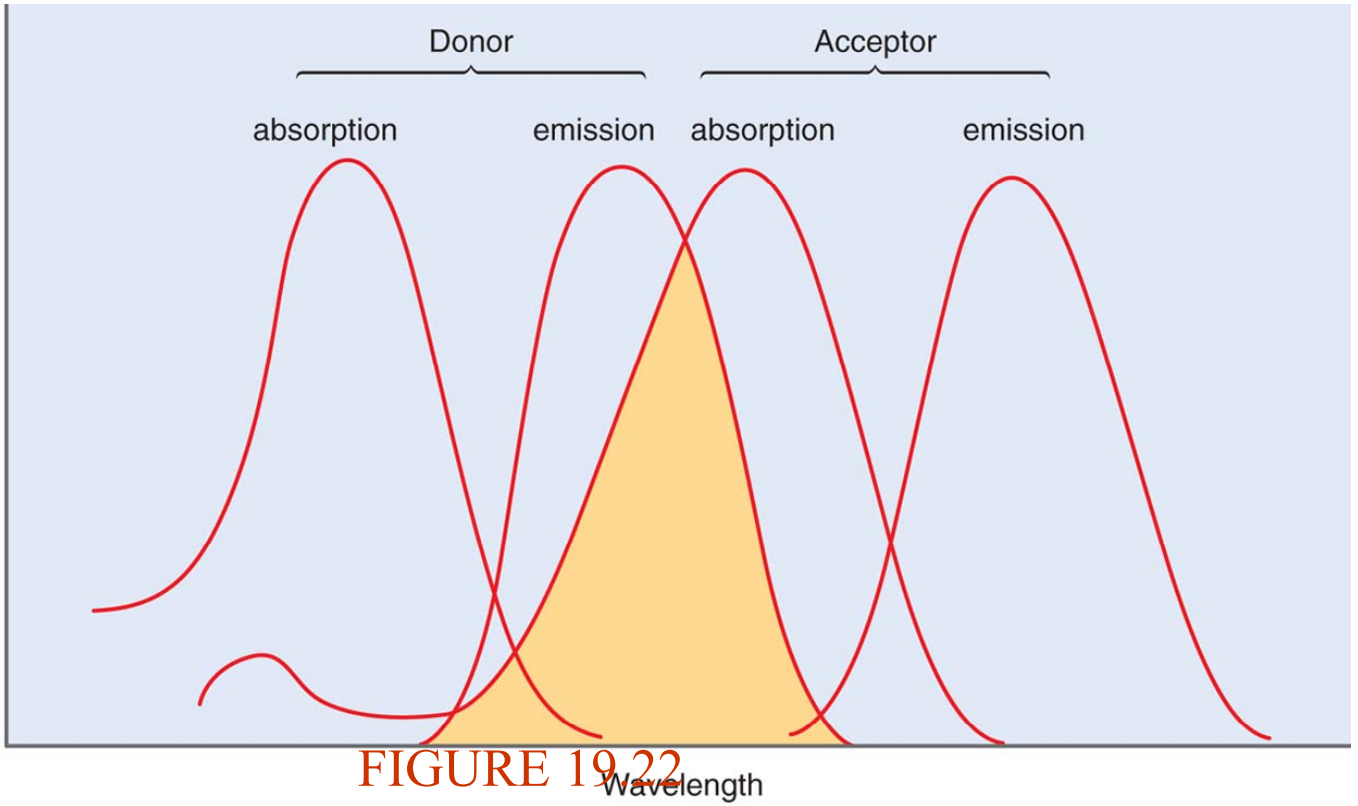

FIGURE 19.22

The emission spectrum of the excited donor occurs at a longer wavelength than the absorption as discussed in Section 19.9. If the emission spectrum of the donor overlaps the absorption spectrum of the acceptor, resonant energy transfer between the donor and acceptor can occur. Note the shift in the wavelength of the light emitted by the acceptor and the light absorbed by the donor. This shift allows the use of optical filter to detect acceptor emission in the presence of scattered light from the laser used to excite the donor.

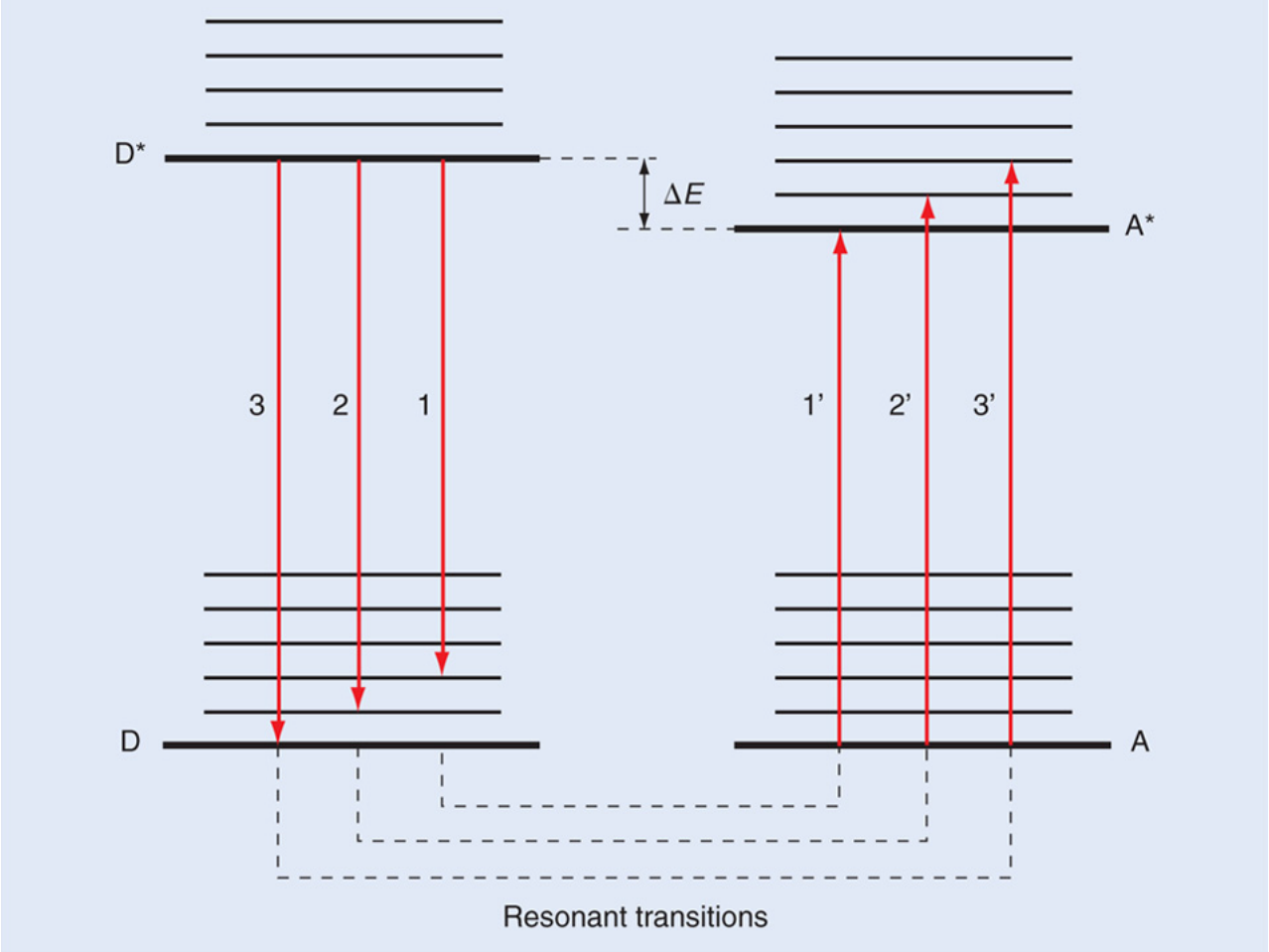

FIGURE 19.23

The energy levels of the ground-state and excited-state donor and acceptor are shown. Resonant energy transfer only occurs if the donor and acceptor match up in energy.

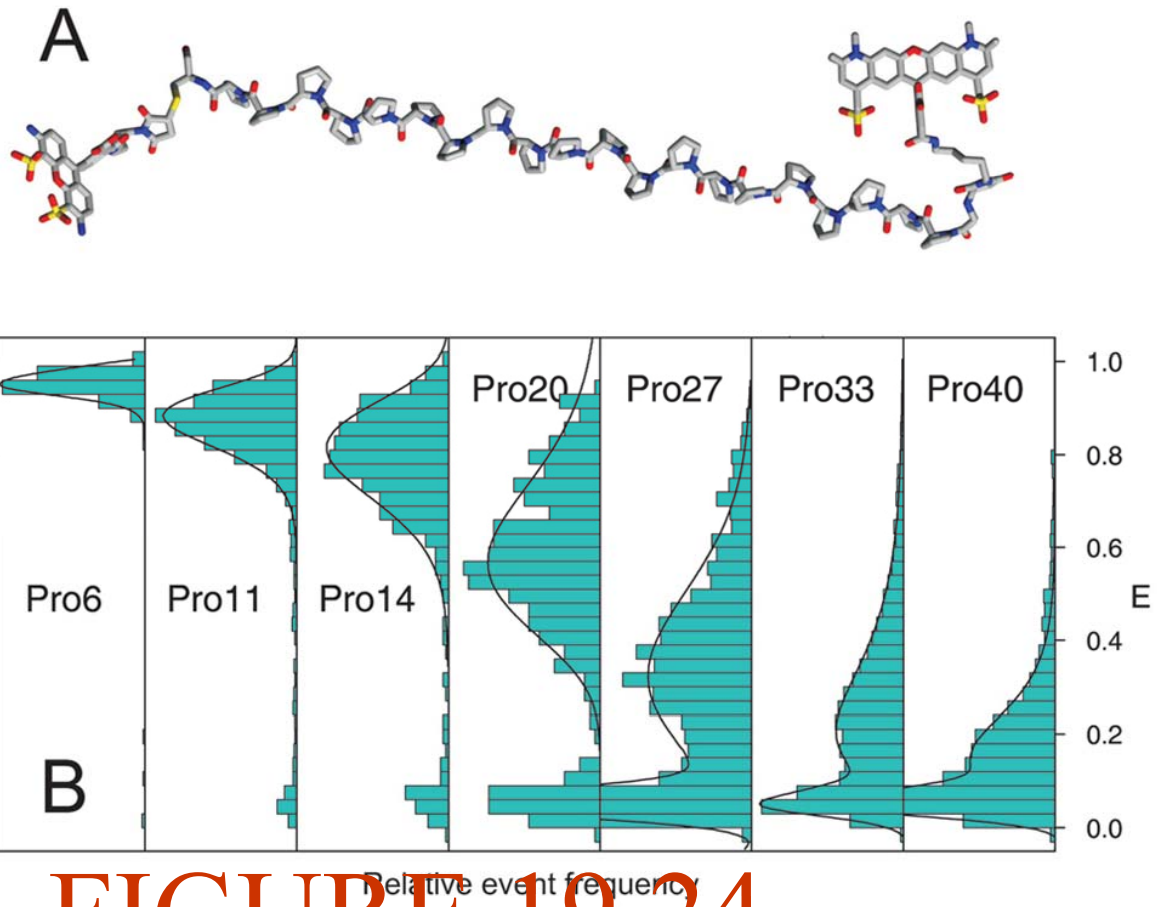

FIGURE 19.24

(a) Donor (left) and acceptor (right) dyes are attached to a polyproline peptide that becomes increasingly

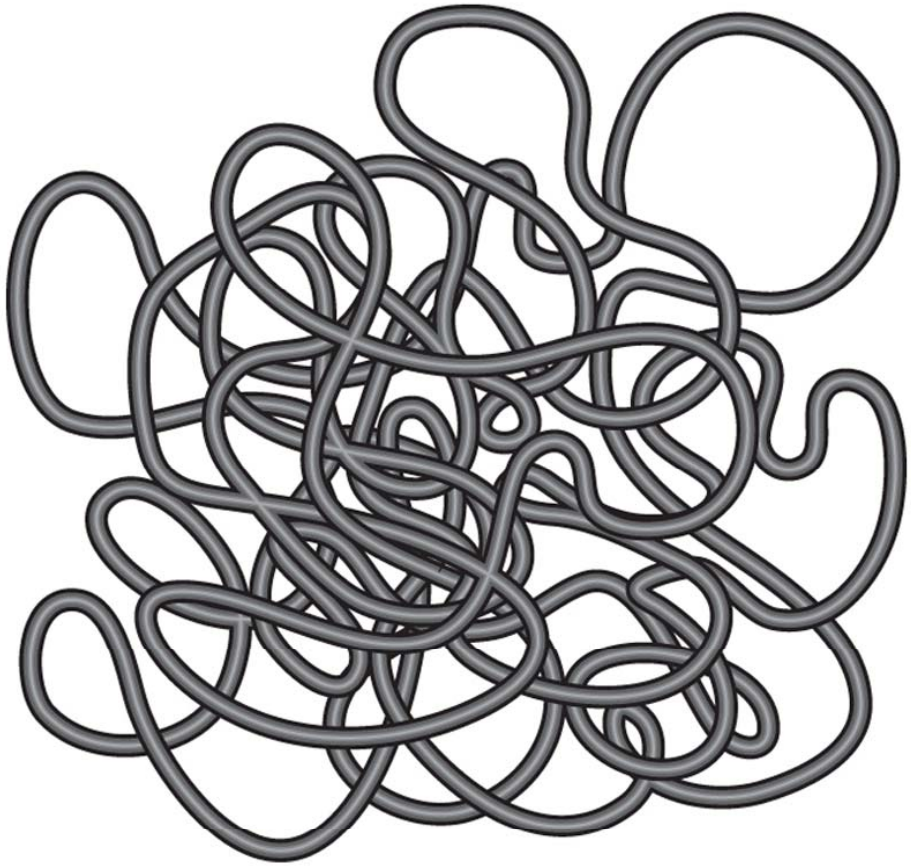

FIGURE 19.25

The conformation of long rod-like molecule in solution can be highly tangled.

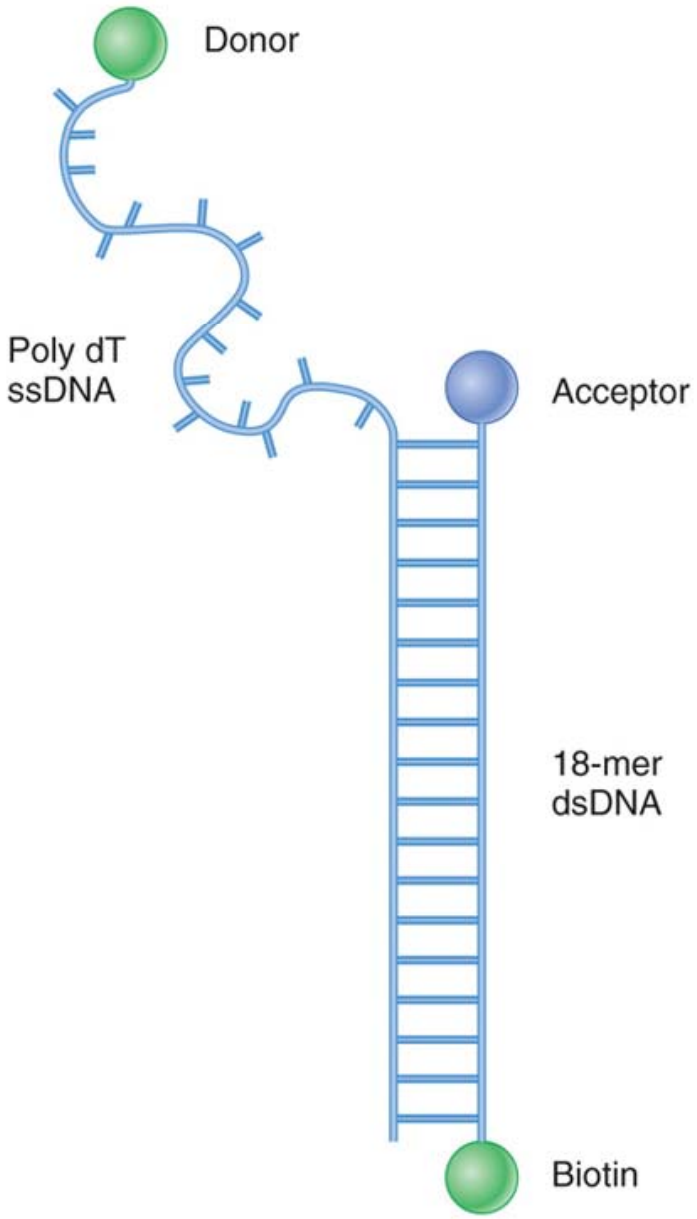

FIGURE 19.26

A donor and acceptor are attached to opposite ends of single strands of DNA. The strands are attached to a silica substrate. The function of the 18-mer dsDNA is to isolate the single strand from the substrate.

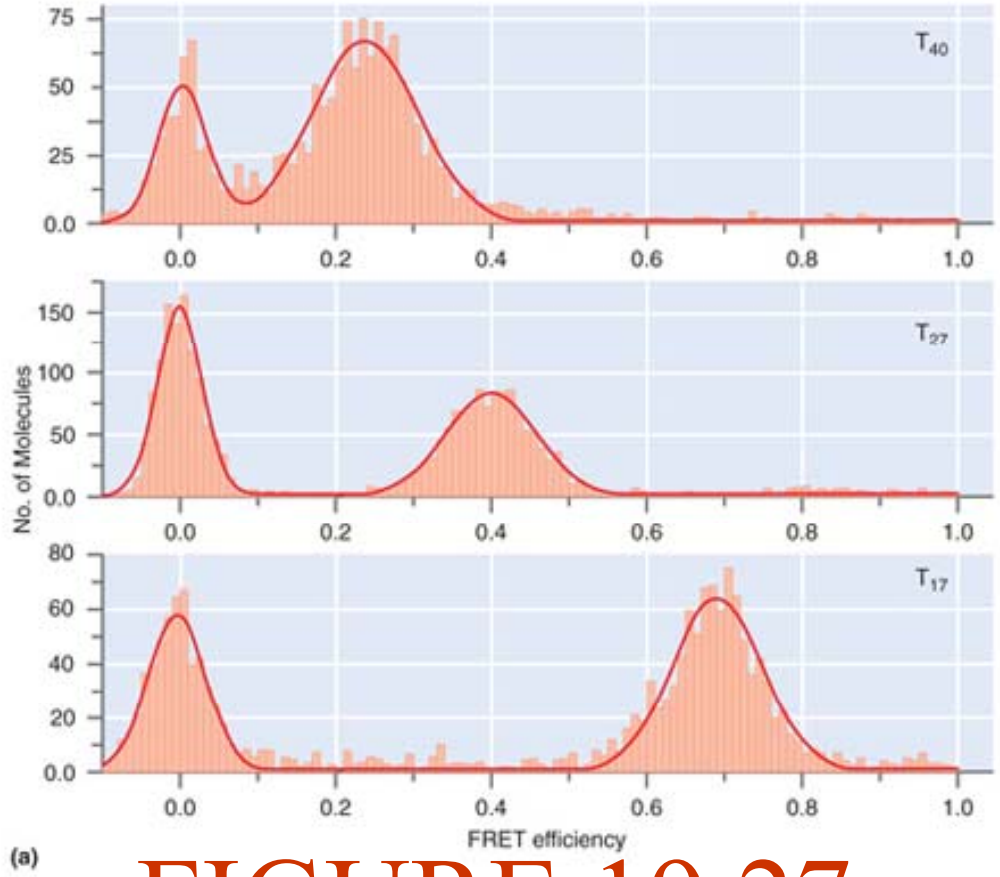

FIGURE 19.27

(a) The FRET efficiency is shown for Poly dT ssDNA of length 40, 27, and 17 nucleotides (top to bottom panel).

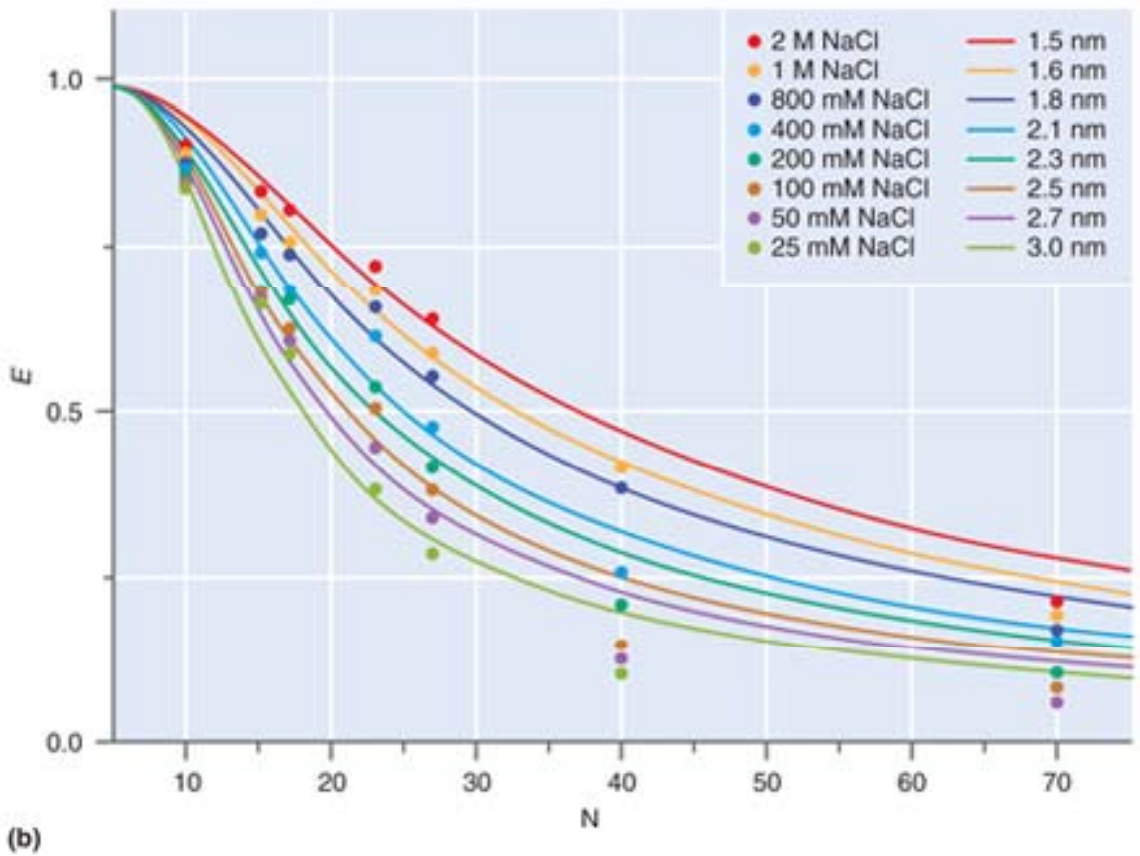

FIGURE 19.27

(continued)

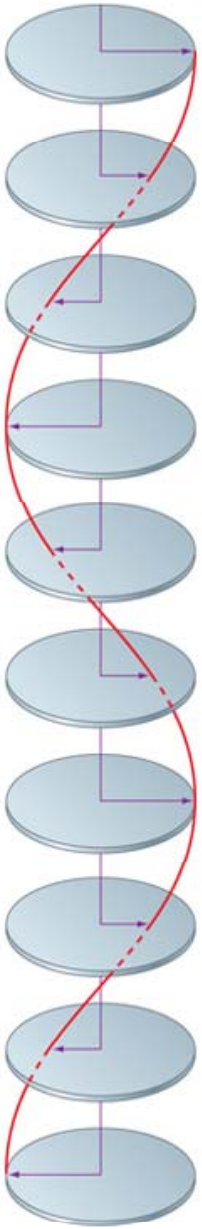

FIGURE 19.28

The arrows in successive images indicate the direction of the electric field vector as a function of time or distance. For linearly polarized light, the amplitude to the electric field vector changes periodically, but is confined to the plane of polarization.

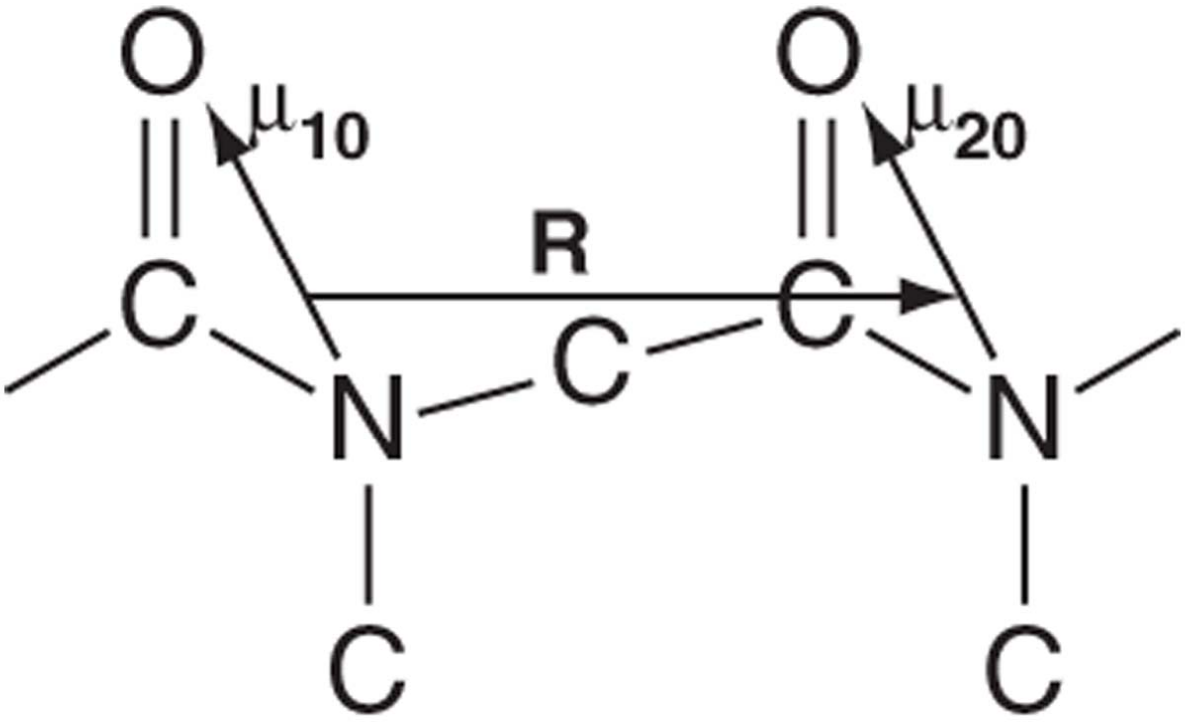

FIGURE 19.29

The amide bonds in a polypeptide chain are shown. The transition dipole moment is shown for a $n \rightarrow \pi^*$ transition.

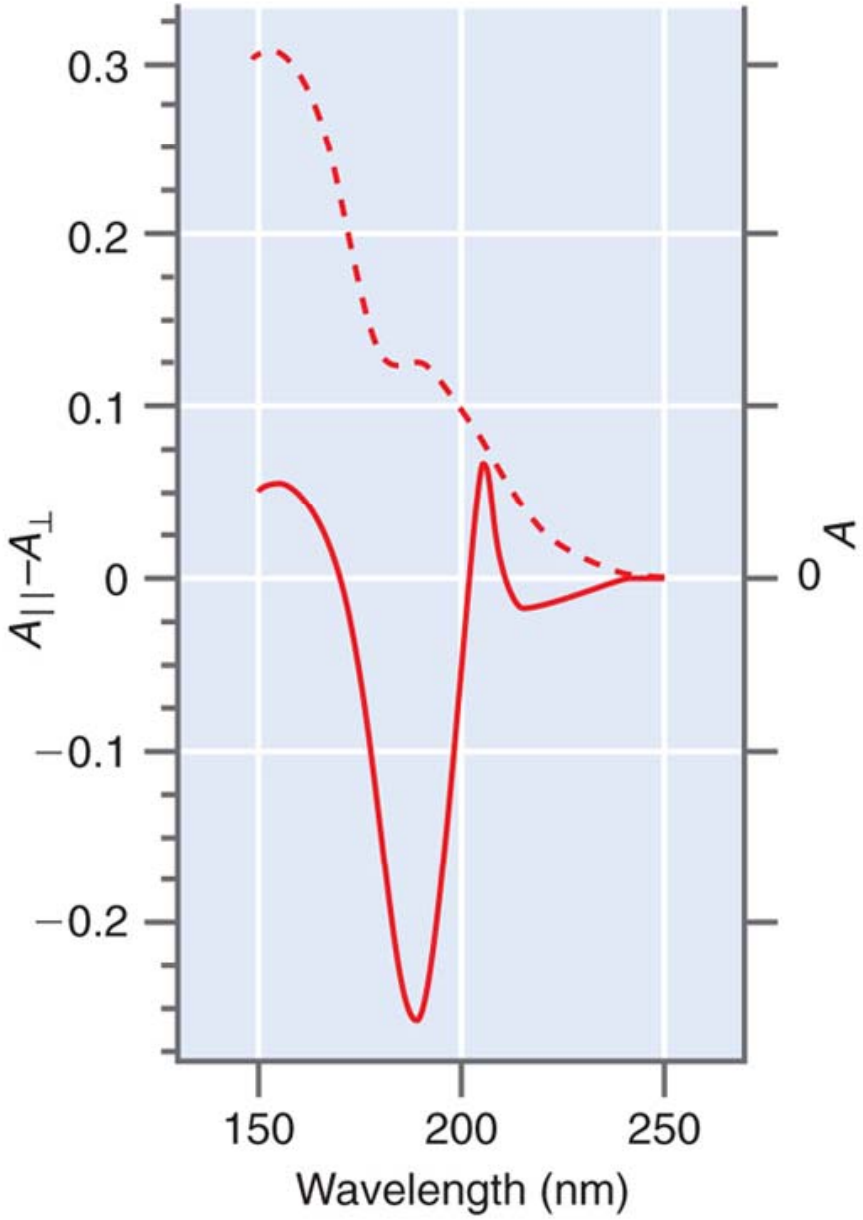

FIGURE 19.30

The normal isotropic absorbance, A, and $A_{\parallel}$ and $A_{\perp}$ are shown as a function of the wavelength for an oriented film of poly (g-ethyl-L-glutamate) in which it has the conformation of an α-helix.

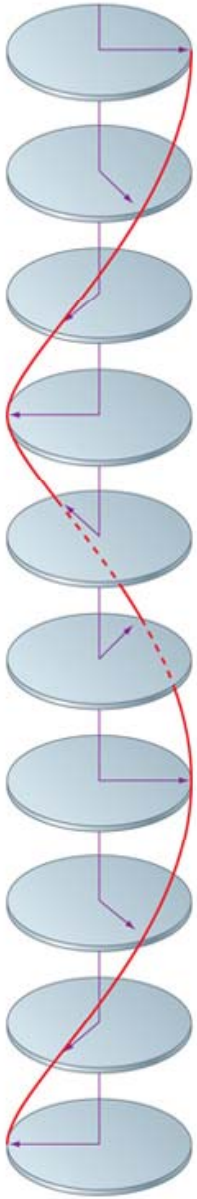

FIGURE 19.31

The arrows in successive images indicate the direction of the electric field vector as a function of time or distance. For circularly polarized light, the amplitude of the electric field vector is constant, but its plane of polarization undergoes a periodic variation.

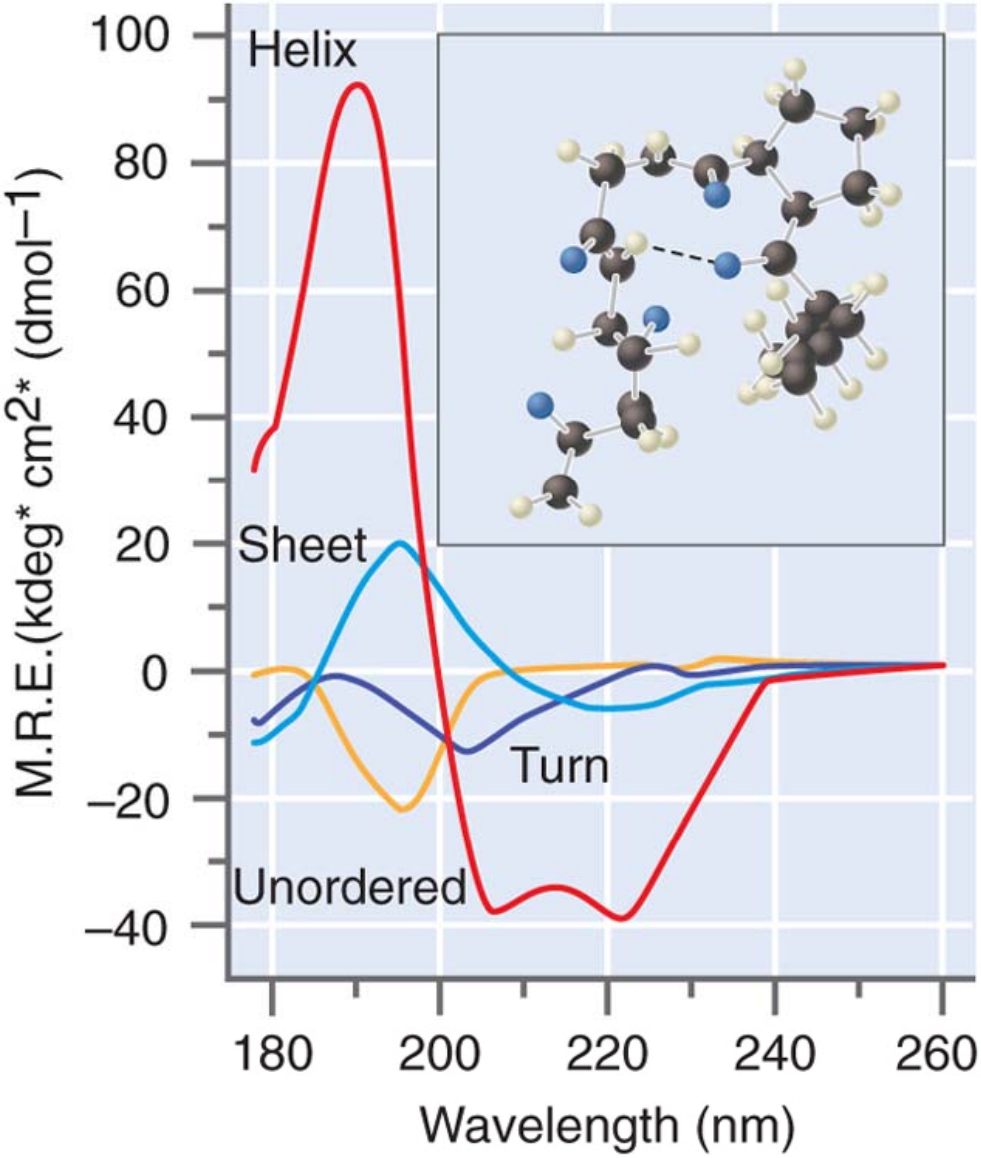

FIGURE 19.32

The rotation angle θ is shown as a function of wavelength for biomolecules having different secondary structures. Because the curves are distinctly different, circular dichroism spectra can be used to determine the secondary structure for optically active molecules. The inset shows the hydrogen bonding between different amide groups that generates different secondary structures.

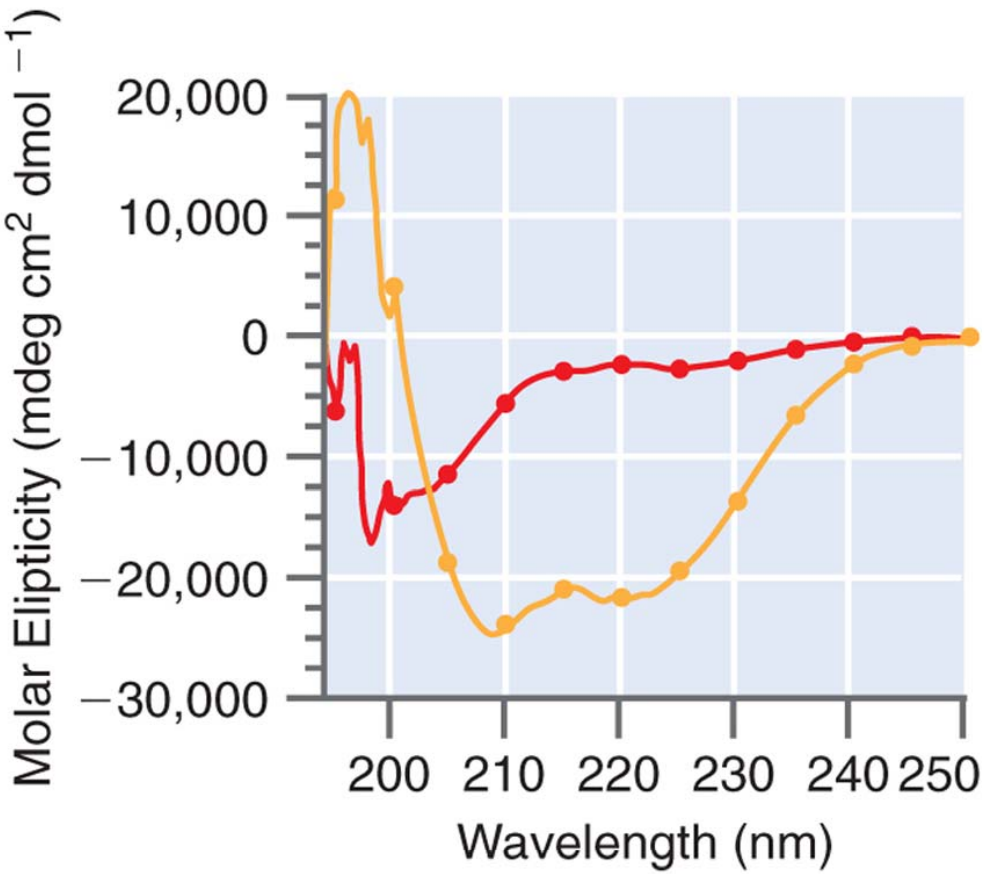

FIGURE 19.33

The molar ellipticity is shown as a function of the wavelength for α-synuclein in solution (yellow curve) and for α-synuclein bound to unilamellar phospholipid vesicles (red curve).

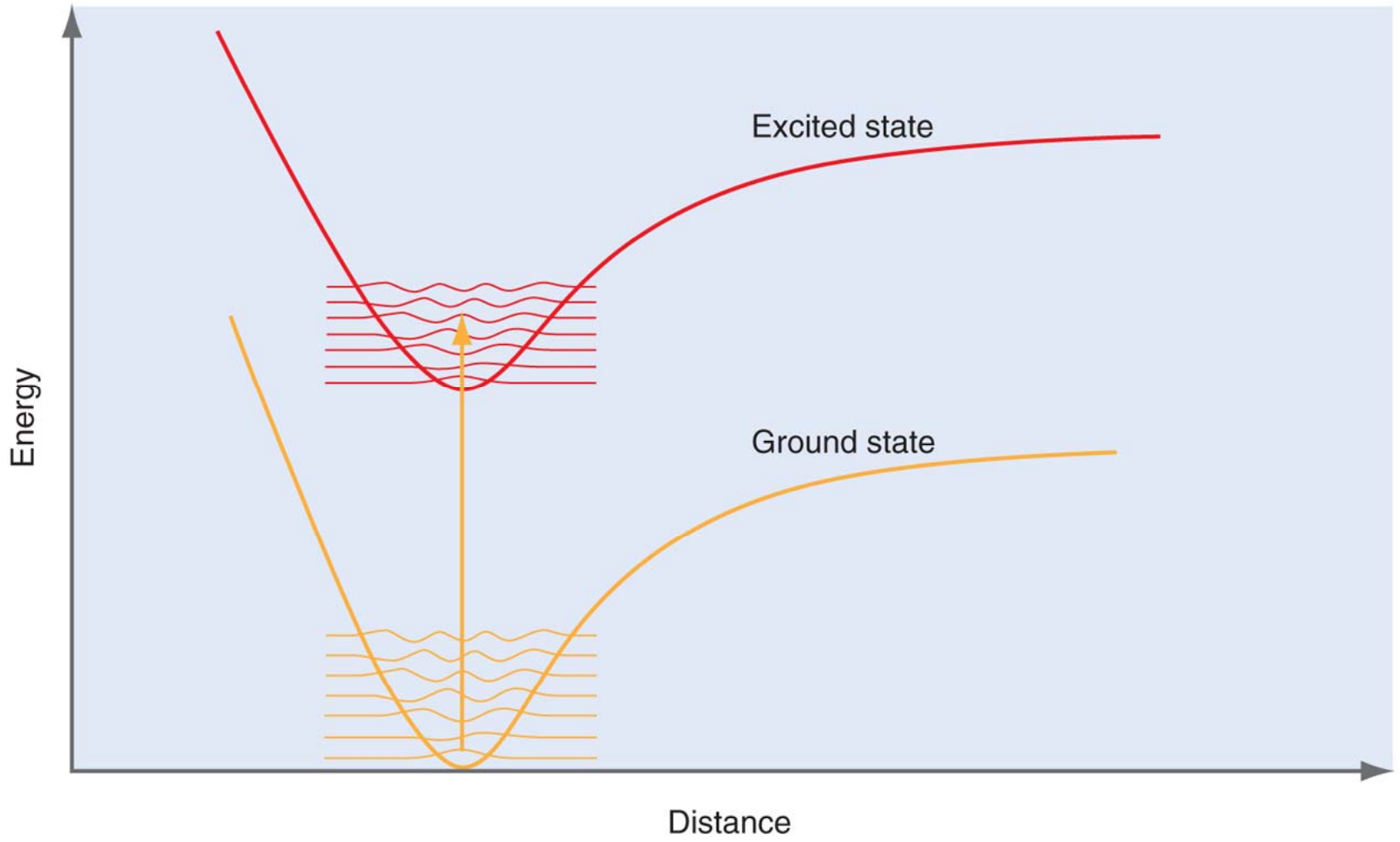

Questions 19.6

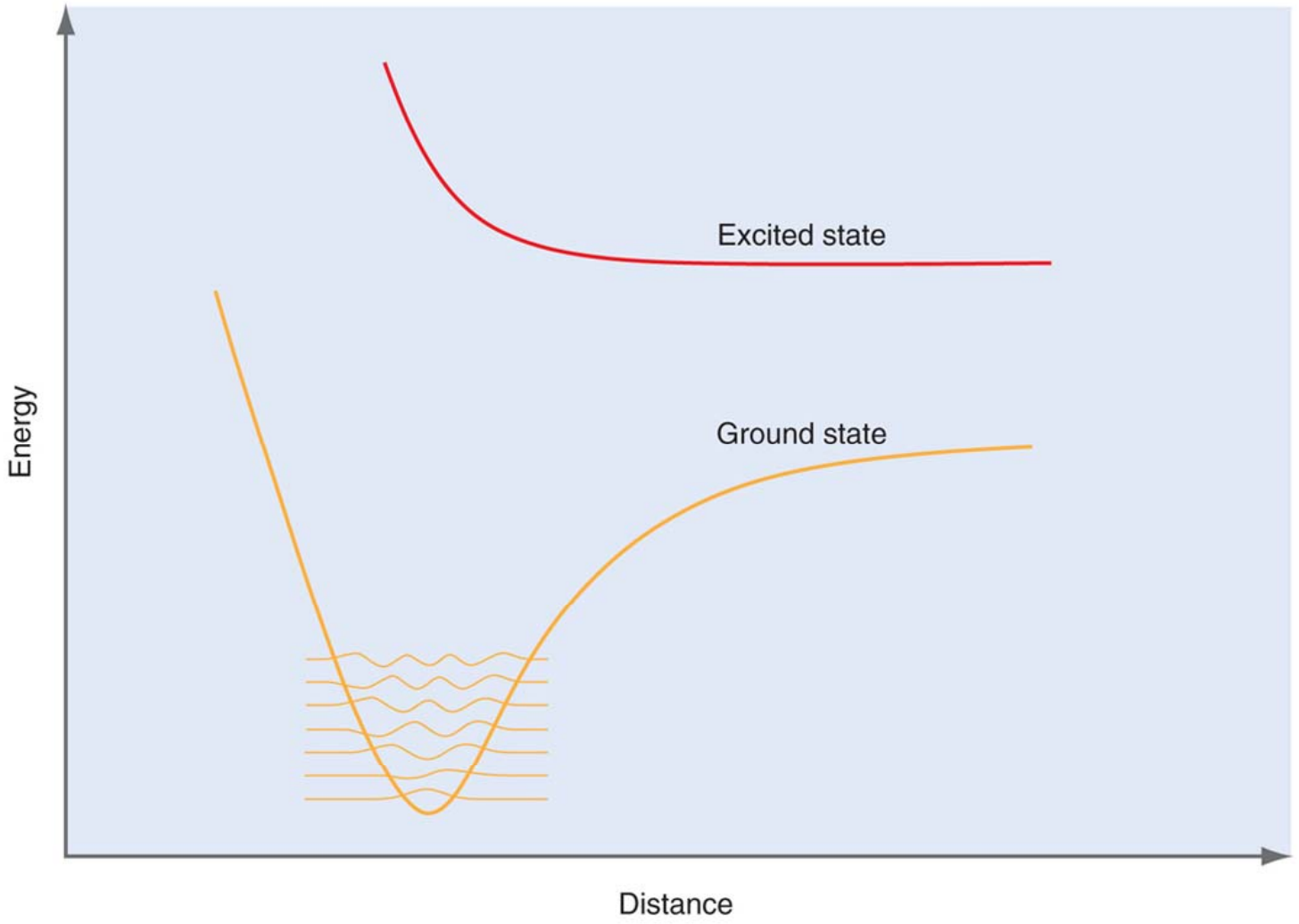

Questions 19.7

Physical Chemistry

For the Life Sciences

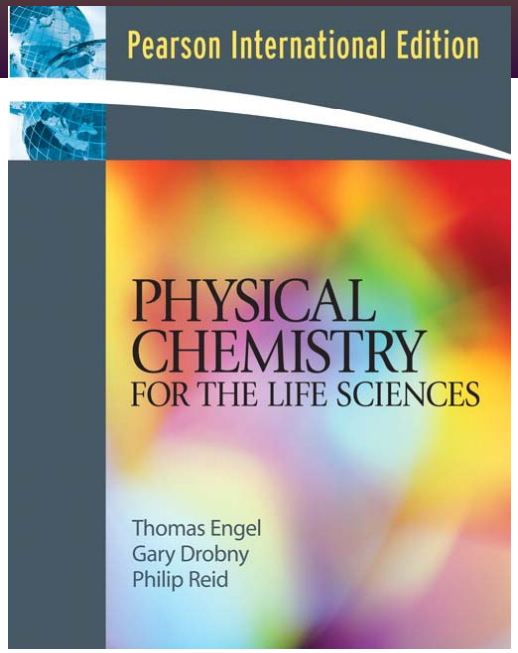

CHAPTER 20

Nuclear Magnetic Resonance Spectroscopy

- 20.1 Nuclear spins external fields
- 20.2 Transient response and relaxation
- 20.3 The spin-echo
- 20.4 Fourier transform NMR spectroscopy
- 20.5 NMR spectra: chemical shifts and spin-spin couplings
- 20.6 Multidimensional NMR
- 20.7 Solution NMR studies of biomolecular structure
- 20.9 NMR imaging
- 20.10 Electron spin resonance spectroscopy

TABLE 20.1 Parameters for Spin Active Nuclei

Nucleus	Isotopic Abundance (%)	Spin	Nuclear factor g_N	Magnetogyric Ratio ($\gamma/10^7$ rad T^{-1} s^{-1})
^{1}H	99.985	1/2	5.5854	26.75
^{19}F	100	1/2	5.2546	25.18
^{17}O	0.037	5/2	−1.8928	−3.63
^{13}C	1.108	1/2	1.4042	6.73
^{31}P	100	1/2	2.2610	10.84
^{15}N	0.37	1/2		−2.71
^{2}H	0.015	1	0.8574	4.11
^{14}N	99.63	1	0.4036	1.93

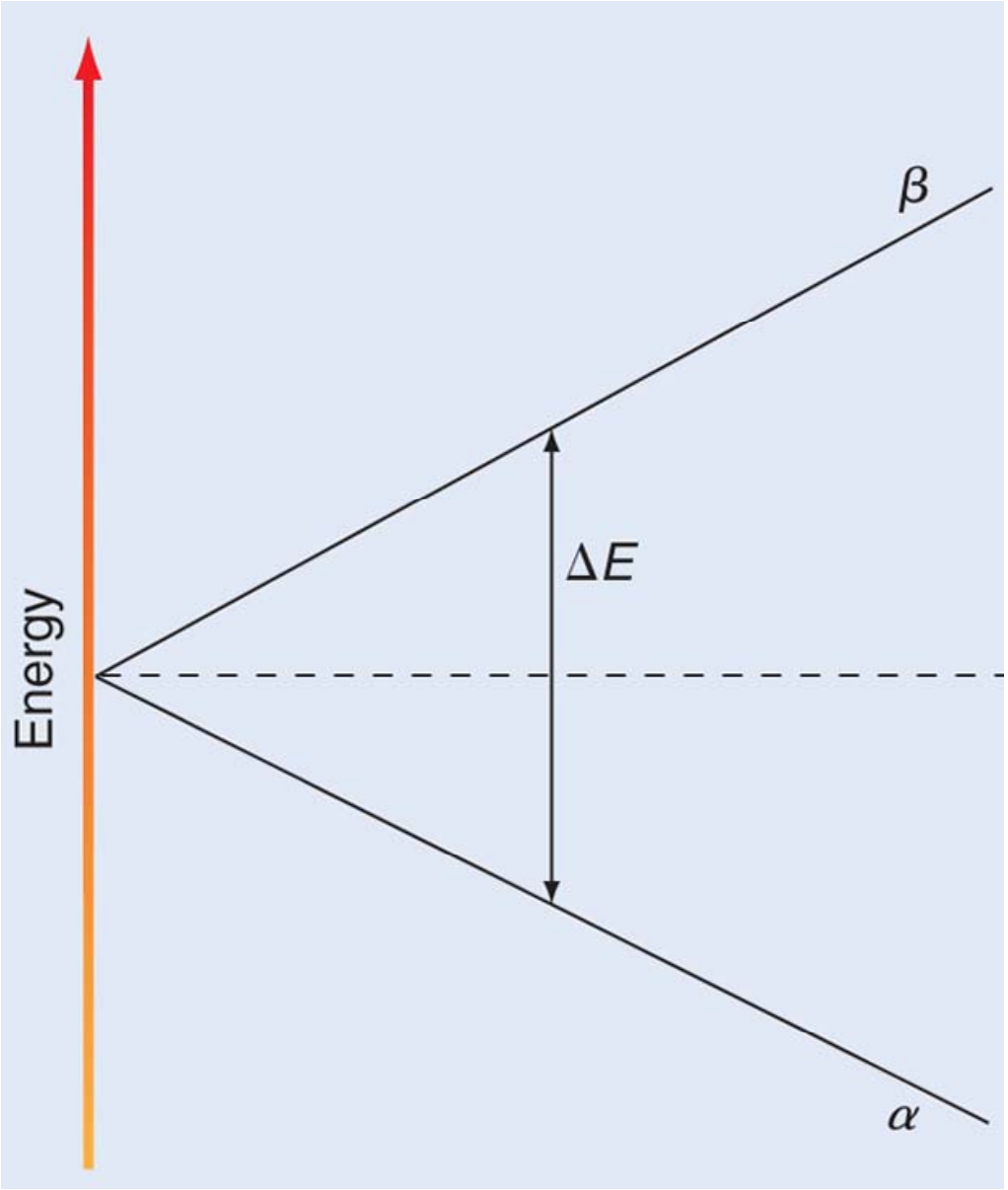

FIGURE 20.1

Energy of a nuclear spin of quantum number ½ as a function of the magnetic field.

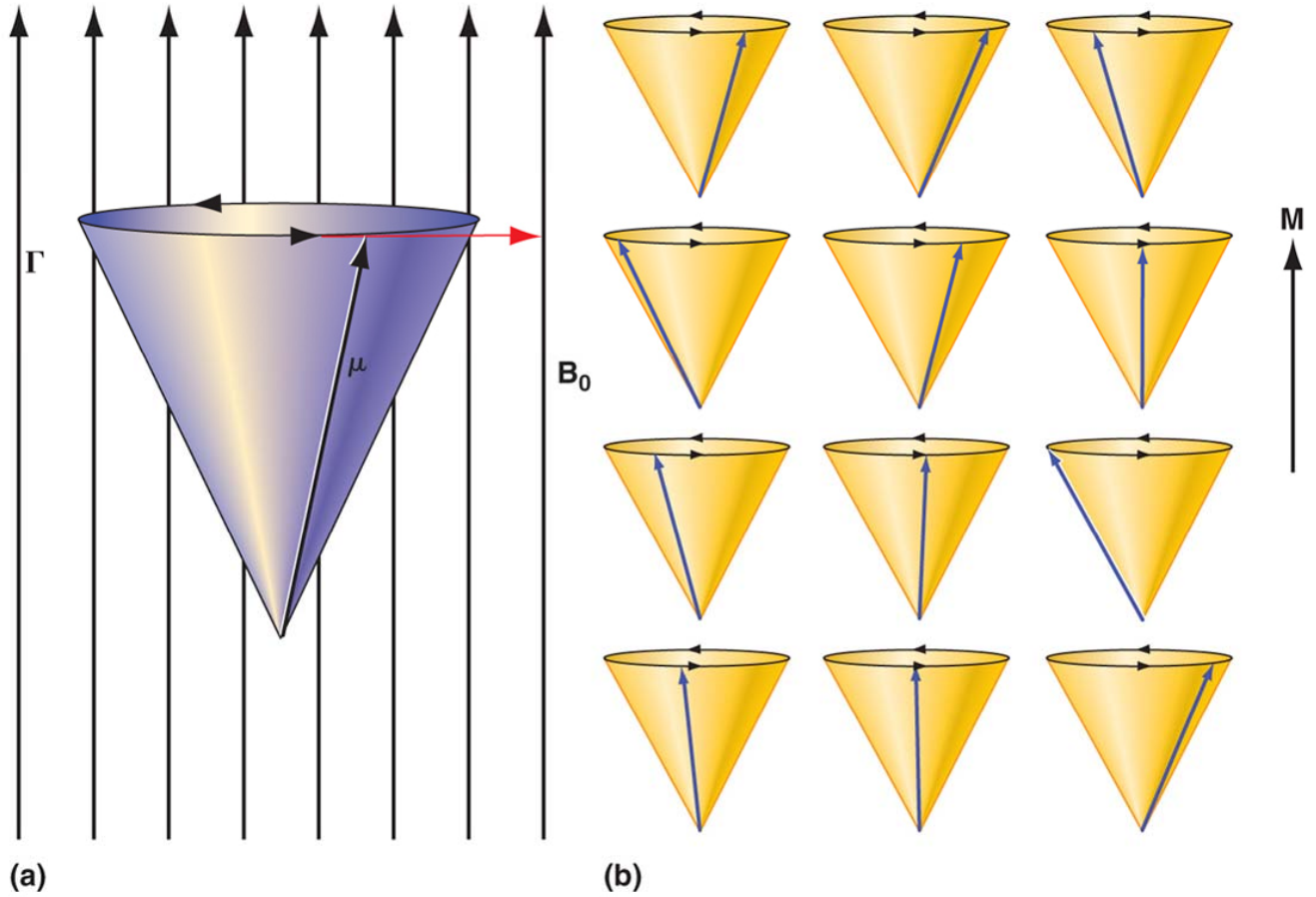

FIGURE 20.2

Precession of a nuclear spin about the magnetic field direction for α spins. The right side of the figure shows that the magnetization vector $\vec{M}$ resulting from summing the individual spin magnetic moments is oriented parallel to the magnetic field. It has no transverse component.

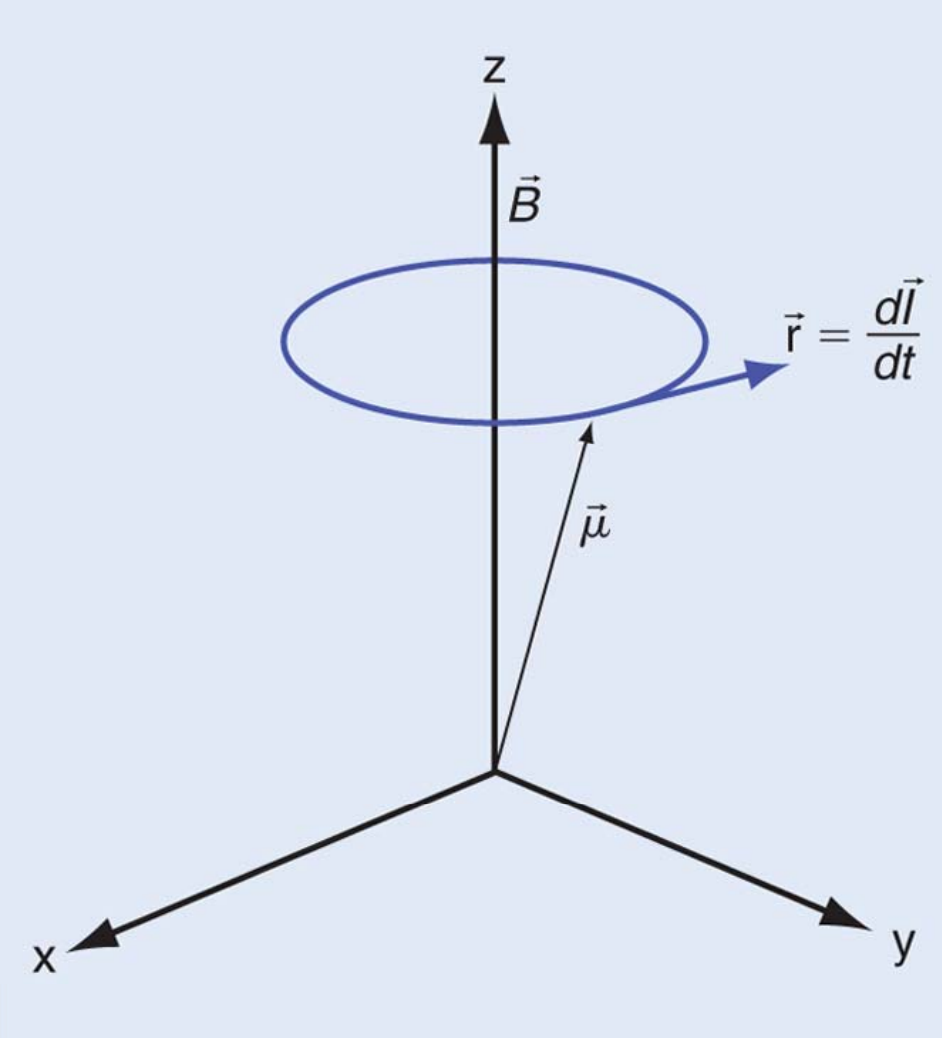

FIGURE 20.3

The effect of a static field $\vec{B}$ is to apply a torque $\vec{\Gamma}$ to the nuclear magnetic moment, which causes a precesstion of the moments about the static magnetic field

$$\vec{\Gamma} = d\vec{I} / dt = \vec{\mu} \times \vec{B}_0 .$$

The precessional frequency is called the Larmor frequency

$$v_0 = \gamma \vec{B}_0 / 2\pi .$$

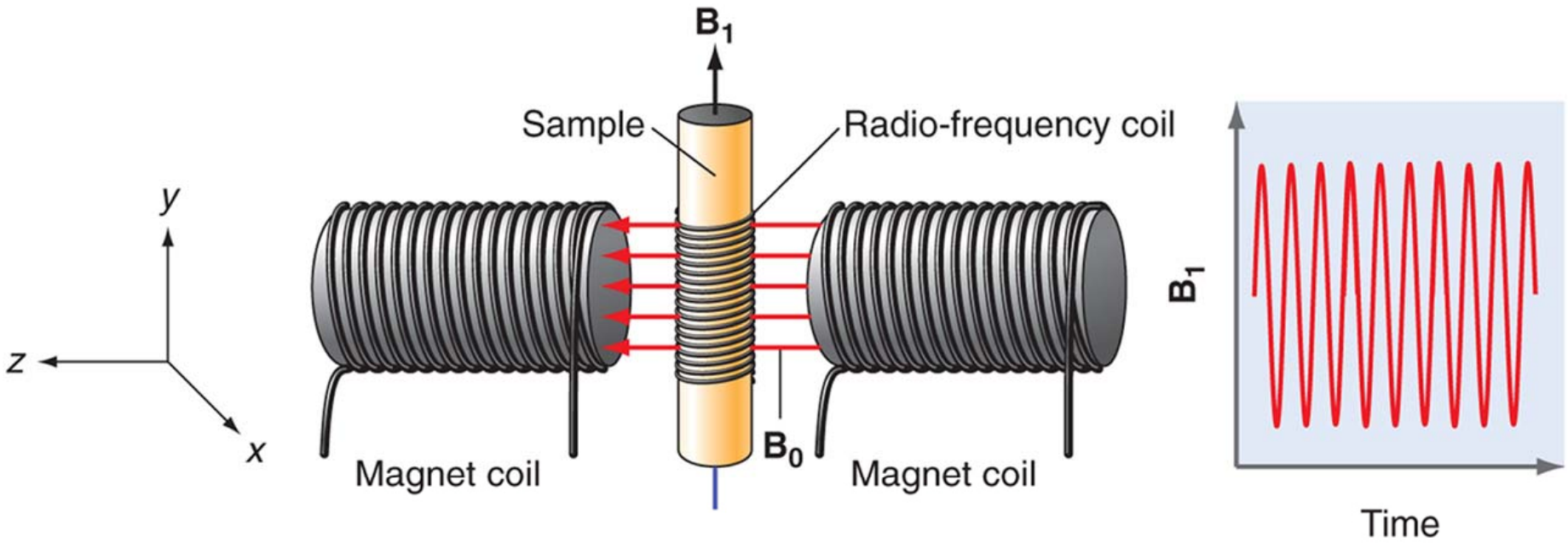

FIGURE 20.4

Schematic picture of the NMR experiment showing the static field, and the rf field coil.

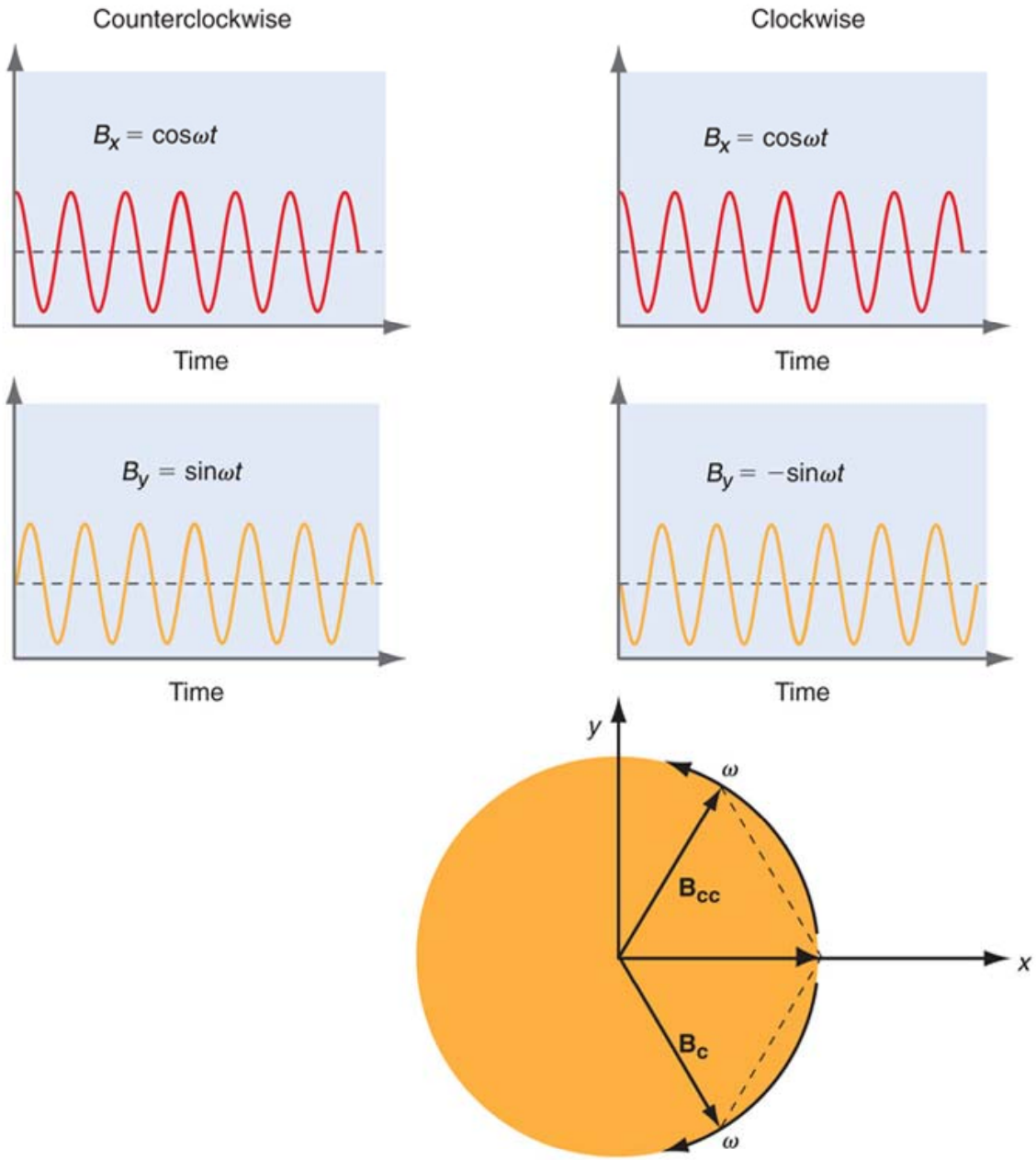

FIGURE 20.5

The expression for the field $B_1^c(t)$ is identical to that for $B_1^{cc}(t)$ except the frequency ω is replaced by –ω, so $B_1^{cc}(t)$ is said to be rotating counterclockwise while $B_1^c(t)$ rotates clockwise. Of these two circularly polarized fields, only

$B_1^{cc}(t)$ rotates in the same sense as the magnetic moments and for this reason only $B_1^{cc}(t)$ can induce transitions between nuclear spin states.

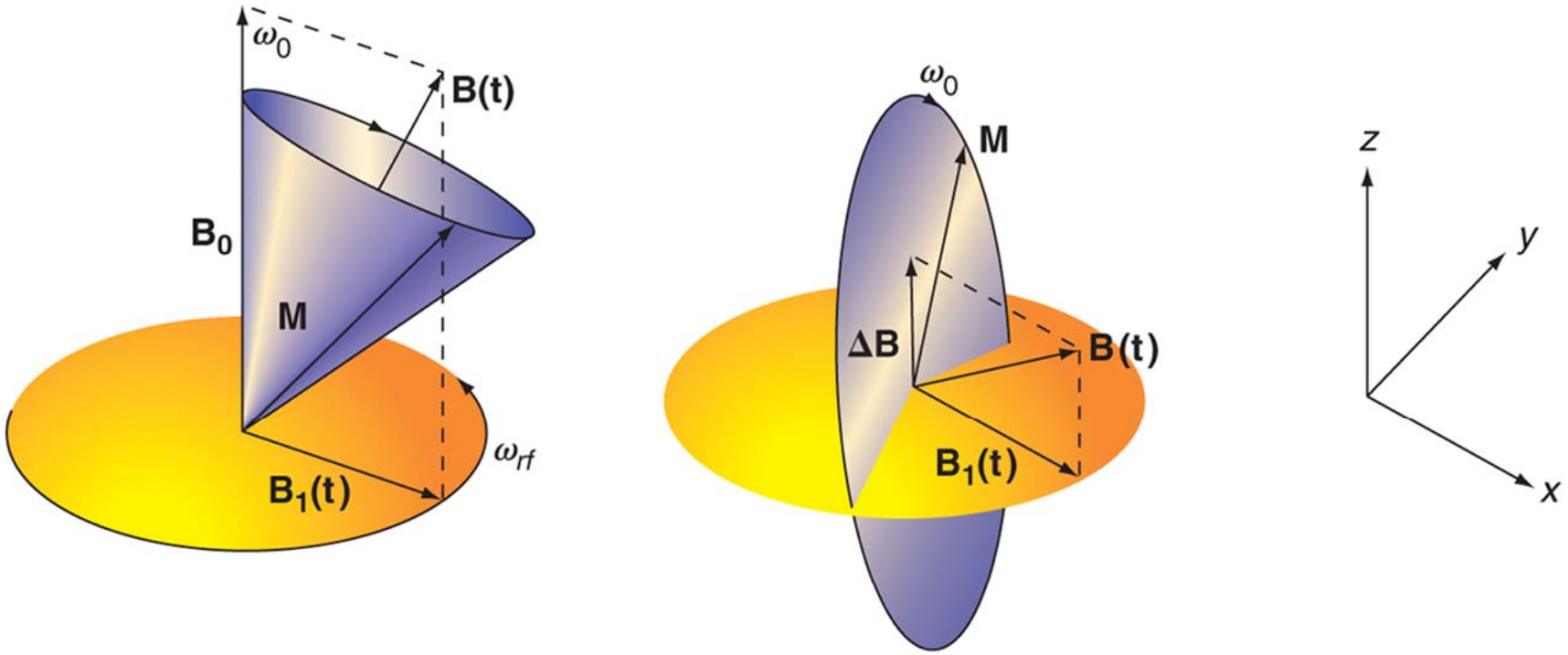

FIGURE 20.6

The NMR experiment as viewed from the laboratory and rotating frame of reference.

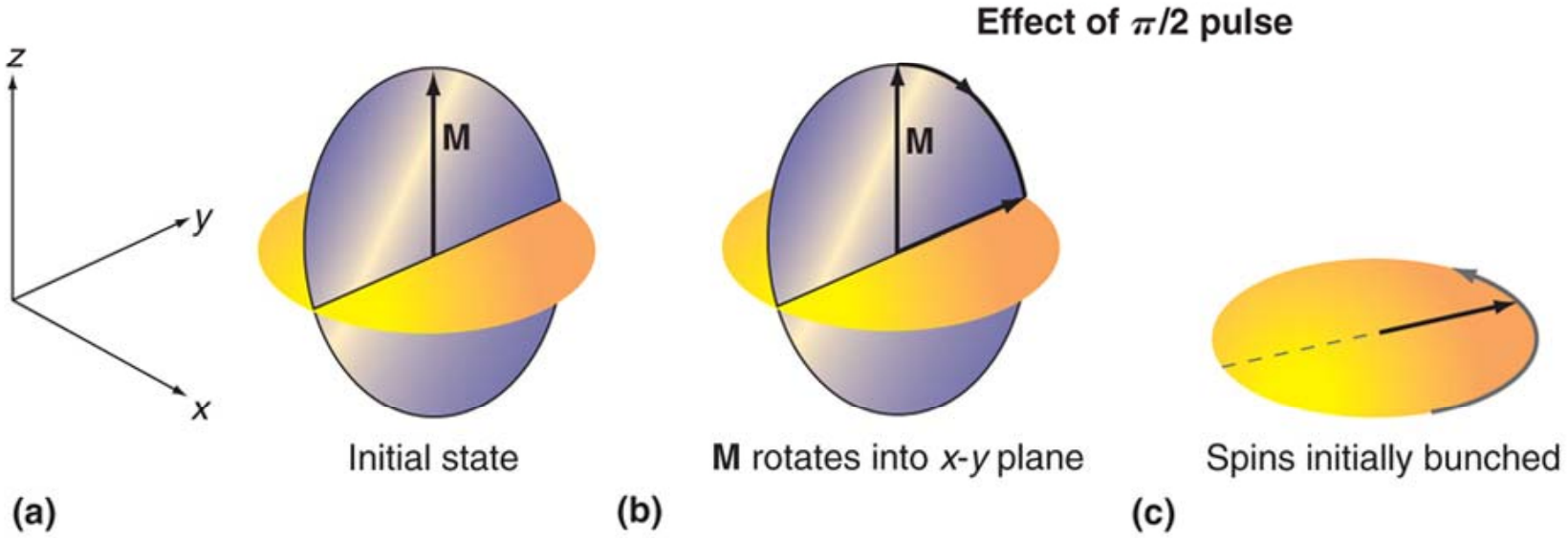

FIGURE 20.7

RF pulse timing and the effect on $\vec{M}$ as viewed from the rotating frame. At time a, $\vec{M}$ points along the z axis. As the π/2 pulse is applied, $\vec{M}$ precesses in the x-y plane and point along the y axis as shown in c. After the pulse is turned off, $\vec{M}$ relaxes to its initial orientation along the z axis. The z component increases with the relaxation time T_1. Simultaneously, the x-y component of $\vec{M}$ decays with relaxation time T_2 as the individual spins dephase.

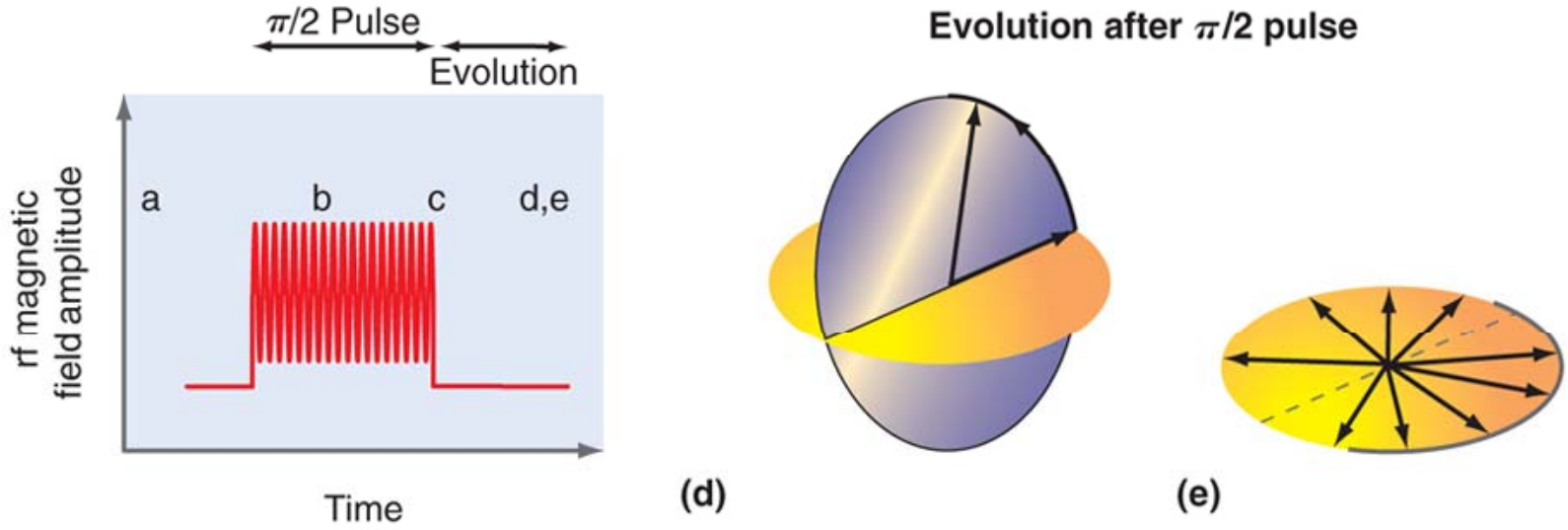

FIGURE 20.7

(continued)

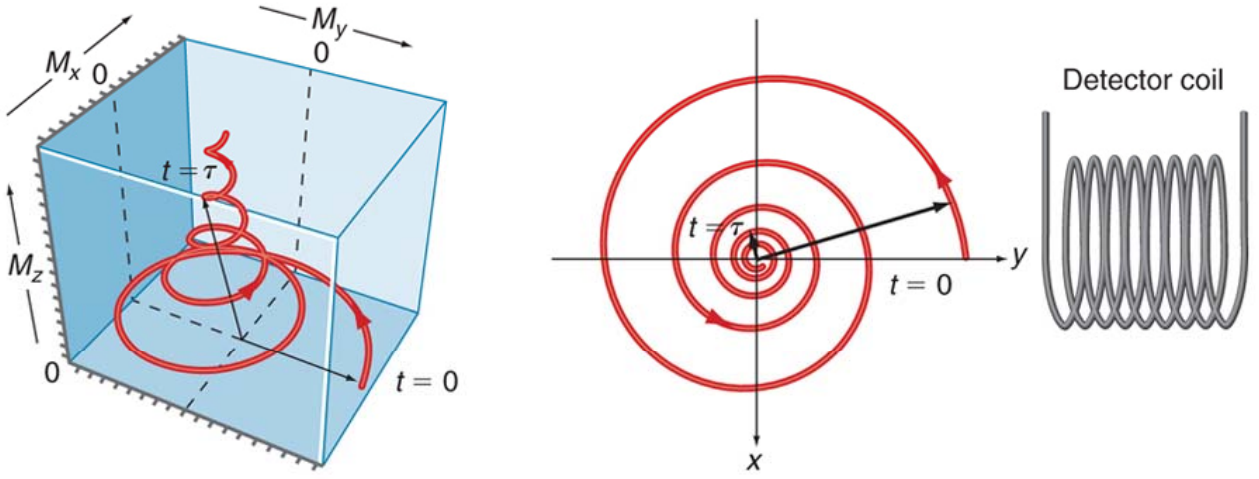

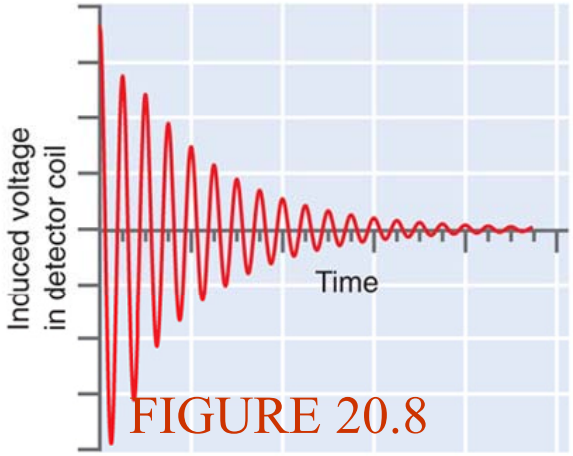

FIGURE 20.8

Evolution of the magnetization vector M in three dimensions and $M_{x\text{-}y}$ as a function of time. The variation of $M_{x\text{-}y}$ with time leads to an exponentially decaying inducted rf voltage in the detector coil.

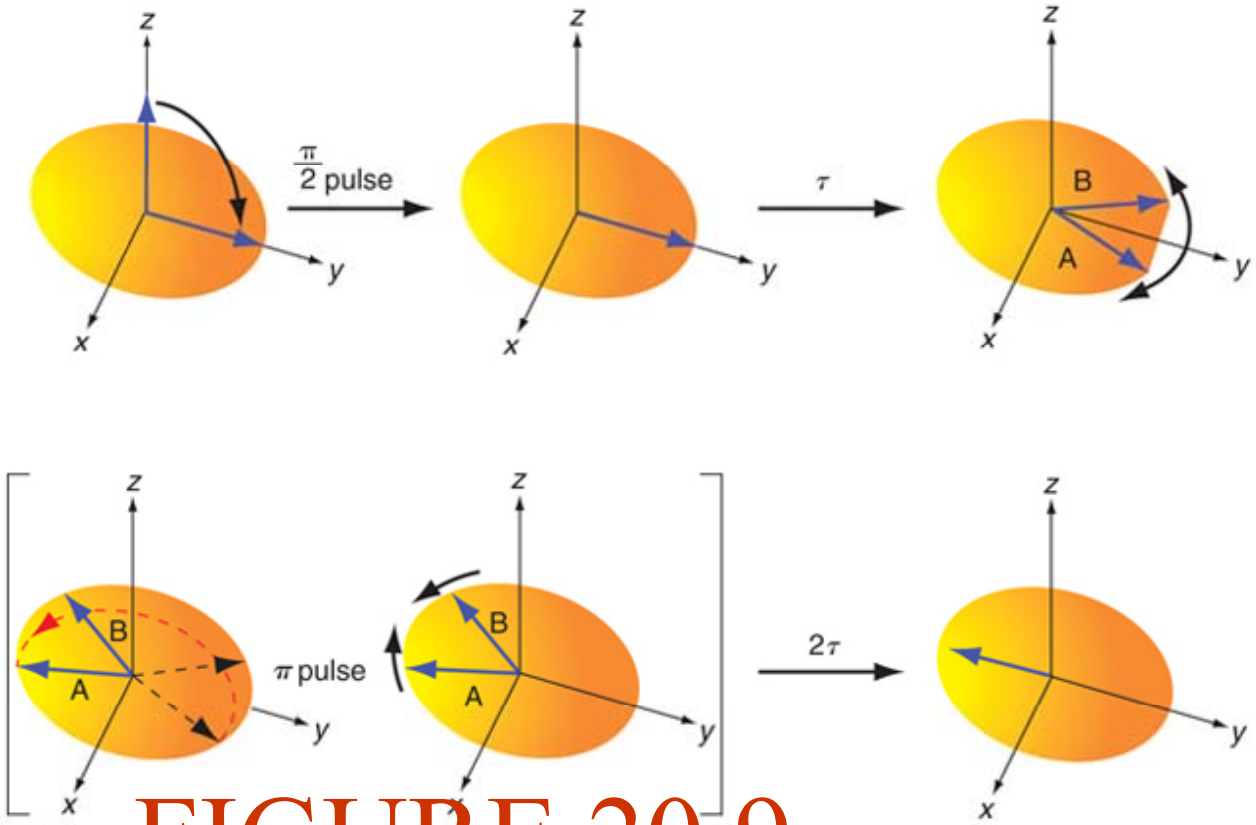

FIGURE 20.9

$\vec{M}$

Schematic representation of the spin-echo experiment. The π/2 pulse applied along the *y* axis rotates

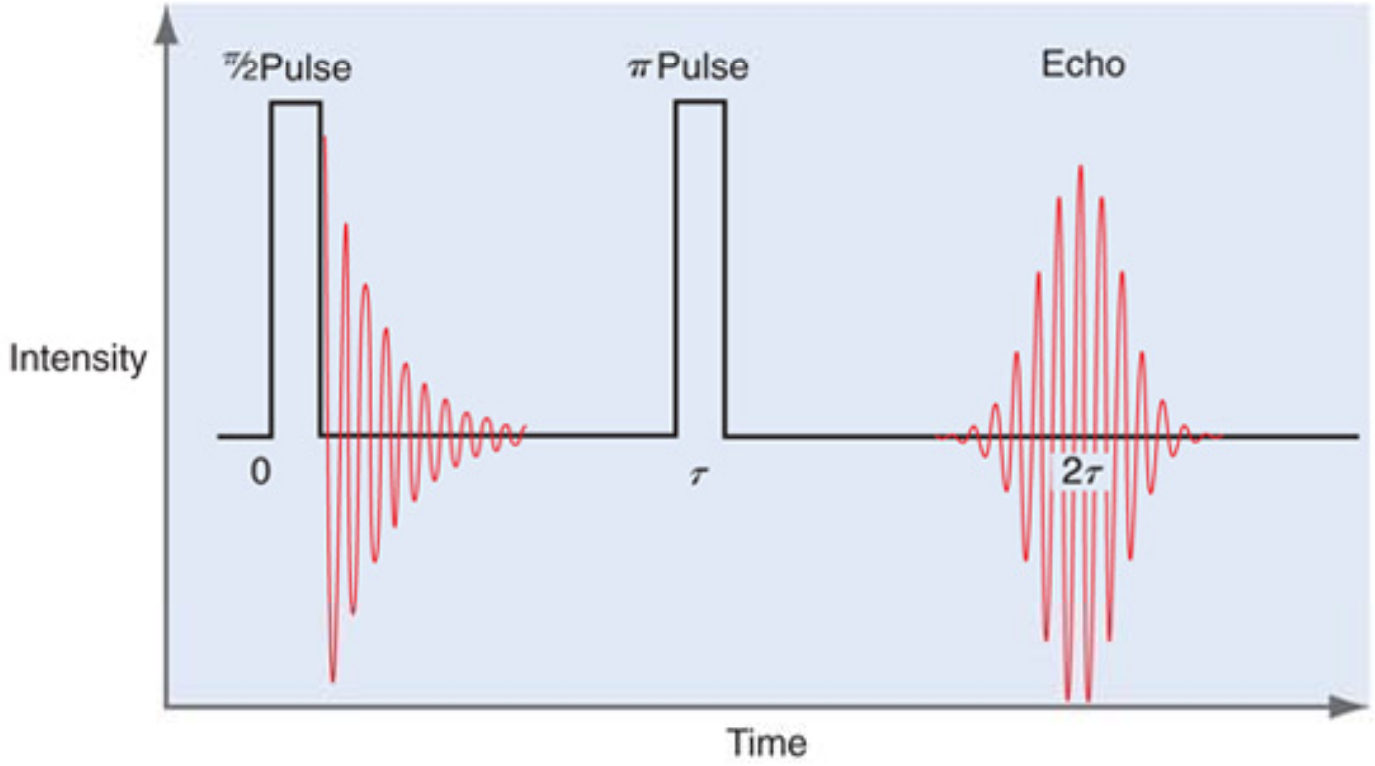

FIGURE 20.9

(continued)

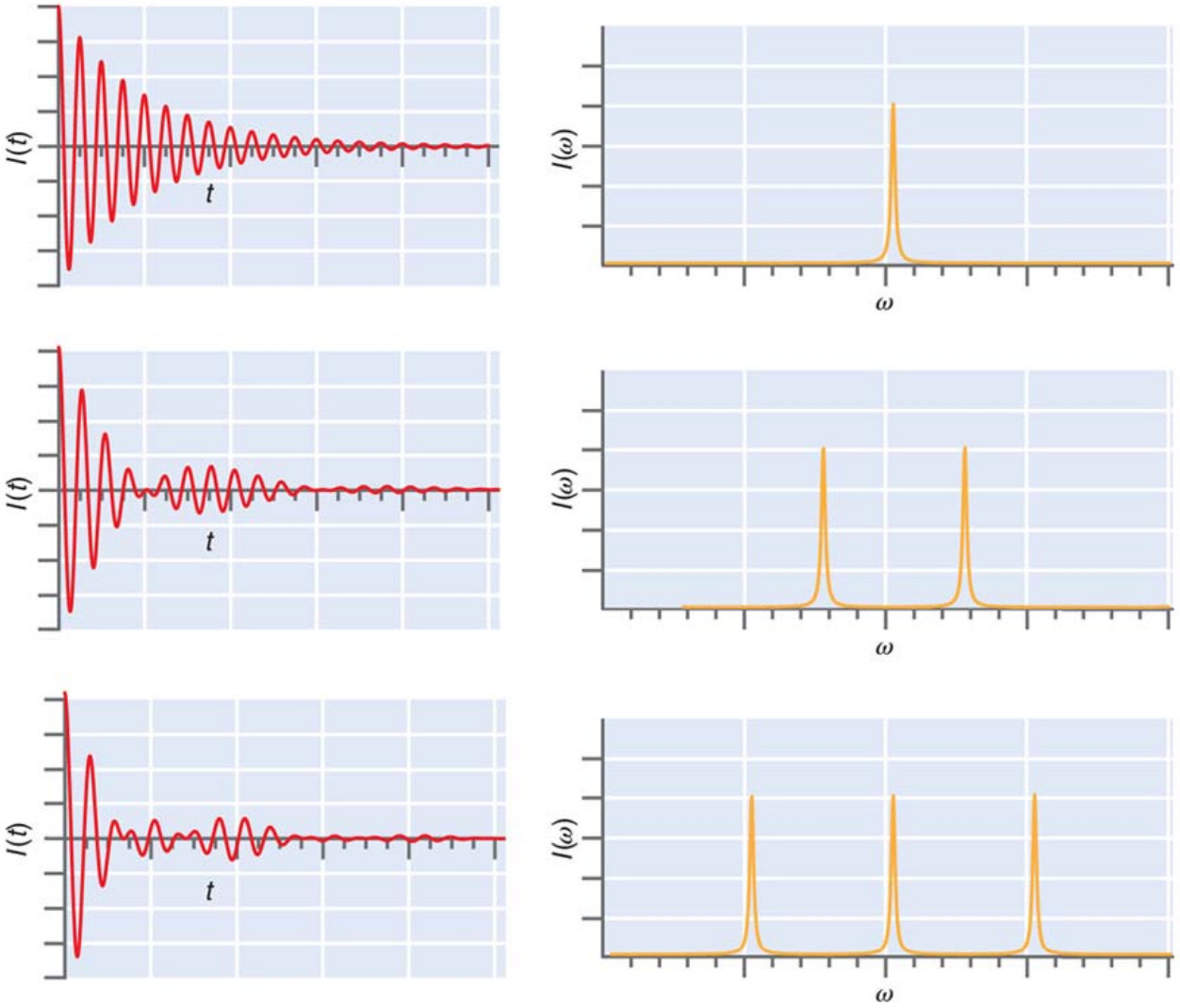

FIGURE 20.10

Juxtaposition of three induction decays containing one (top), two (center), and three (bottom) frequency components with the respective absorption spectra obtained by Fourier transformation.

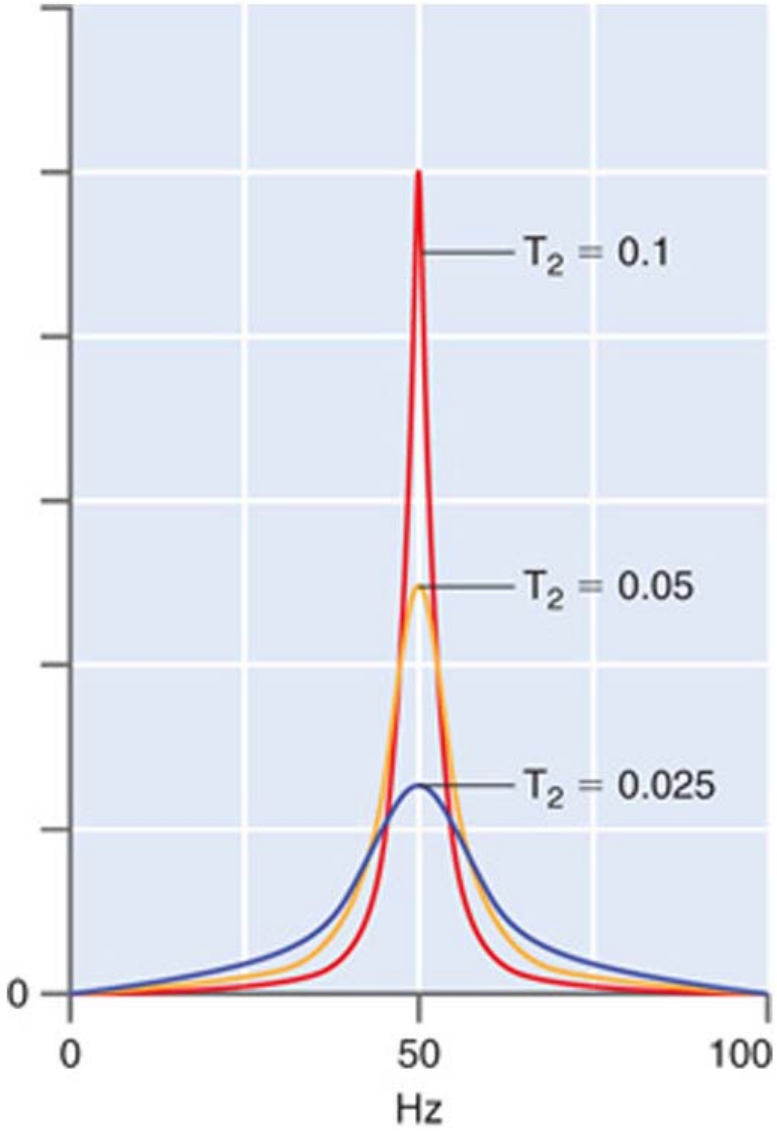

FIGURE 20.11

The NMR absorption line shape plotted as a function of T_2. The full-width at half-maximum is $\Delta\nu_{1/2} = 1/\pi T_2$.

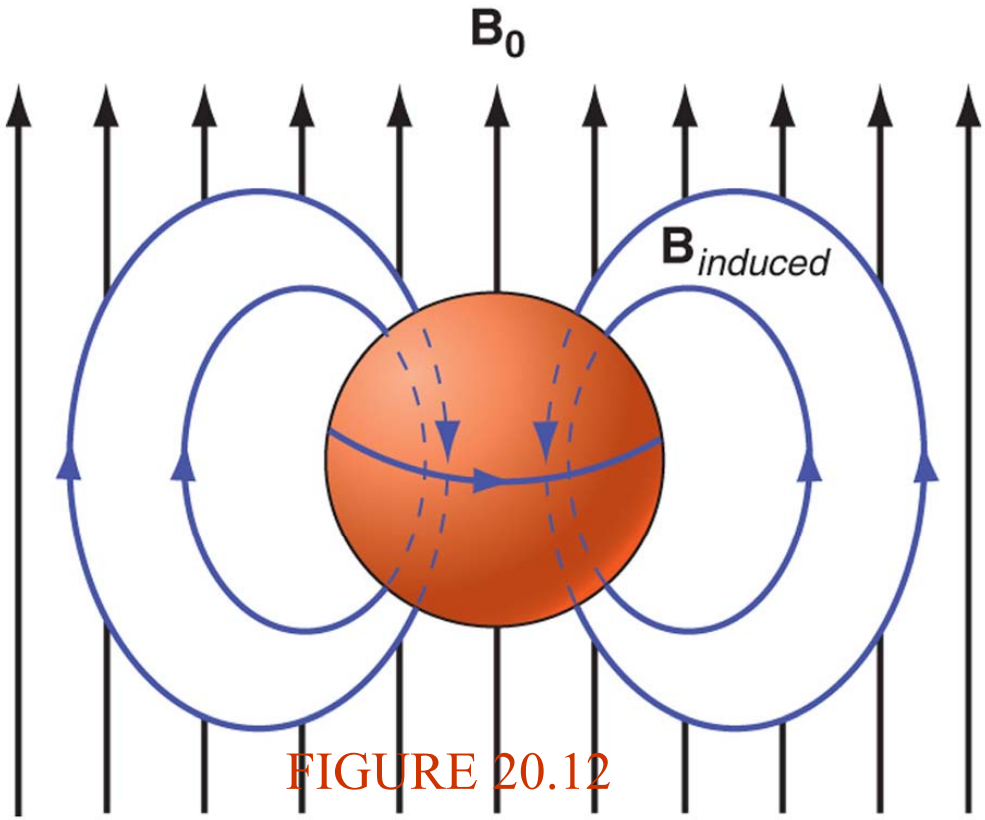

FIGURE 20.12

The shaded spherical volume represents a negatively charged classical continuous charge distribution. When placed in a magnetic field, the distribution will circulate as indicated by the horizontal orbit, viewed from the perspective of classical electromagnetic theory. The motion will induce a magnetic field at the center of the distribution that opposes the external field. This classical picture is not strictly applicable at the atomic level, but the outcome is the same as a rigorus quantum mechanical treatment.

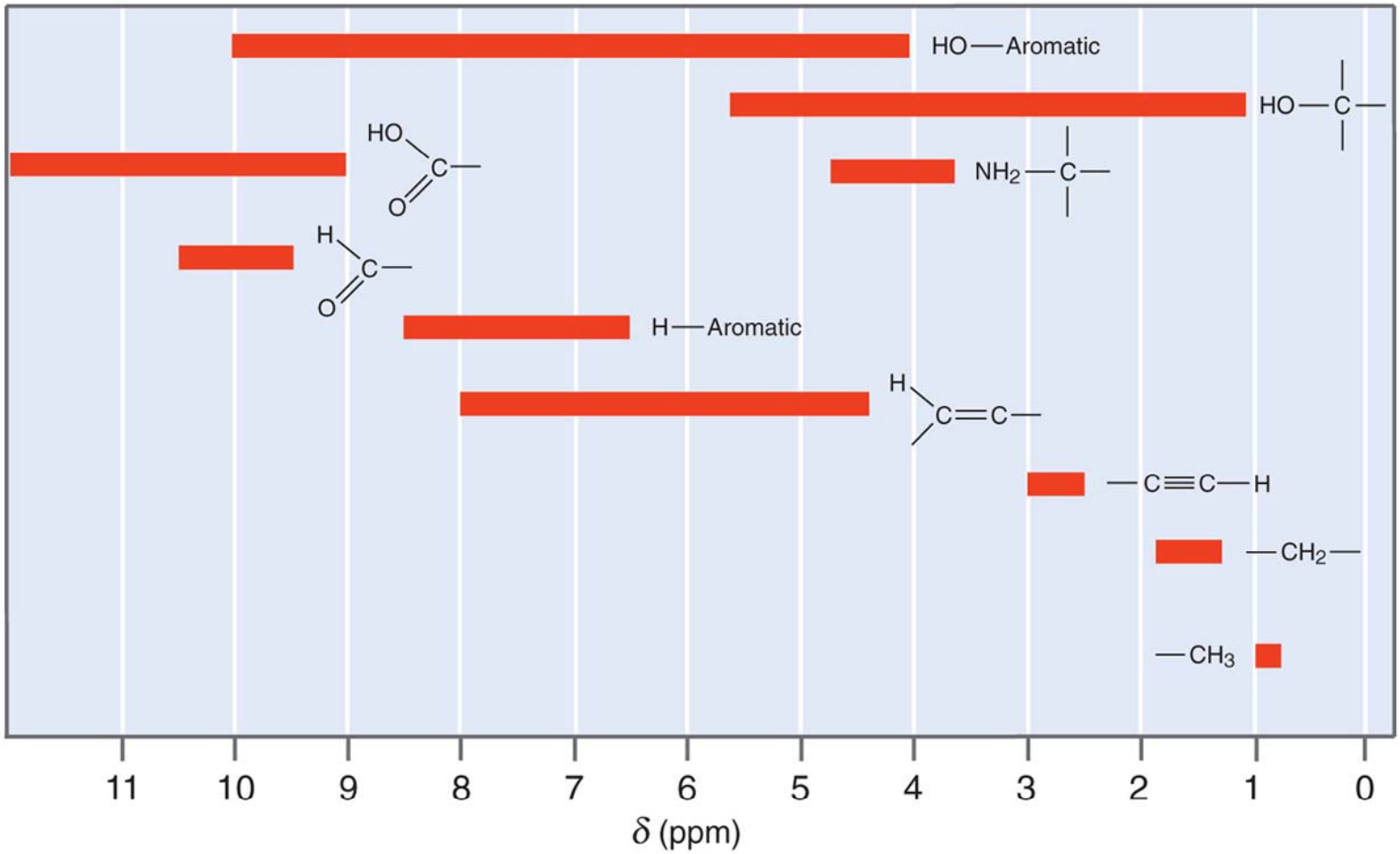

FIGURE 20.13

Chemical shifts δ as defined by Equation (20.29) for ^{1}H in different classes of chemical compounds. Extensive compilations of chemical shifts are available in the chemical literature.

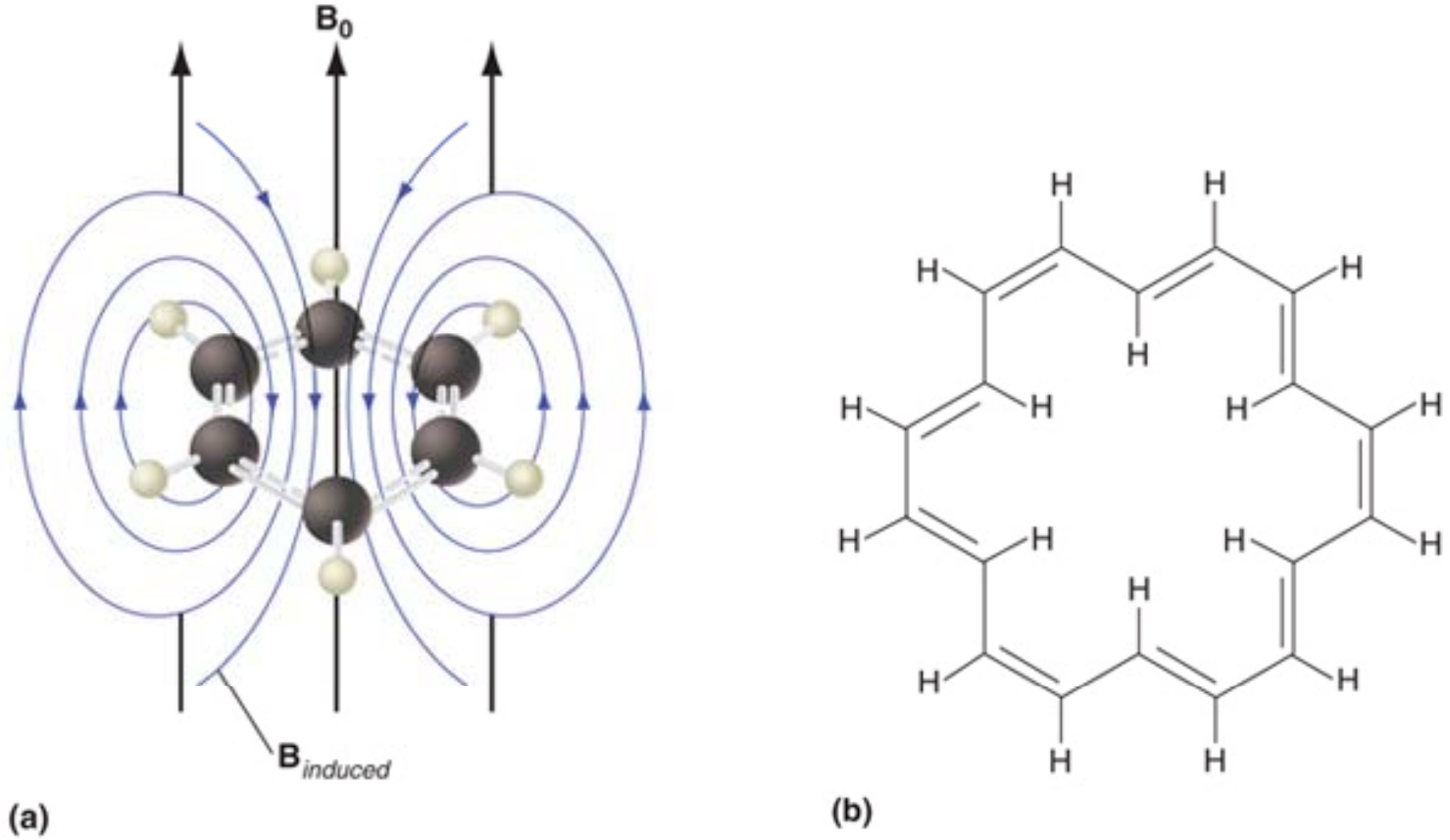

FIGURE 20.14

(a) The induced magnetic field generated by a circulating ring current in benzene. Note that within the ring of the molecule, the induced field is opposed to the external field while outside in the ring the induced field is along the applied field. (b) 18-Annulene provides a confirmation of this model.

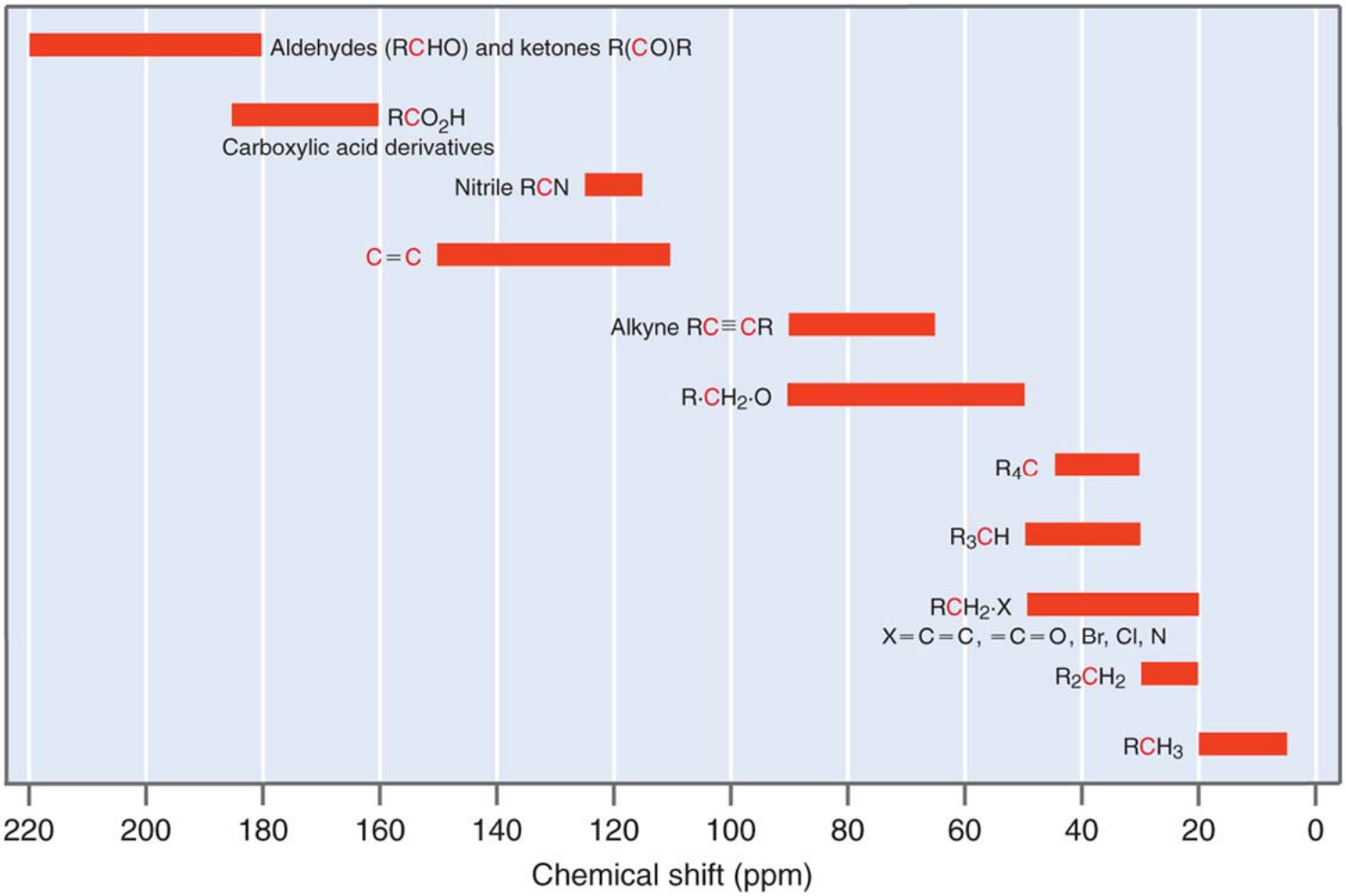

FIGURE 20.15

Typical chemical shifts for ^{13}C.

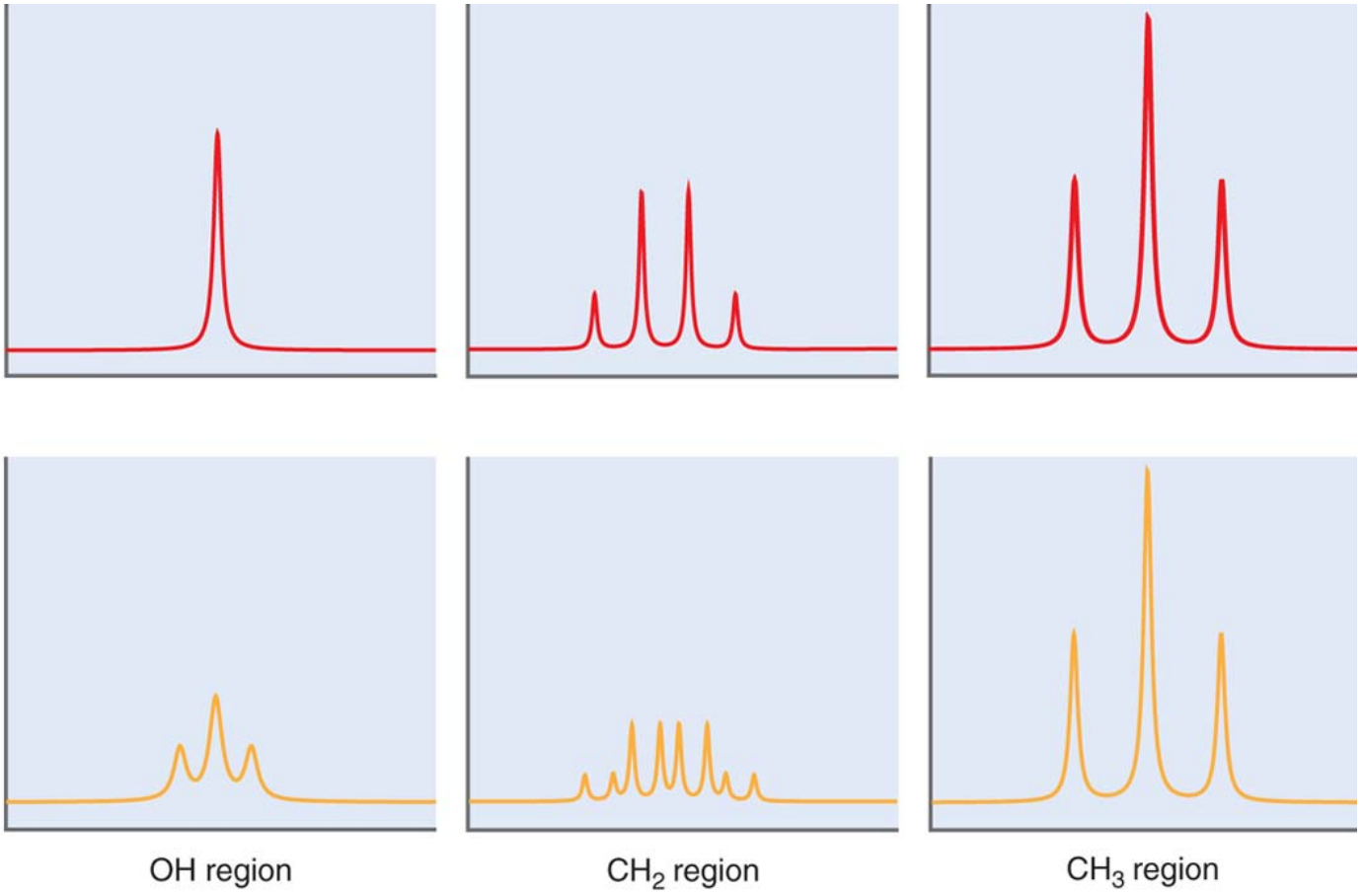

FIGURE 20.16

Simulated NMR spectrum for ethanol. The top panel shows the multiplet structure at room temperature. The lower panel shows the multiplet structure observed at lower temperature in acid-free water. The different portions of the spectrum are not to scale, but have relative areas discussed in the text.

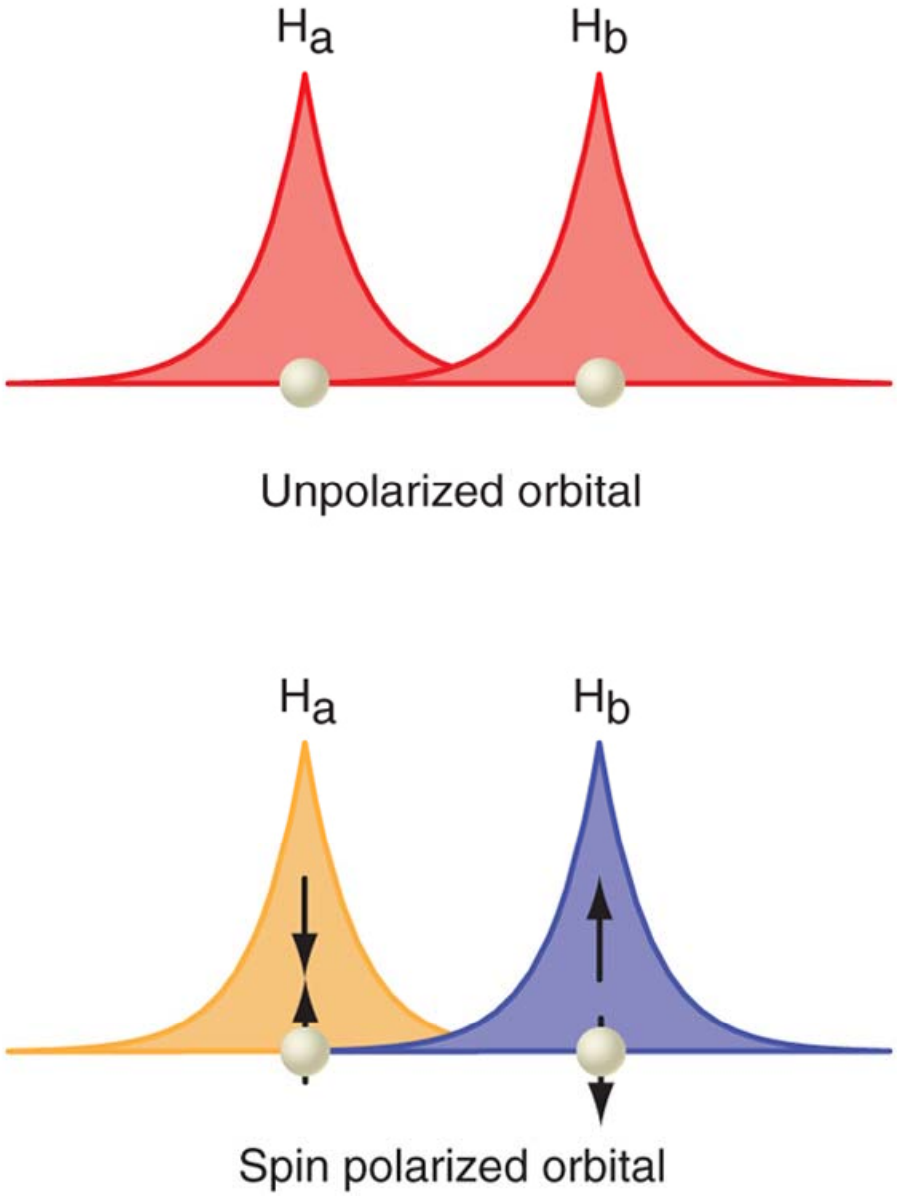

FIGURE 20.17

Schematic illustration of how spin-polarized orbitals couple nuclear spins even though they are highly shielded from one another through the electron density. The upper (lower) arrows in the right part of the figure indicate the electron (unclear) spin.

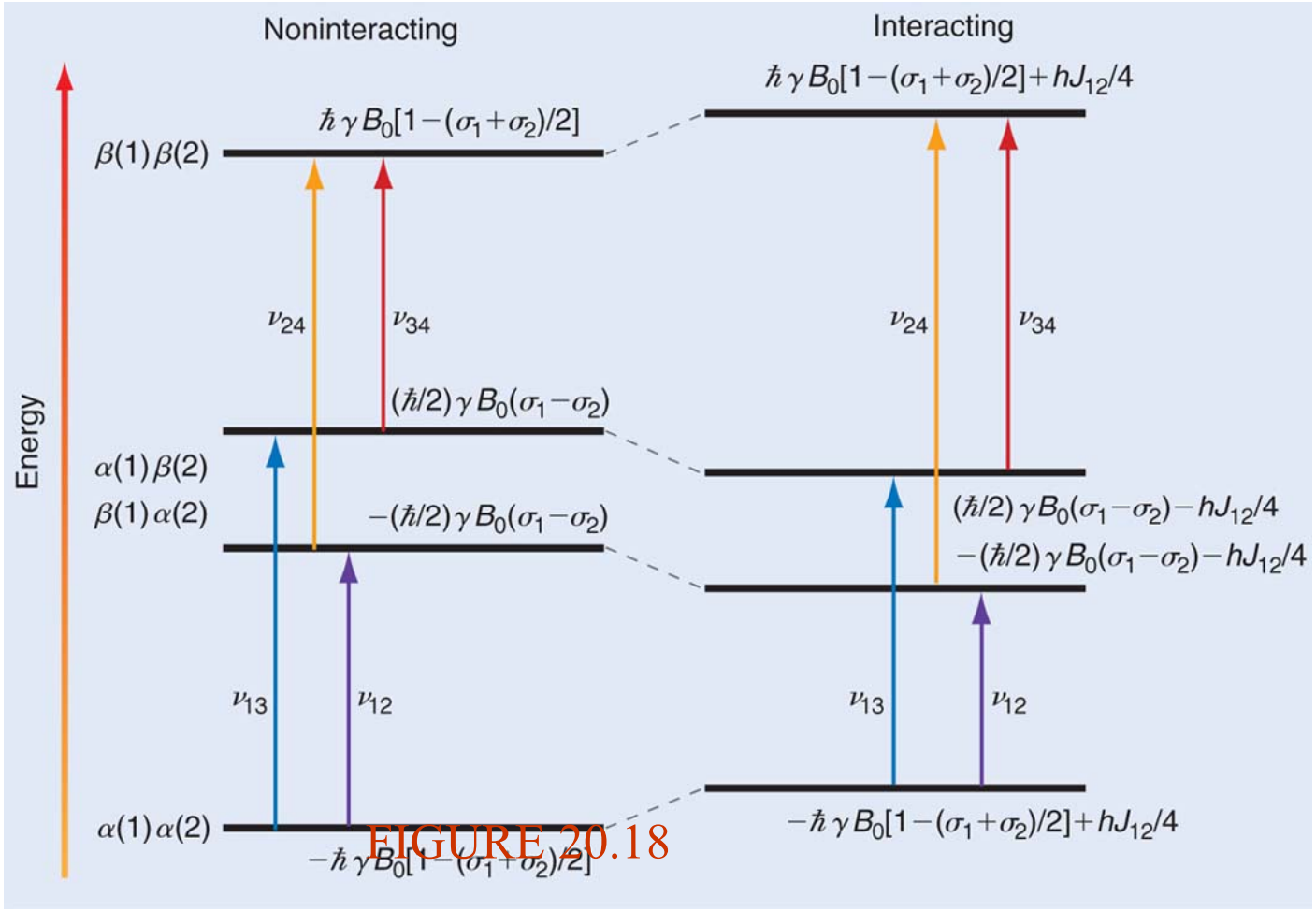

FIGURE 20.18

The energy levels for two noninteracting spins and the allowed transitions between these levels are shown on the left. The same information is shown on the right for interacting spins in the weak coupling limit. The splitting between levels 2 and 3 and the energy shifts of all four levels for interacting spins are greatly magnified to emphasize the spin-spin interactions.

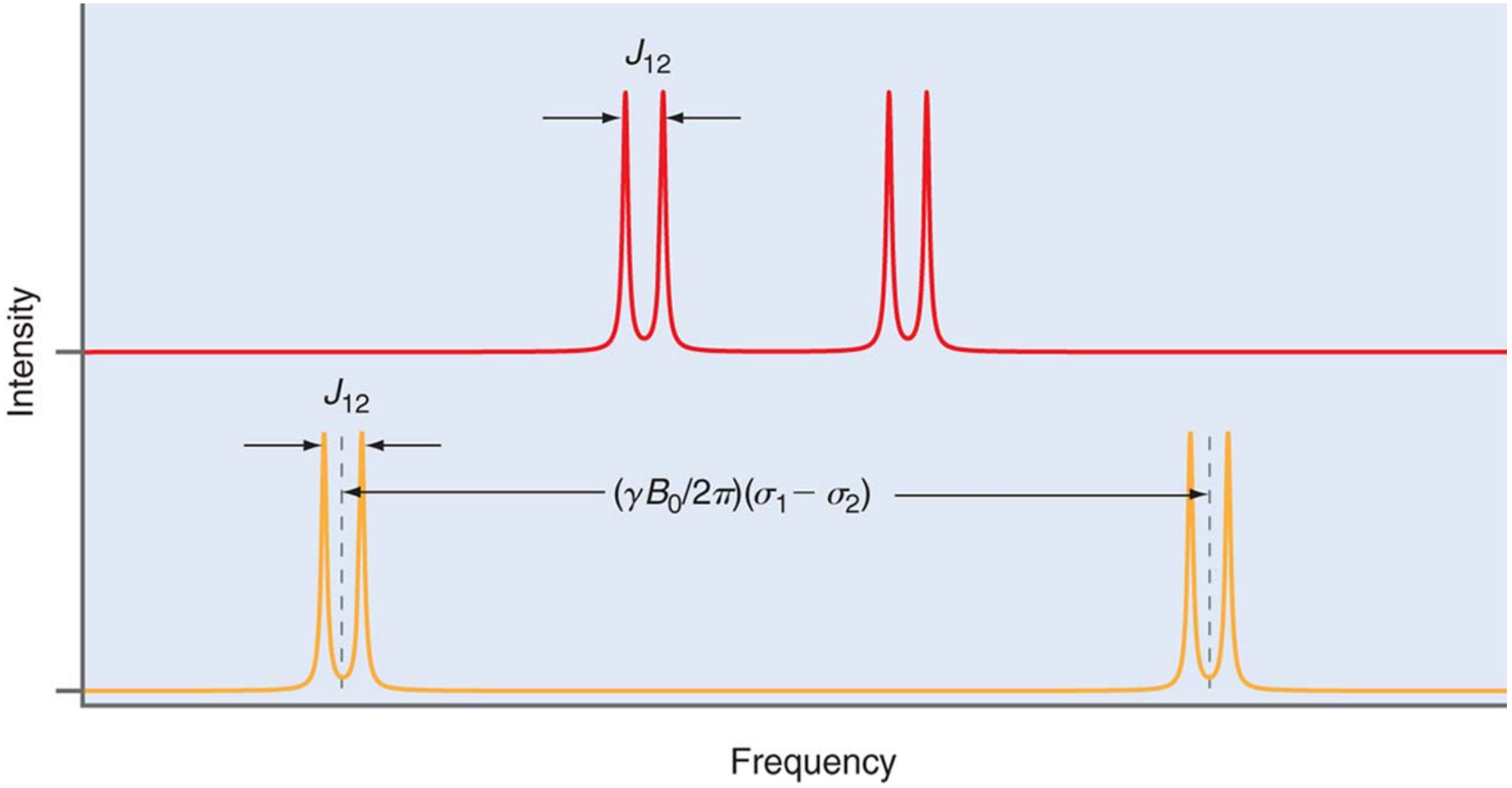

FIGURE 20.19

Splitting of a two interacting spin system into doublets for two values of B. The spacing within the doublet is independent of the magnetic field strength, but the spacing of the doublets increases linearly with B.

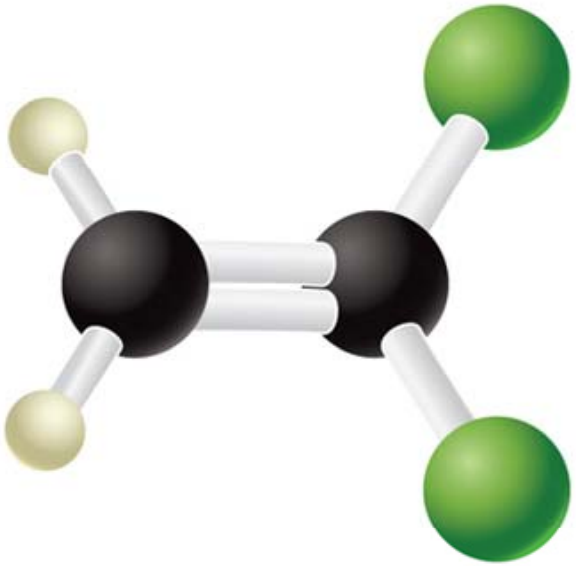

FIGURE 20.20

The H atoms in CH_2F_2 are chemically and magnetically equivalent. The H atoms in CH_2CF_2 are chemically equivalent, but magnetically inequivalent.

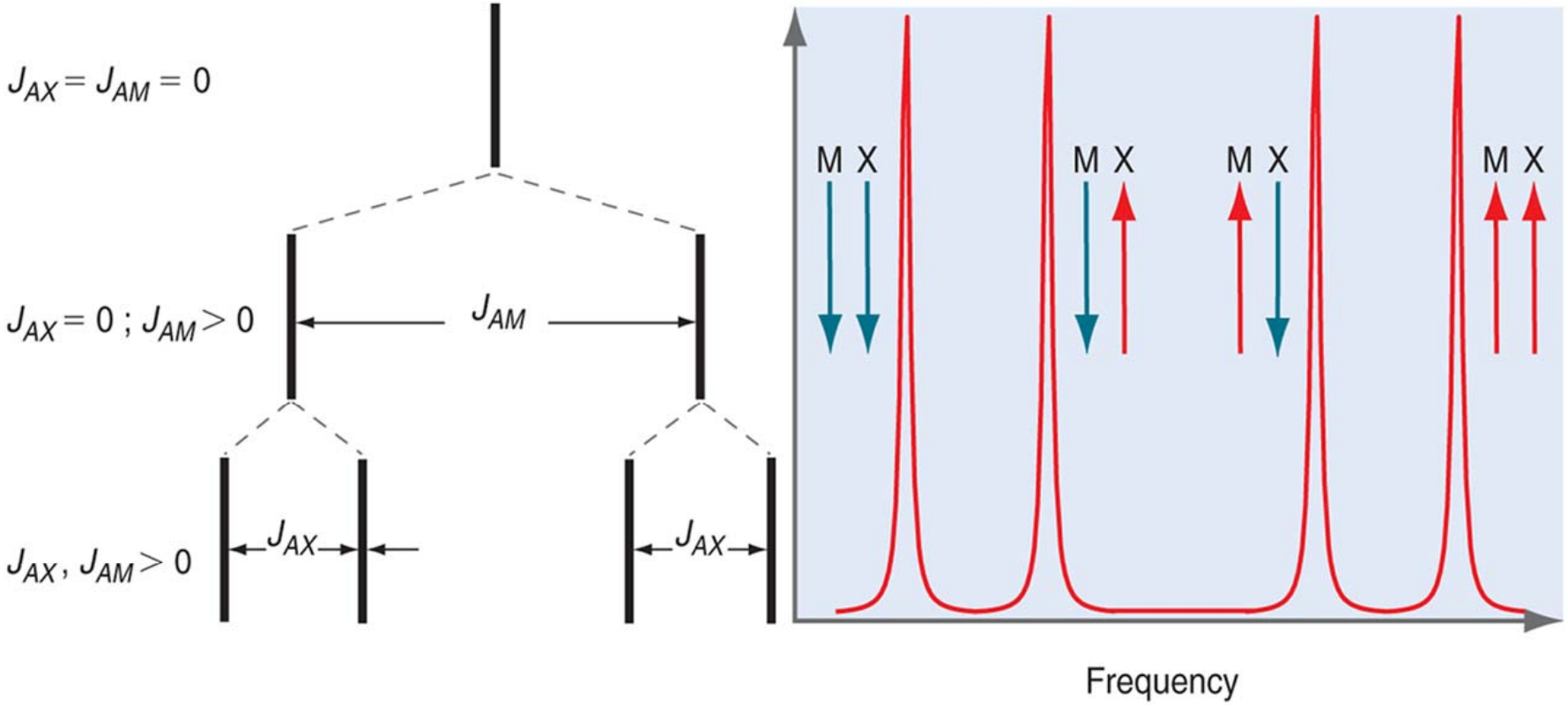

FIGURE 20.21

Coupling scheme and expected NMR spectrum for three coupled spins with different coupling constants J_{AX} and J_{AM}.

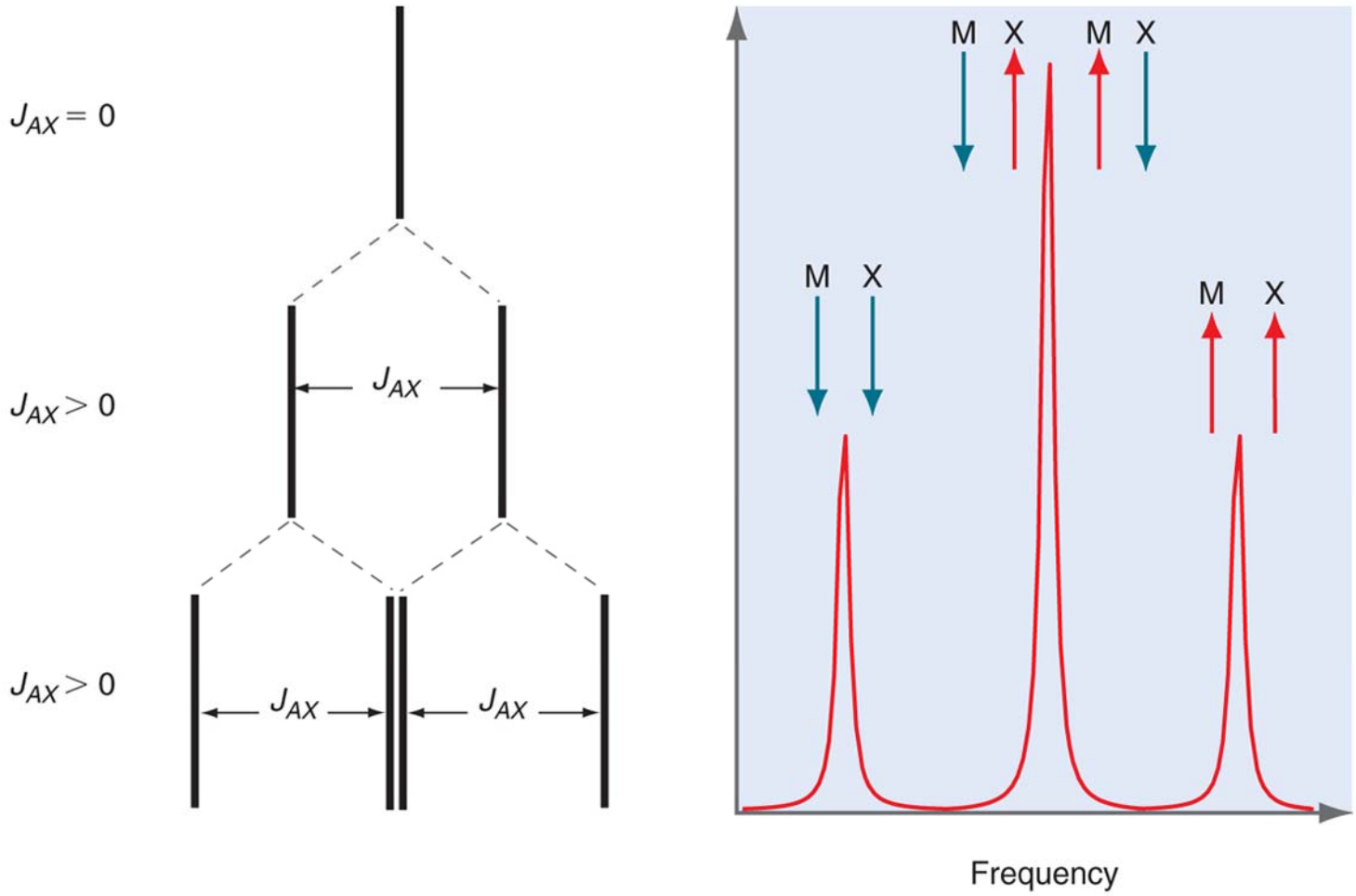

FIGURE 20.22

Coupling scheme expected NMR spectrum for three coupled spins with only one coupling constant J_{AX}.

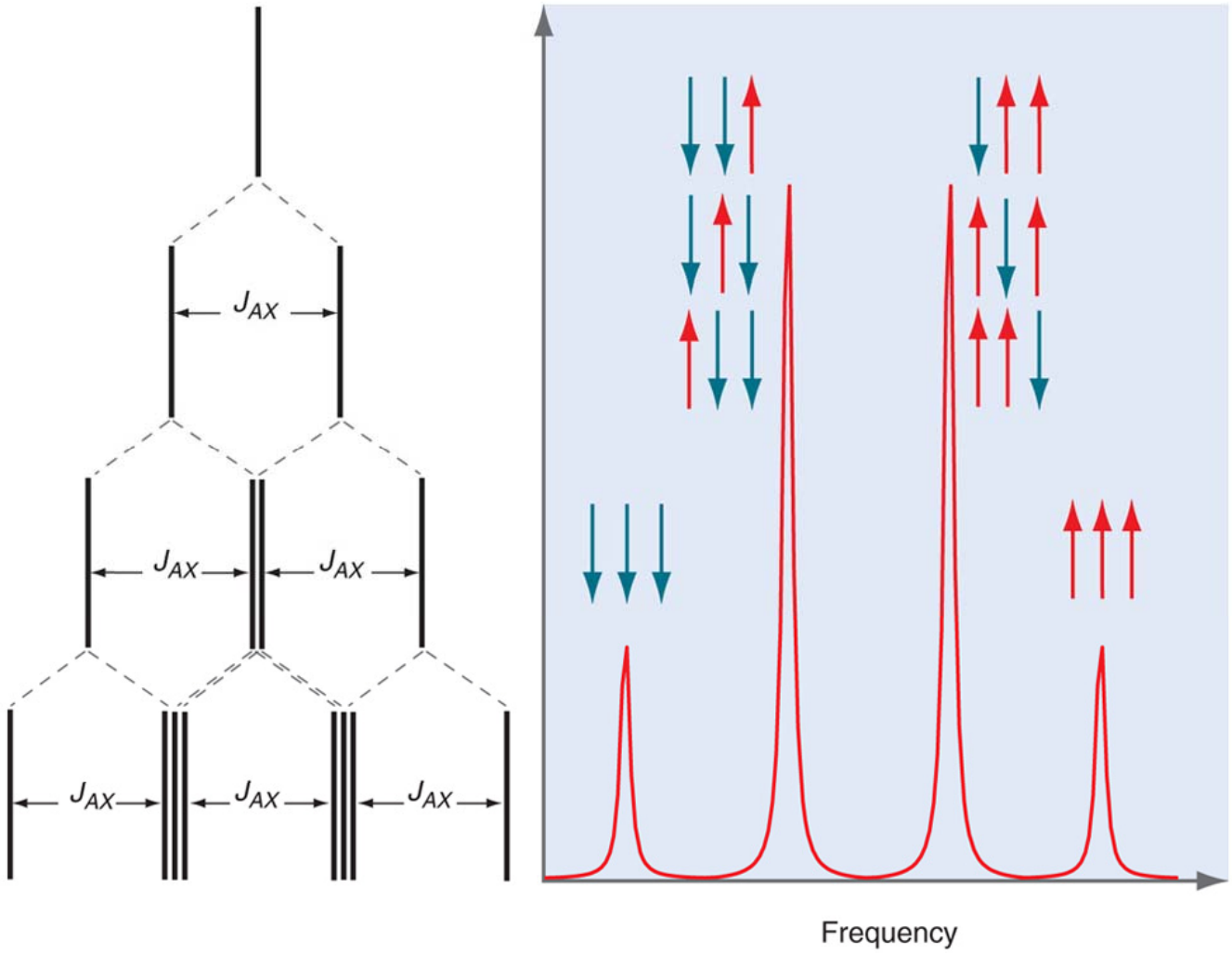

Example Problem 20.2

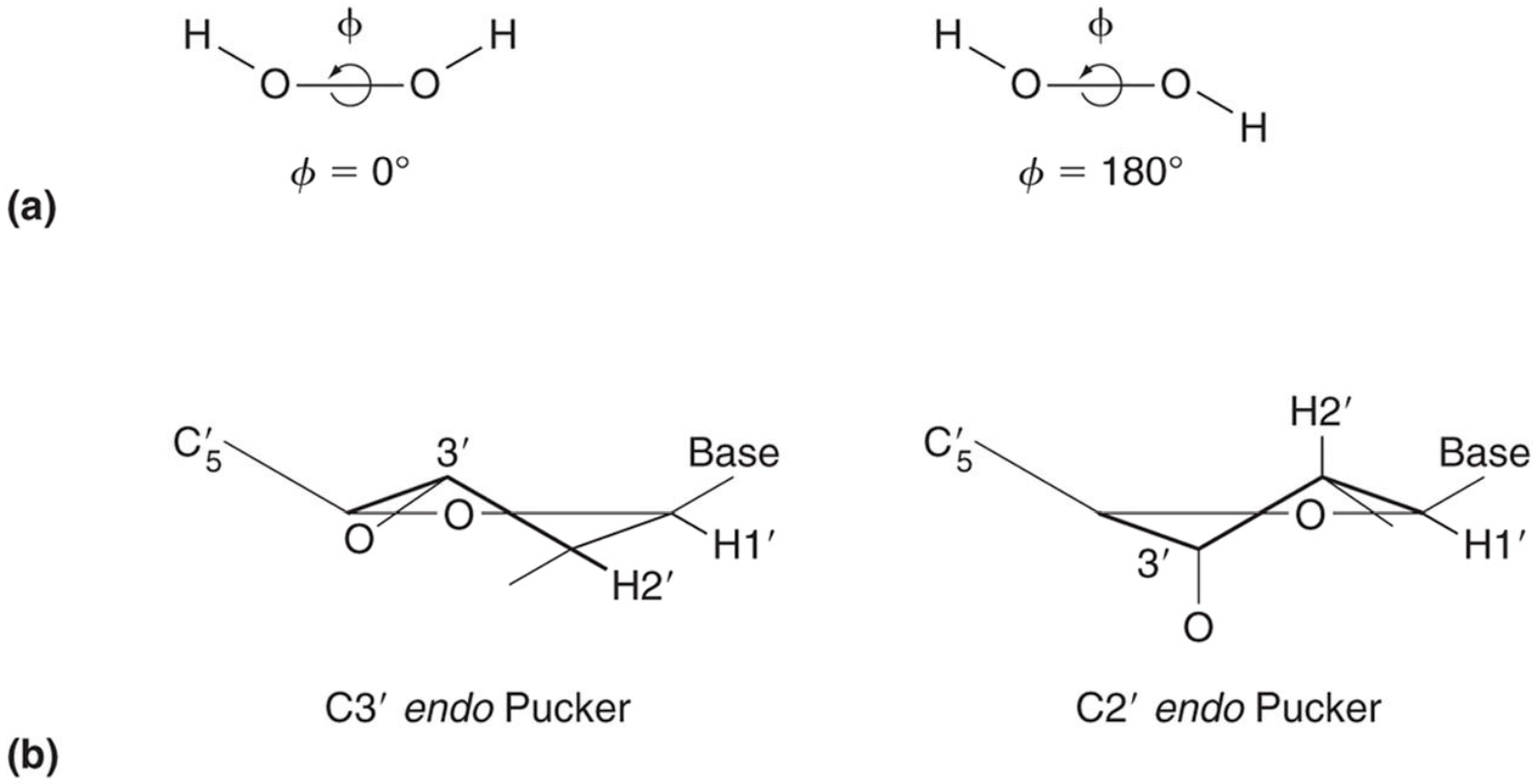

FIGURE 20.23

(a) The dihedral angle ϕ for a H—C — C — H moiety varies from 0 degrees in the *cis* conformation to 180 degrees in a *trans* conformation. (b) A five-membered furanose ring in a nucleoside is thought to adopt one of two low-energy puckering conformations where the dihedral angle between the $1'$ and $2'$ protons is 90 degrees in the $C3'$ *endo* conformation and 180 degrees in the $C2'$ *endo* conformation.

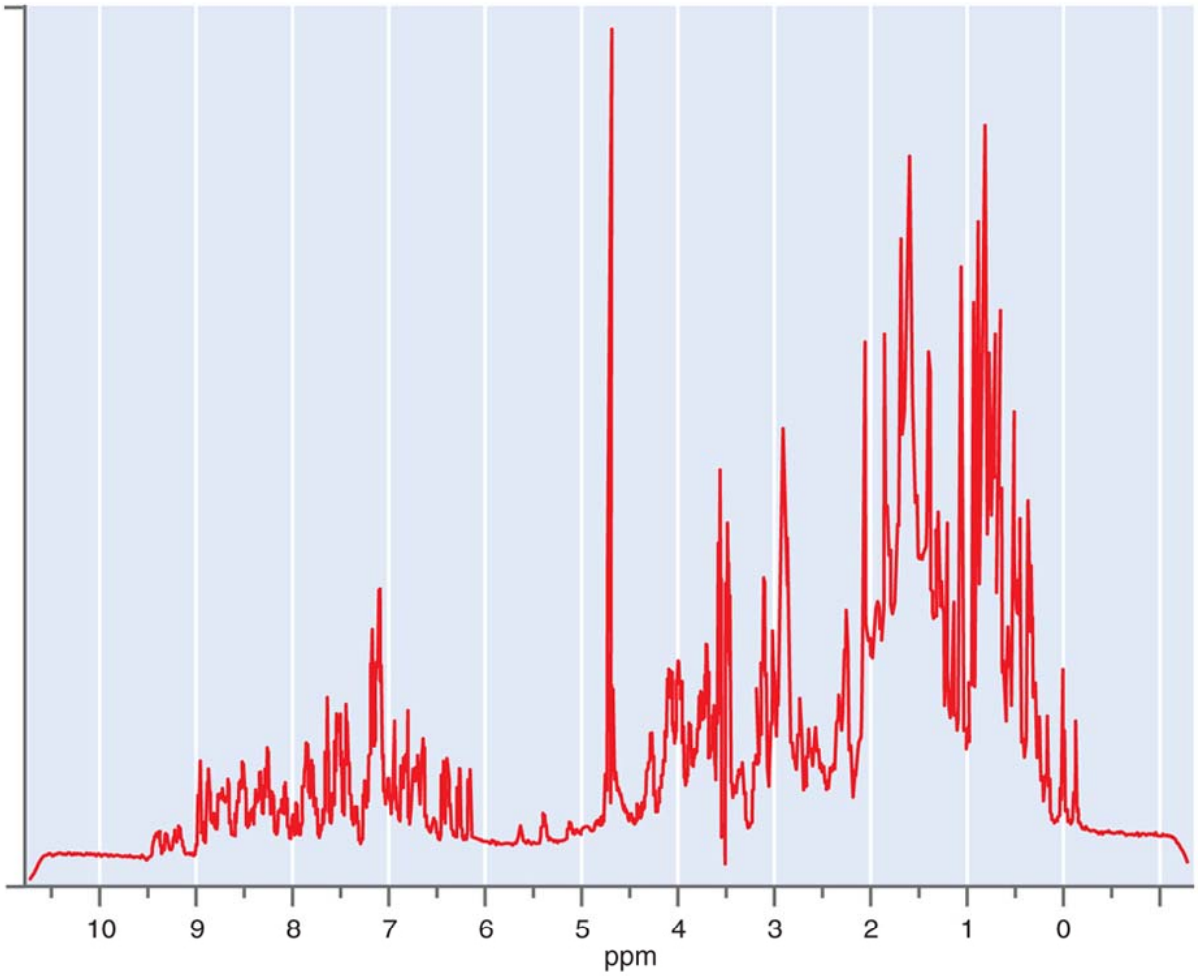

FIGURE 20.24

One-dimensional (1D) ^{1}H NMR spectrum of the protein U1A (molecular weight ~ 10kDa) in aqueous solution. The large number of overlapping broad peaks precludes a detailed structural determination on the basis of the 1D spectrum.

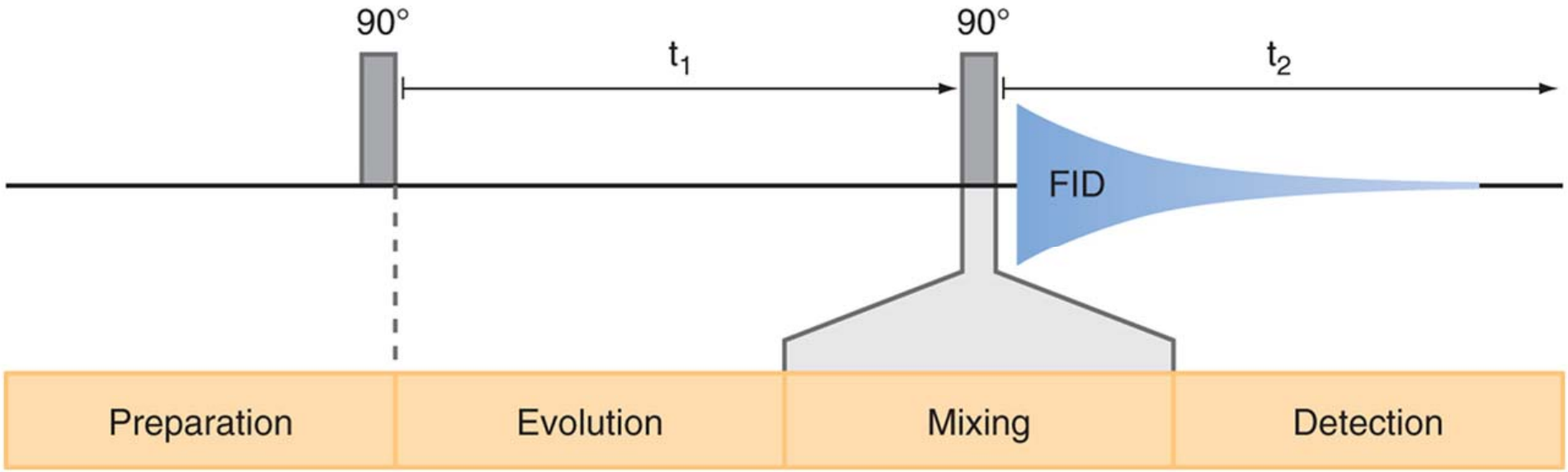

FIGURE 20.25

General scheme for a two-dimensional NMR experiment.

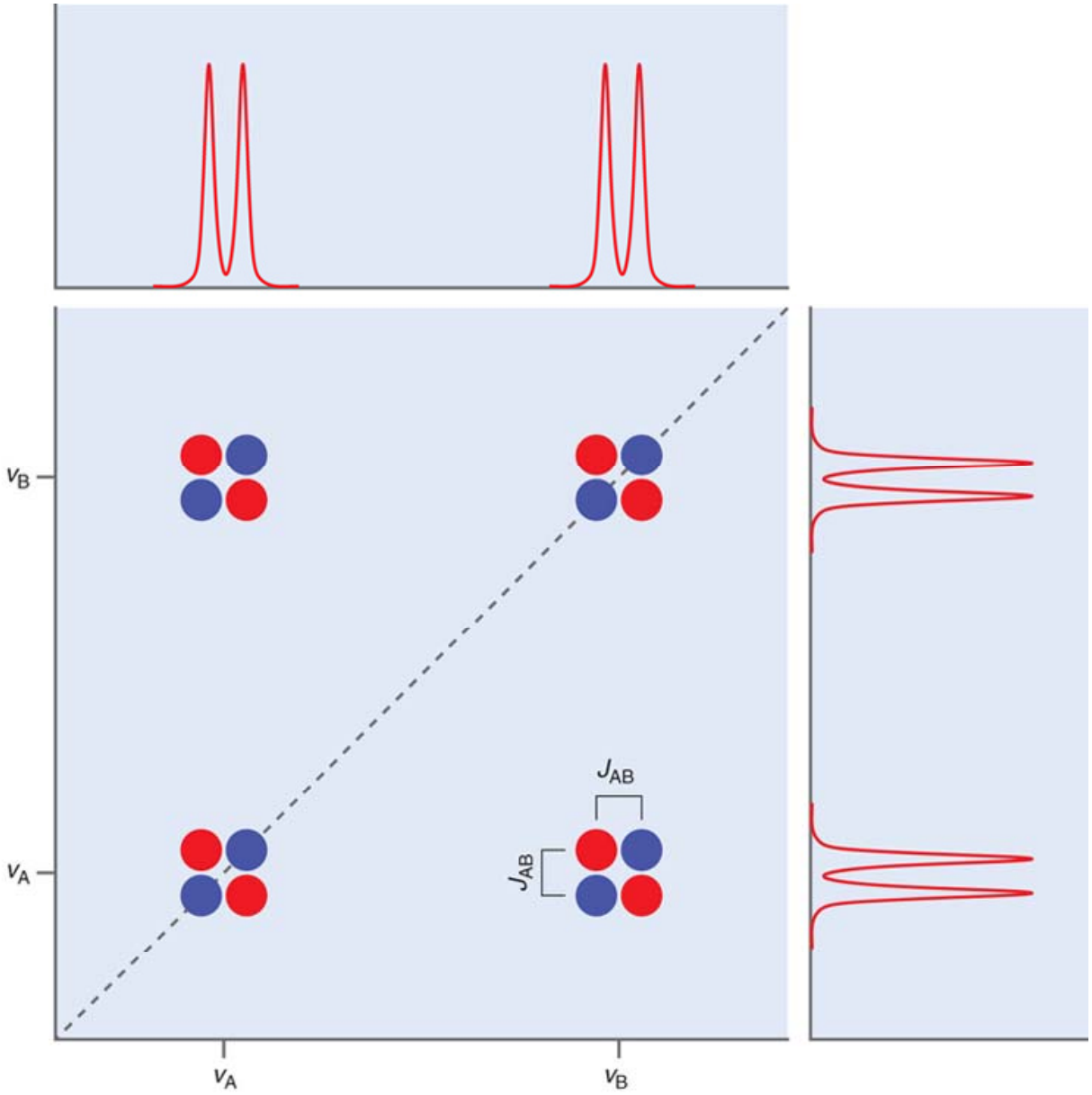

FIGURE 20.26

Two-dimensional NMR spectrum of two coupling spins *A* and *B* obtained using the COSY experiment shown in Figure 20.25.

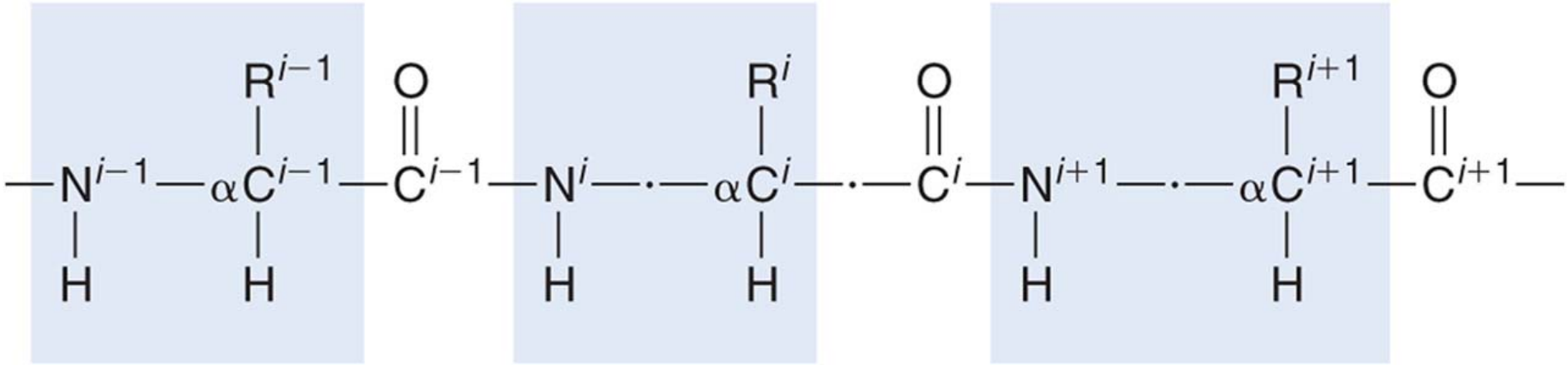

FIGURE 20.27

Schematic of a tripeptide segment derived from a polypeptide chain. R^i indicates the amino acid side chain associated with the amino acid that occupies the *i*th position in the primary sequence. The rectangles delimit the regions to which are confined connectivities established by proton COSY experiments.

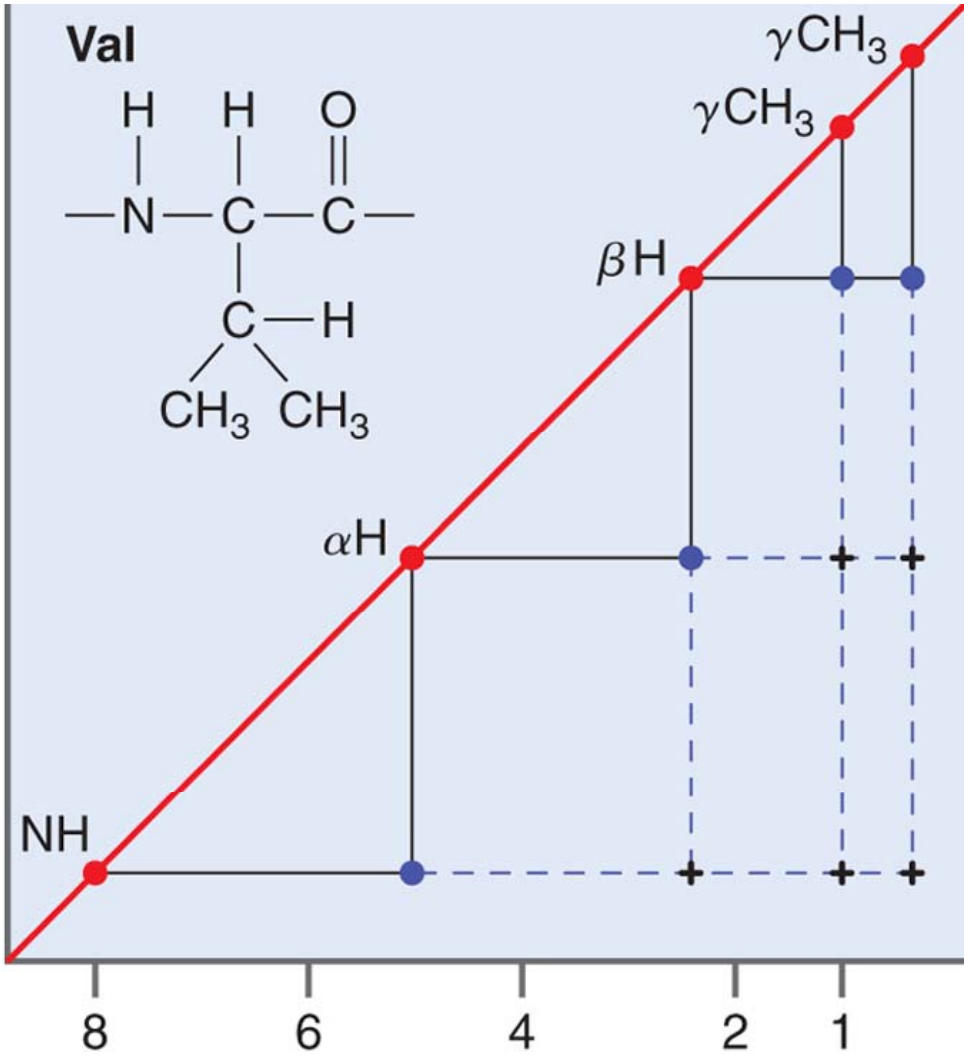

FIGURE 20.28

Schematic of the COSY spectra of valine. Cross-peak multiple normally observed in COSY spectra are indicated by open circles. Cross peaks observed only in TOCSY spectra are indicated by crosses. COSY connectivities are solid lines. TOCSY connectivities are dotted lines. The frequency axis is in ppm.

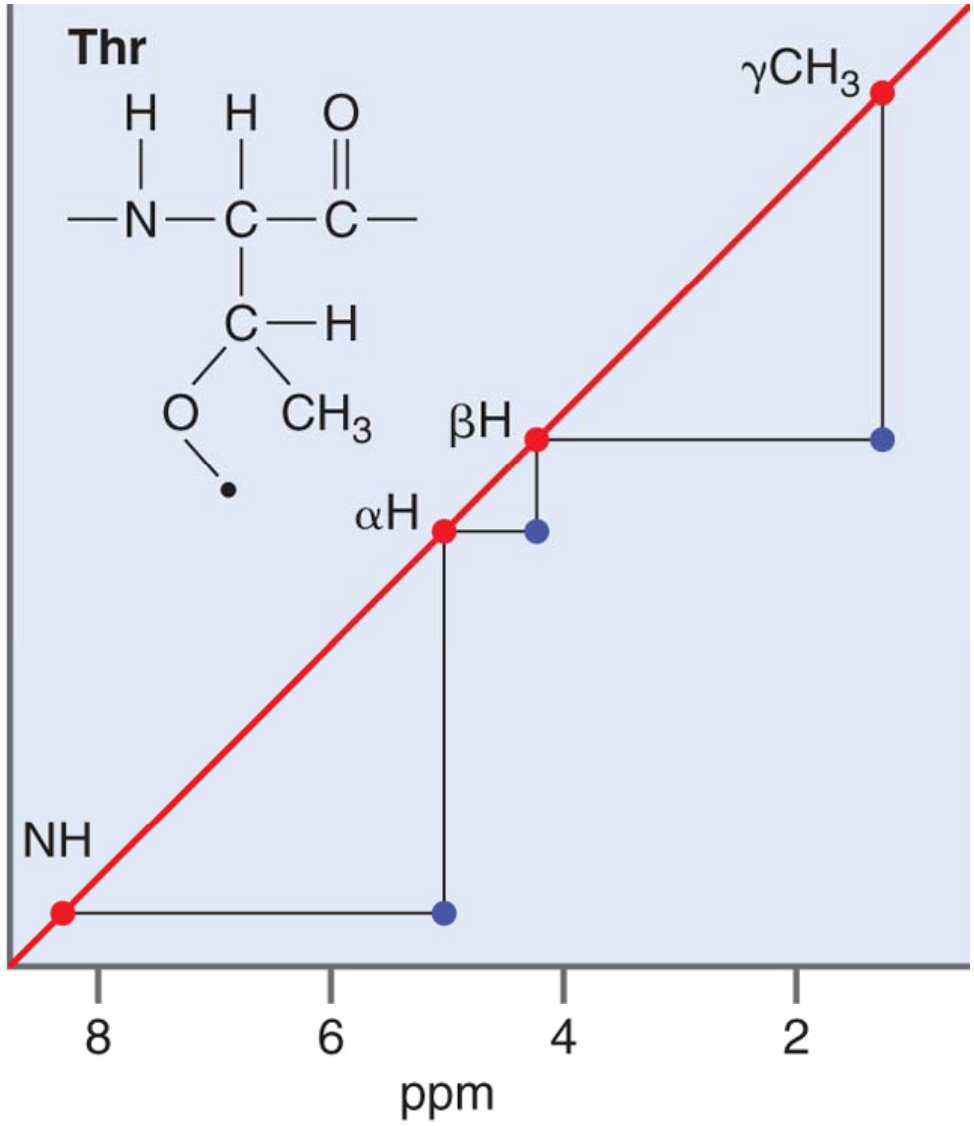

Example Problem 20.4

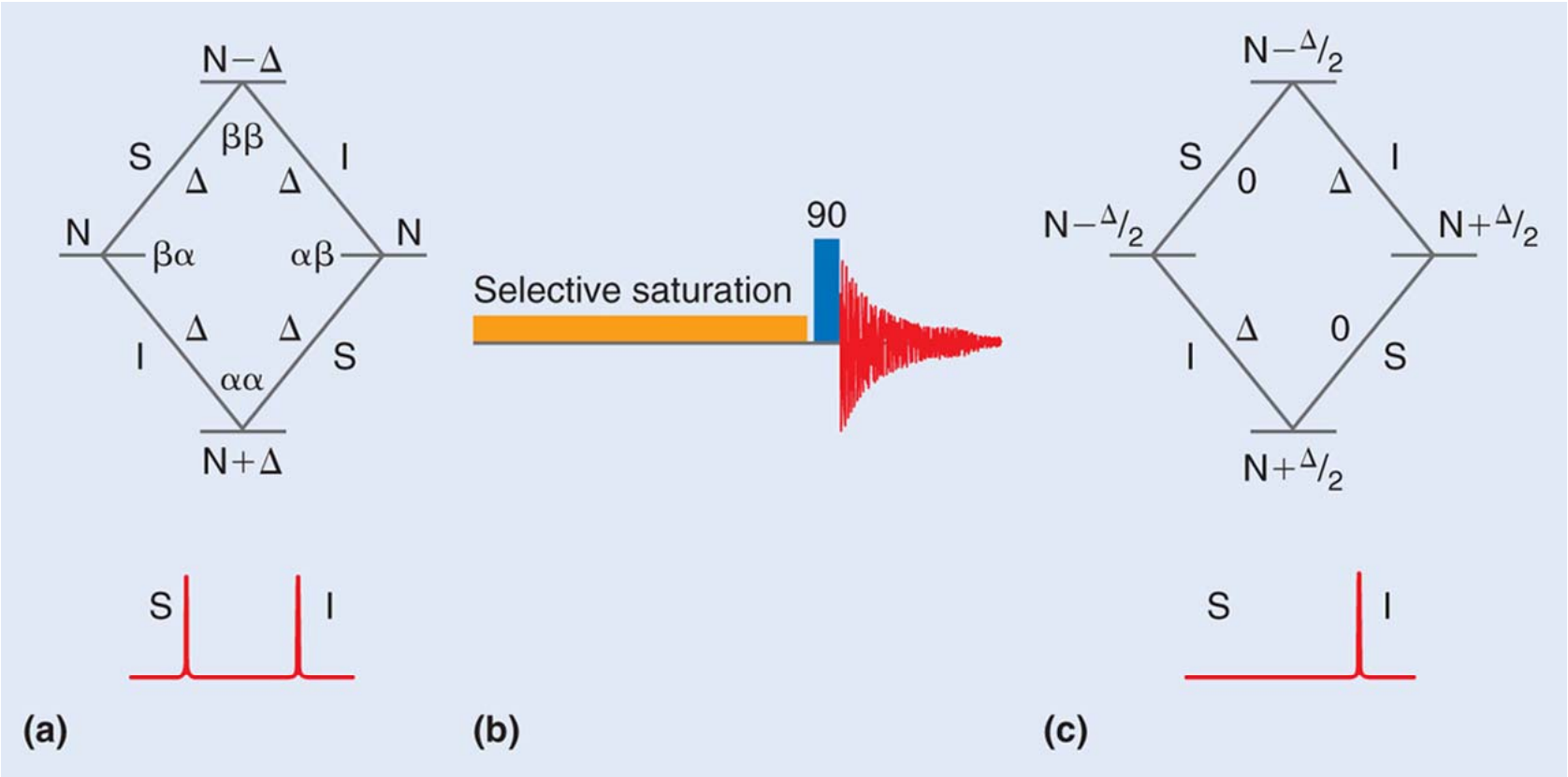

FIGURE 20.29

Selective saturation of spin *S* equalizes the populations of *S* spins in spin-up and spin-down orientations. Cross relaxation to the *I* spins perturbs the *I* spin populations. The *I* and *S* spin population differences are probed by observing the intensity of magnetization following a 90-degree pulse.

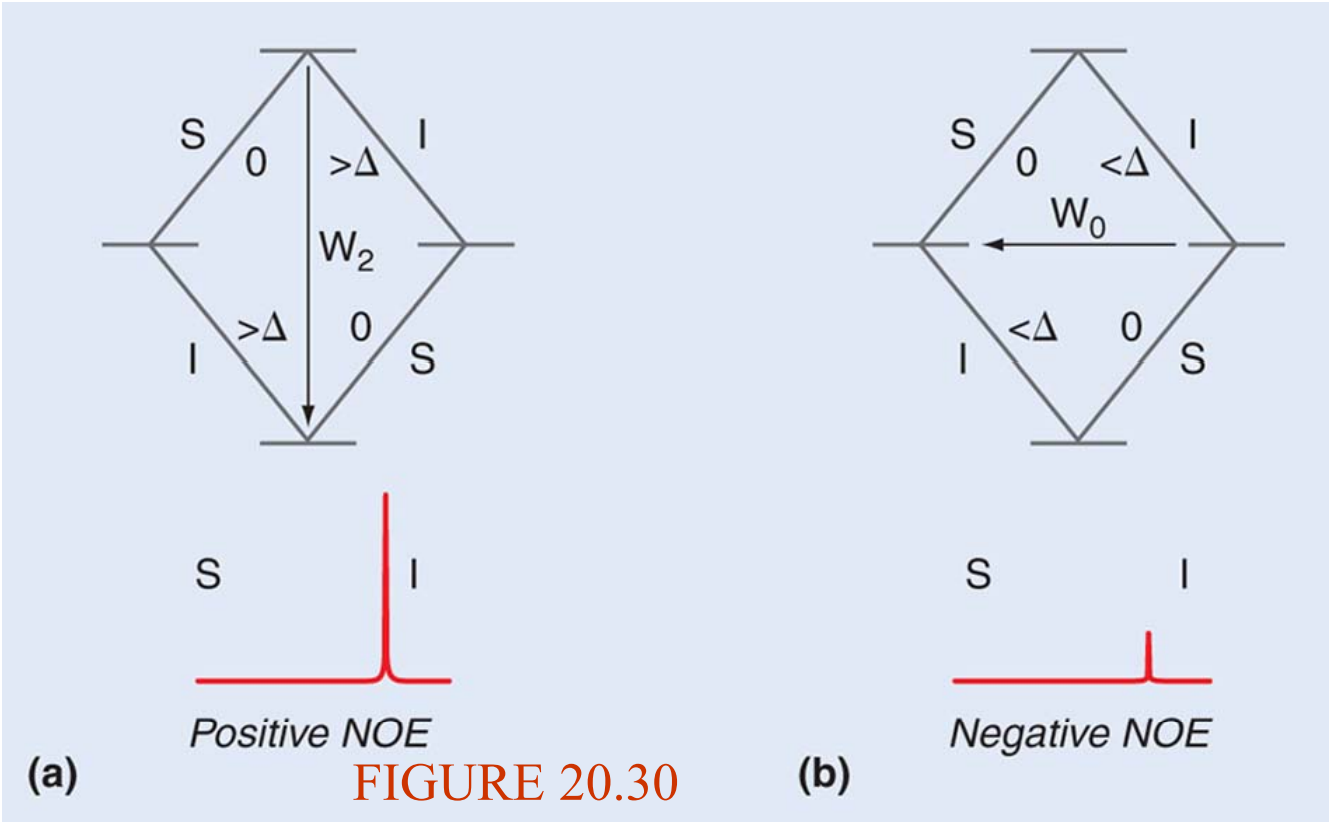

FIGURE 20.30

The sign of the NOE depends on the rate of molecular tumbling relative to the Larmor frequency. For small molecules where the rate of tumbling is fast compared to the Larmor frequency, spins relax via the double quantum transition at a rate W_2. This produces a positive NOE (left). Slow tumbling macromolecules will relax via zero quantum transitions at a rate W_0 and will display a negative NOE (right). The arrow in the spectrum indicates the intensity of the C spin line without cross relaxation.

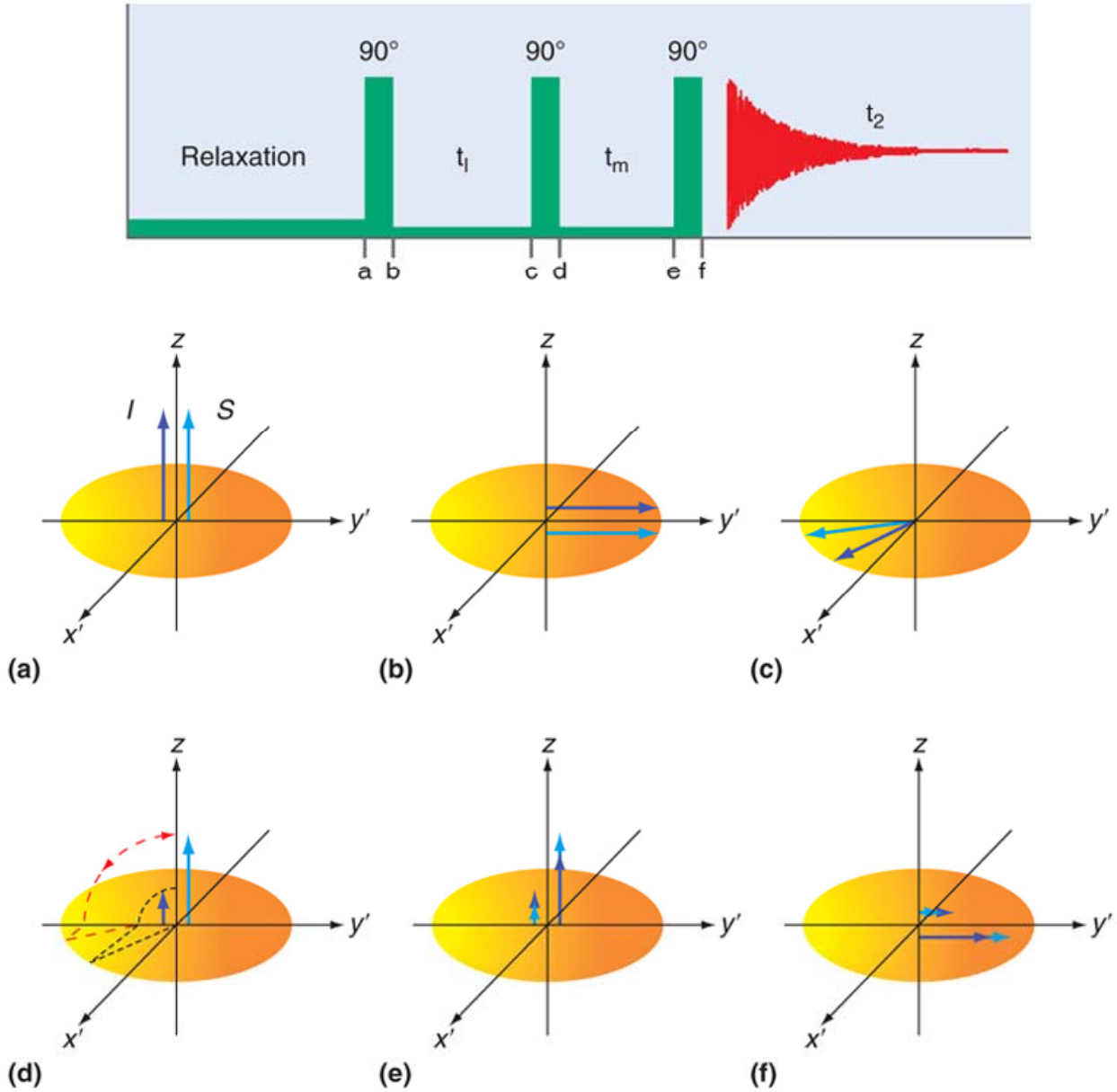

FIGURE 20.31

The NOESY pulse sequence and a vector picture of cross relaxation between two spin ½ nuclei during a NOESY experiment.

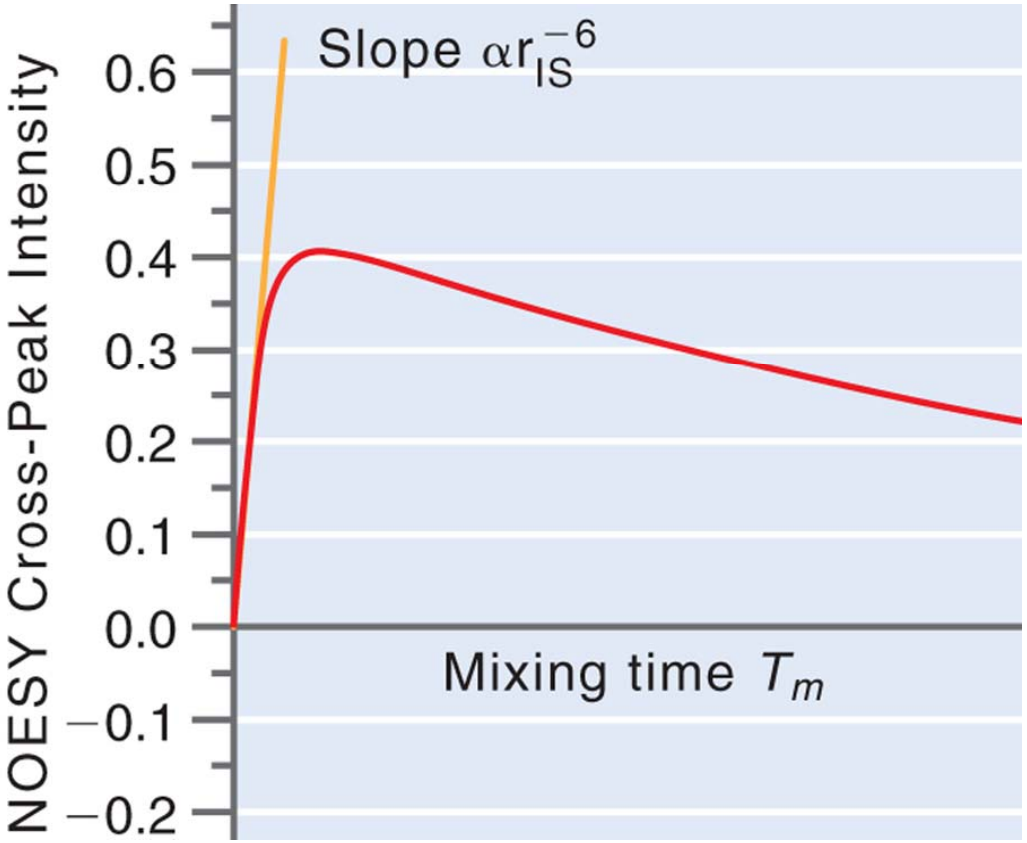

FIGURE 20.32

The buildup of a NOESY cross peak between two cross-relaxing spins I and S in the slow molecular tumbling limit. The slope of the NOE buildup curve extrapolated to zero mixing time is proportional to the inverse sixth power of the internuclear distance.

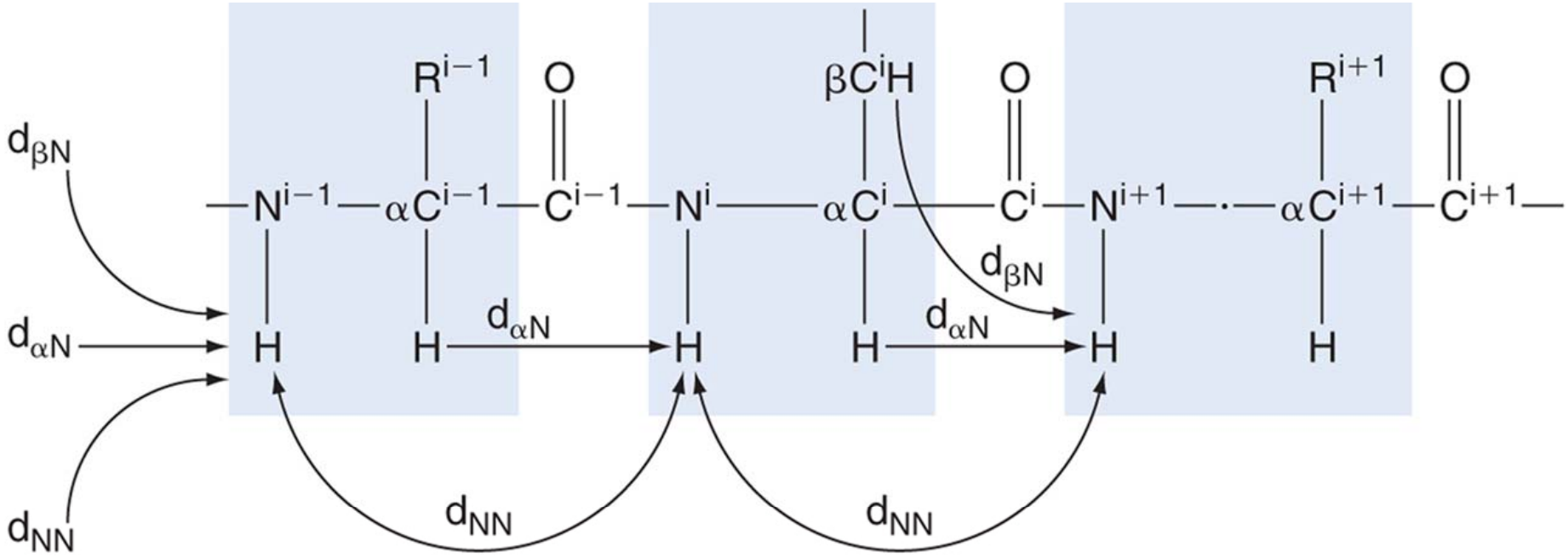

FIGURE 20.33

Distances between protons on adjacent amino acids that can be measured by NOESY. Many of these distances are sensitive to secondary structure.

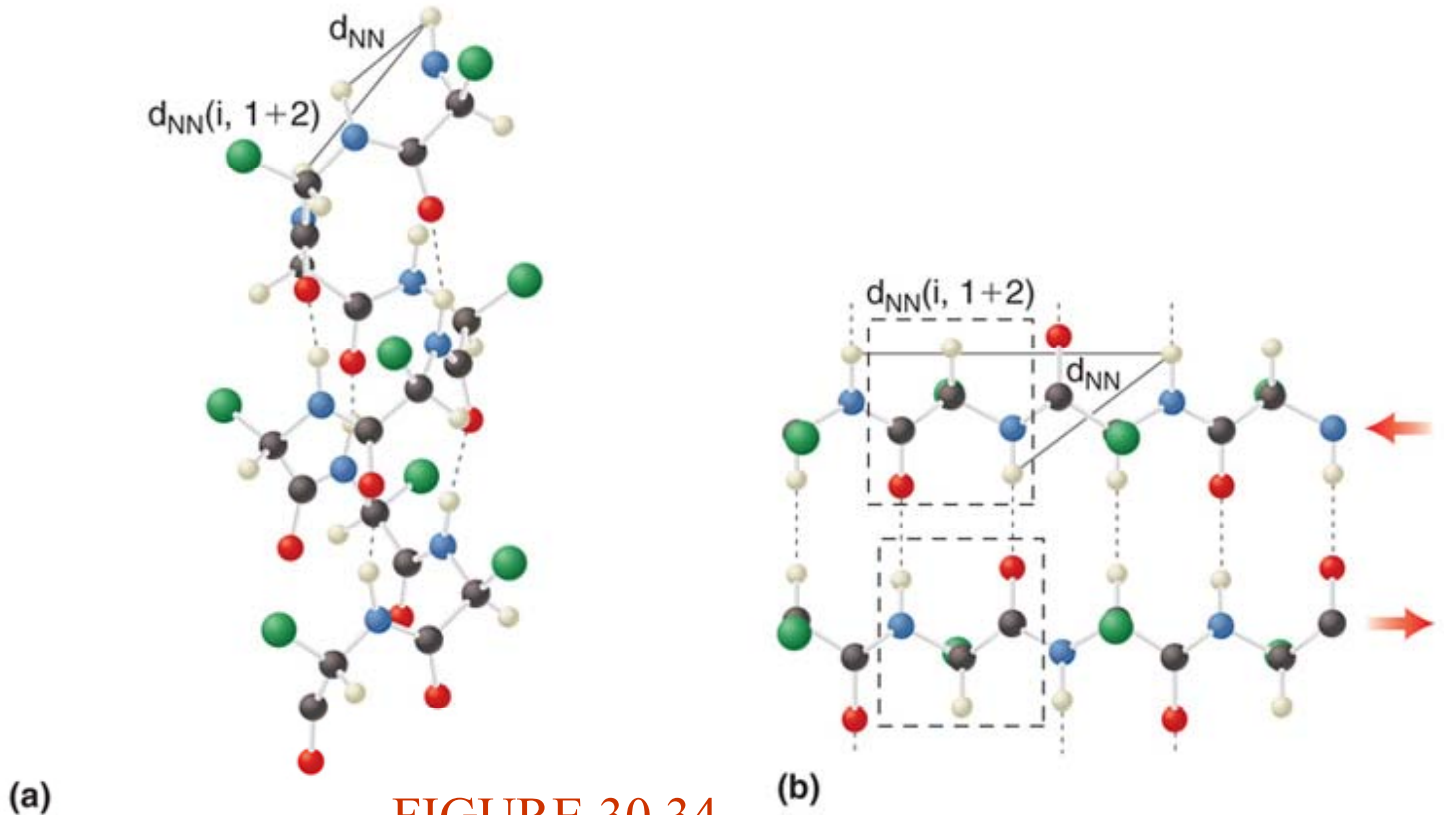

FIGURE 30.34

The proximity of amide protons in two secondary structural motifs. (a) The periodic structure of the α-helix brings both the adjacent and once removed amide protons into proximity. (b) The extended structure of the β-sheet causes adjacent amide pairs to be farther removed than adjacent amide pairs in the α-helix. Amide proton pairs on adjacent amino acids are too distant in the β-sheet to produce observable NOESY cross peaks.

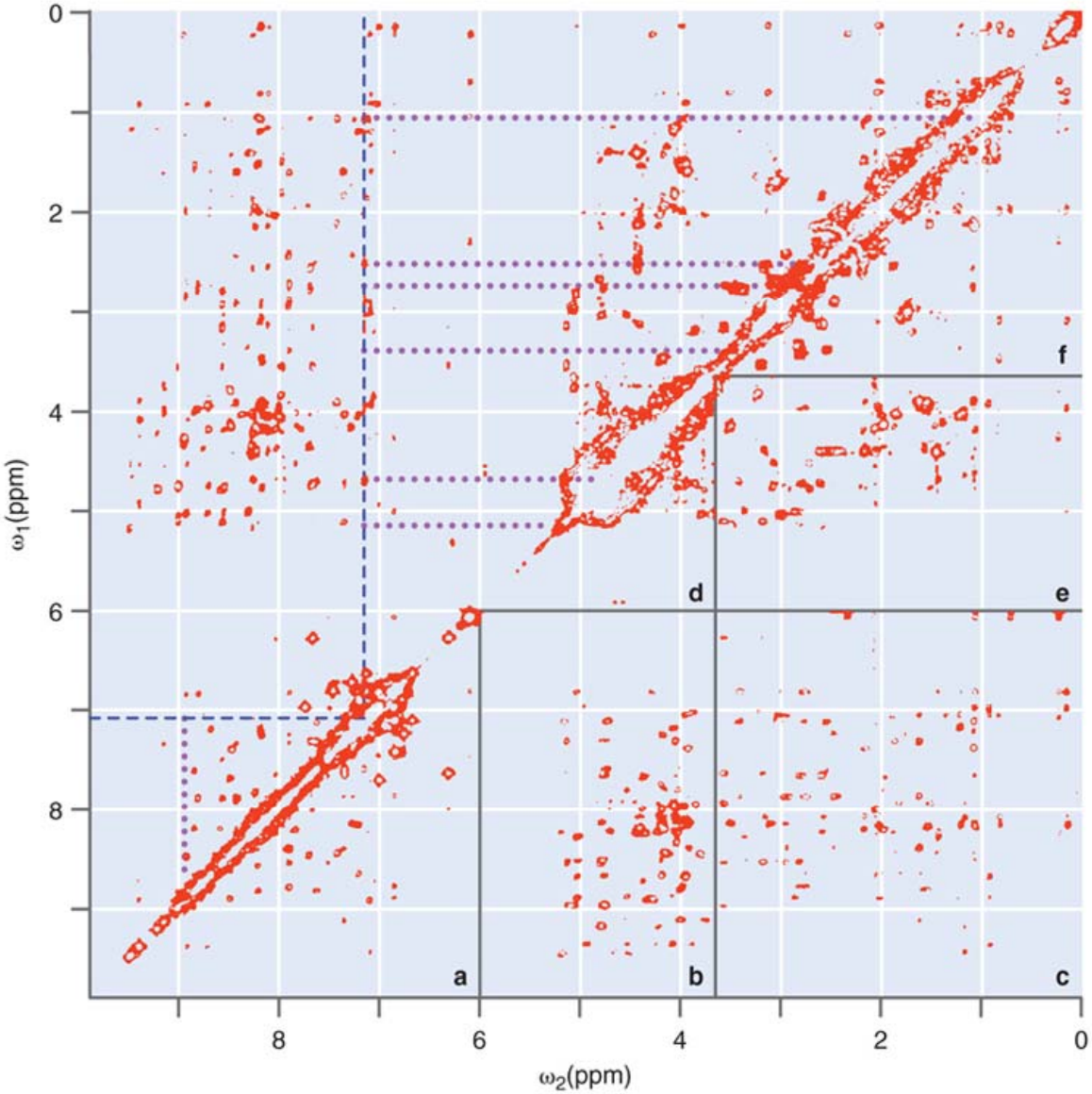

FIGURE 20.35

The proton NOESY spectrum of the proteinase inhibitor BUSI II. The spectrum below the diagonal is divided into six regions a through f that denote cross peaks between distinct proton types (see text). Above the diagonal, the vertical dotted line identifies cross peaks, between an amide proton at 7.2 ppm to six other types of protons, indicated by horizontal dotted lines. The amide proton at 7.2 ppm also has an NOE cross peak to another proton at 8.9 ppm.

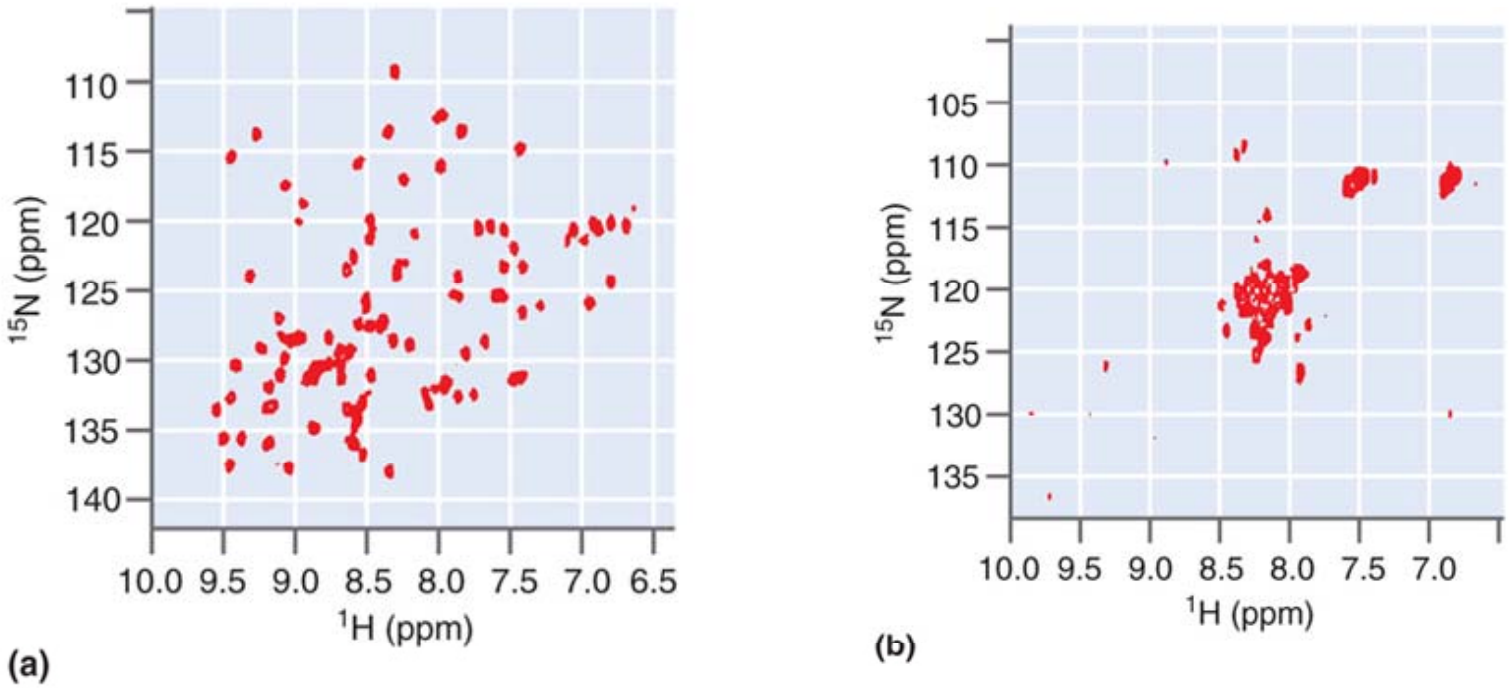

FIGURE 20.36

^{15}N-^{1}H HSQC spectra show the correlation of ^{15}N amide chemical shifts of their attached amide protons. The HSQC spectrum of a folded protein is shown at the right in part (a). The unfolded protein is shown at the right in part (b).

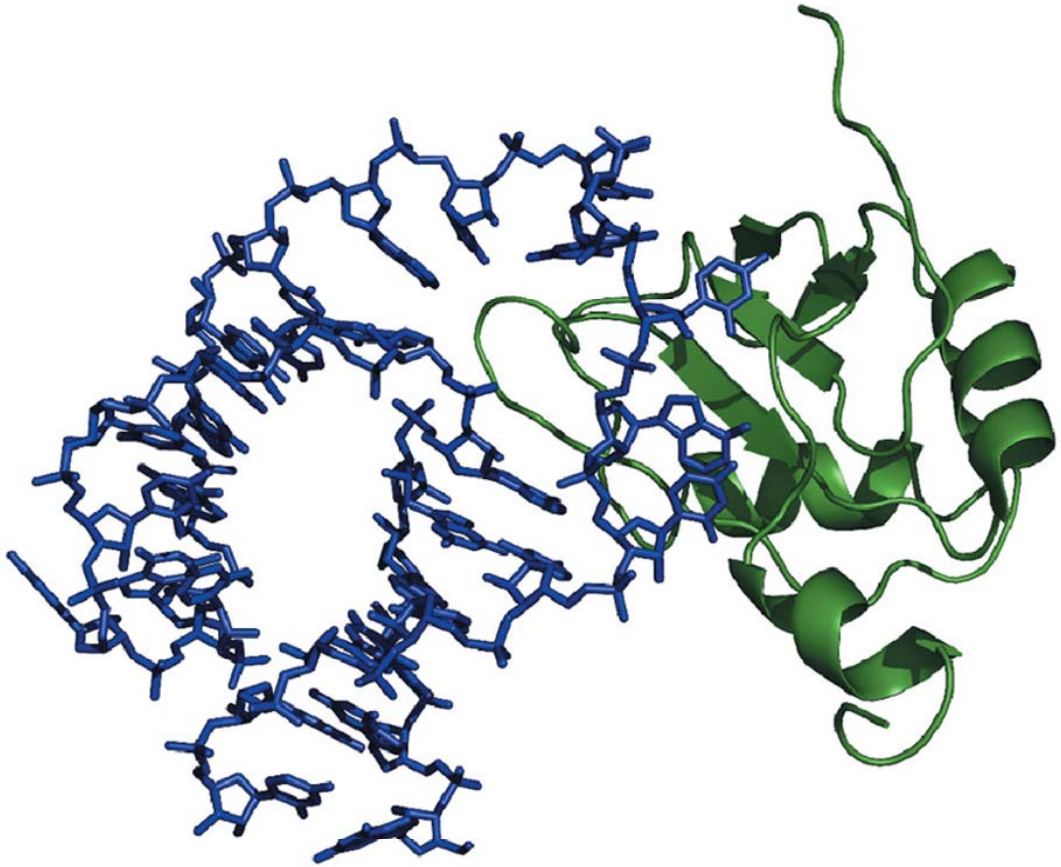

FIGURE 20.37

The structure of the complex formed between UTR RNA (shown in blue) and the U1A protein (show in green).

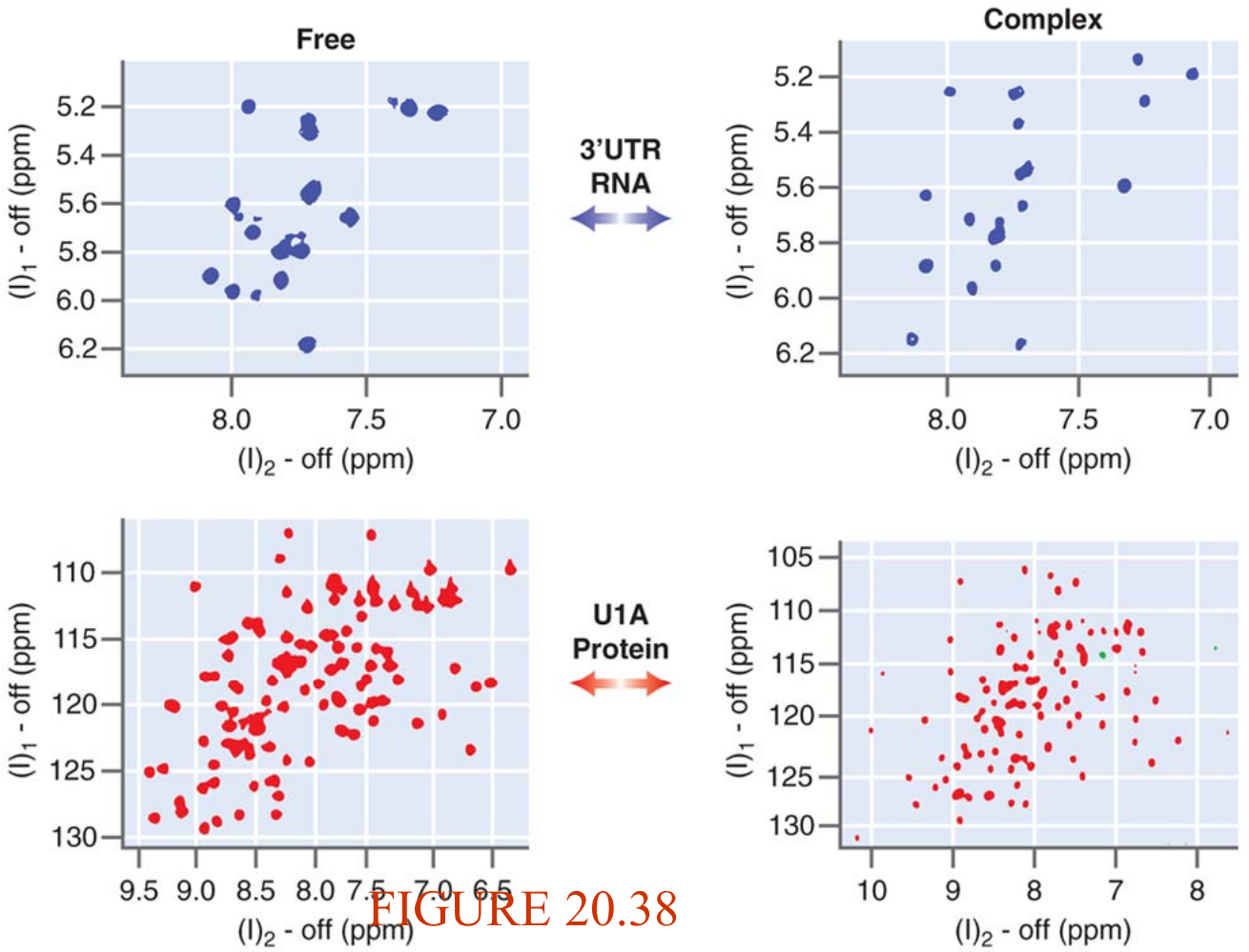

FIGURE 20.38

The TOCSY spectra of the aromatic protons of UTR RNA, shown in blue, when the RNA is free (left) and complexed (right) to U1A. The ^{15}N-^{1}H HSQC spectra of U1A are shown in red for the free protein (left) and the protein complexed to the RNA (right).

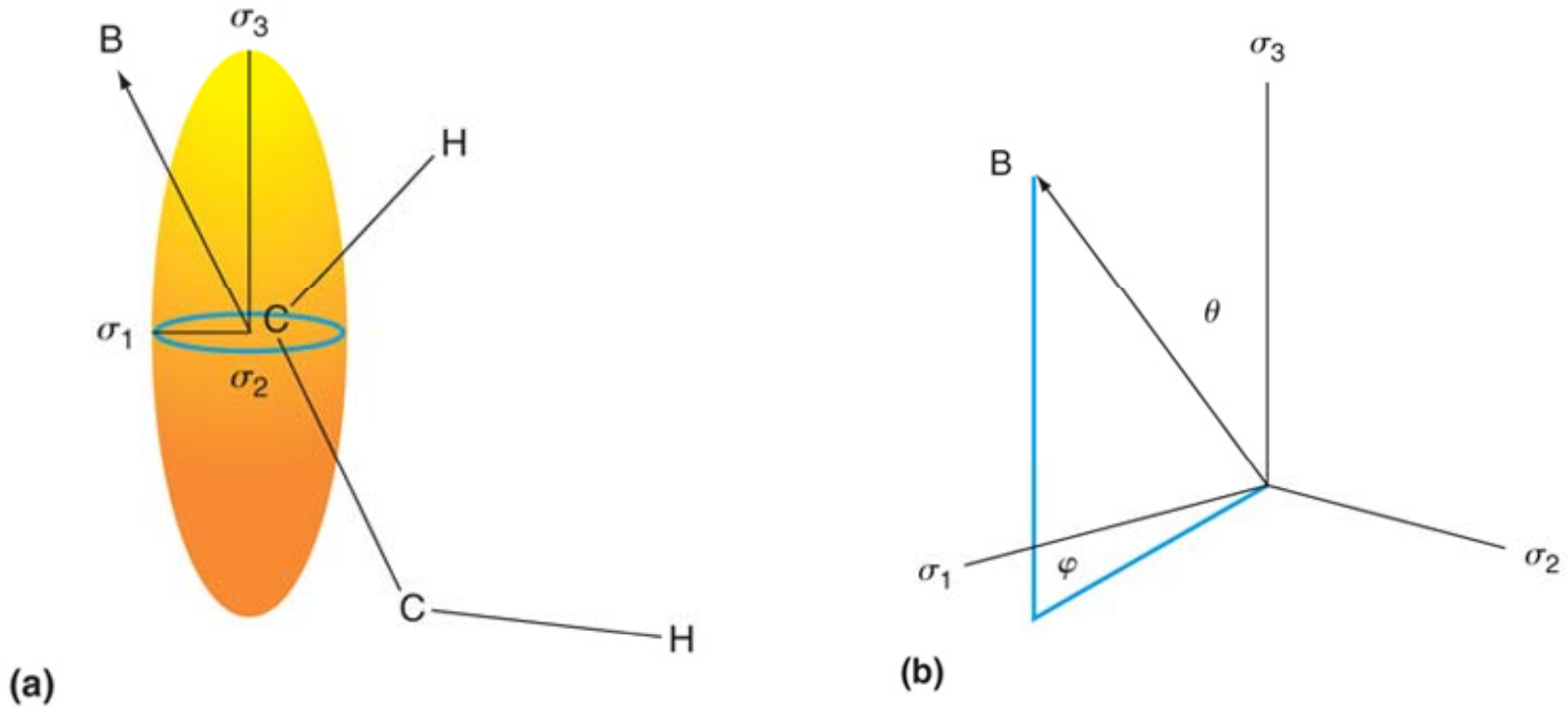

FIGURE 20.39

The principal values of the chemical shift represented as the semi-axes of an elliposoid. The angles θ and ϕ orient the magnetic field vector $\vec{B}$ in the coordinate system formed by these semi-axes.

FIGURE 20.40

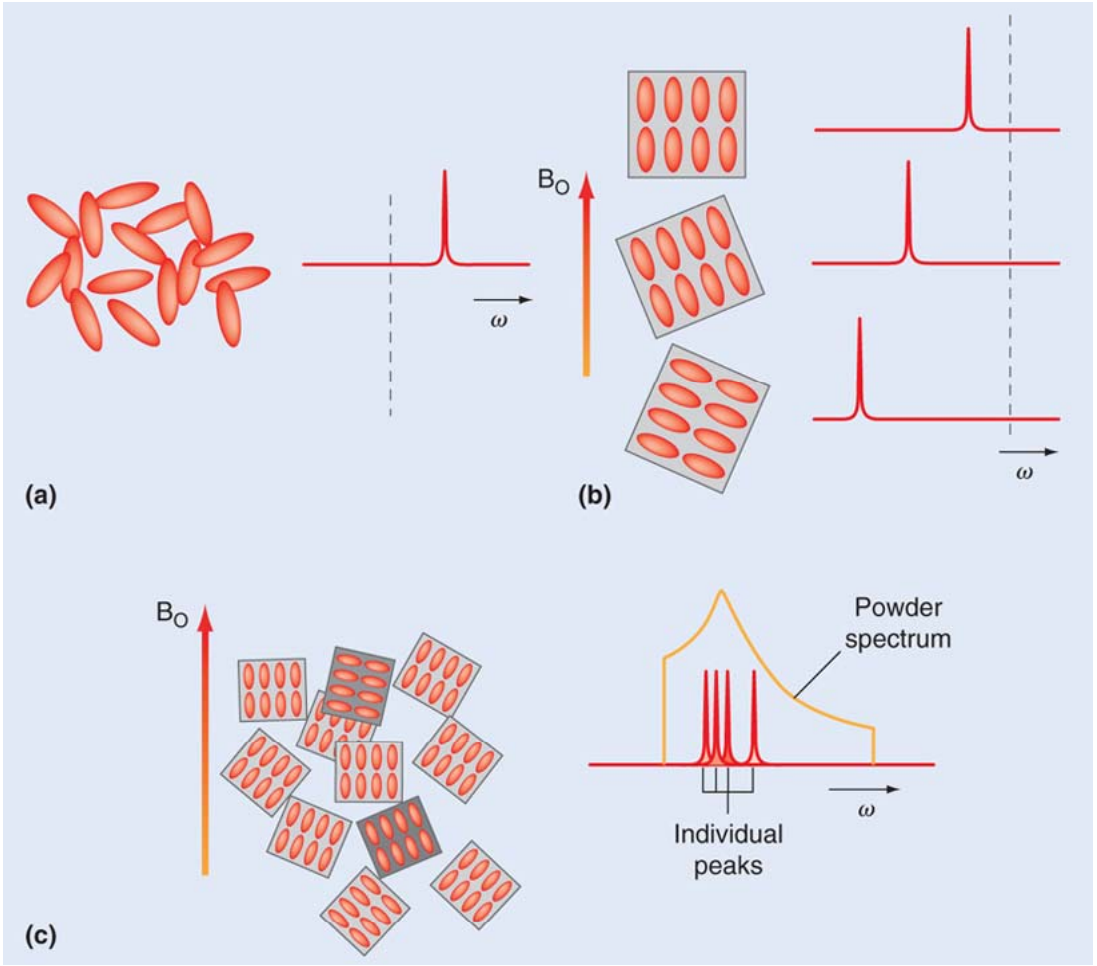

(a) Molecules tumble isotropically at a rate fast compared to the Larmor frequency, causing the chemical shift to be averaged to its isotropic value σ_{iso}. (b) If the molecules are located in a perfect crystal such that they are oriented identically relative to the magnetic field, the line is observed at the anisotropic chemical shift σ_{aniso}, which is dependent on the orientation of the crystal relative to the field. (c) In a polycrystalline solid a random distribution of orientations occurs, producing a broad chemical shift powder pattern.

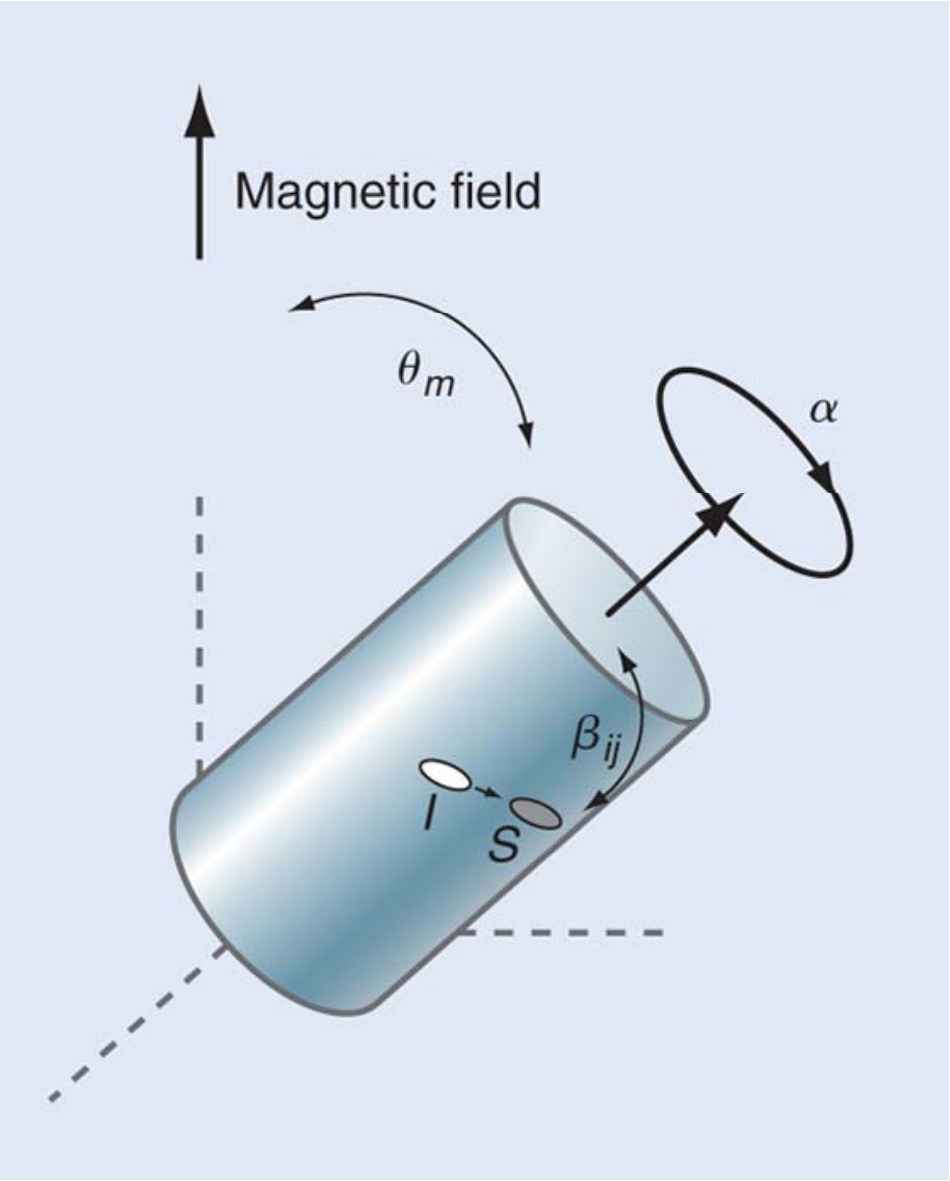

FIGURE 20.41

In magic angle spinning, the sample is rapidly spun about its goniometer axis, which is tilted $\theta_m = 54.74^\circ$ with respect to the static magnetic field. The angles α and β orient a specific *I*-*S* internuclear vector in the frame of the goniometer.

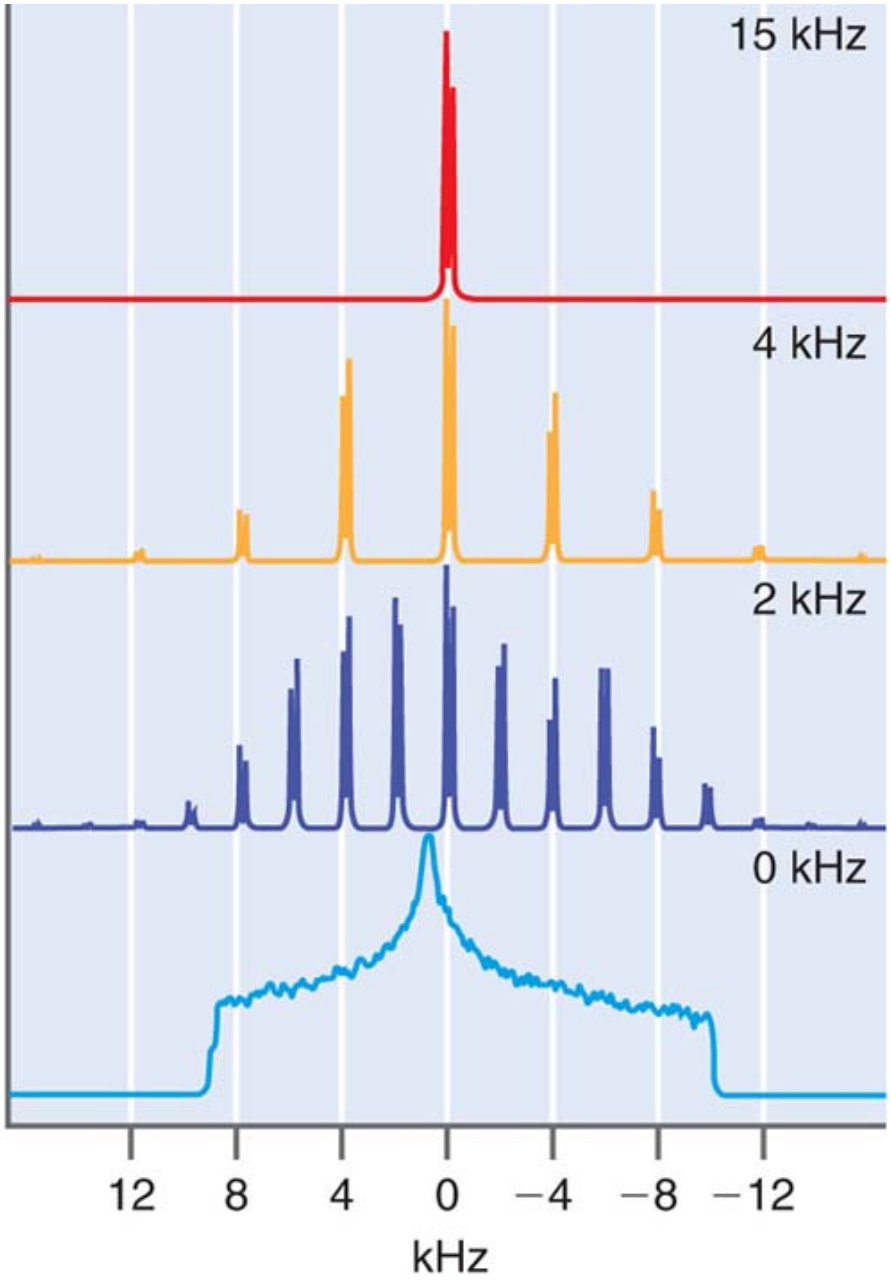

FIGURE 20.42

A ^{13}C NMR spectrum displayed as a function of spinning rate of a polycrystalline sample in which the unit cell contains a molecule with two chemically inequivalent ^{13}C-labeled carbonyl group (see text).

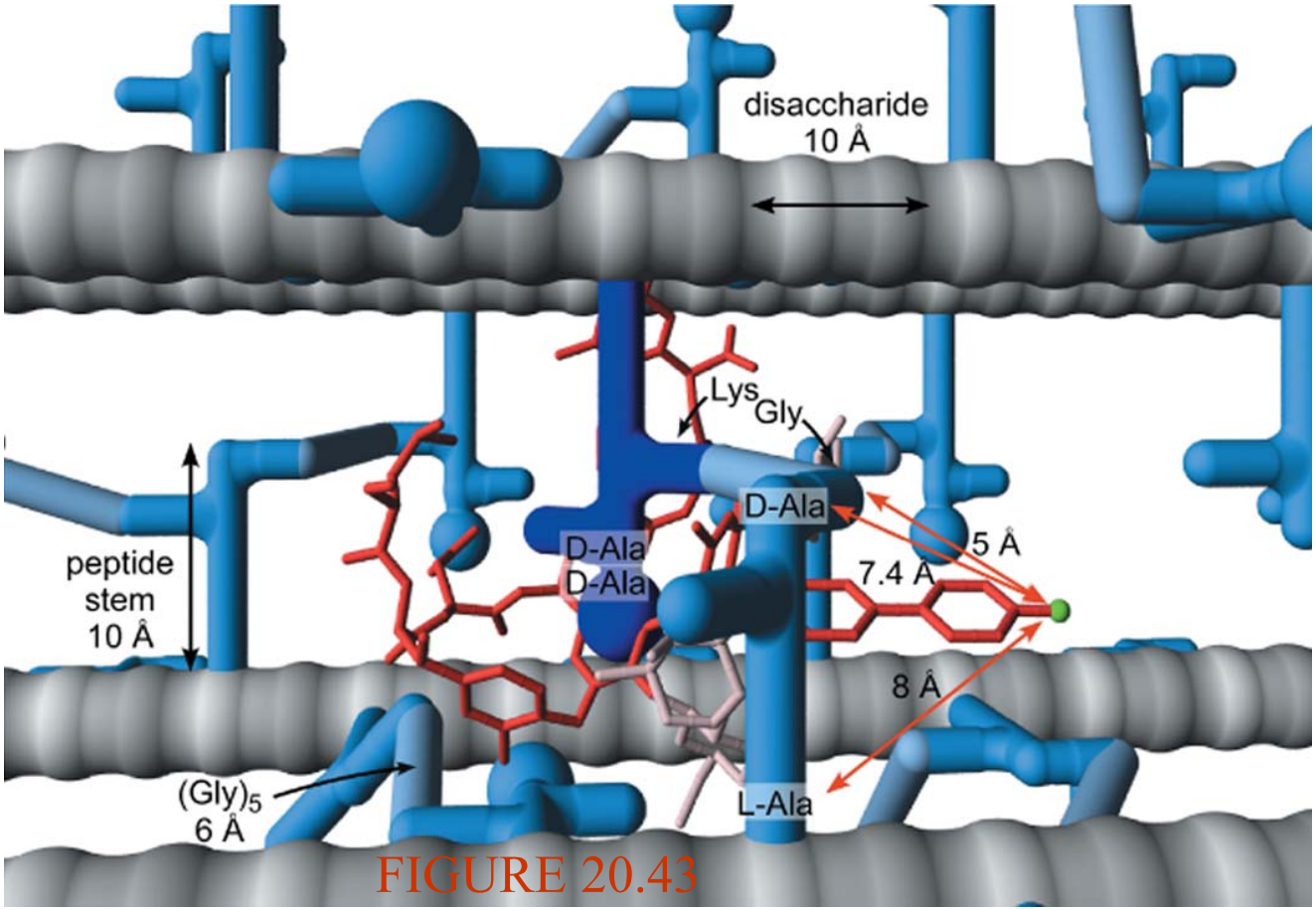

FIGURE 20.43

REDOR-derived structural model of fluorinated vancomycin derivative bound to the mature peptidoglycan of *S. aureus*. The glycan strands are represented as gray cylinders and amino acids at blue pipes. Rounded ends of the blue pipes are terminal D-alanines. The carbon framework of vancomycin is in red, and the ^{19}F spin is the green sphere at the right.

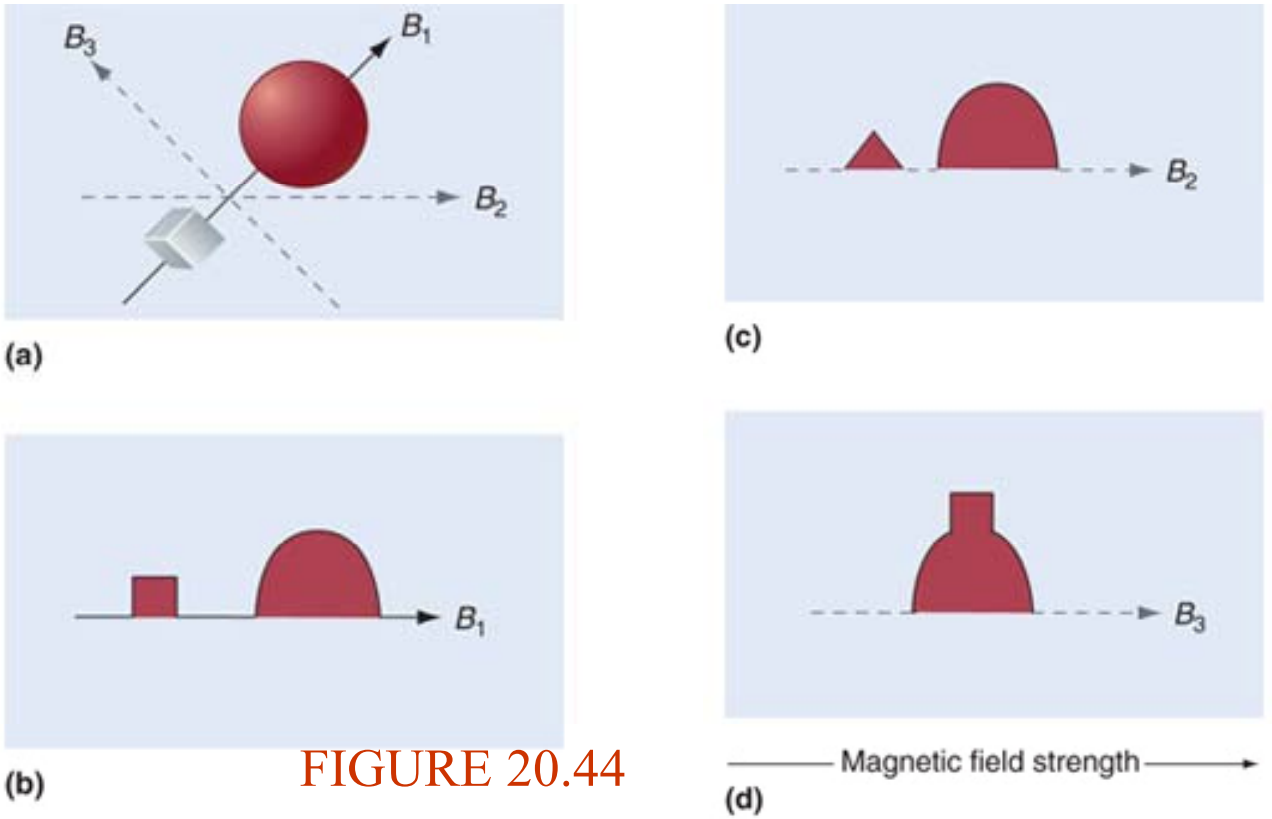

FIGURE 20.44

(a) Two structures are shown along with the three gradient directions indicated along which NMR spectra will be taken. In each case, spins within a thin volume element slice along the gradient resonate at the same frequency. The leads to a spectrum that is a projection of the volume onto the gradient axis. Image reconstruction techniques originally developed for X-rays can be used to determine the three-dimensional structure. (b-d) NMR spectra taken along the direction B_1, B_2, and B_3 indicated in part (a).

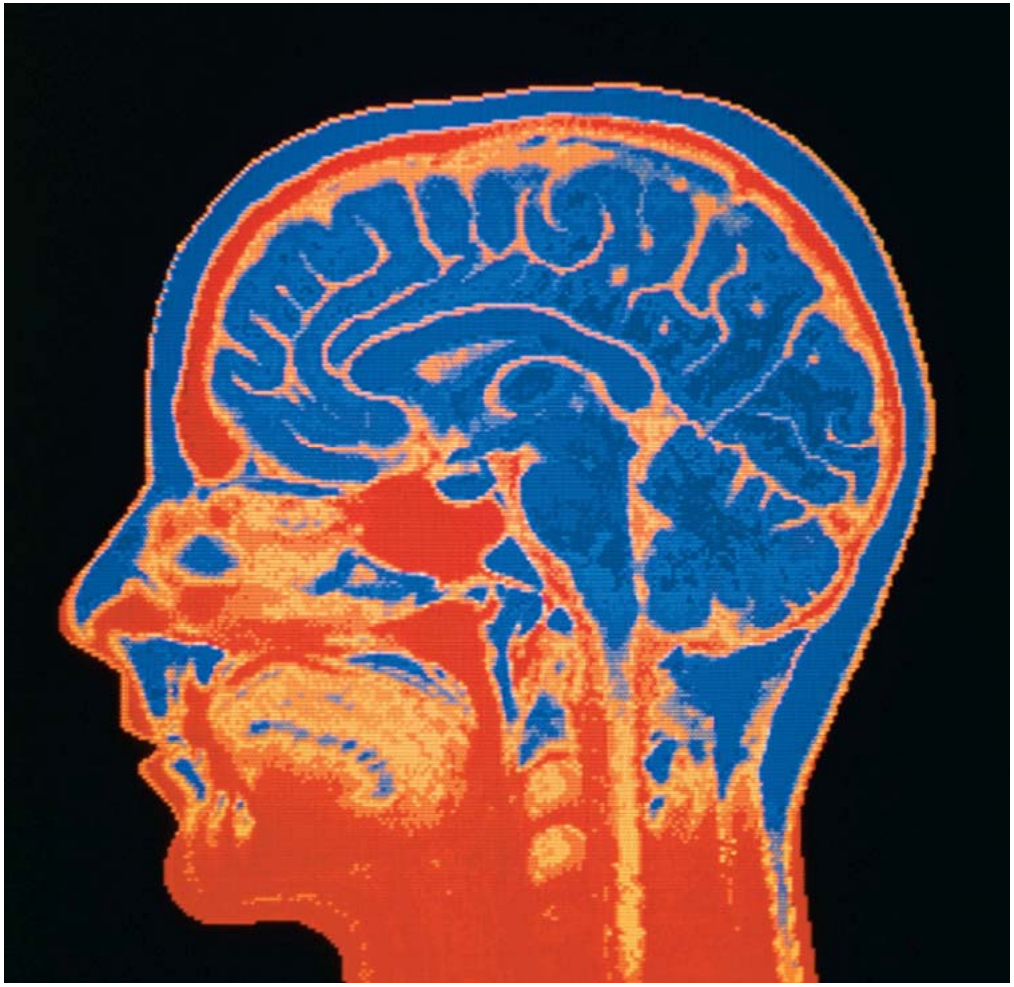

FIGURE 20.45

This figure shows an NMR image taken of a human brain. The section shown is obtained from a noninvasive scan of the patient's head. The contrast has its origin in the dependence of the relaxation time on the strength of binding of the water molecule to different biological tissues.

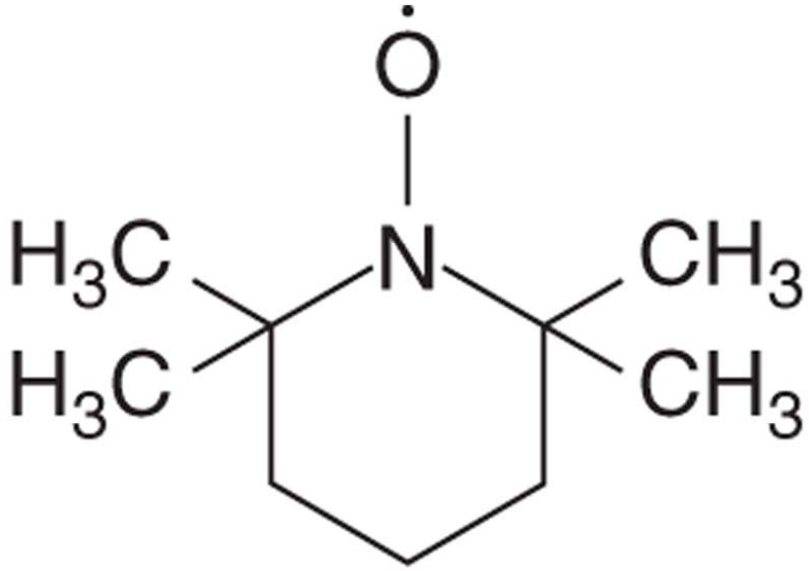

TEMPO

FIGURE 20.46

The stable nitroxide radical TEMPO.

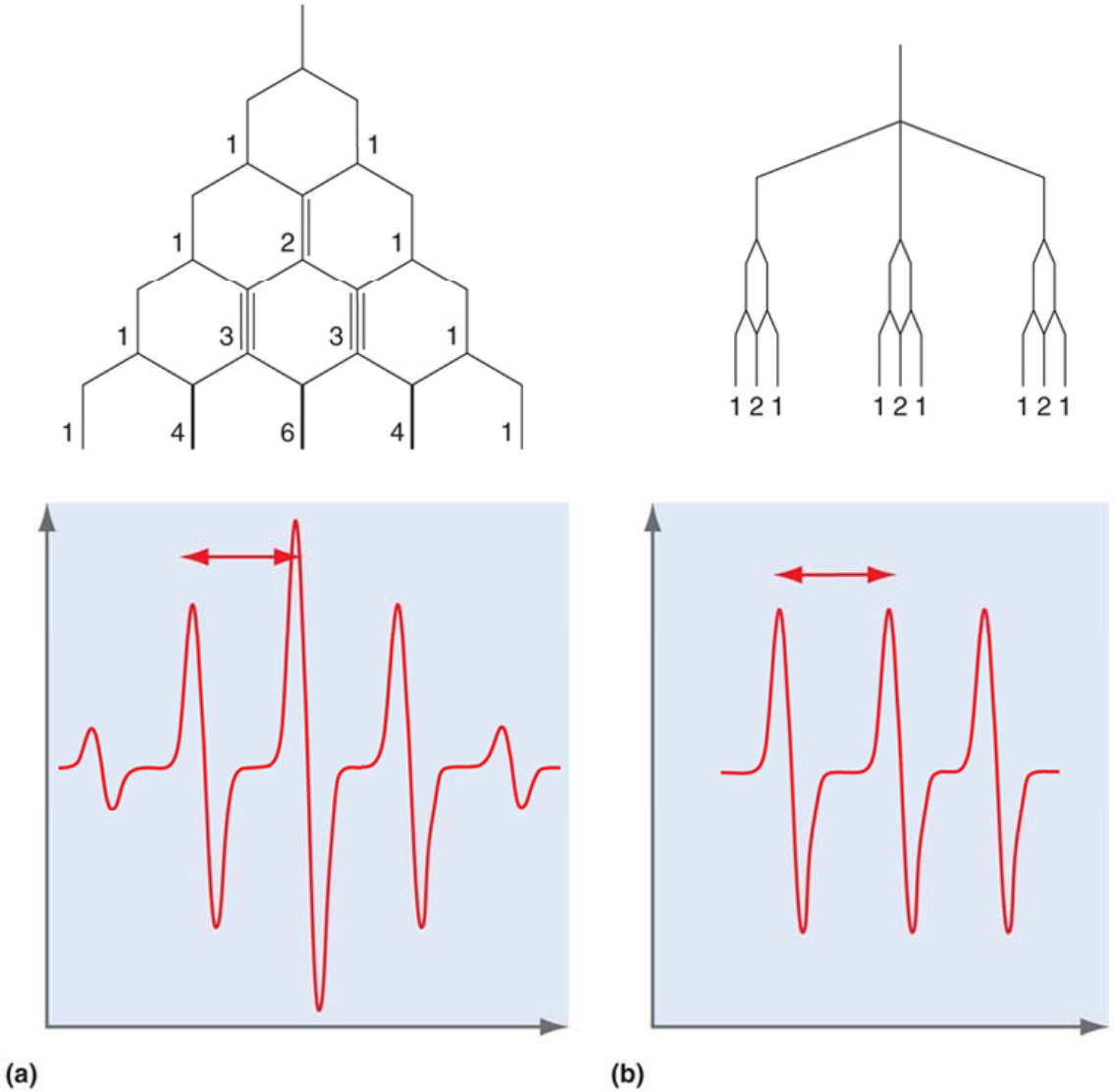

FIGURE 20.47

(a) The ESR spectrum of an electron coupled equally to four spin ½ unclei. The red arrow denotes the size of the hyperfine coupling. (b) The ESR spectrum of an electron coupled to a single ^{14}N nucleus and coupled weakly to two spin ½ nuclei. The ^{14}N nucleus is spin 1 and splits the ESR transition into a triplet. The red arrow denotes the ^{14}N hyperfine coupling. Due to rapid molecular tumbling, the components of the triplet are narrowed and the weaker hyperfine couplings are not observed.

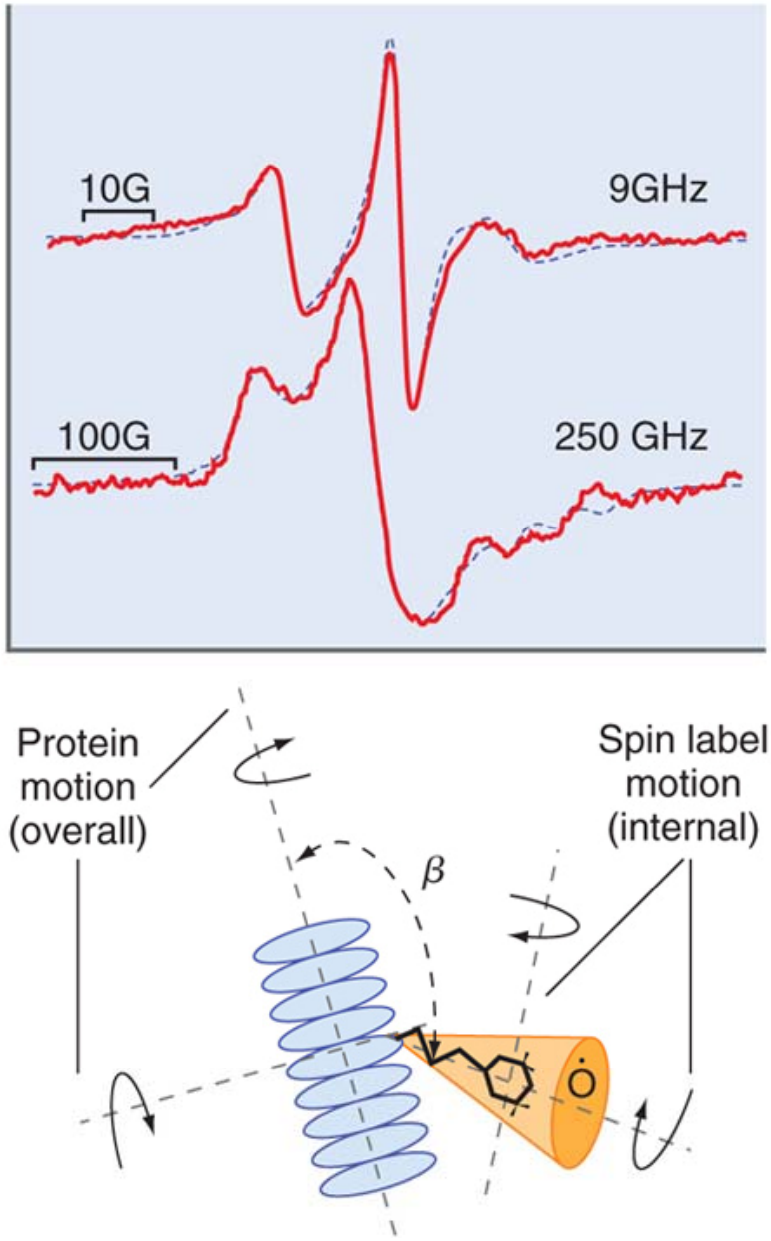

FIGURE 20.48

A multifrequency ESR study of the motions of T4-lysozyme. A nitroxide spin label is tethered to residue 44. The relevant molecular motions are schematized below the spectra. The ESR spectrum at 9 GHz is sensitive to slow, overall protein motions, whereas at 250GHz, the slow motions appear "frozen out" and the spectrum is sensitive to faster local motions within the polymer. Dotted lines are the simulated line shapes based on the author's model for protein.

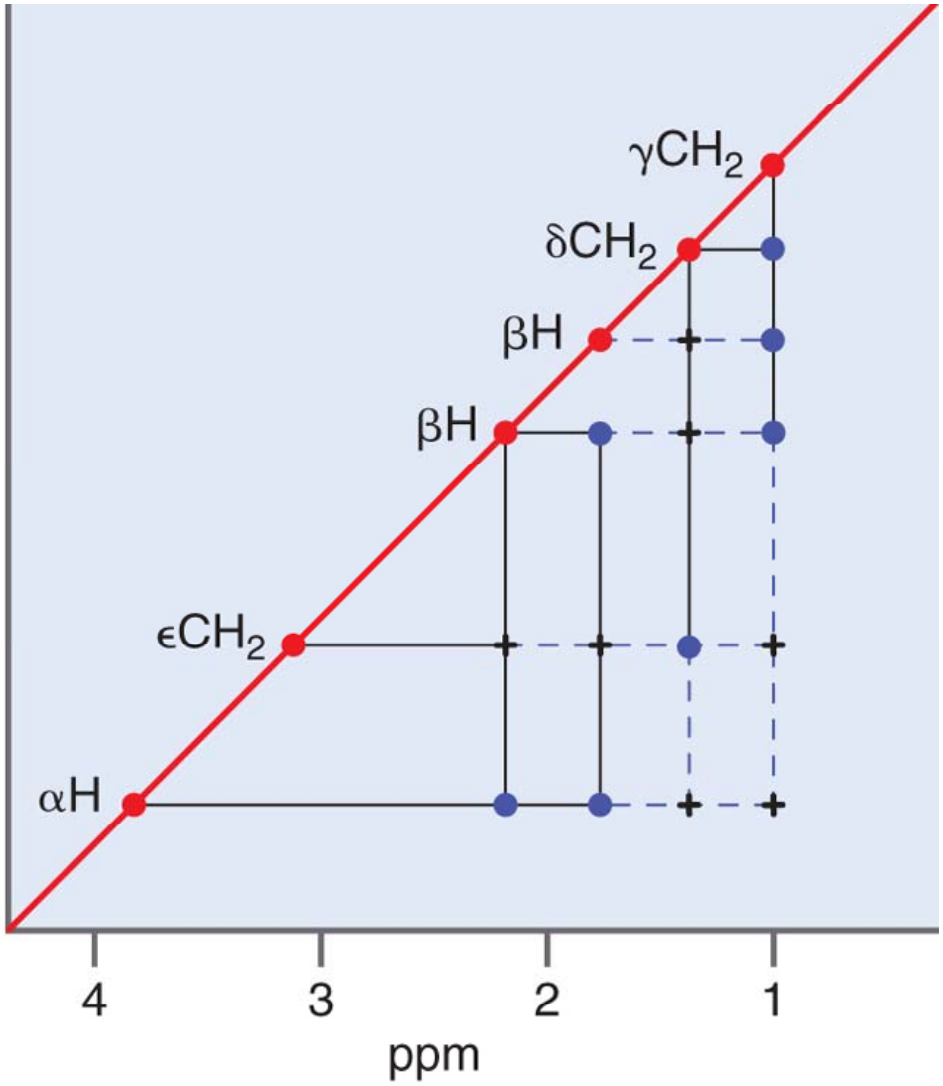

Problems P20.17

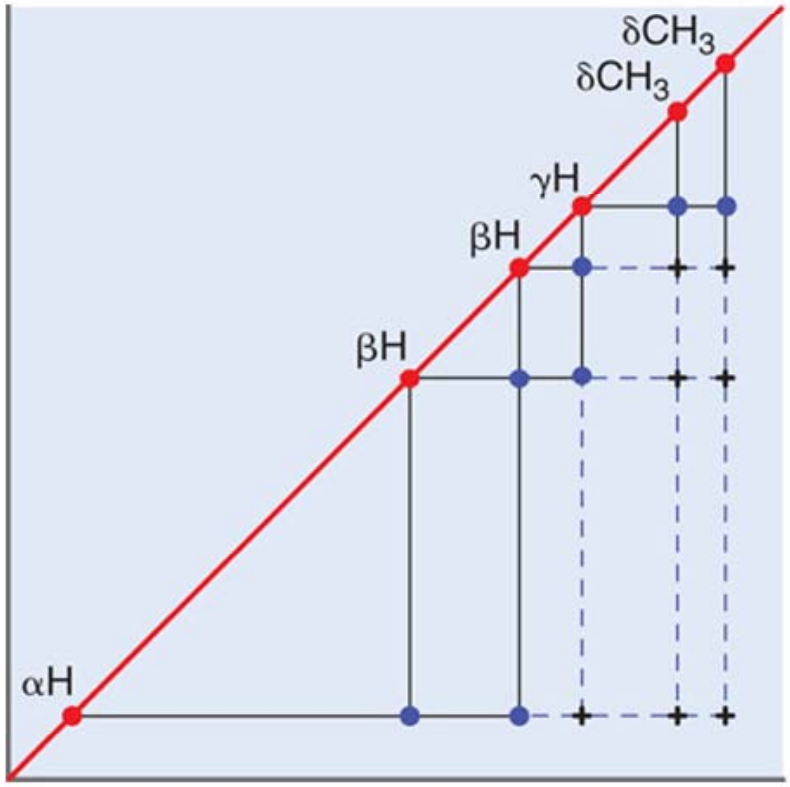

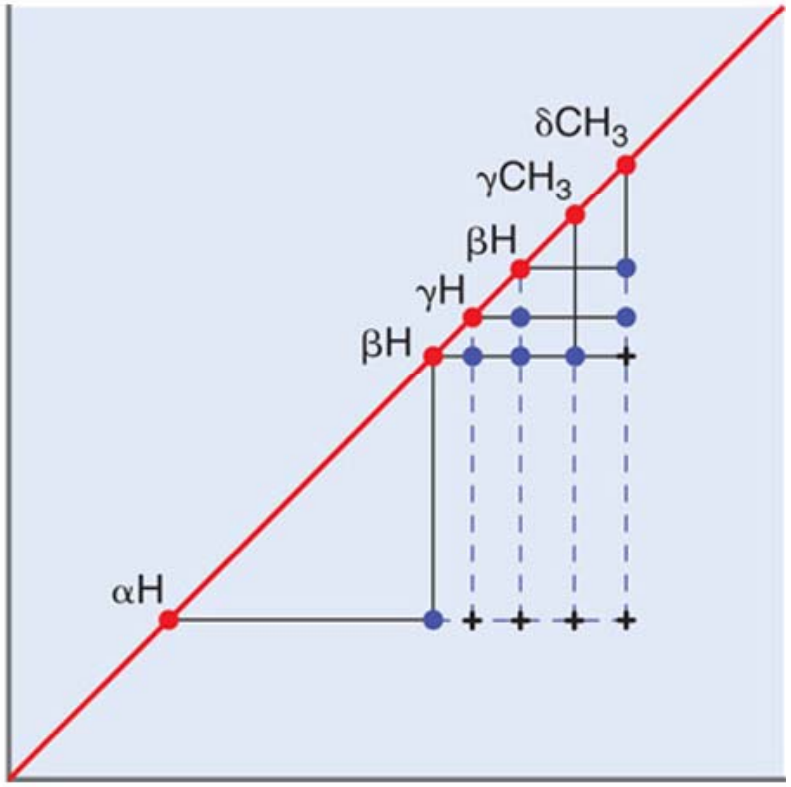

Problems P20.18

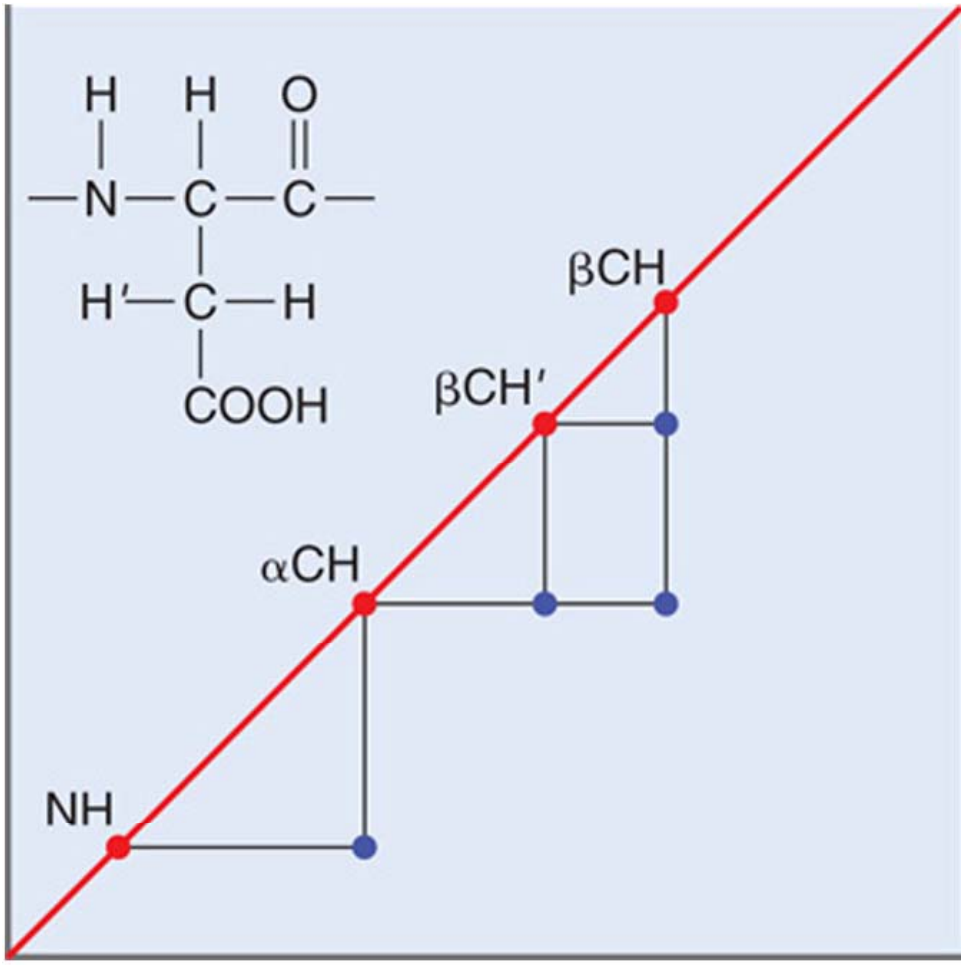

Problems P20.19

Physical Chemistry

For the Life Sciences

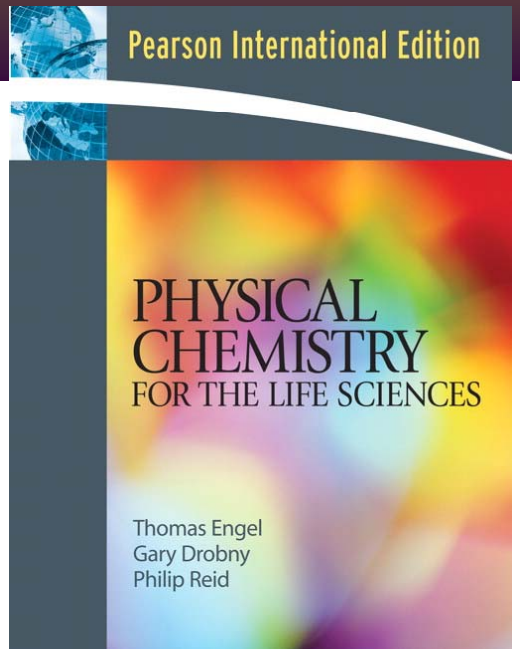

CHAPTER 21

The Structure of Biomolecules at the Nanometer Scale: X-Ray Diffraction and Atomic Force Microscopy

- 21.1 Unit cells and Bravais lattices
- 21.2 Lattice planes and Miller indices
- 21.3 The Von Laue and Bragg equations for X-ray diffraction
- 21.4 The unit cell parameters can be determined from a diffraction pattern
- 21.5 The electron distribution in the unit cell can be calculated from the structure factor
- 21.6 Solutions to the phase problem
- 21.7 Structure determinations are crucial to understanding biochemical processes

- 21.8 The atomic force microscope
- 21.9 Measuring adhesion forces between cells and molecular recognition imaging using the atomic force microscope
- 21.10 Nanodissection using the atomic force microscope
- 21.11 The atomic force microscope as a probe of surface structure
- 21.12 Observing biochemical processes in real time using the atomic force microscope

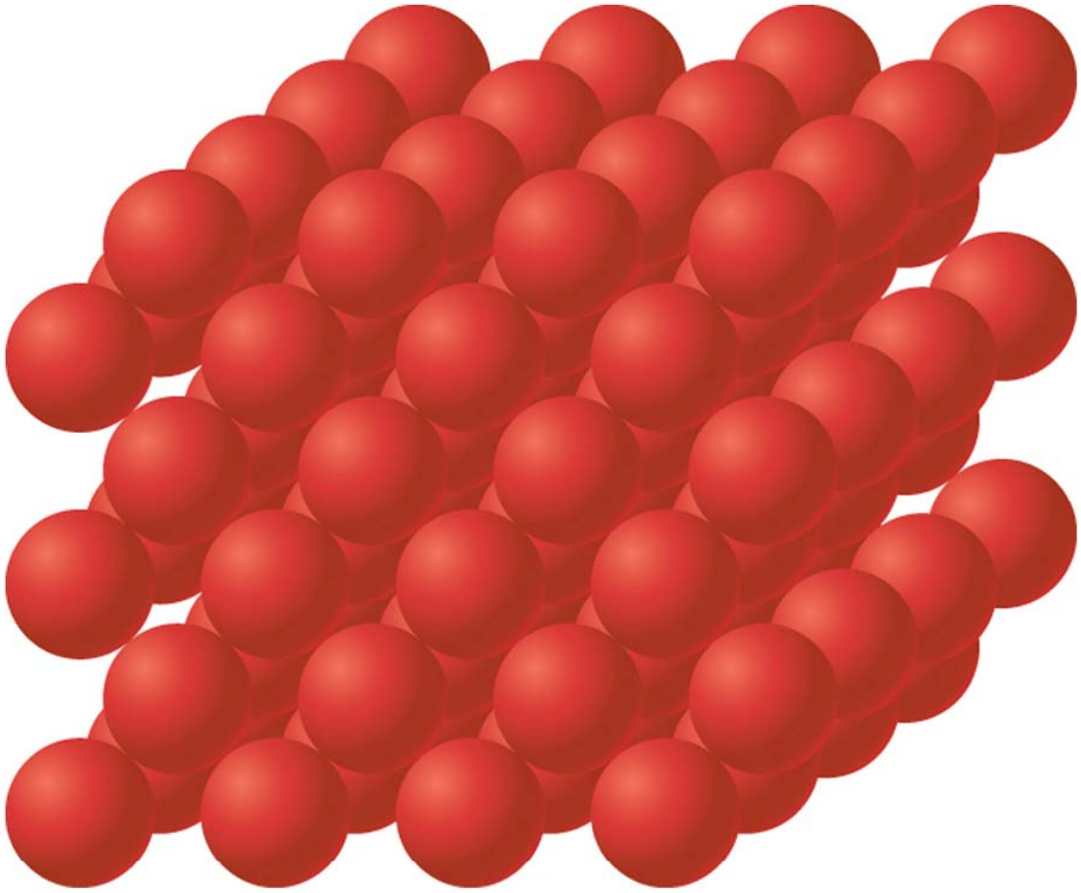

FIGURE 21.1

A portion of a crystal of nickel is shown that is large compared to atomic dimension, but small compared to a macroscopic crystal.

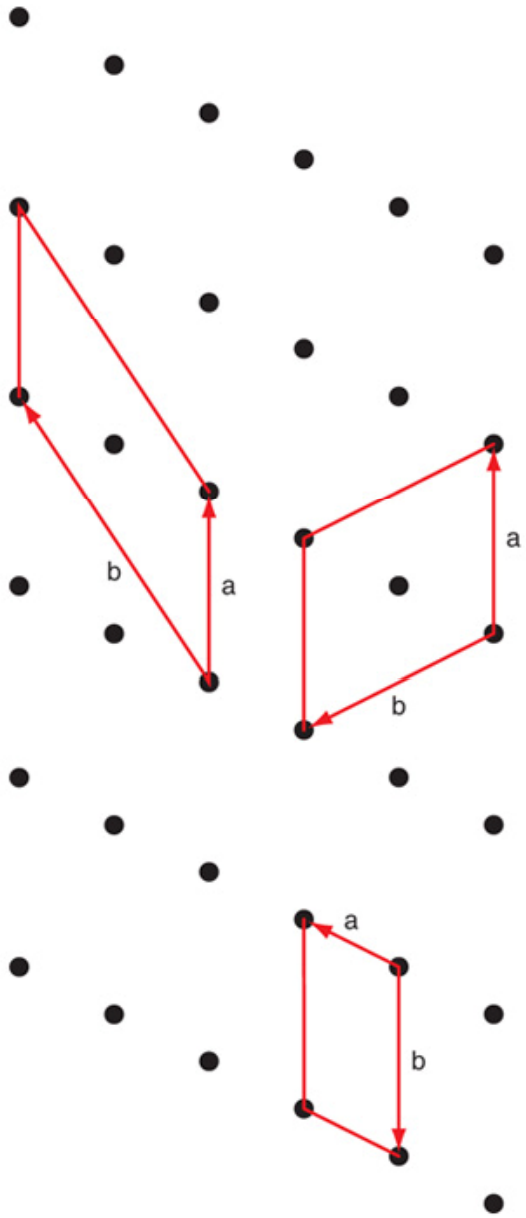

FIGURE 21.2

Three different choices for a unit cell in a two-dimensional lattice are shown. Which are primitive unit cells?

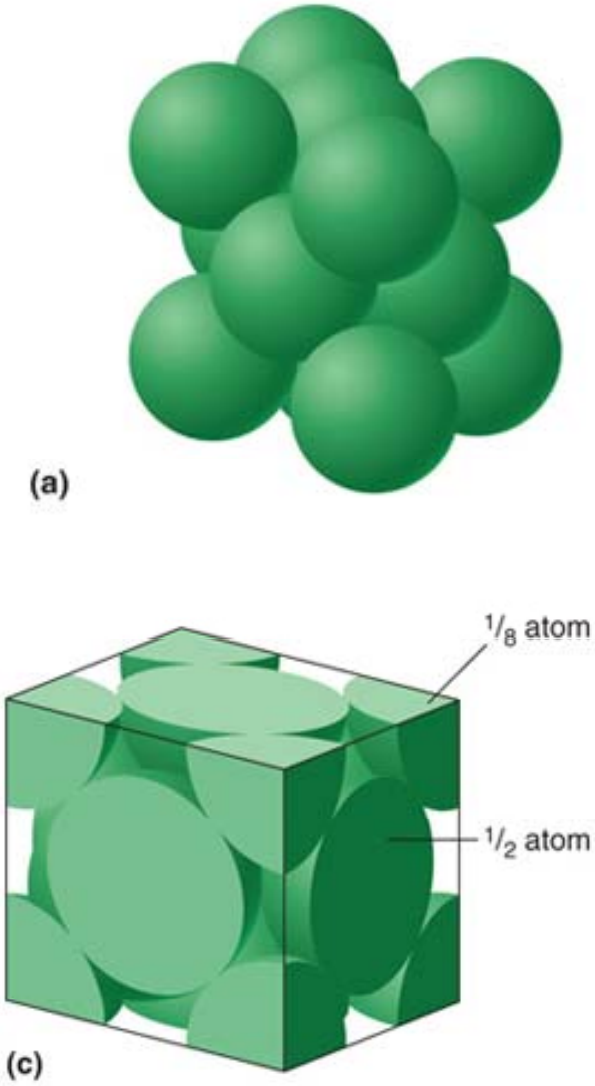

FIGURE 21.3

(a) Close-packed sphere model of the unit cell of a face-centered cubic lattice. (b) View that shows the relative positions of the atoms in the unit cell. (c) The unit cell contains four atoms as the atoms at the corners and on the faces are shared among adjoining unit cells.

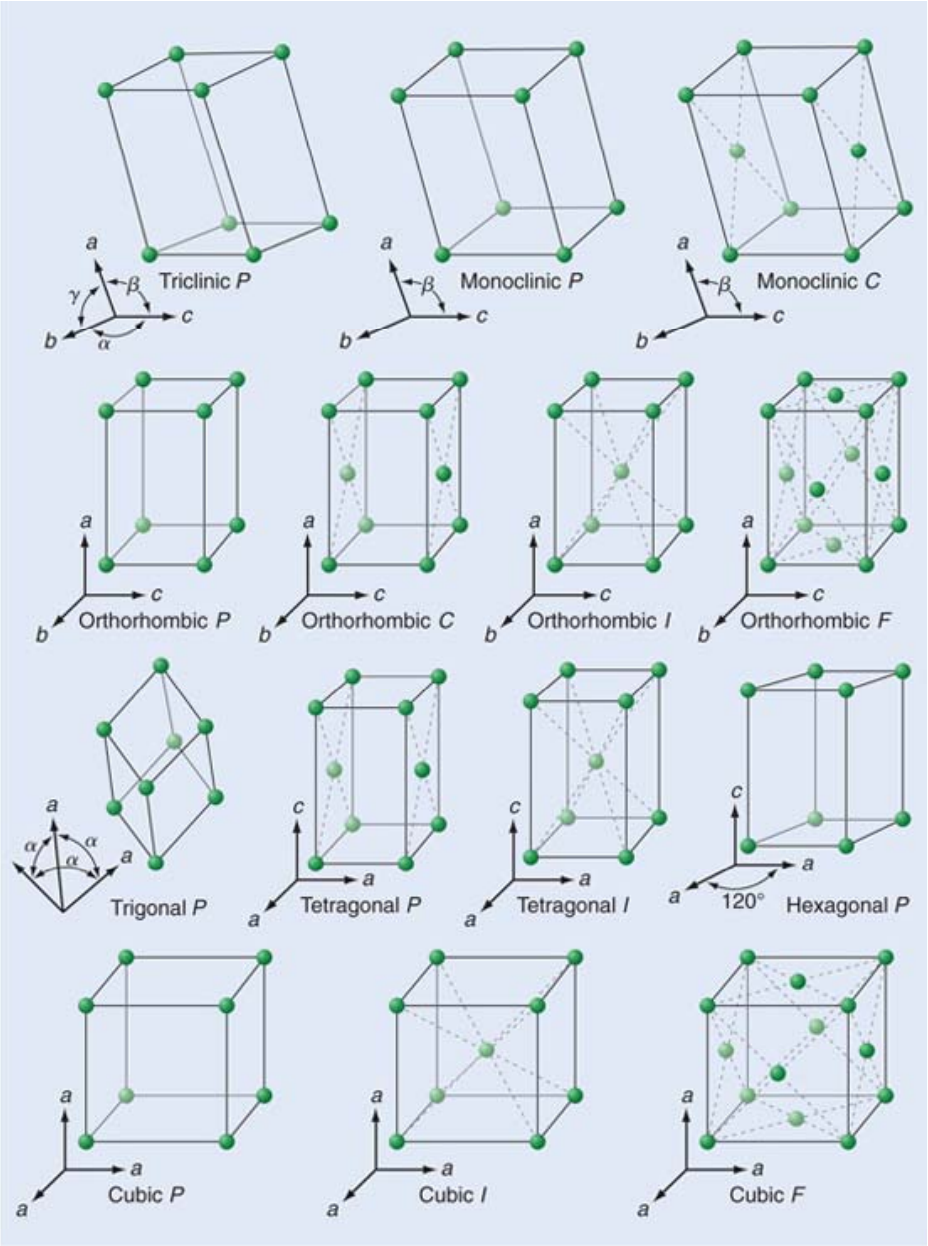

FIGURE 21.4

The 14 Bravais lattices include 7 fundamental lattices, some of which can have atoms at the center of the cell, or at the center of some or all faces of the cell.

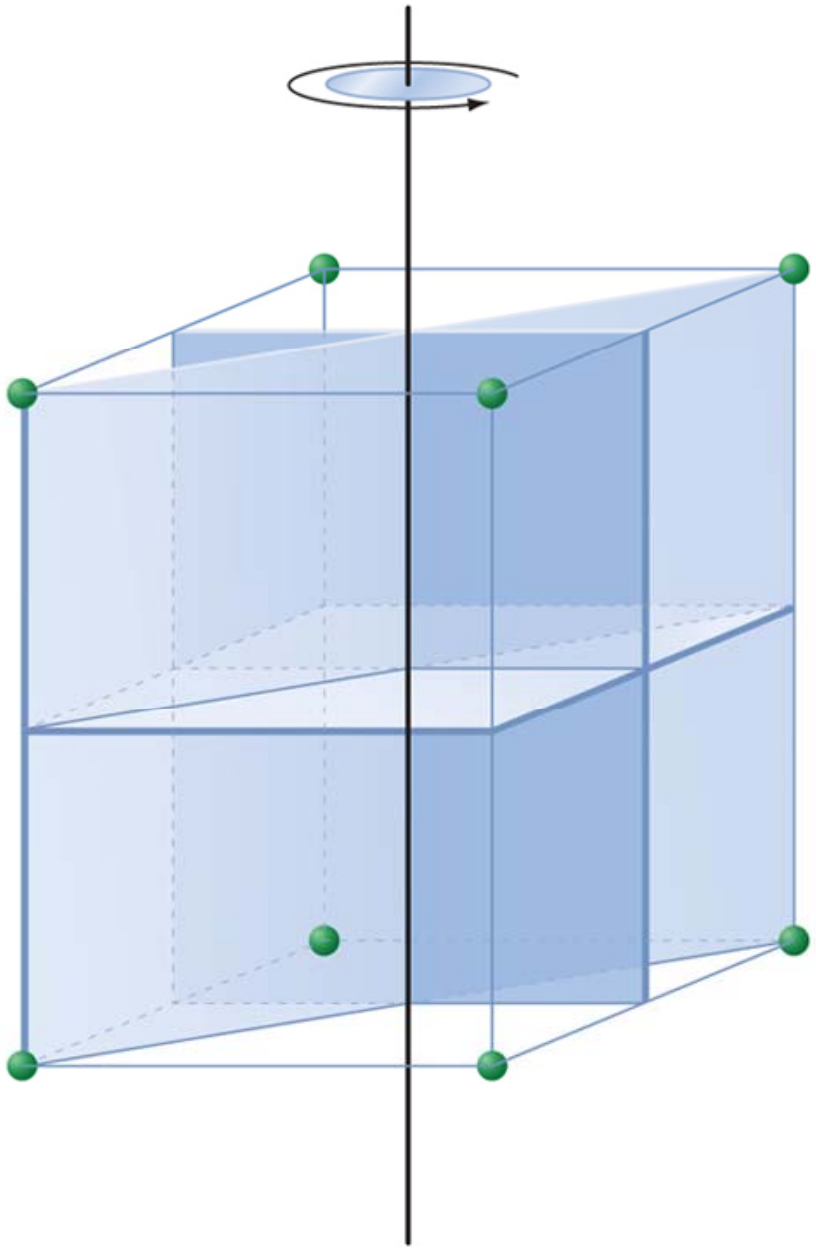

FIGURE 21.5

The unit cell of a tetragonal lattice has a fourfold rotation axis and only two unique mirror planes, because one of the mirror planes containing the rotation axis is produced from the other by rotation through 90°. What additional mirror plane(s) is (are) produced by applying the rotations to the indicated planes?

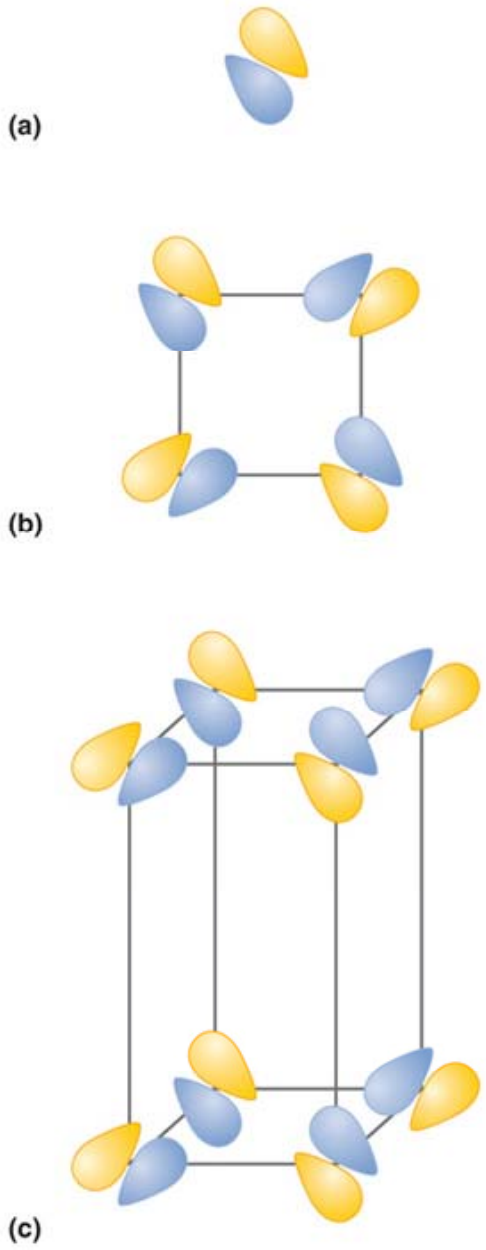

FIGURE 21.6

The unit cell is formed by combining the Bravais lattice with (a) a lattice motif. The lattice is combined with the lattice motif to form the crystal structure. (b) Top and (c) side views of the crystal structure are shown. The lattice motif lies in the plane shown in (b).

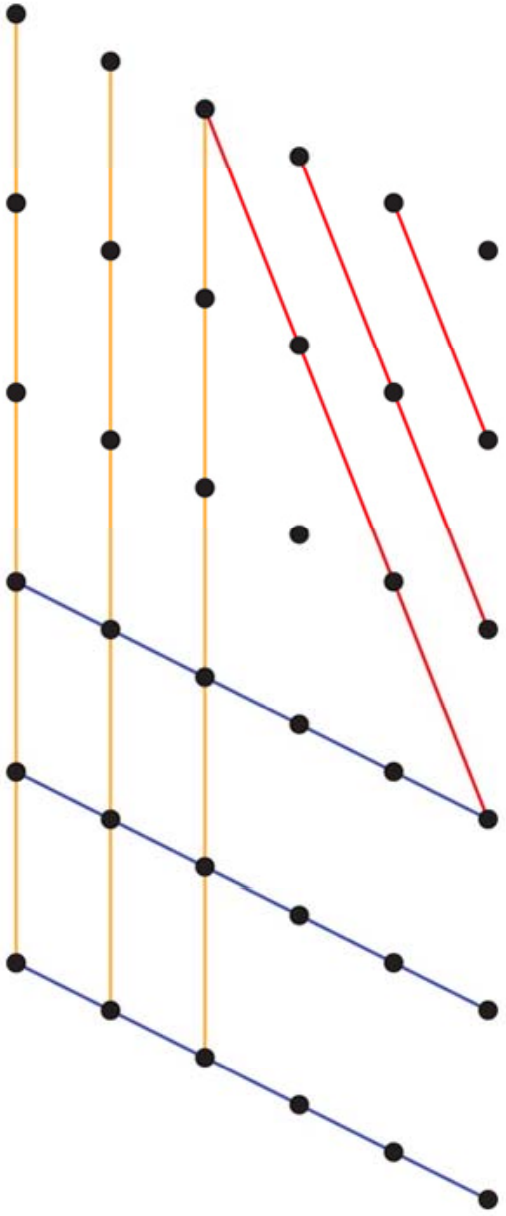

FIGURE 21.7

Three different sets of plane s are shown that reproduce all of the lattice.

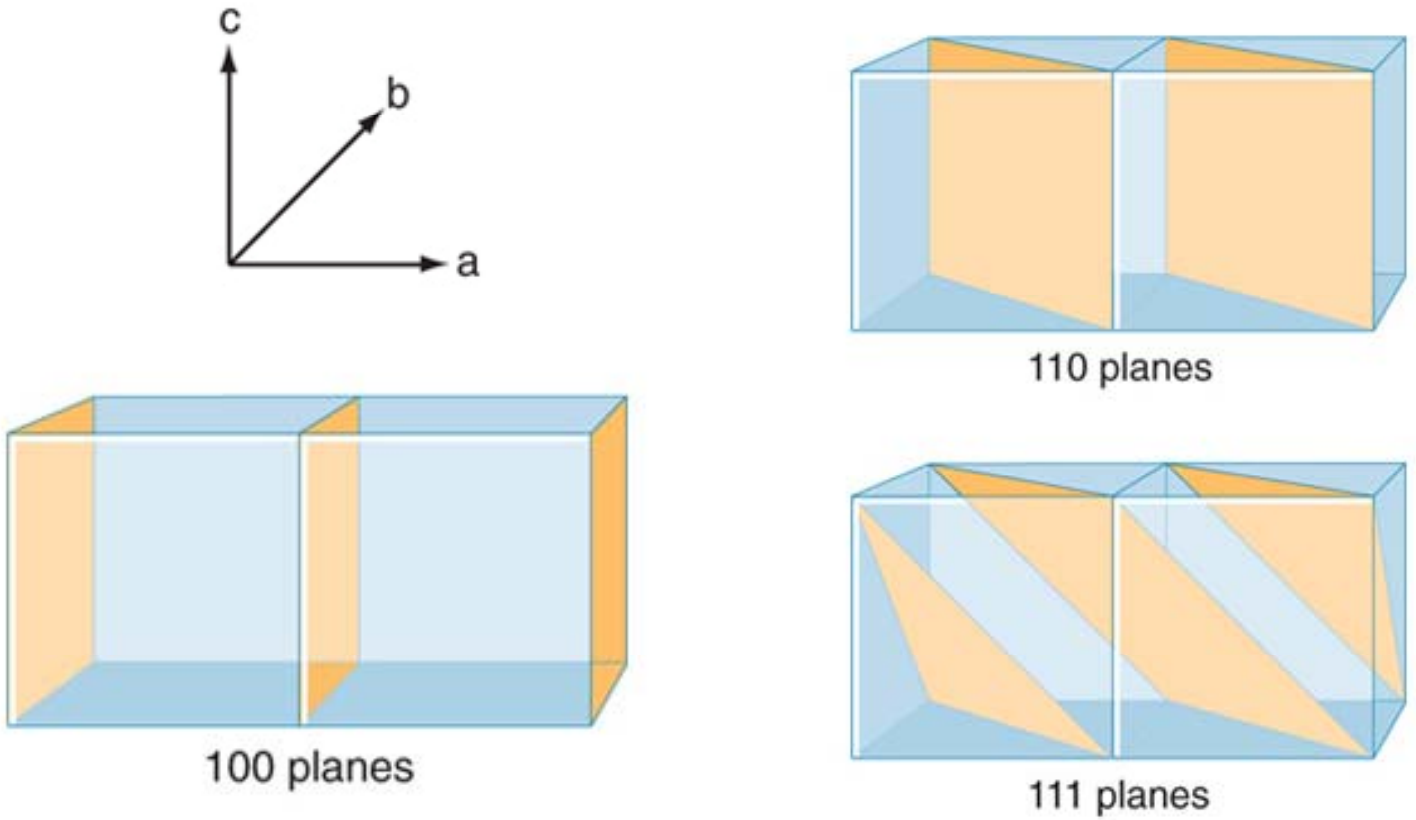

FIGURE 21.8

A cubic lattice can be represented by a set of lattice planes, some of which are shown.

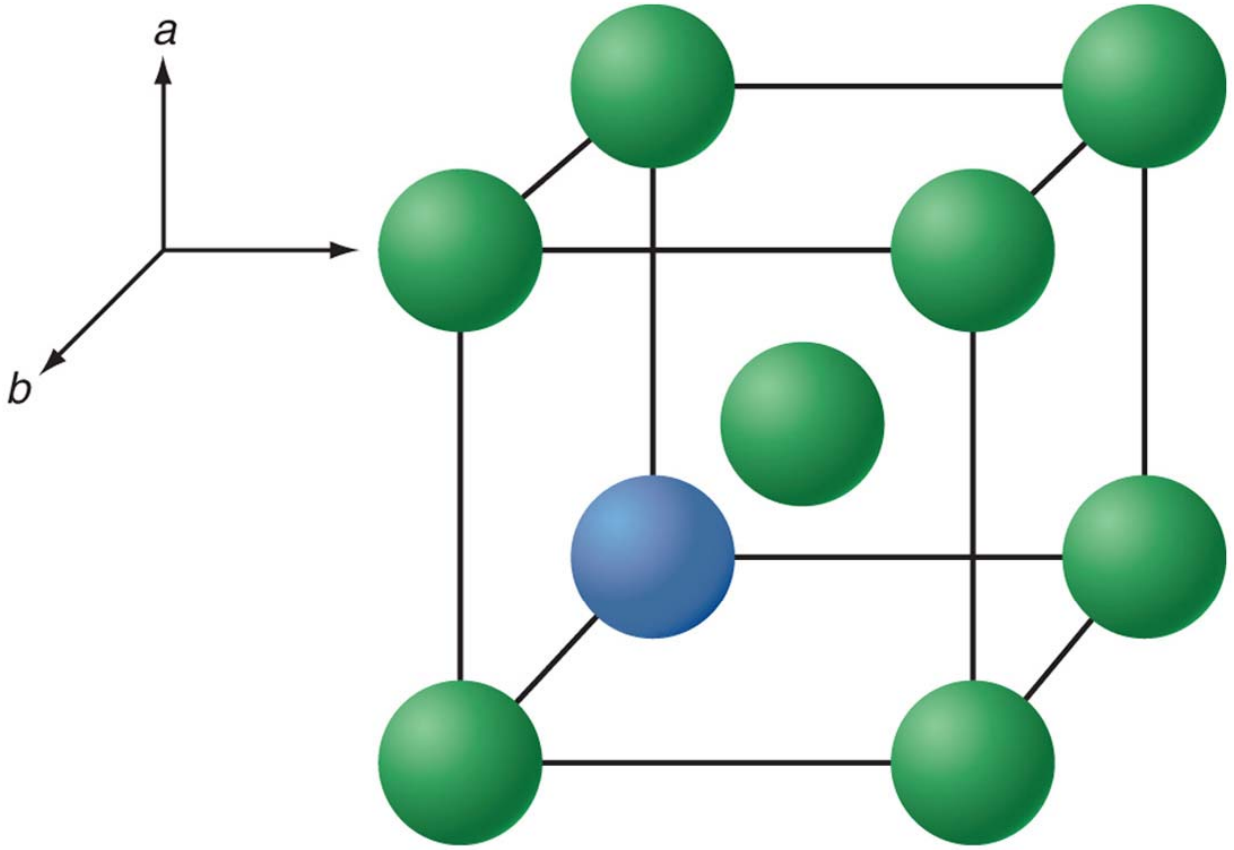

Example Problem 21.2

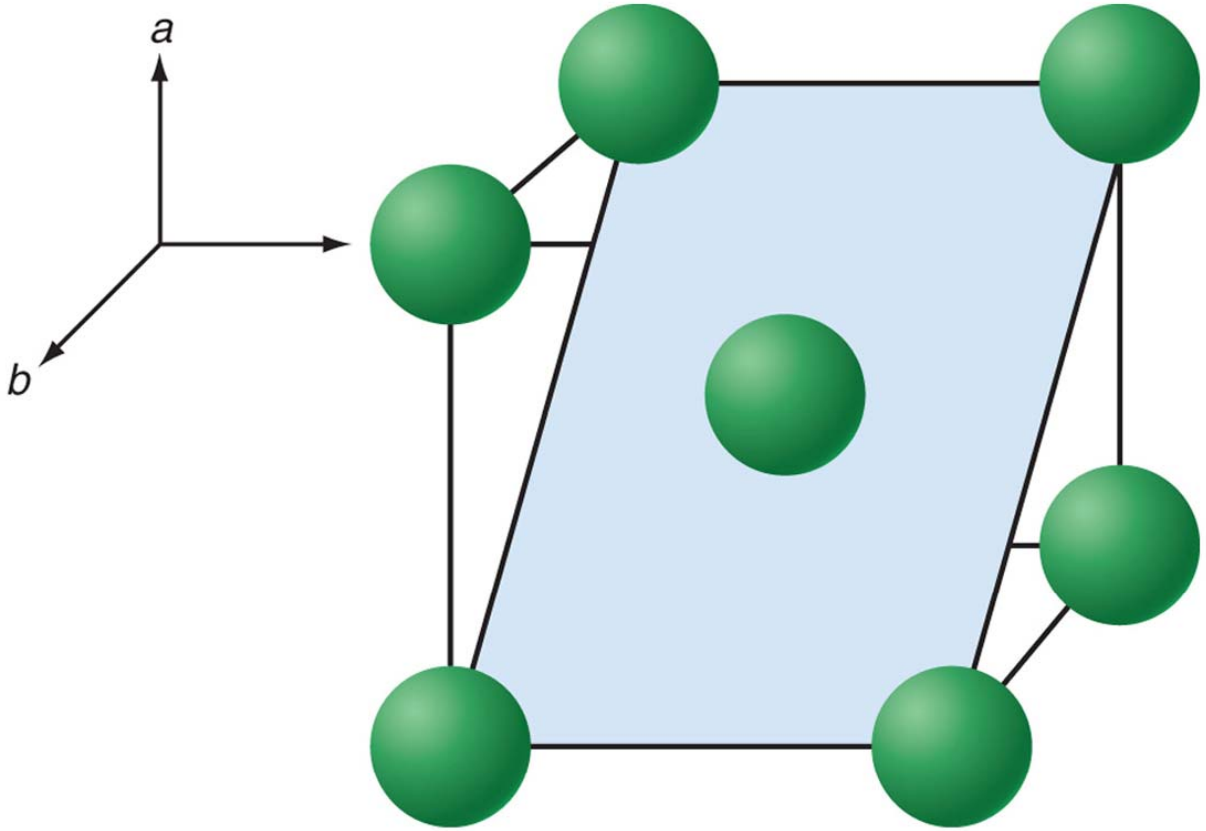

Example Problem 21.2 (continued)

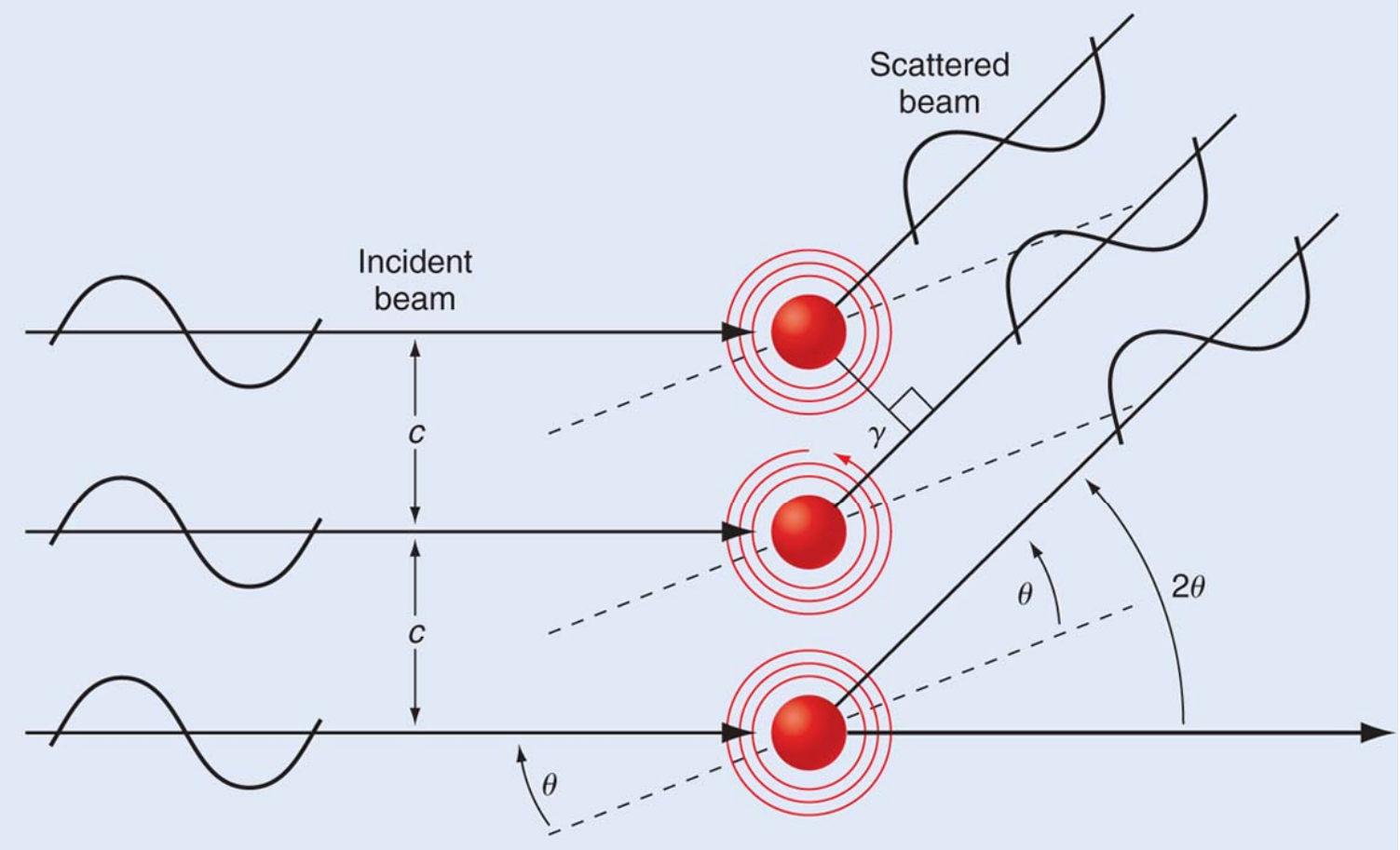

FIGURE 21.9

Diffraction is shown from a one-dimensional crystal. Constructive interference is observed between the waves scattered from the individual atoms if the path length differences are an integral multiple of the wavelength. The X-ray beam is incident perpendicular to the line of atoms.

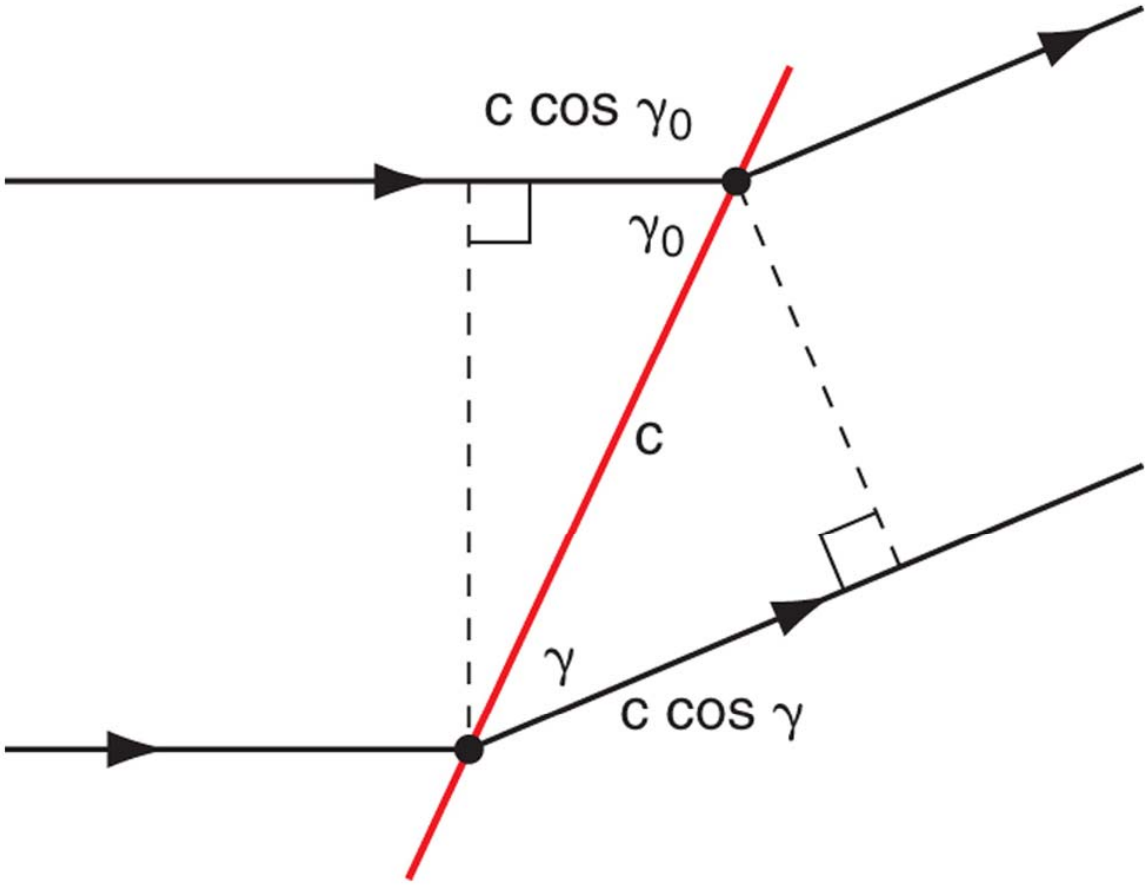

FIGURE 21.10

If the beam is incident at an angle other than 90°, the path difference before scattering must be included in the constructive interference in the constructive interference condition.

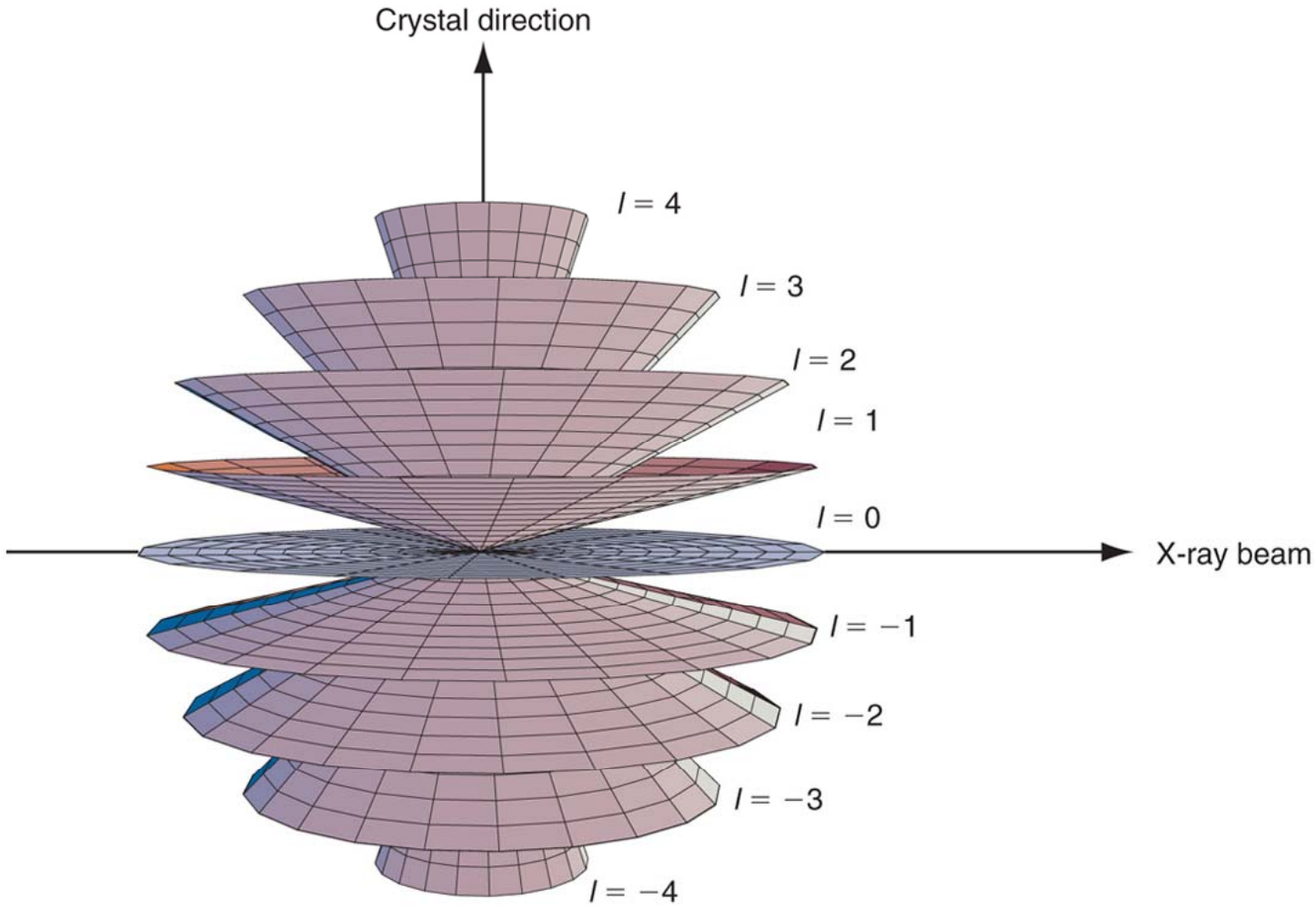

Example Problem 21.3

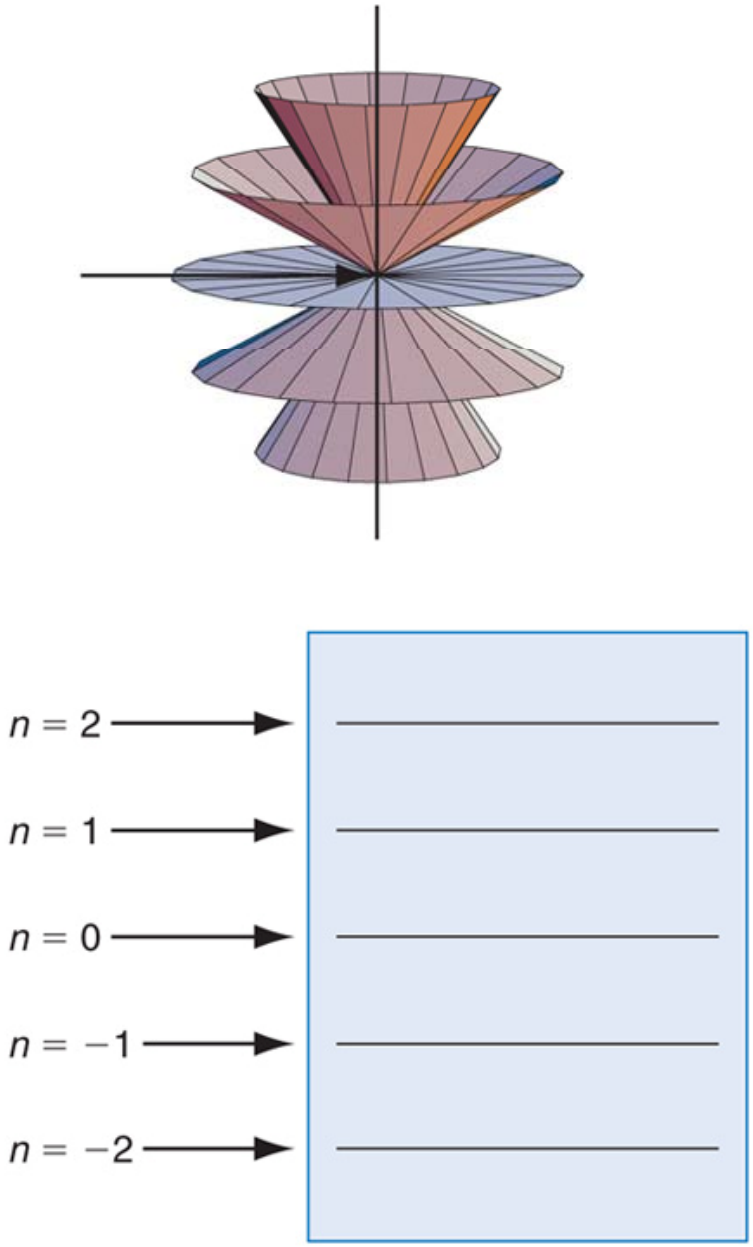

FIGURE 21.11

Consider the case in which the X-ray beam is incident perpendicular to the line of atoms. (Upper) The constructive interference condition is satisfied if the sdattered beam lies on the surface of one of the depicted cones. (Lower) The cones intersect the spherical detector surface centered at the crystal in a set of parallel lines, one for each diffraction order.

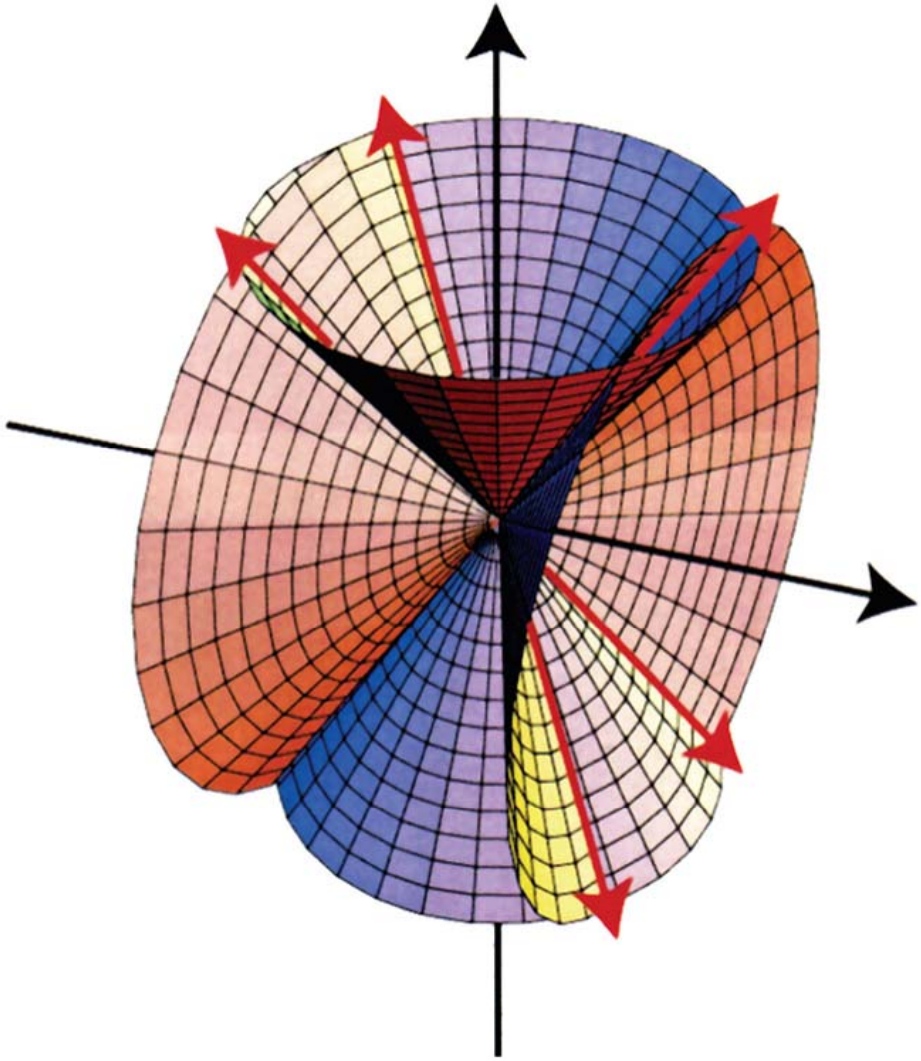

FIGURE 21.12

The constructive interference condition for a two-dimensional crystal is satisfied if the scattered beam lies on the intersection of the two sets od depicted cones. The black arrows are aligned along the mutually perpendicular rows of scattering centers in the plane of the two-dimensional crystal and five of the eight lines of intersection of the two cones are shown in red. To simplify the presentation, not all of the cones are shown.

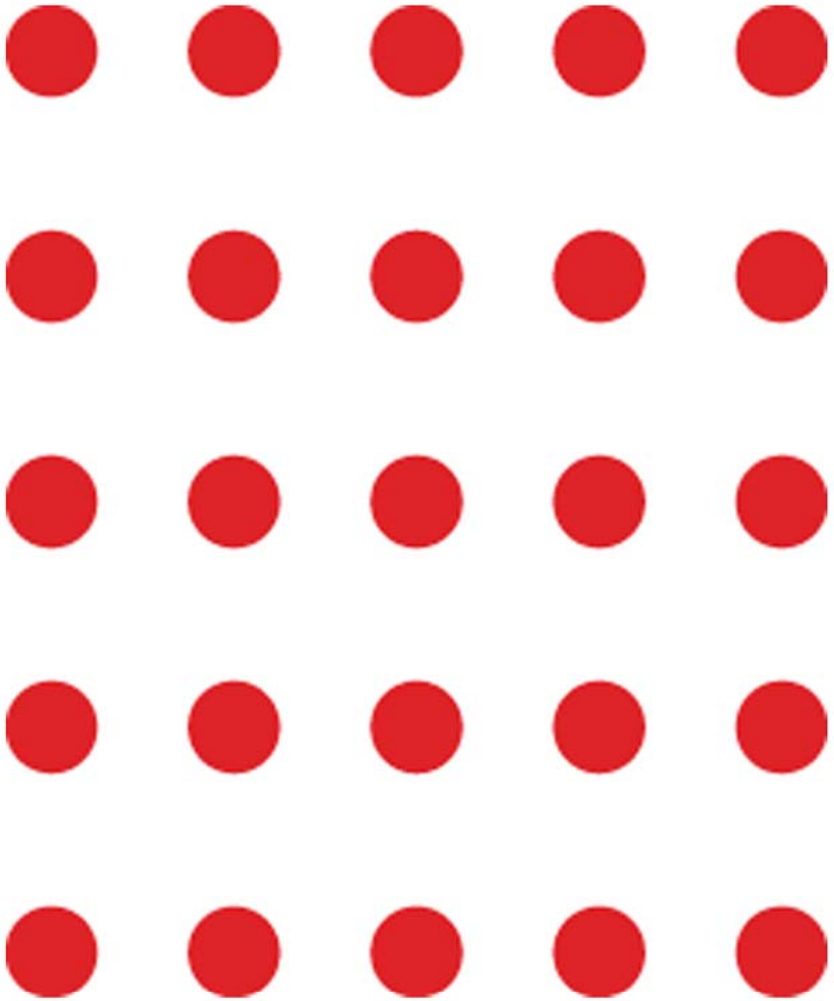

FIGURE 21.13

The diffraction pattern of a two-dimensional crystal, the axes of which are perpendicular, is a rectangular array of points that we call diffraction spots.

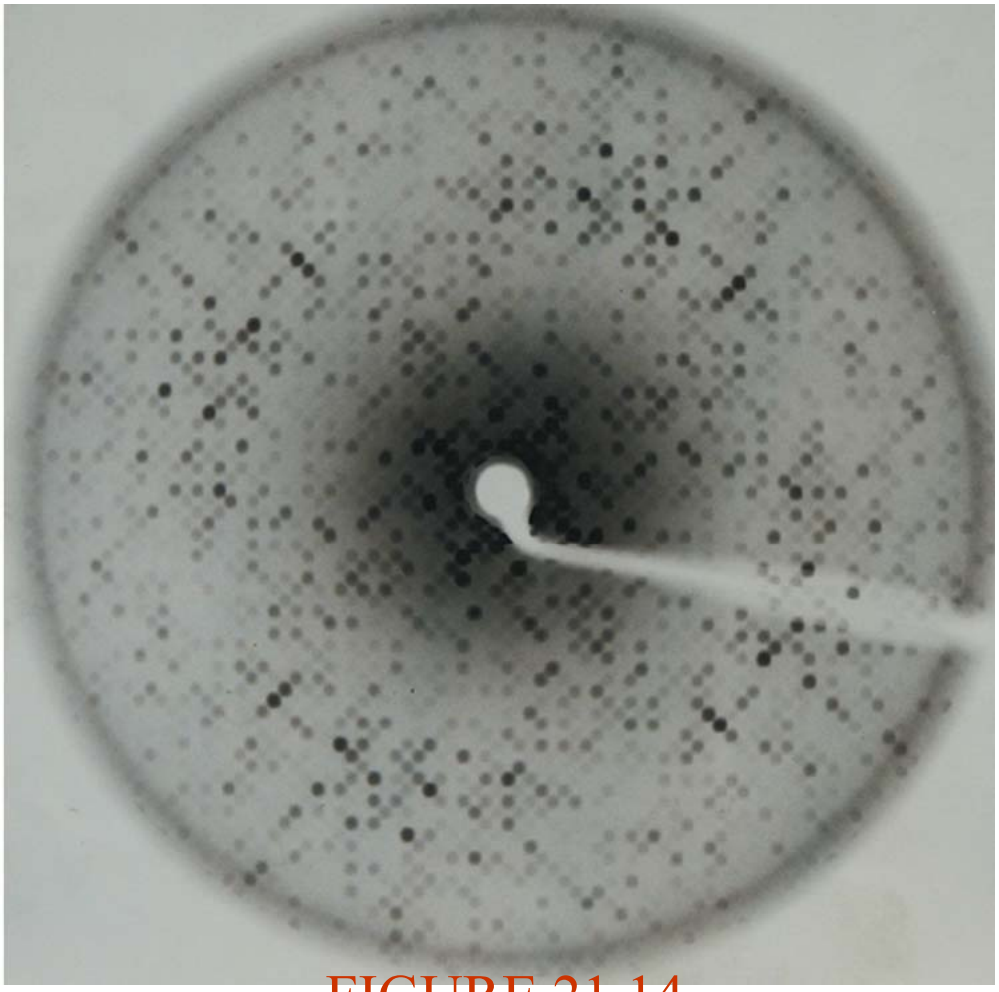

FIGURE 21.14

A diffraction image taken using the precession method is shown for the metalloprotein hemerythrin. All of the diffraction spots can be assigned indices h and k and $l = 0$.

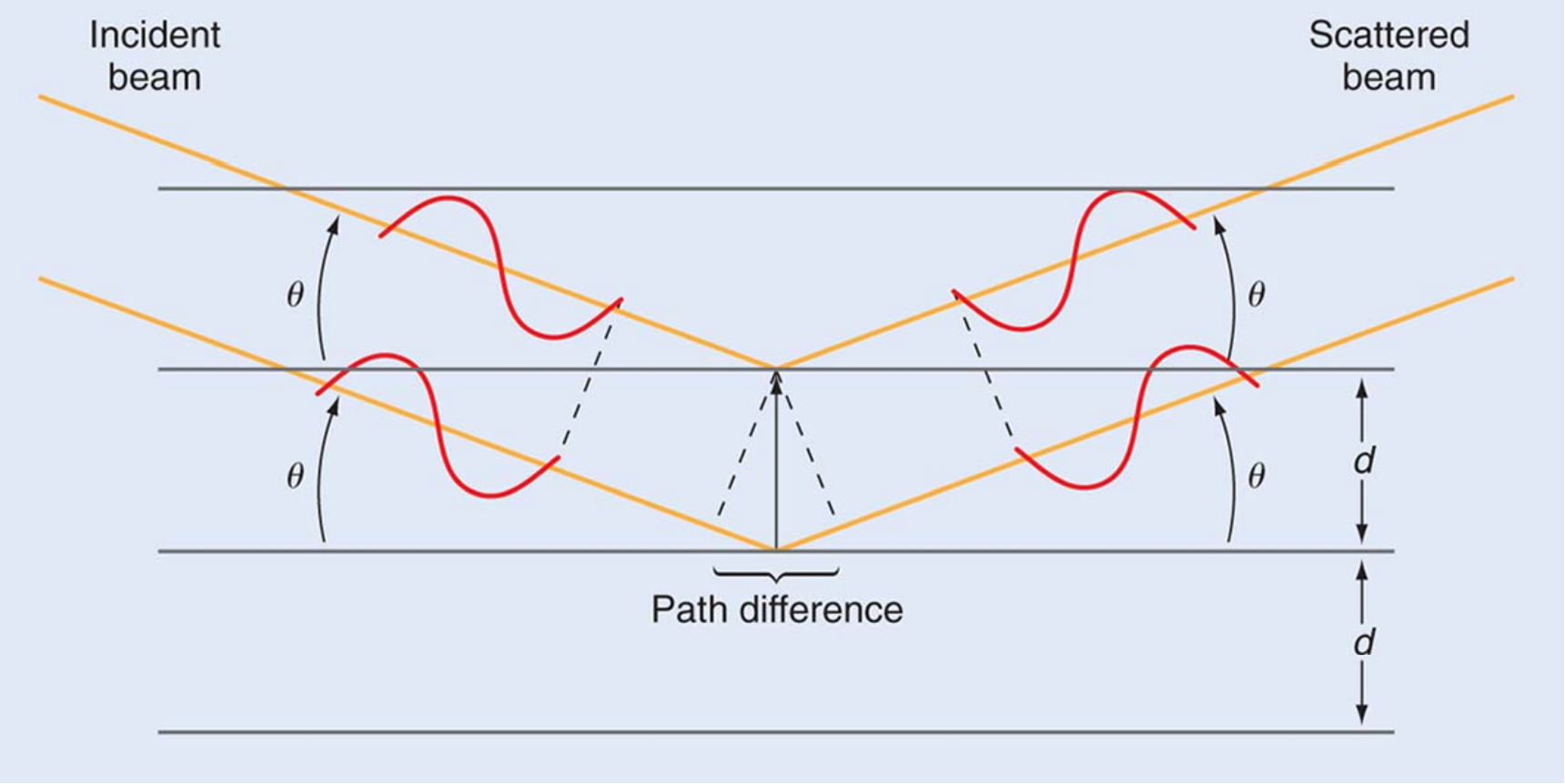

FIGURE 21.15

Diffraction from a set of parallel crystal planes is depicted. To simplify the drawing, the lattice motif is not shown. Diffraction or constructive interference is observed if the path difference between adjacent planes is an integral multiple of the X-ray wavelength.

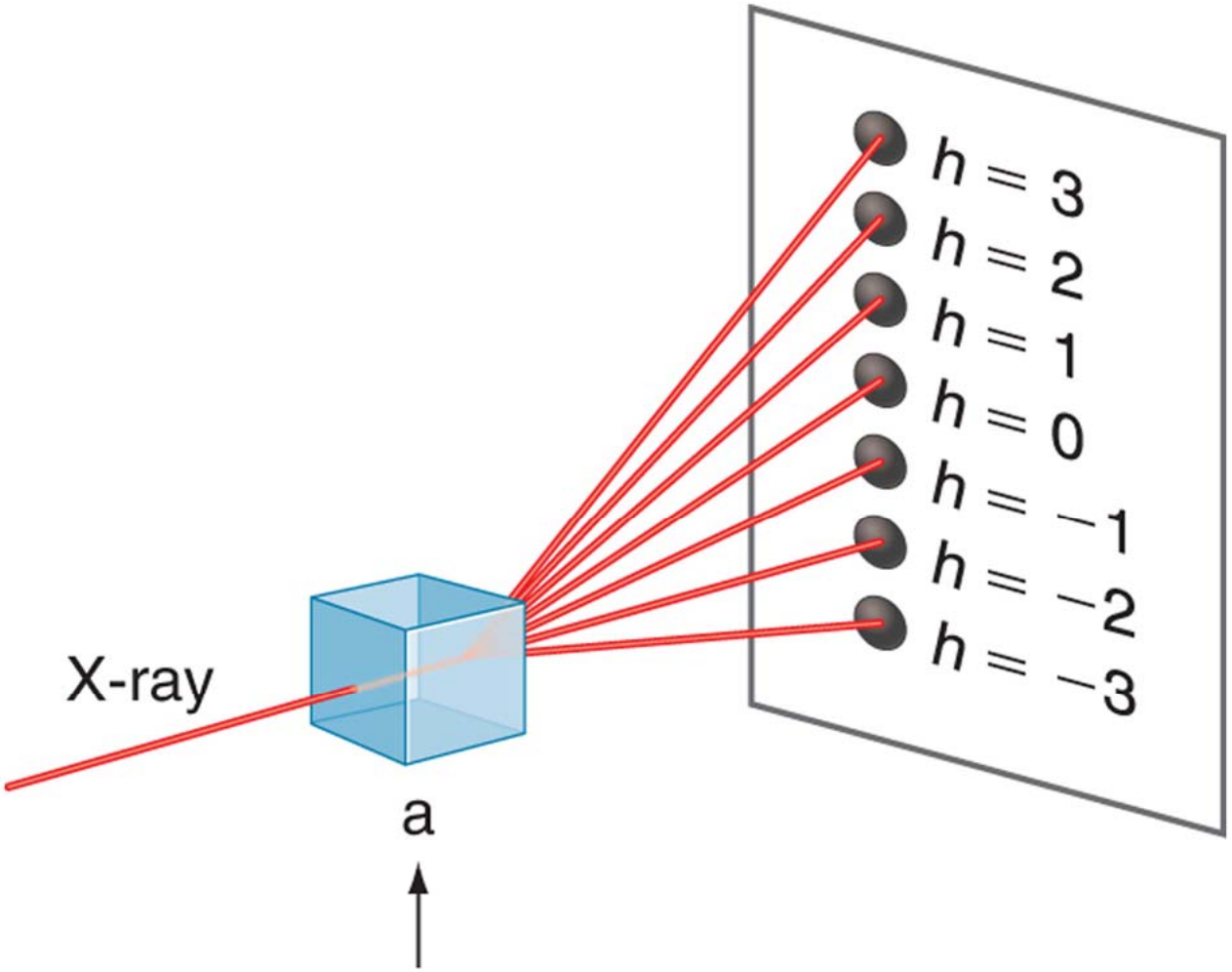

FIGURE 21.16

The diffraction pattern from the set of (100) planes is shown. Each spot corresponds to a different diffraction order.

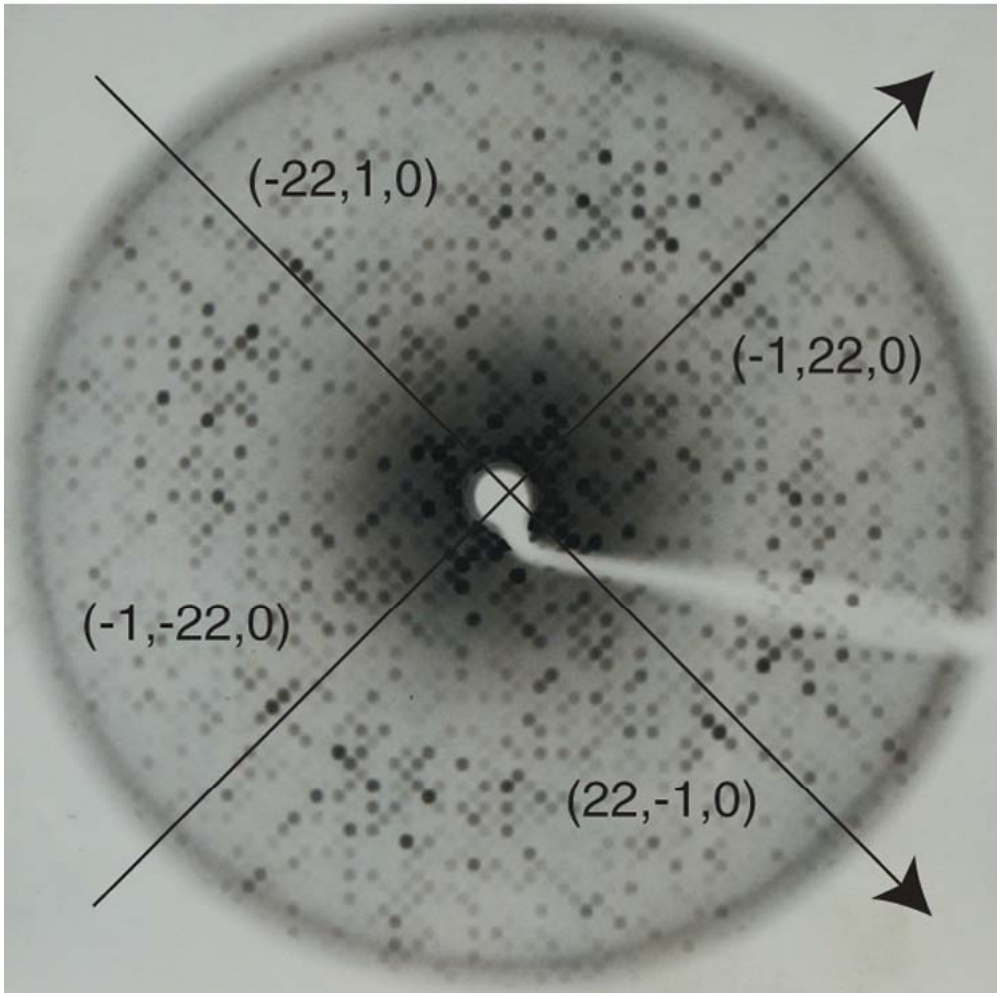

FIGURE 21.17

The diffraction pattern of Figure 21.14 with the indices of four planes giving rise to the diffraction spots is shown. On the basis of this indexing, the unit cell for hemerythrin has the dimensions $a = b = 8.66$ nm. The diffraction pattern obtained by rotating the crystal by 90° gives $c = 8.08$ nm.

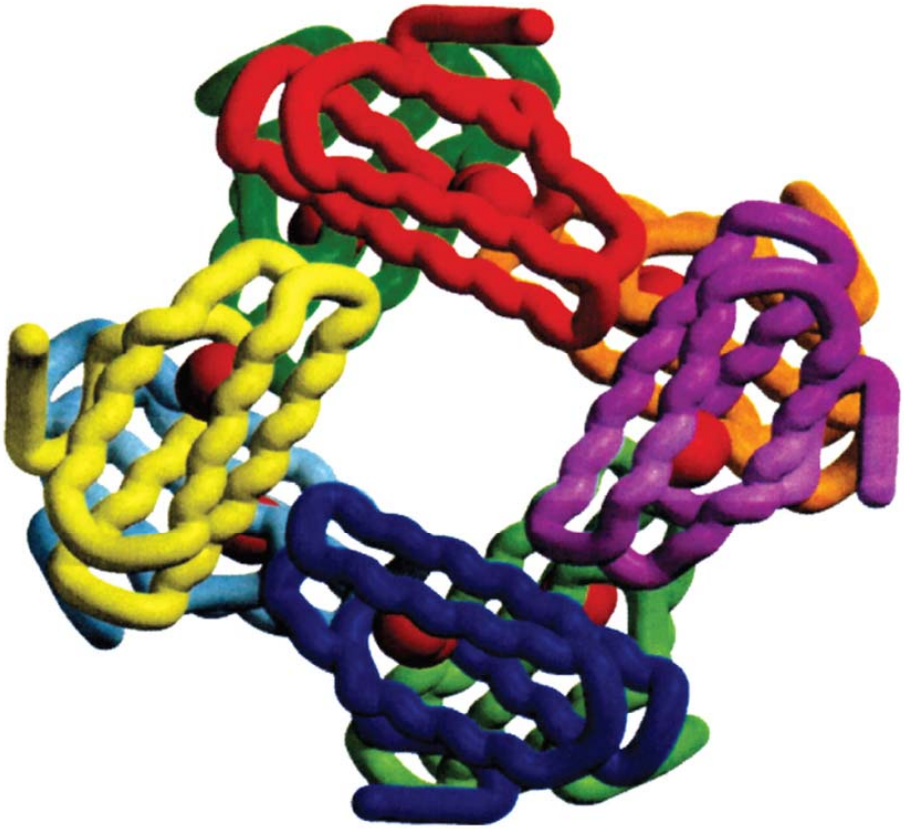

FIGURE 21.18

Hemerythrin consists of eight identical subunits, each of which is made up of a polypeptide containing 113 amino acids, two iron atoms (red spheres), and a single oxygen atom bridging the iron atoms. The polypeptide folds into four α-helices that pack in an antiparallel arrangement forming the tertiary structure of the subunit.

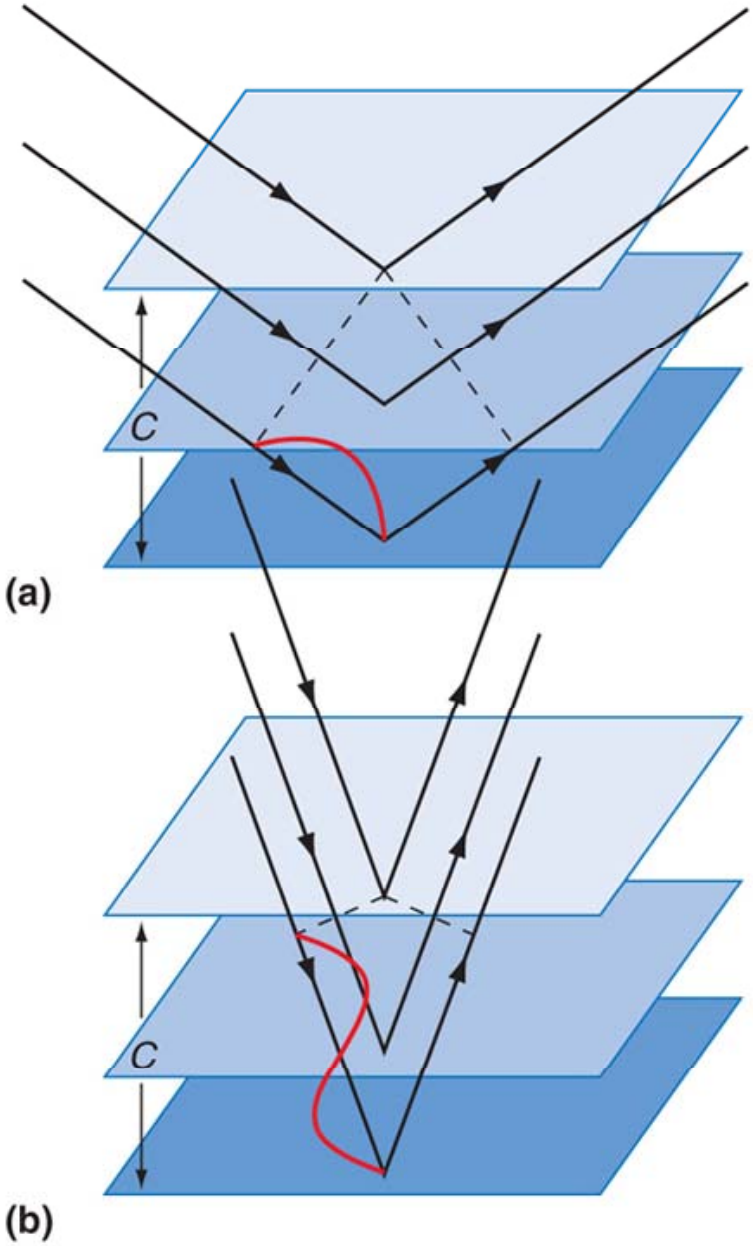

FIGURE 21.19

The top and bottom planes in (a) and (b) are (001) planes, and the middle plane is located somewhere between adjacent (001) planes. (a) At an angle corresponding to in-phaes scattering of the two (001) planes for $n = 1$, the difference in path length is one wavelength, so that the difference in phase angle is 2π. (b) At an angle corresponding to in-phase scattering of the two (001) planes for $n = 2$, the difference in path length is two wavelengths, so that the difference in phase angle is 4π.

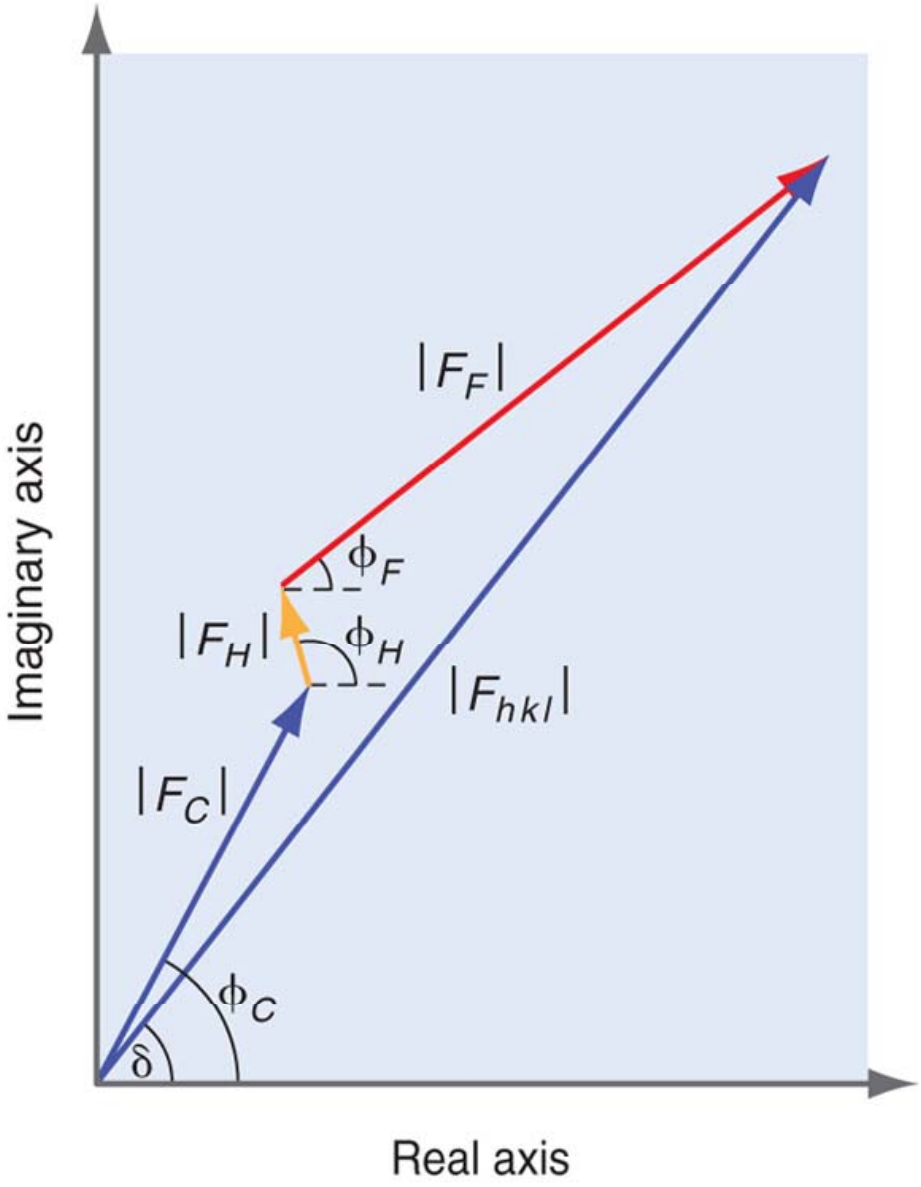

FIGURE 21.20

The scattering factor F_{hkl} can be represented as a vector in the complex number plane. It arises from vector addition of the individual scattering factors of the atoms in the unit cell, each of which has a magnitude proportional to its atomic number, and a phase determined only by the position of the atom in the cell. The superposition is shown for C. H, and F atoms.

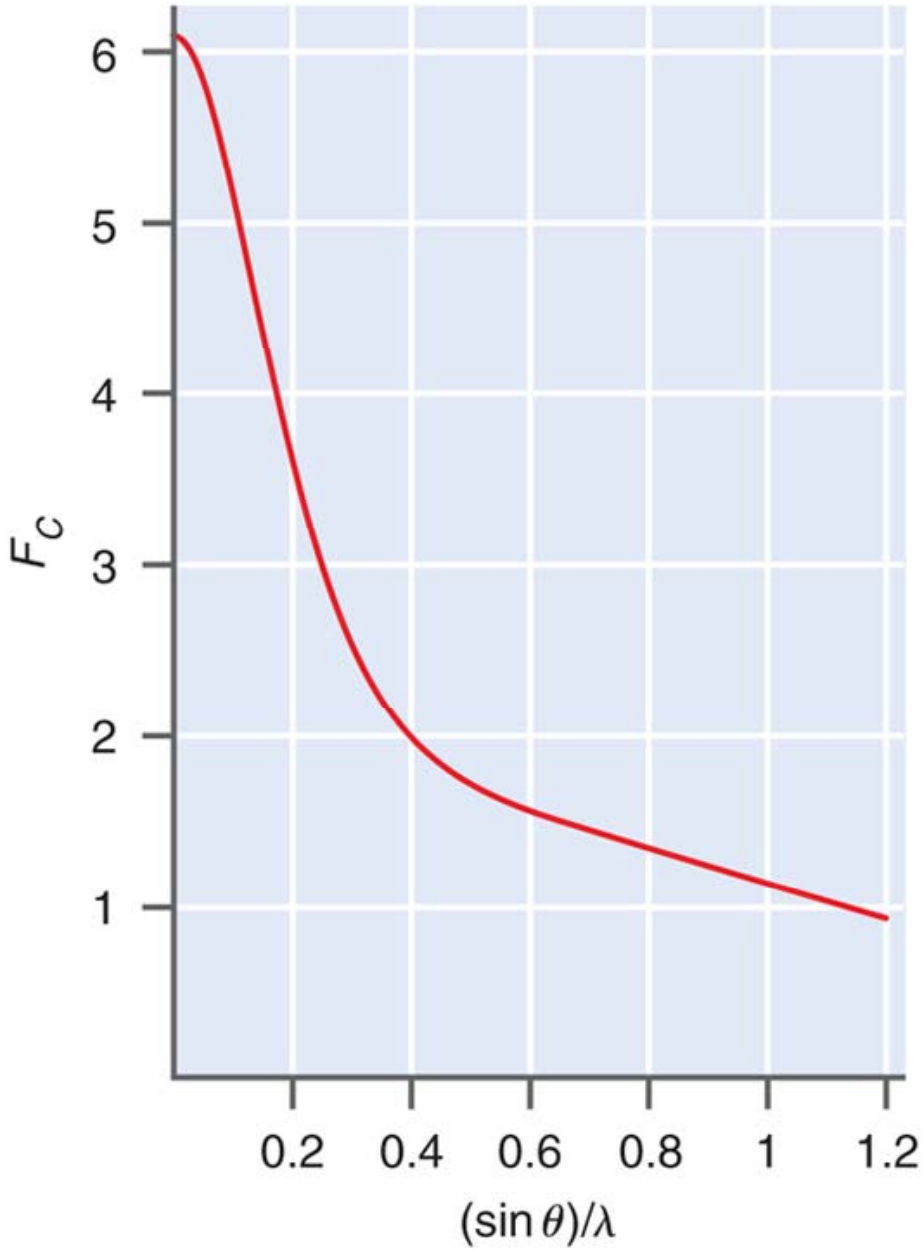

FIGURE 21.21

The magnitude of the scattering factor for atomic carbon is shown as a function of (sin θ)/λ.

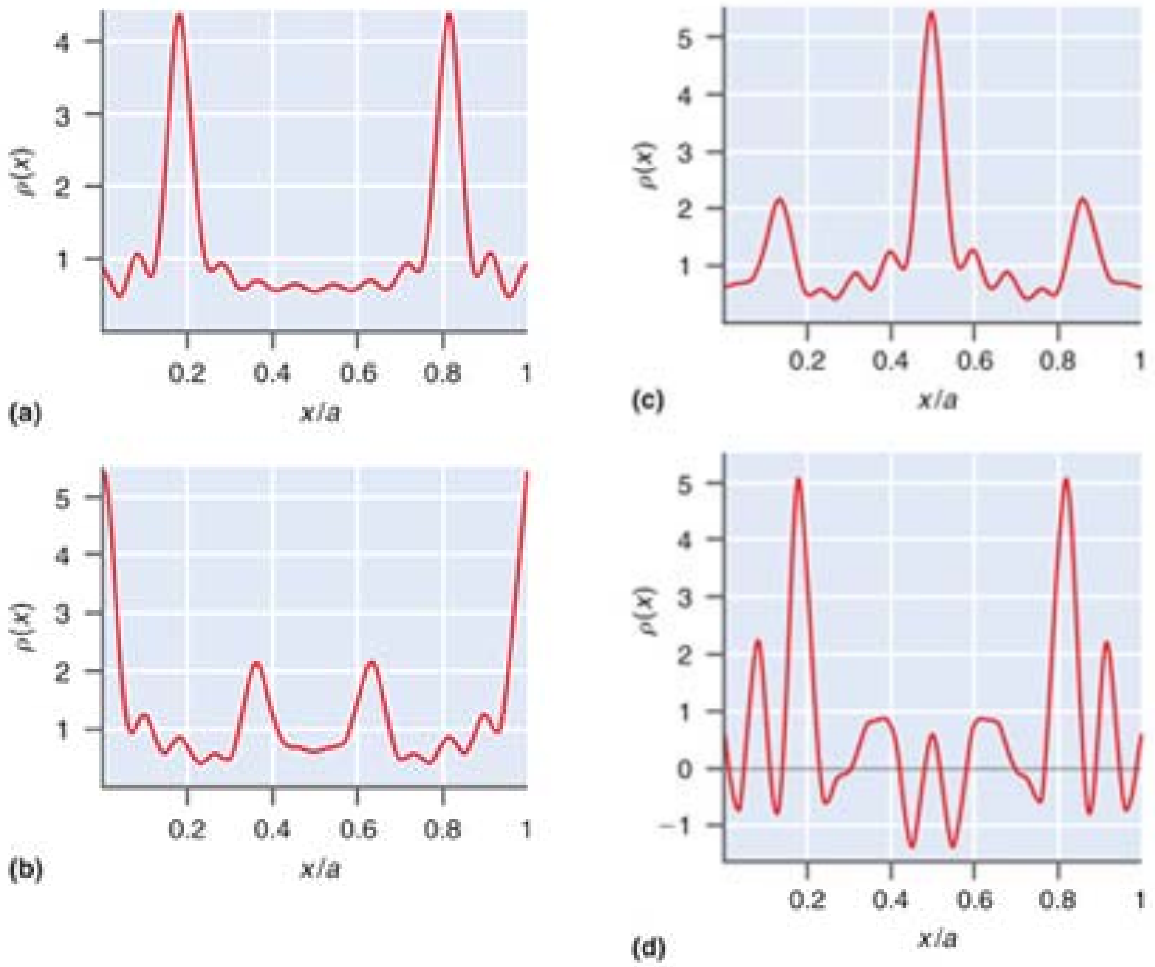

FIGURE 21.22

The electron density function calculated from the F_h in Table 21.1 is shown (a) for the correct phases, (b) for all phases set equal to 0, (c) for the phases set alternately equal to 0 and π, and (d) for the correct phases but with all f_C set equal to 6.

TABLE 21.1 Calculating for f_C and F_h for Diffraction from the One-Dimensional Lattice Discussed in the Text

h	$\sin\theta$	f_C	F_h
0	0	6.00	12.0
±1	0.077	5.63	4.58
±2	0.154	4.89	−6.54
±3	0.231	4.23	−8.04
±4	0.308	3.65	−0.769
±5	0.385	3.15	5.44
±6	0.463	2.72	4.39
±7	0.504	2.35	−0.968
±8	0.617	2.04	−3.99
±9	0.694	1.79	−2.11
±10	0.771	1.59	1.58
±11	0.848	1.43	2.85
±12	0.925	1.31	0.818

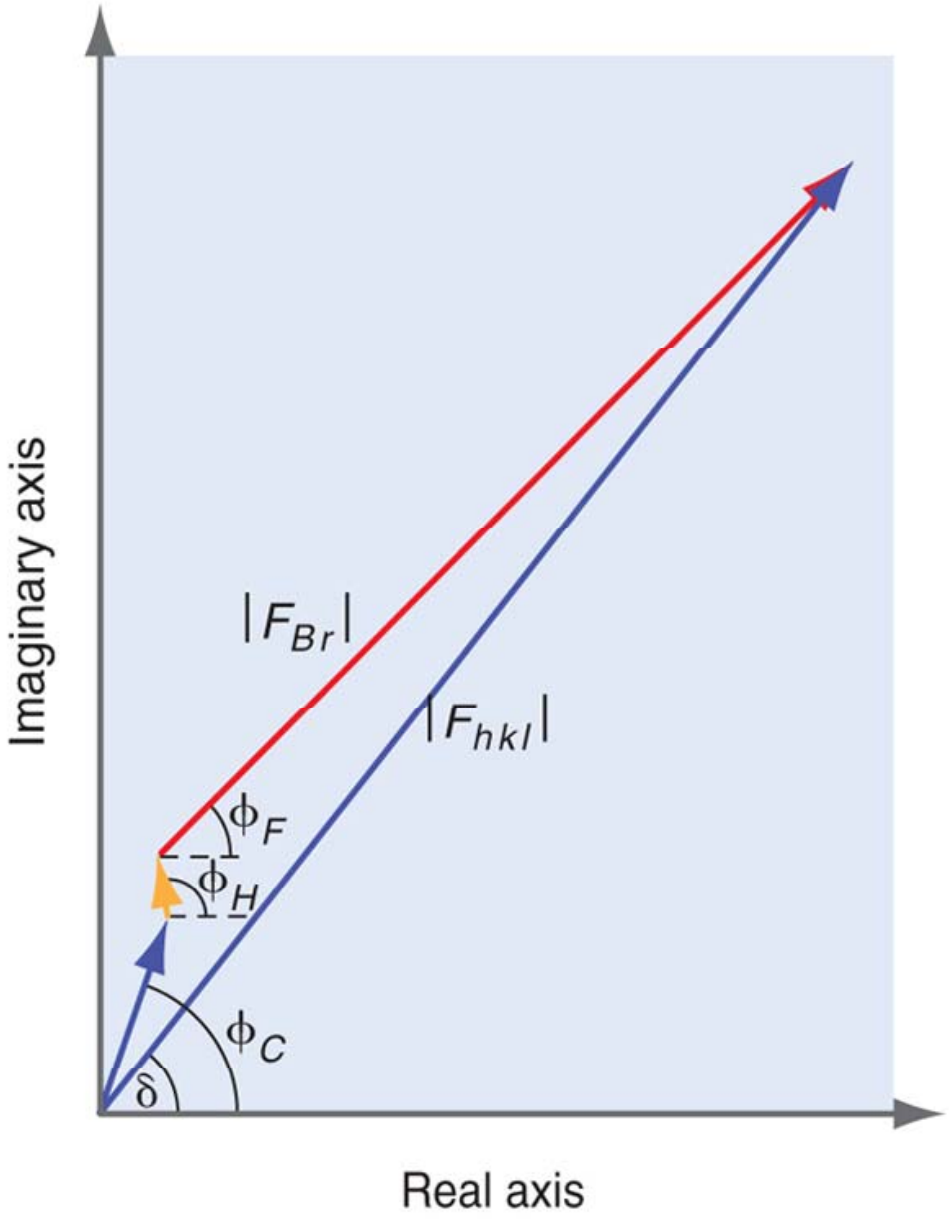

FIGURE 21.23

Figure 21.20 is redrawn after a Br atom is substituted in place of the F atom. It is seem that $|F_{hkl}|$ is largely determined by the Br atom.

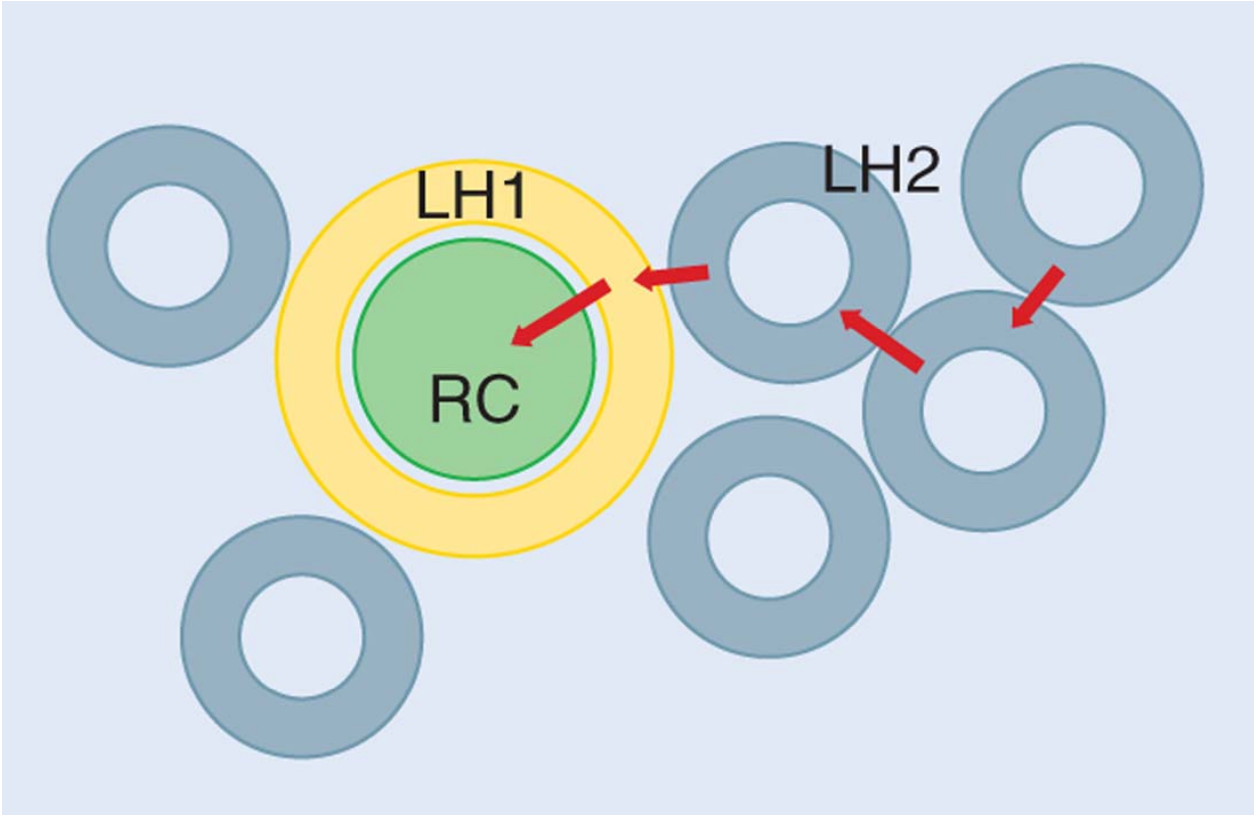

FIGURE 21.24

The transmembrane units involved in purple bacterial photosynthesis are shown looking down on the membrane surface. Light is captured by two light-harvesting systems, designated LH1 and LH2. The harvested energy is transferred to the reaction center (RC) where ATP synthesis is initiated. The orange arrows indicate energy transfer from LH2 to LH1, and from LH1 to the reaction system.

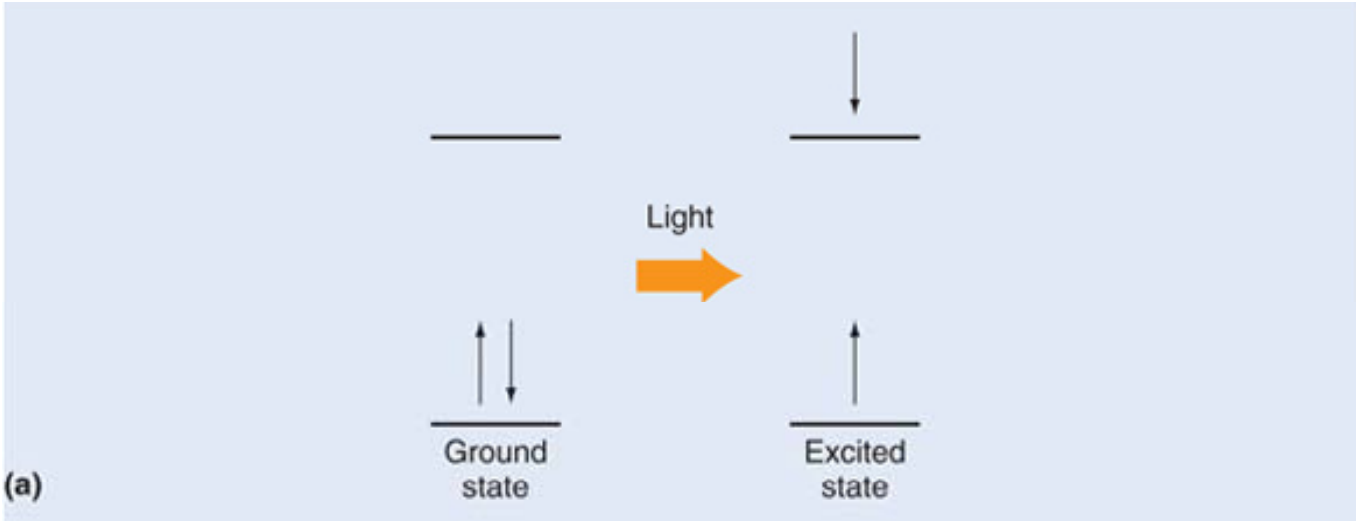

FIGURE 21.25

(a) Light absorption in LH1 and LH2 occurs through electronic excitations. (b) Energy can also be transferred from one molecule to another through an electron transfer (redox) reaction.

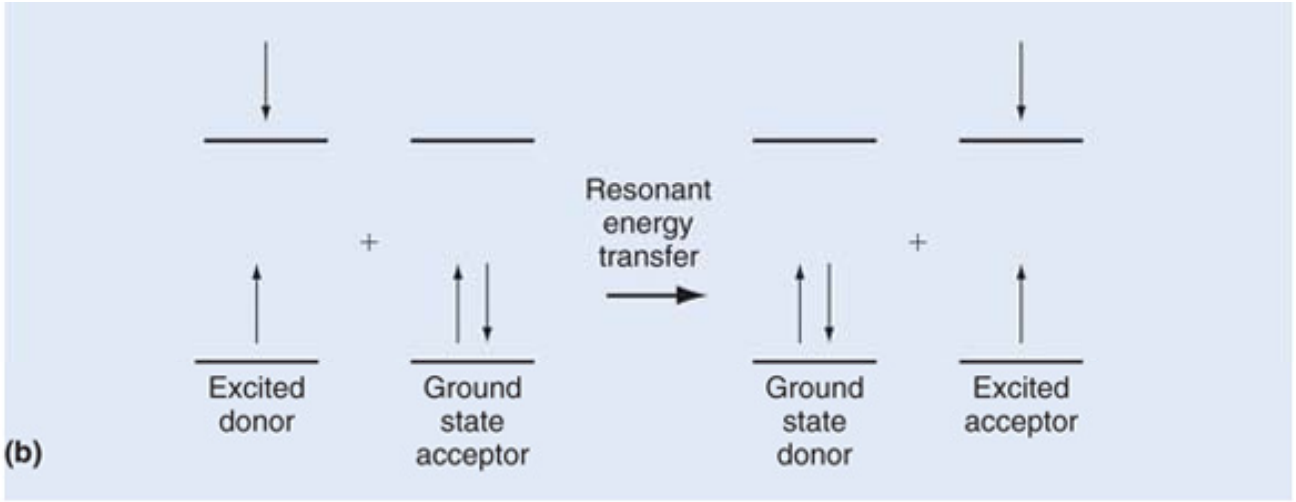

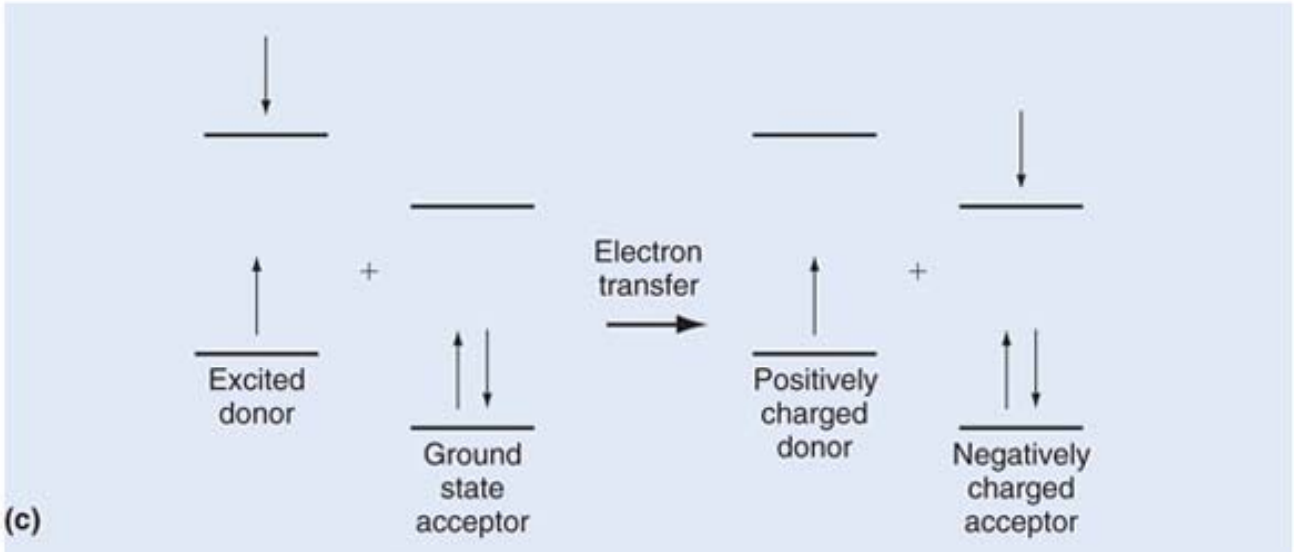

FIGURE 21.25

(continued)

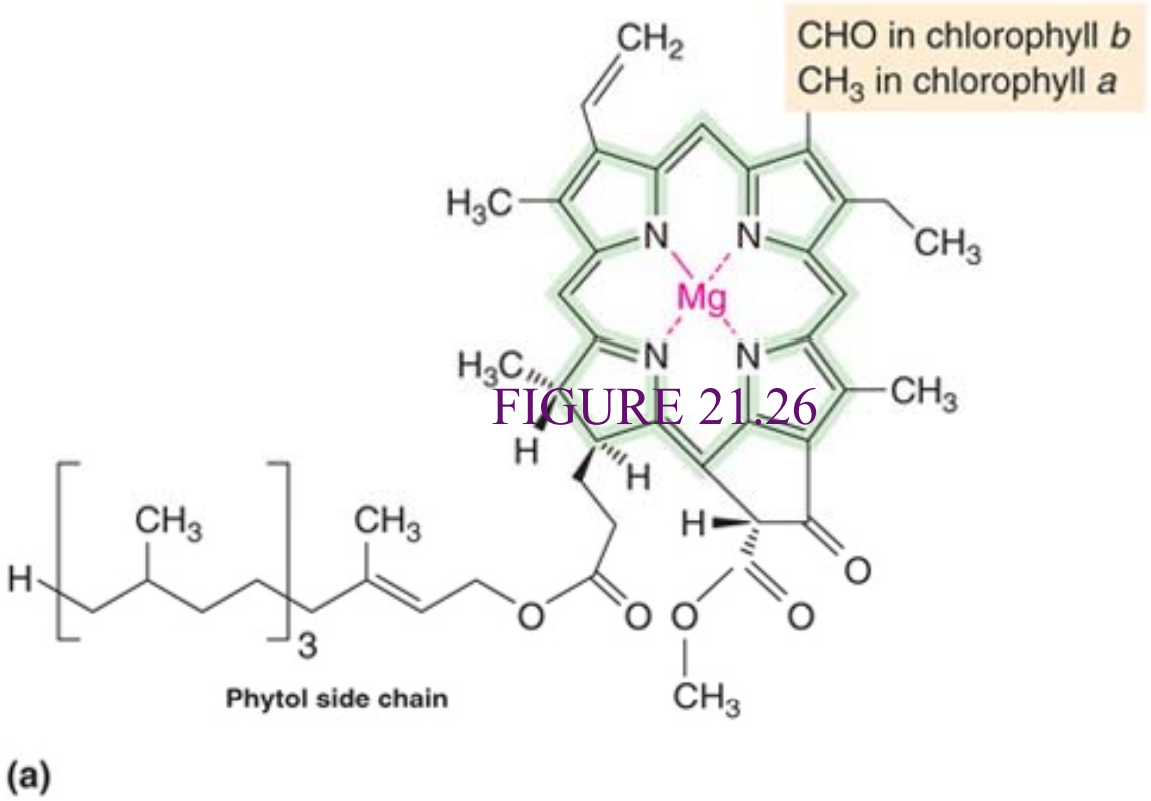

FIGURE 21.26

FIGURE 21.26

(a) Chlorophylls *a* and *b* and bacteriochlorophyll are the primary light absorbers in photosynthesis. The shading indicates the conjugated π-electron network. (b) β-cartene and (c) phycocyamin are examples of additional pigments that also absorb sunlight.

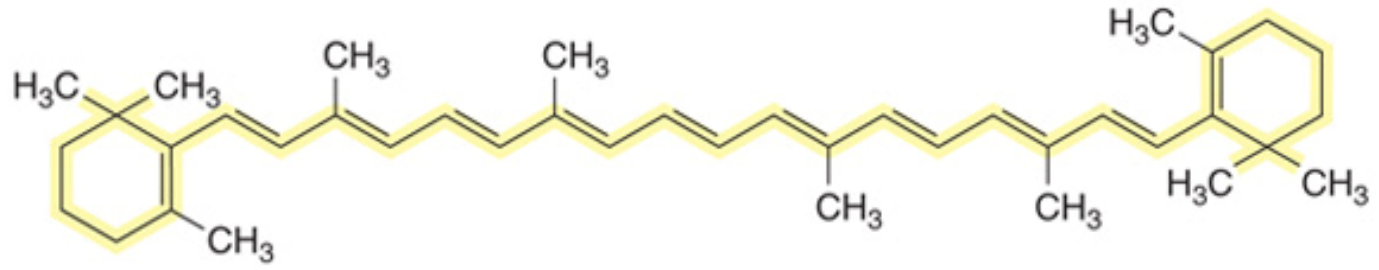

(b)

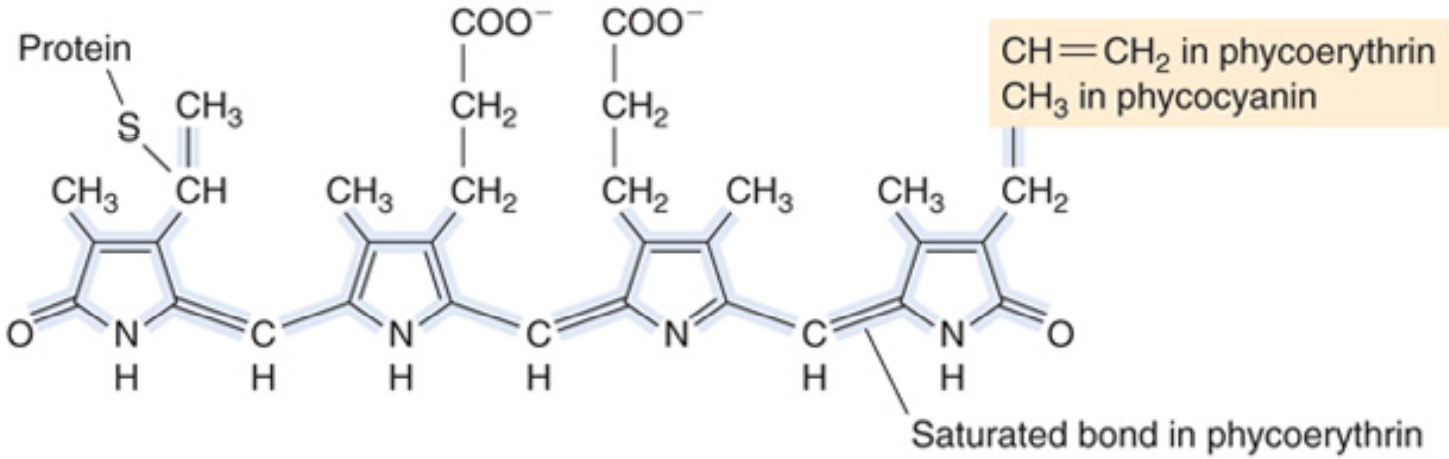

(c)

FIGURE 21.26

(continued)

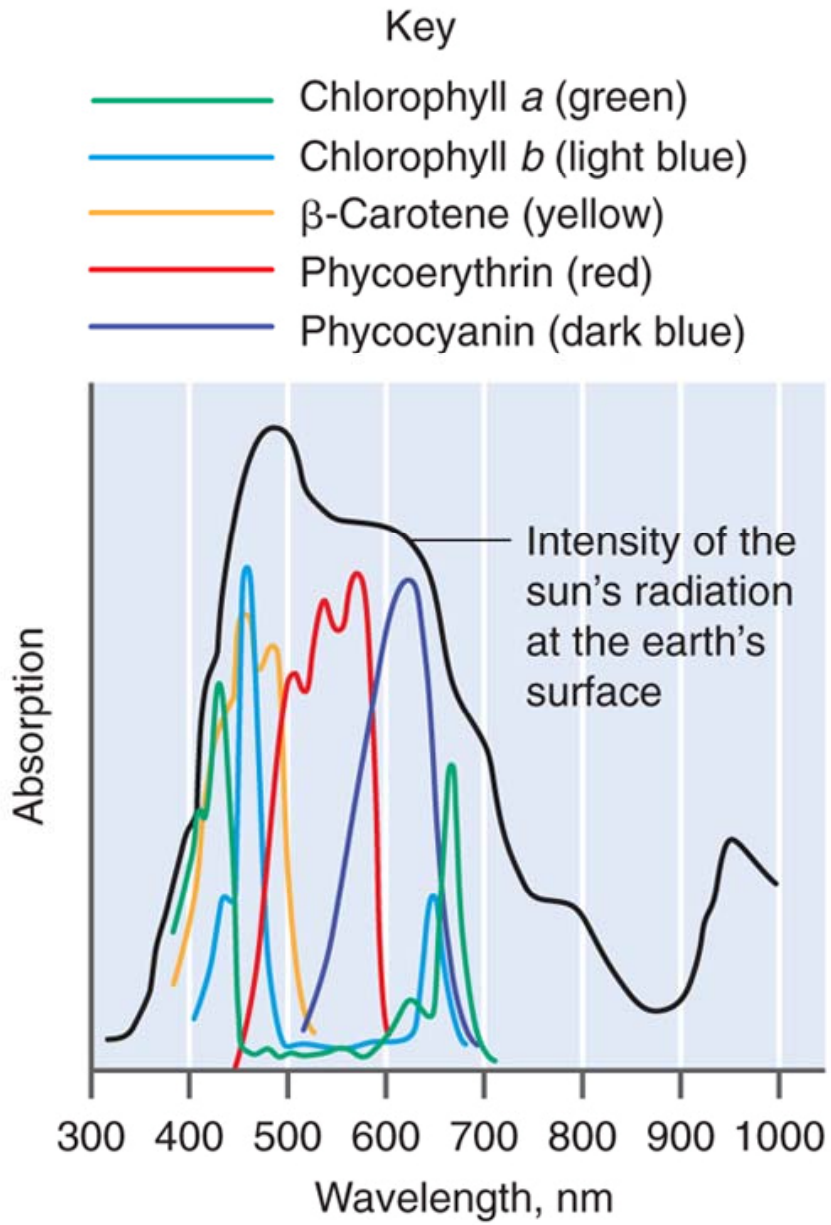

FIGURE 21.27

The colored curves show the absorption spectrum of the light absorbers shown in Figure 21.26. The black curve shows the wavelength distribution in sunlight.

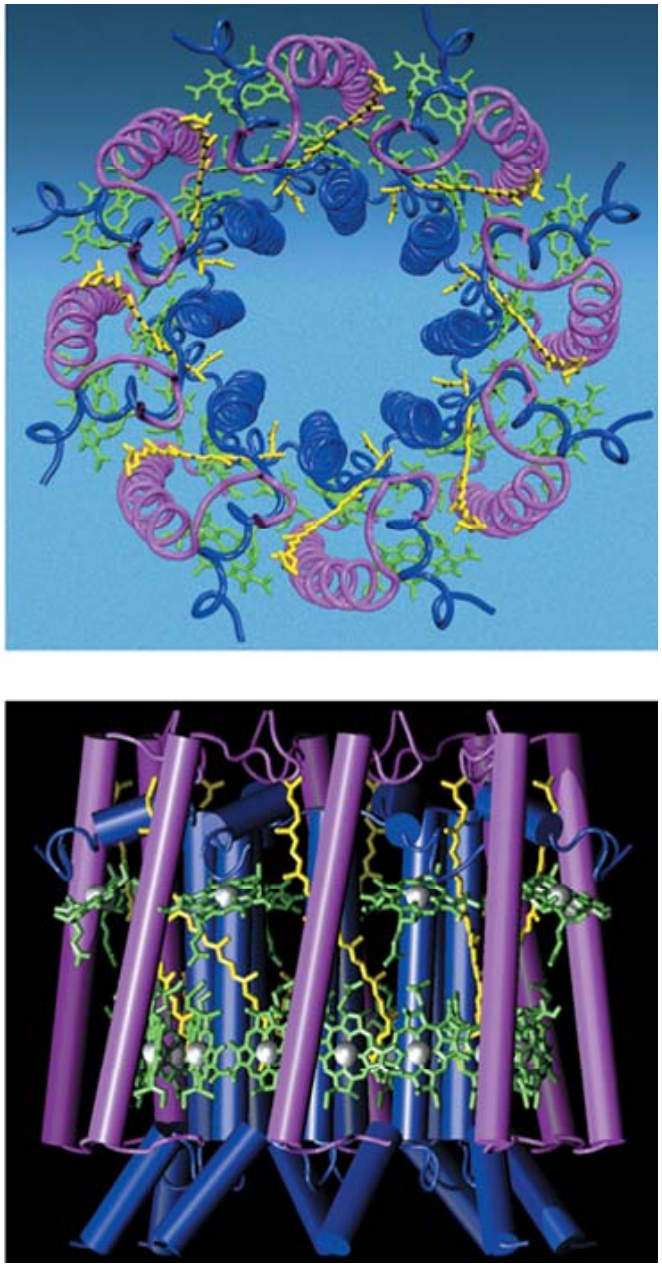

FIGURE 21.28

The LH2 complex of *Rhodospirillum molischianum* is shown in (a) atop view and (b) a side view. The α and β membrane-spanning helices are shown in blue and magenta, respectively. The Bchl-a molecules are shown in green and their phytol tails have been omitted for clarity. The additional lycopene photopigments are shown in yellow. In (b), the membrane-spanning α-helices are shown as rods.

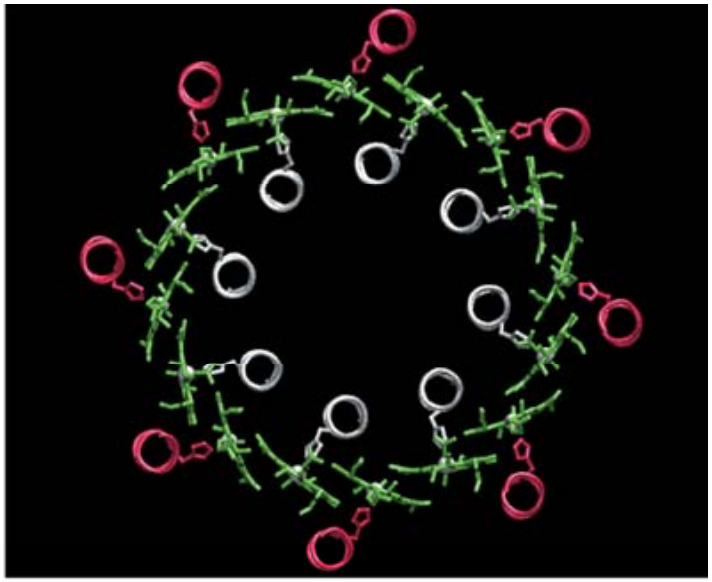

(a)

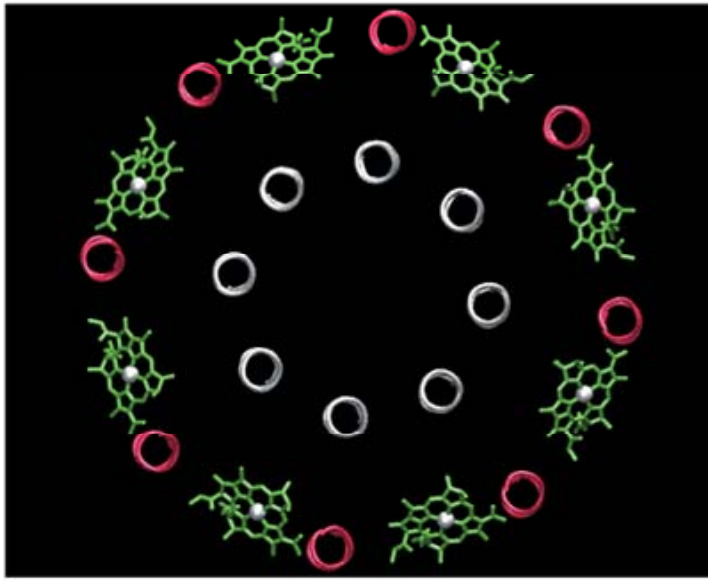

(b)

FIGURE 21.29

The orientation of the Bchl-*a* molecules relative to the LH2 unit is shown. (a) Sixteen Bchl-*a* molecules are situated in the space between the outer and inner cylindrical arrays. The plane of the these Bchl-*a* molecules is oriented perpendicular to the membrane surface. (b) Eight Bchl-a molecules is tilted by 38° with respect to the membrane surface.

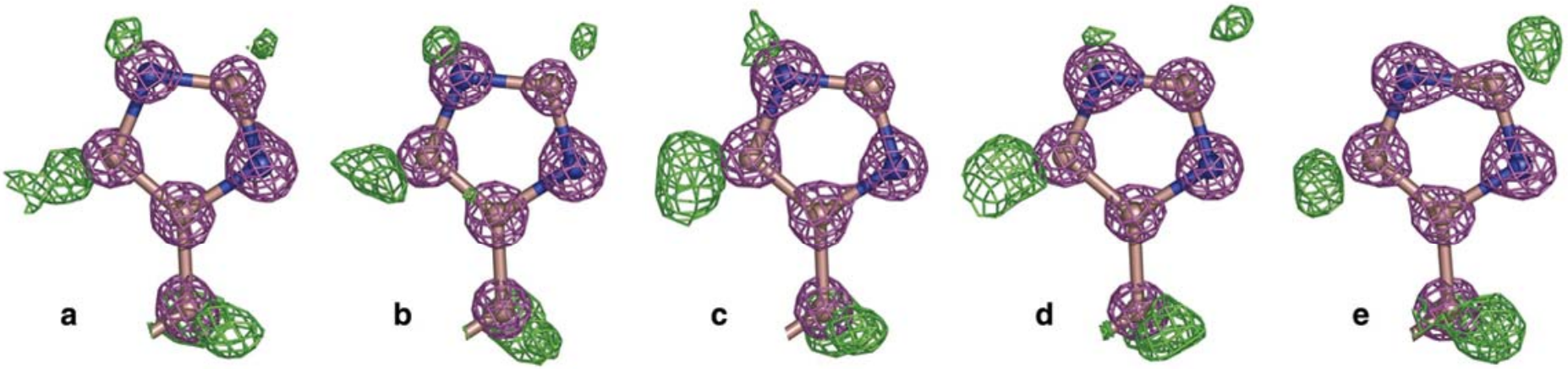

FIGURE 21.30

The protonation state of His447 is shown for various pH values. Note changes in the region labeled NE2 as the pH changes takes on the values (a) 5.2, (b) 5.8, (c) 7.3, and (d) 9.0. Part (f) shows that the negative change left on the imidazole ring by removal of the H on NE2 is stabilized by hydrogen bonds formed to the nitrogen ND1.

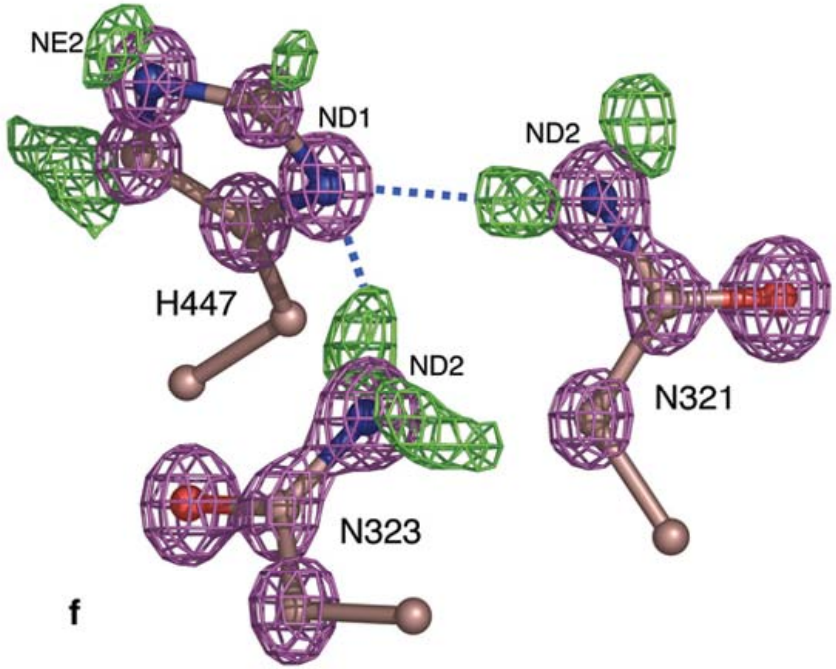

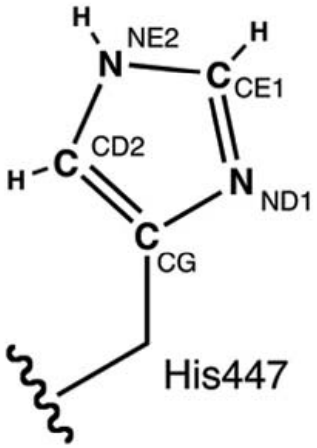

FIGURE 21.30

(continued)

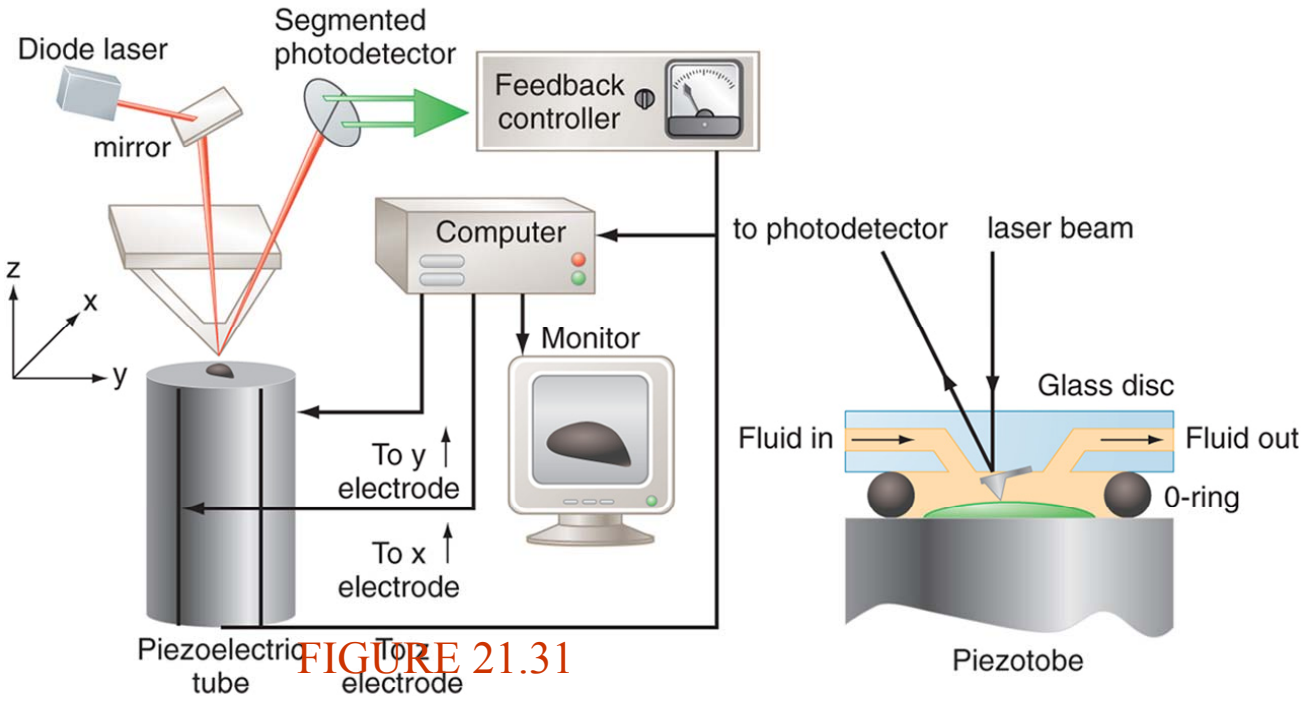

FIGURE 21.31

Schematic diagram of an atomic force microscope. (a) A tip mounted on a microfabricated cantilever is scanned over a surface in the x-y plane by applying dc voltages to a segmented piezoelectric tube. If the tip experiences an attractive or repulsive force from the surface, the cantilever is deflected from its horizontal position. As a result, the laser light reflected from the back of the cantilever onto a segmented photodetector is differently distributed on the segments, giving rise to a difference current, which is the input to a feedback controller. The controller changes the length of the piezoelectric tube in such a way to keep the cantilever deflection constant as the tip scans across the surface. Therefore, the surface image obtained corresponds to a constant force that can be varied using the feedback circuit. (b) The AFM can be modified to allow measurements in a liquid or controlled atmosphere using an O-ring seal mounted on the piezoelectric tube.

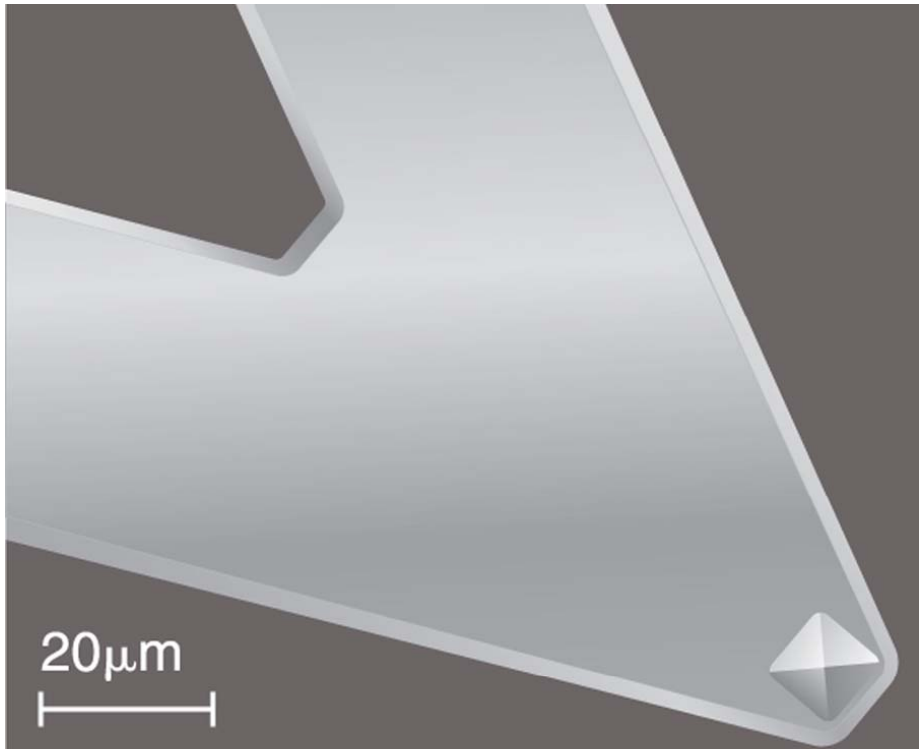

FIGURE 21.32

Image of a cantilever obtained with a scanning electron microscope. The arrow indicates the position of the tip. (Based on work by the NTUF)

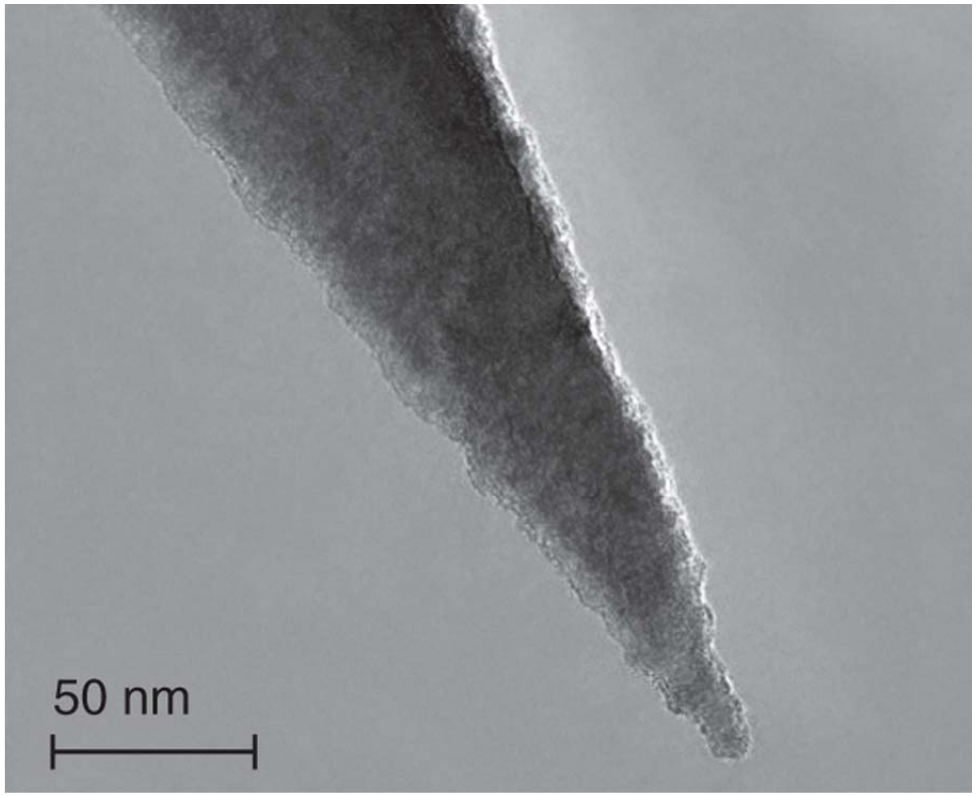

FIGURE 21.33

Electron microscope images of a tip typically used in atomic force microscopy. A radius of curvature of 10 to 20 nm can be routinely obtained.

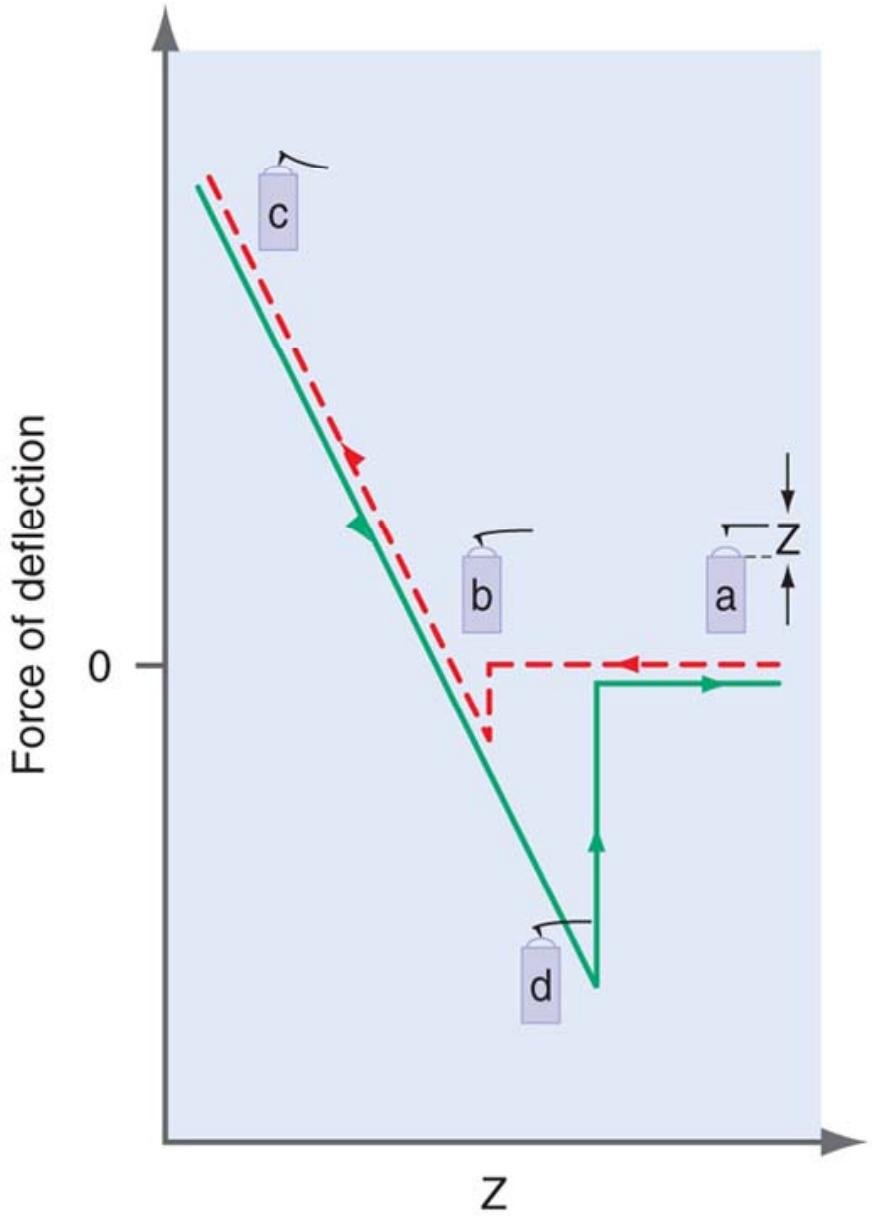

FIGURE 21.34

In an approach diagram, the cantilever deflection or force is shown as a function of the distance between the cantilever base and the sample surface. At large distances (a), the attractive force between the tip and surface is insufficient to cause a downward cantilever deflection. At a distance corresponding to (b), the attractive force is strong enough to deflect the cantilever until the tip and surface are in contact. At smaller distances where the force is repulsive, the cantilever is deflected away from the surface and applied force increase linearly with the deflection.

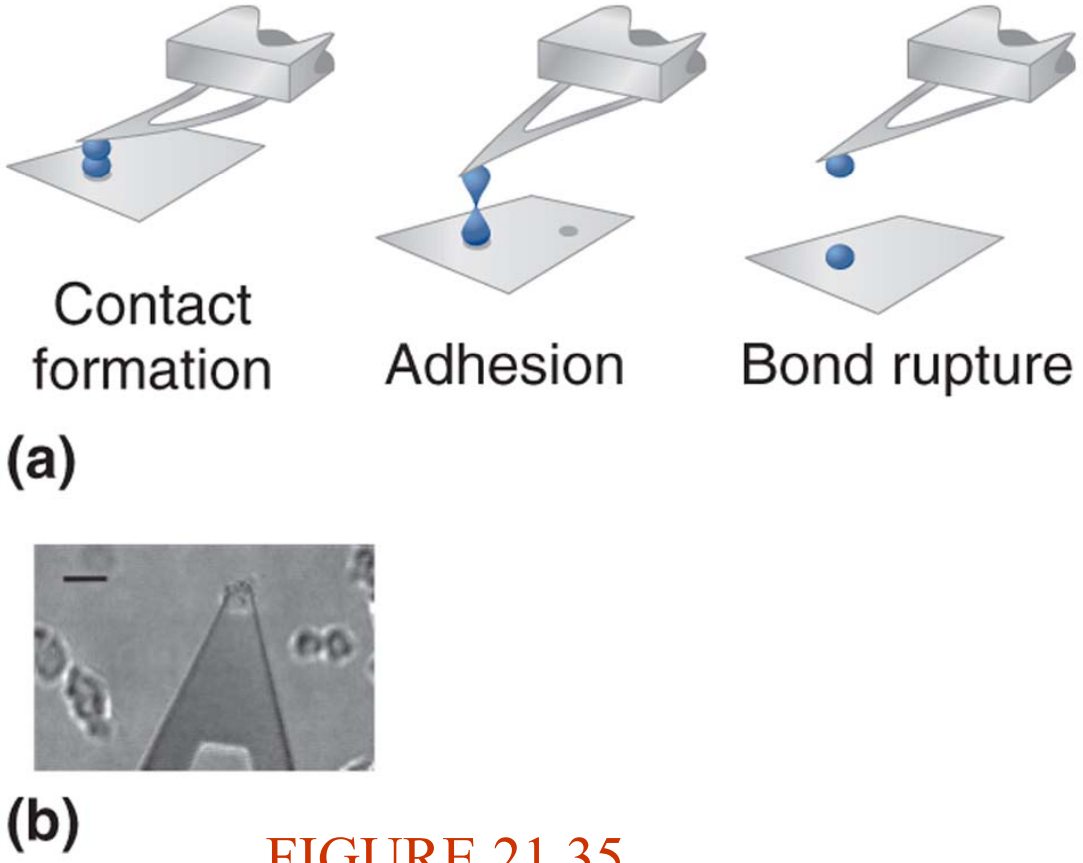

FIGURE 21.35

(a) The left panel shows contact formation between the cells on the substrate and the cantilever. (b) As *z* is increased (middle panel in part a), the contact areas is stretched and the bond is ruptured if the deflection force is sufficiently high (right panel in part a). The black bar corresponds to a distance of 20 μm.

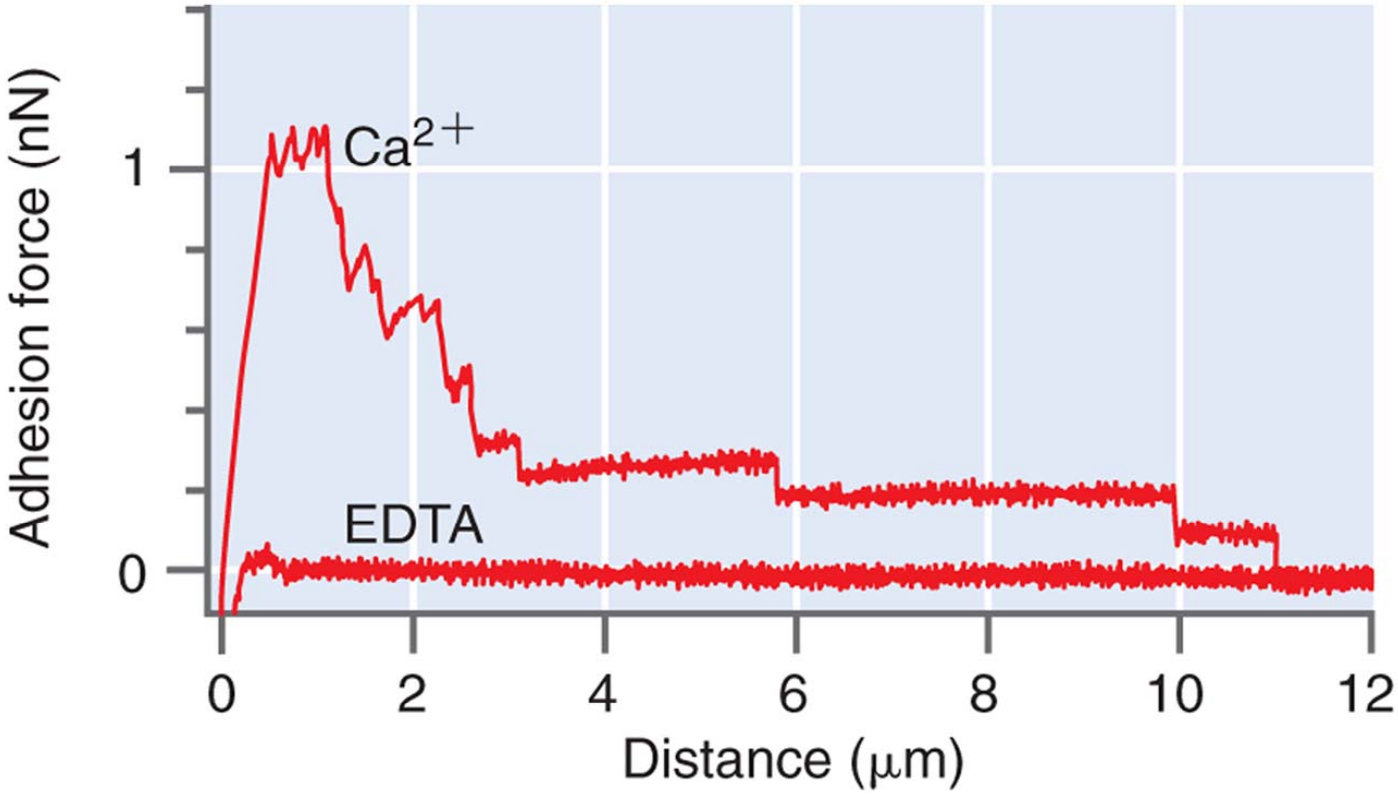

FIGURE 21.36

The measurement of adhesion force for *D. discoideum* cells is depicted. Contact between the cells immobilized on the substrate and cantilever was maintained for 20 s at a force of 150 pN. The cells were pulled apart as a rate of 1.5 μm s^{-1}.

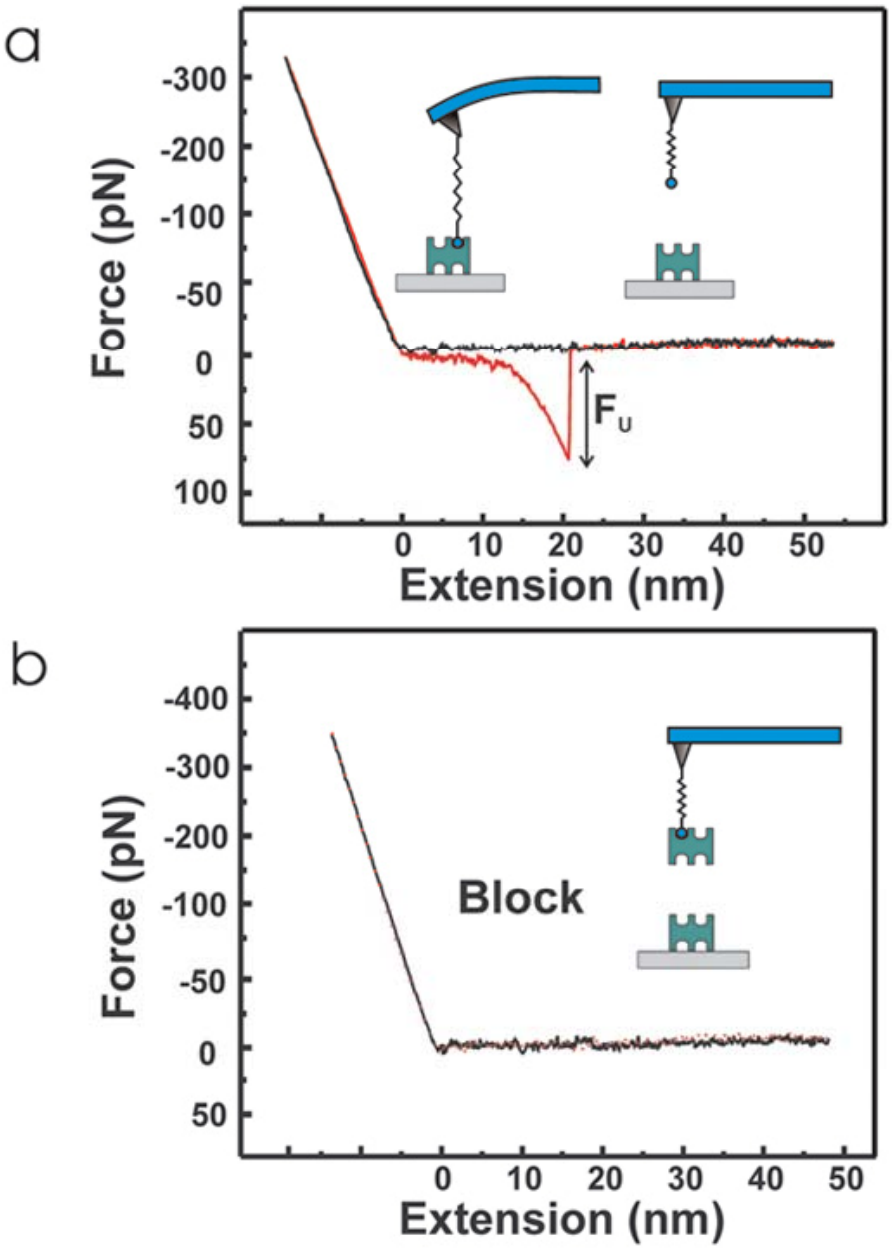

FIGURE 21.37

(a) A strong unbinding event is observed as the tip is withdrawn after having been brought into vontact with the surface (red trace). (b) If the biotin on the tip is saturated with avidin added to the solution, the unbinding event is not seen.

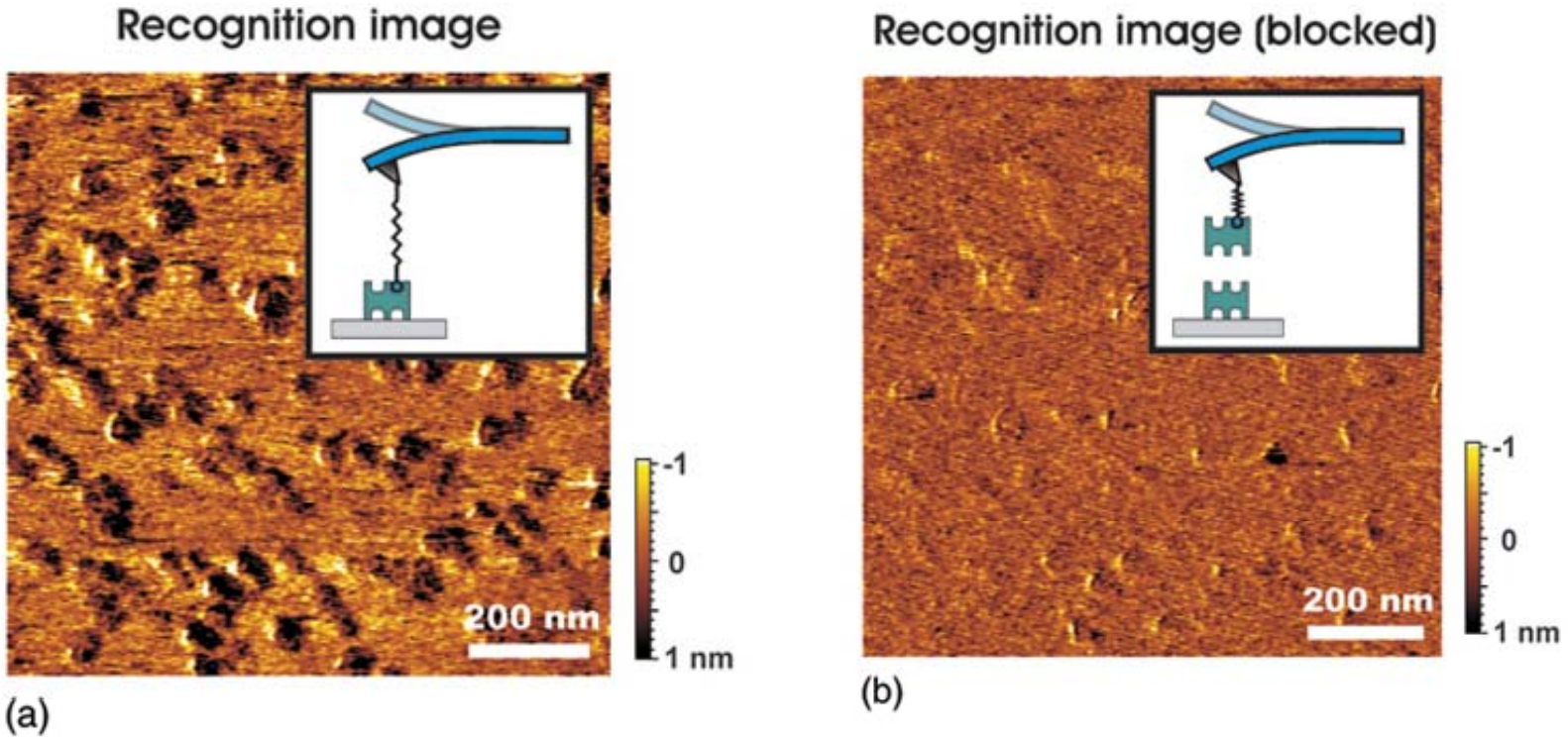

FIGURE 21.38

(a) Scanning a functionalized tip over a surface with binding sites gives an image that reflects both variations in local force and variations in height. (b) If the biotin on the tip is bound by avidin added to the solution, only variations in the surface height are seen.

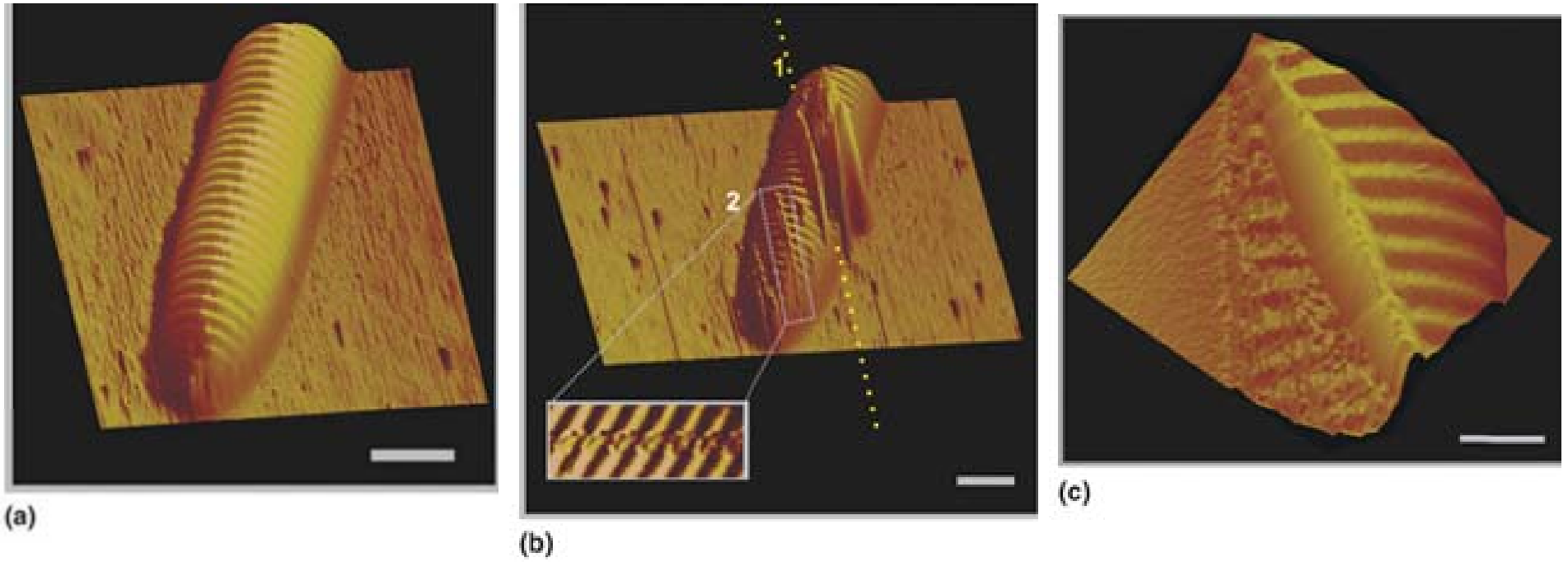

FIGURE 21.39

(a) The intact collagen fibril of ~210 nm diameter is seen prior to nanodissection. (b) The line labeled 1 shows an incision that is ~140 nm deep. The line labeled 2, also shown magnified in the box, is ~2 nm deep. (c) A three-dimensional height image of the dissected area is seen. The cross-section shows parallel-aligned fibrillar subcomponents. The scale bar 1 μm in length.

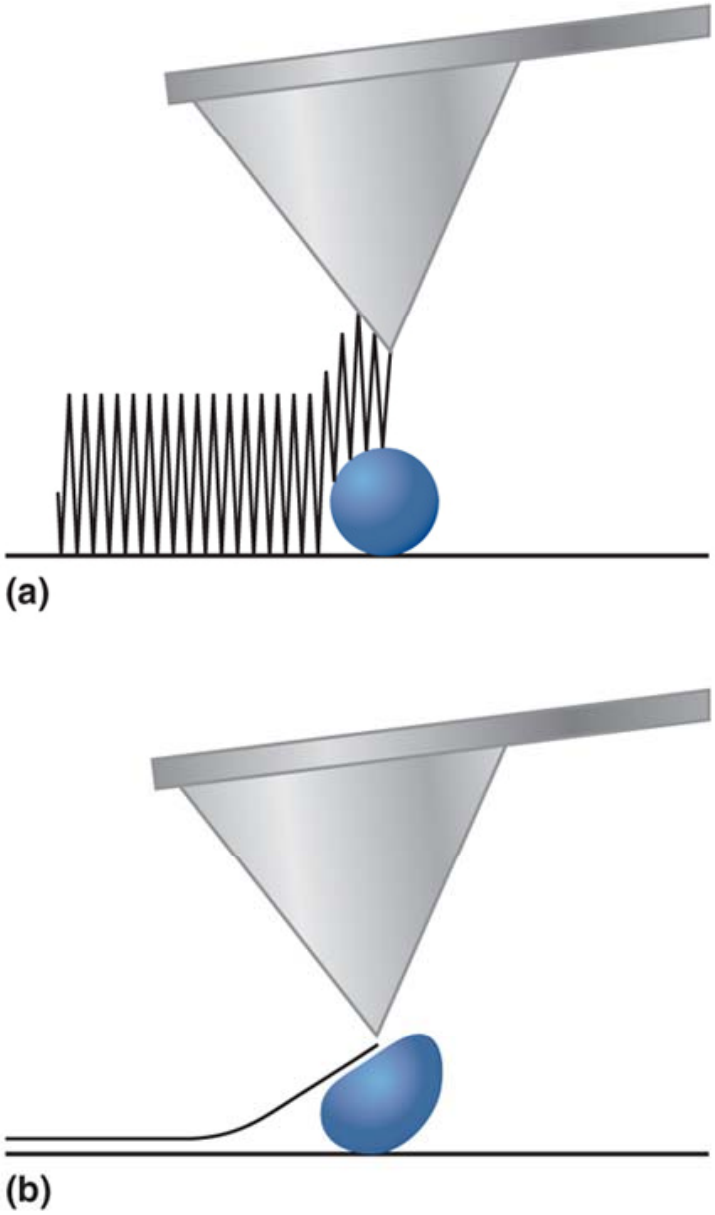

FIGURE 21.40

(a) In the intermittent contact mode, the cantilever is vibrated at its resonance frequency and touches the surface for a small fraction of the time needed for a scan. (b) The contact mode is suitable for hard surfaces, but can lead to reversible or irreversible deformation of a soft sample as shown.

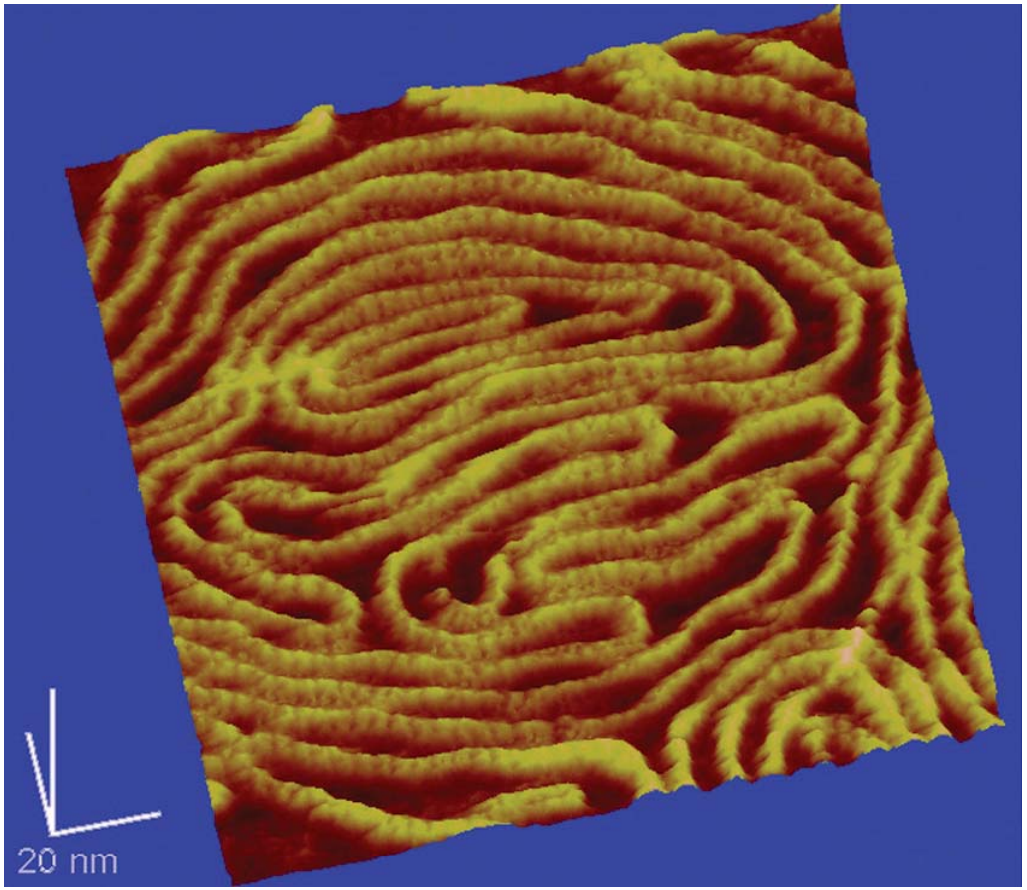

FIGURE 21.41

High-resolution image of DNA obtained in the intermittent contact mode. The DNA was immobilized by binding it to cationic bilayers on mica.

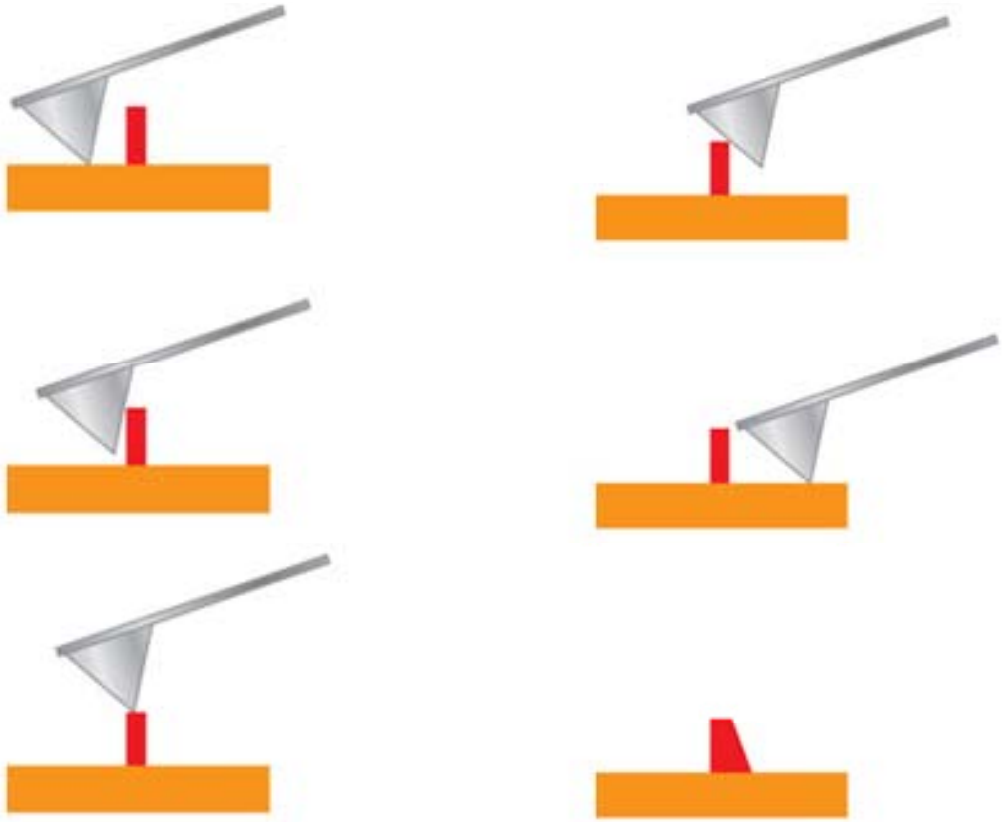

FIGURE 21.42

The apparent size of a scanned object in the scanning plane is a convolution of the tip shape with the object shape. The top five images show the positions that a cantilever will take while scanning over the surface feature shown in red. The bottom image shoes the apparent shape obtained from the scan.

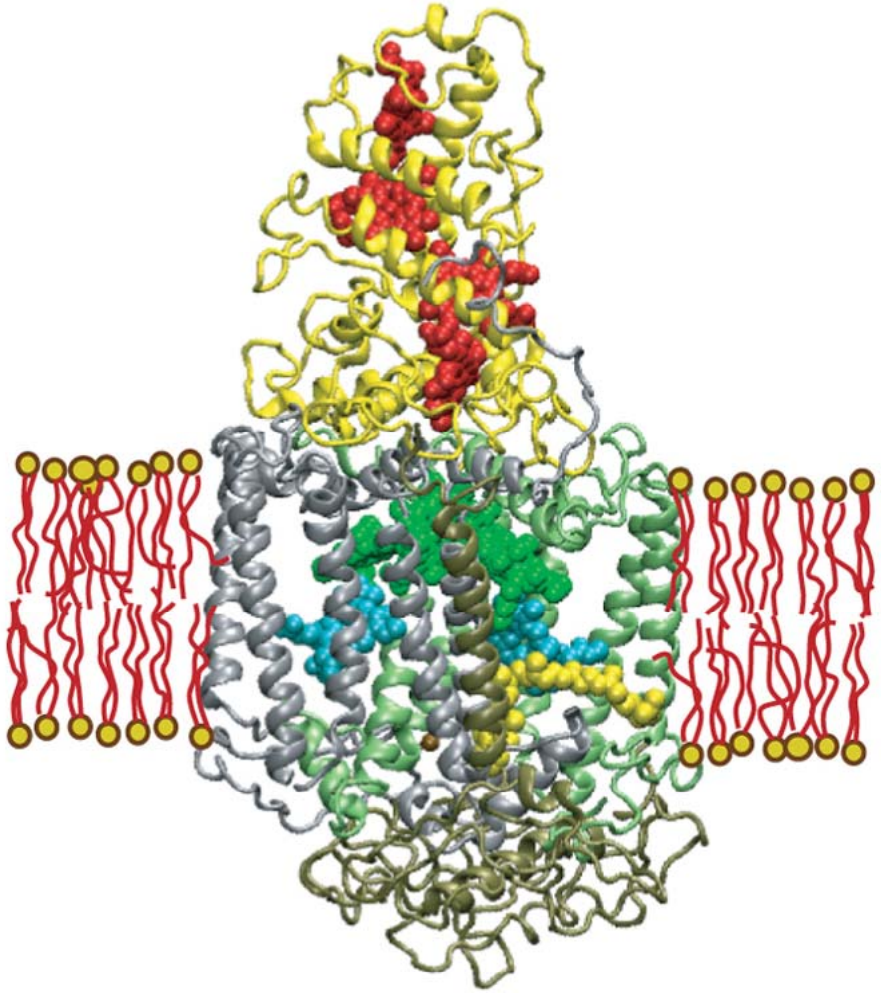

FIGURE 21.43

The photosynthetic reaction in the membrane of the purple bacterium. The four hemes in the cytochrome subunit are shown in red. The LH1 light-harvesting system that surrounds the reaction center is not shown. (Figure provided by William Parson)

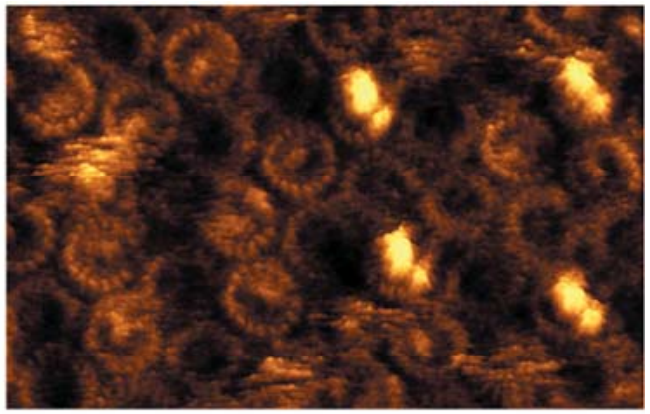

(a)

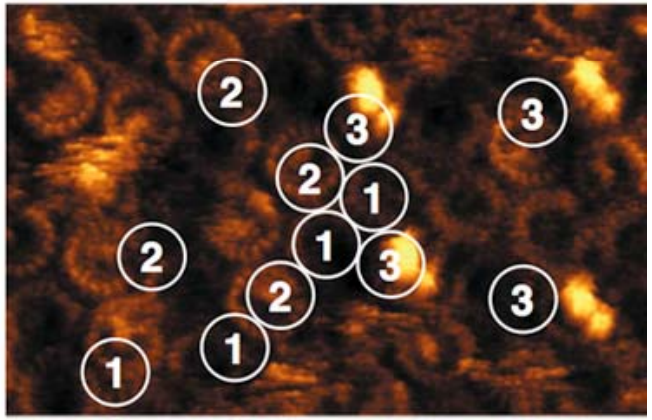

(b)

(c)

FIGURE 21.44

(a, b) A scan is shown over a cluster of LH1 complexes after a portion of the surface has been removed through nanodissection. The regions labeled 1, 2, and 3 correspond to the LH1 complex without a reaction center, the LH1 complex containing a reaction center without the cytochrome subunit, and the intact LH1-reaction center complex including the cytochrome subunit, respectively. (c) Higher resolution images are shown of 1, 2, and 3 obtained by averaging over similar unit in part (a).

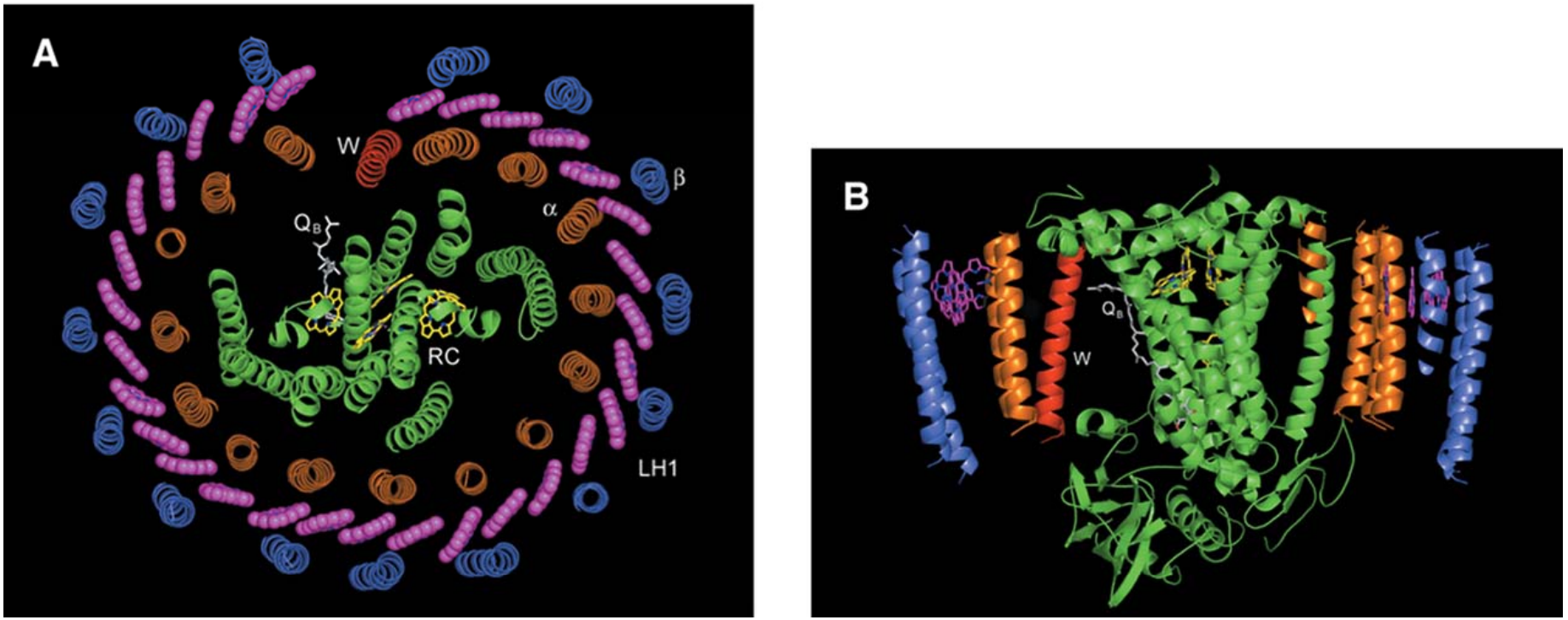

FIGURE 21.45

Schematic model of the RC-LH1 core complex in *Rhodoseudomonas palustris* obtained from X-ray diffractions studies. The views are (A) perpendicular and (B) parallel to the membrane plane. The most important elements of LH1 are Bchl proto absorbers, shown in red, and the transmembrane helical proteins, shown in green and light blue. Note the gap in LH1 to the left of the helical protein labeled W.

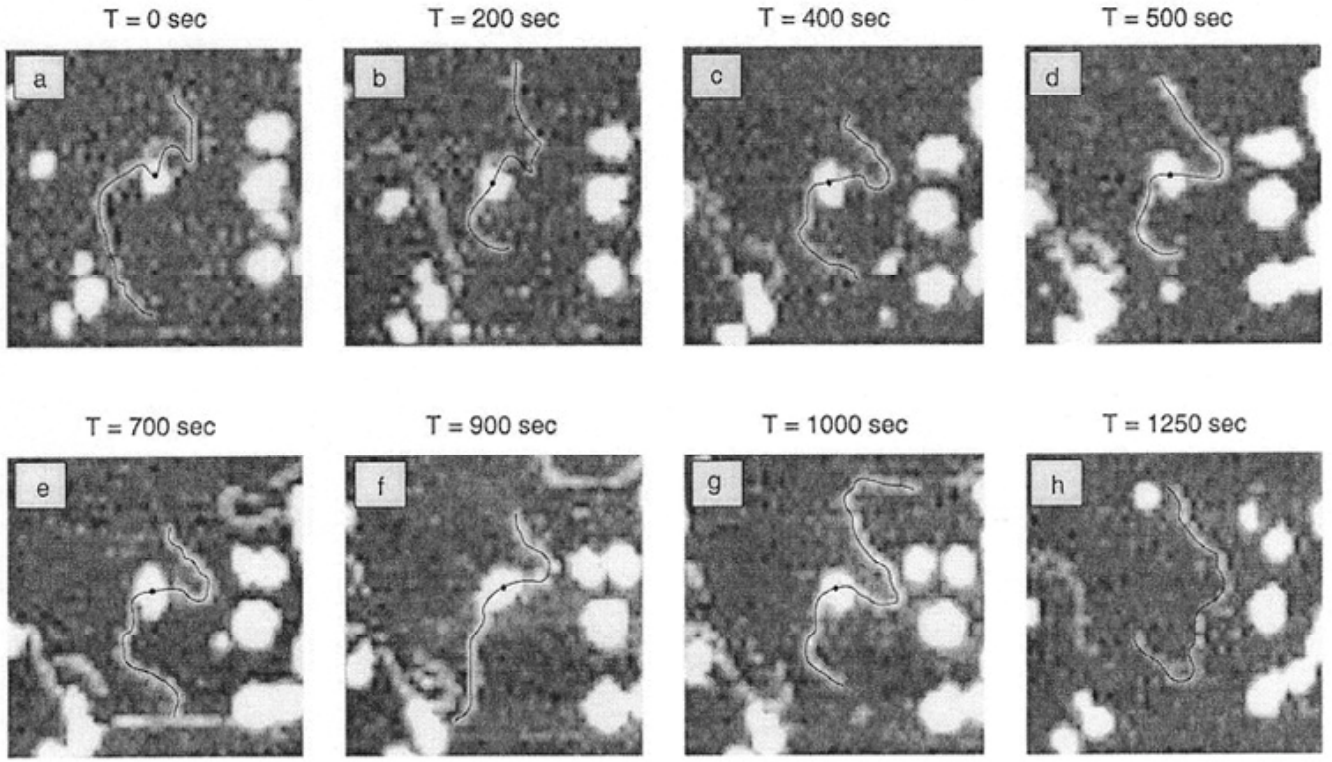

FIGURE 21.46

(a-h) Images are shown of the diffusion of nonspecific binary complexes of RNAP along the 1001

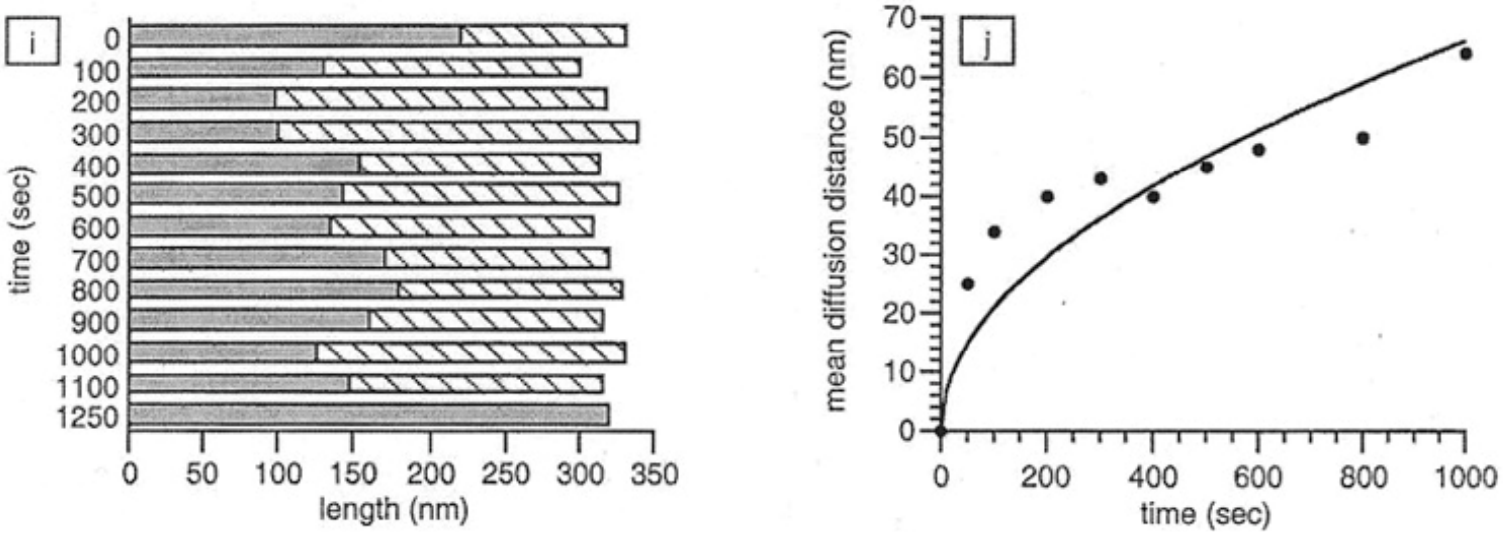

FIGURE 21.46

(continued)

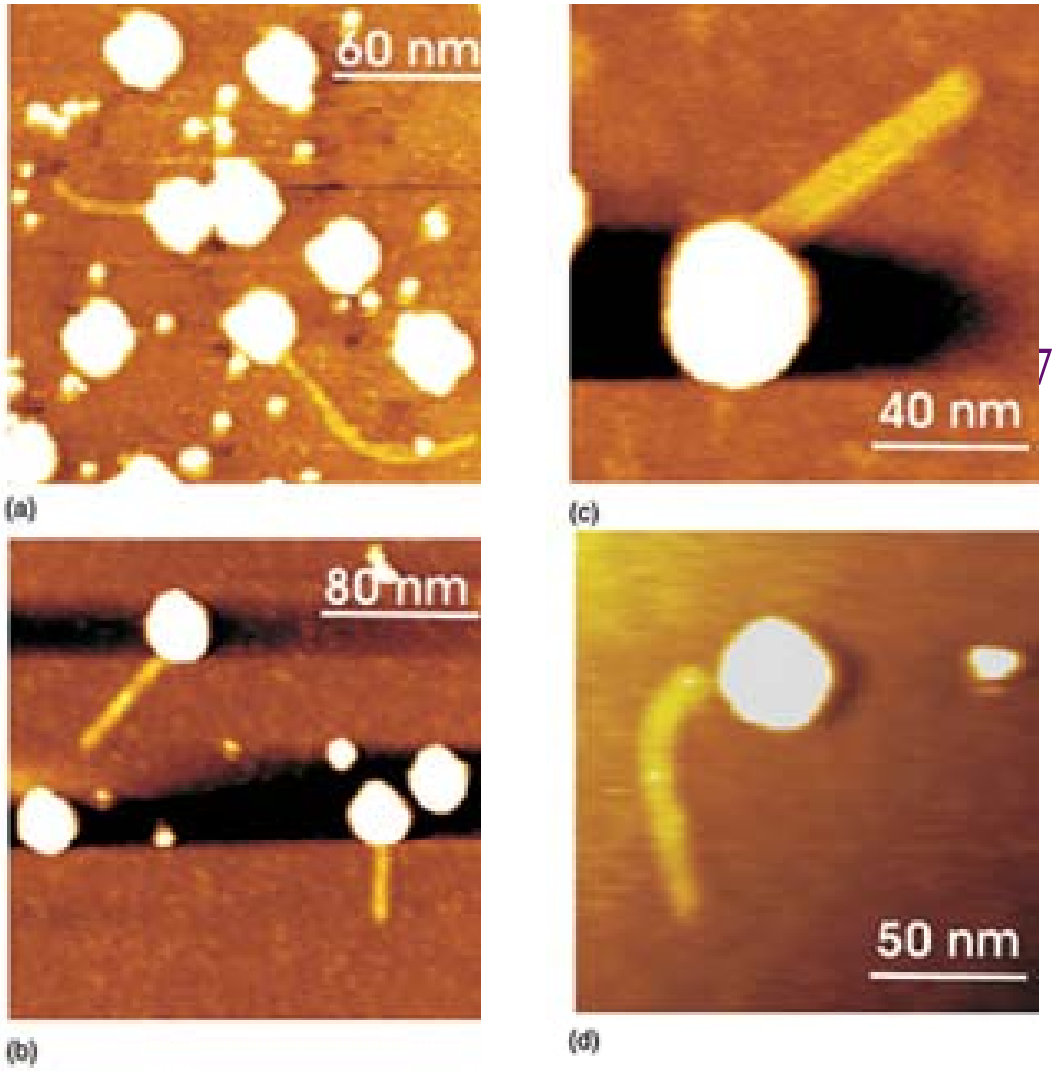

FIGURE 21.47

Partially released RNA molecules are seen as they are being released from the virus capsid. (a) Bent strands emerge from the ~31-nm-diameter virus capsids. Smaller white dots are debris of the virus capsid. (b, c) Straight RNA segments are shown emerging from the capsid. (d) A bent segment at higher magnification than the other parts. The apparent width of the RNA is due to a convolution of the true width with the ~20-nm-tip radius.

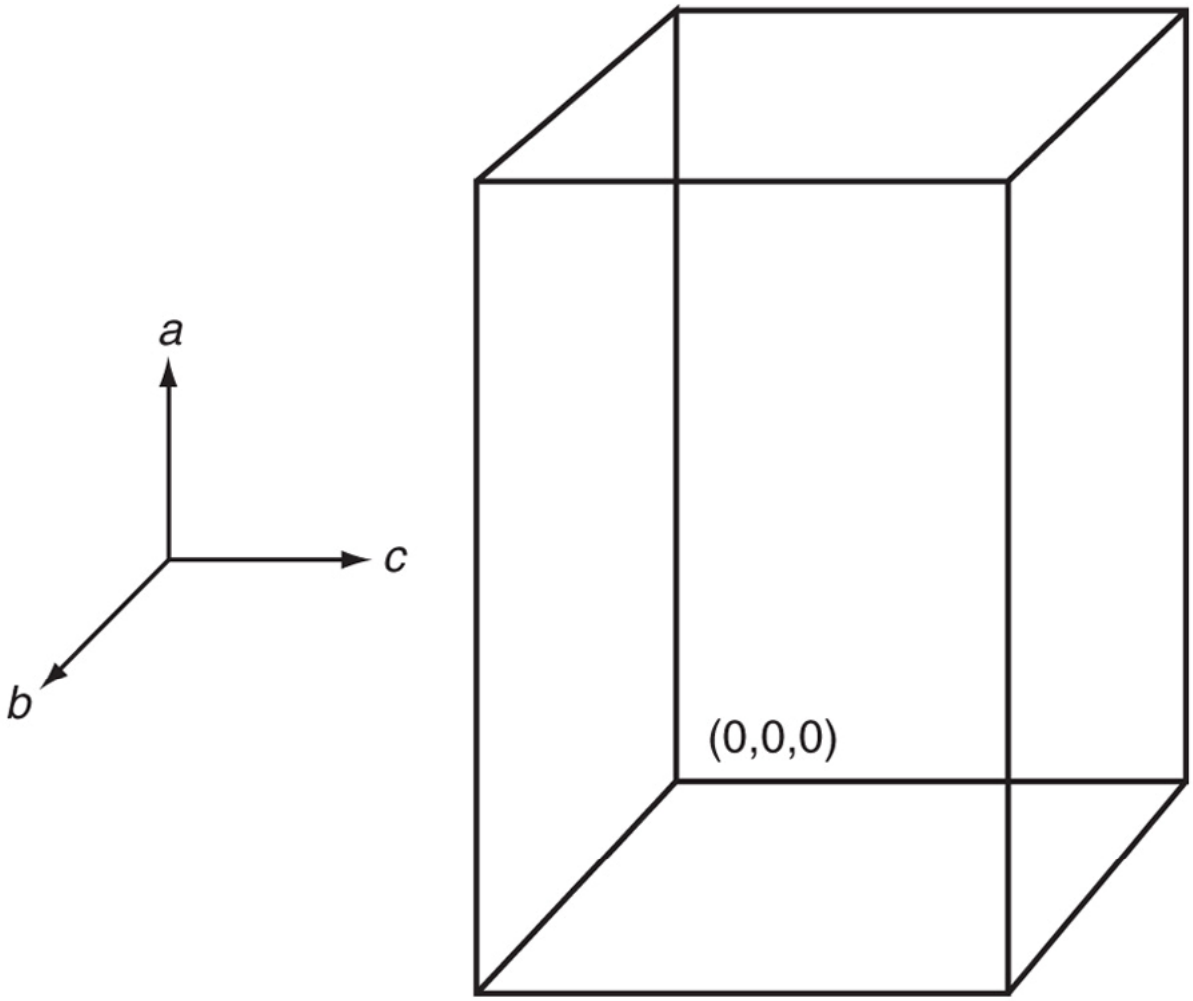

Problems 21.5

End of Lecture

Slide Downloading

http://ytlab.kmu.edu.tw